Large Eddy Simulation of Flow Over Submerged Cylinders and Leaky Barriers

Fawaz Mohammed Y Alzabari
School of Engineering
Cardiff University, Wales, UK

Supervised by:

Dr. Catherine Wilson and Dr. Pablo Ouro

This thesis is submitted in partial fulfillment of the requirements for the degree of

Doctor of Philosophy (Ph.D.)

2023

Acknowledgement

With immense pleasure and a deep sense of gratitude, I wish to express my sincere thanks to my supervisor **Dr. Pablo Ouro** for his guidance throughout my research at the School of Engineering at Cardiff University. Under his supervision, I have significantly enhanced my skills and expertise, which will undoubtedly be invaluable in my future career as a researcher. I also appreciate the valuable inputs from **Dr. Catherine Wilson**; they have been immensely helpful.

Over the years, I have shared many hours of coding, simulating, and post-processing with my colleagues. I am deeply thankful to them, and I would like to give special mention to those who have become close friends and have been a tremendous support: **Nicolas Hanousek** and **Samuel Rowley**. My gratitude also extends to members of the IAHR Cardiff Young Professional Network, as it has been an enriching experience for me.

My sincere thanks go to **Najran University** for funding my PhD. I am also grateful to the research academics and research staff at the School of Engineering who were always eager to assist during my research journey. Furthermore, I would like to acknowledge the support of the Supercomputing Wales project, which provided the essential supercomputing resources for this project.

I wish to extend my profound gratitude to **my parents** for all the sacrifices they made during my research journey. Tragically, my father passed away in the first year of my Ph.D. He had been a pillar of support for me and his absence weighed heavily on my heart. Nonetheless, his memory and encouragement have been guiding lights in my pursuit. My heartfelt thanks to my **sibling**, who gave me the freedom and support to chase my dreams while being away from home for so long. I also extend my deepest appreciation to my **friends** in Saudi Arabia for standing by me throughout this long journey.

Last, but certainly not least, I express my profound thanks to my wife **Rana** and my daughter **Mila** for their constant encouragement, moral support, patience, and understanding.

Cardiff

2023 **Fawaz Alzabari**

Abstract

Extreme weather events are increasing their frequency due to climate change, leading to more recurrent destructive flooding incidents over the recent years, which require the development of potential solutions. For this, leaky barriers are a natural-based flood mitigation solution that can reduce and delay peak flow events. Understanding the local hydrodynamics involved in the flow around these mostly-submerged hydraulic structures is essential to enhance their performance in retaining flood events but also to ensure their structural integrity. Numerical methods arise as a complementary tool to experimental approaches that enable a further understanding of the fluid dynamics around submerged cylinders used in these leaky barriers. This thesis adopts a large-eddy simulation (LES) computational approach, incorporating the level-set method (LSM) to capture free-surface deformation. The hydrodynamics around a single cylinder are investigated, finding a critical Froude number threshold when free-surface effects become pronounced and influence the hydrodynamic coefficients, vortex shedding patterns, and wake structures downstream of the cylinder. Proper-orthogonal decomposition (POD) is employed to quantify and analyse energetic coherent structures developed behind the cylinder, revealing redistribution in the energy contribution as flow conditions approach shallower conditions. Furthermore, POD is used to compare flow pattern predictions from two separate LESs of flow past a single horizontal cylinder in very shallow conditions, highlighting the limitations of traditional rigid-lid modelling and emphasising the importance of adopting LSM for accurate free surface and flow dynamics. The hydrodynamics of leaky barriers are simulated and analysed with LES to investigate the impact of barrier's inclination and length on the flow. Results reveal configurations with flatter inclinations or shorter barrier lengths lead to reduced bed scour risk and improved performance. Two novel methodologies for estimating water depths and velocities around leaky barriers have been proposed and validated using experimental and simulation datasets, providing an easy-to-use design tool for eco-friendly wood structures in future flood management. This thesis seeks to enhance the current understanding of the complex hydrodynamic phenomena developed in the flow around fully-submerged horizontal circular cylinders and leaky barriers, providing essential insights for practical flood management strategies and environmental conservation efforts.

TABLE OF CONTENTS

Acknowledgements ii

Abstract iii

List of figures x

List of tables xxi

List of publications xxii

Nomenclature xxiii

1 Introduction **1**

1.1 Background 1

1.2 Literature review 7

1.2.1 Flow past a circular cylinder and boundary effects 7

1.2.2 Leaky barriers and backwater rise 17

1.2.3 Modelling free-surface flows 22

1.2.3.1 Rigid-lid approximation 23

1.2.3.2 Interface tracking methods 25

1.2.3.3 Interface-capturing methods 27

1.3 Objectives and thesis structure 30

2 Numerical framework **33**

2.1 Governing equations 33

2.2 Fractional-step method 37

2.3 Immersed-boundary method 39

2.4 Level-set method 42

2.5 Free-surface tension 44

2.6 Proper orthogonal decomposition 45

2.7 Summary 48

3 Hydrodynamic Characteristics of Circular Cylinder Flows in Shallow Conditions 49
3.1 Aim of this chapter . . . 49
3.2 Summary . . . 49
3.3 Computational setup . . . 50
3.3.1 Numerical validation . . . 52
3.4 Results and discussion . . . 54
3.4.1 Free surface profiles . . . 54
3.4.2 Instantaneous flow field . . . 54
3.4.2.1 $Fr = 0.26$ ($h/D = 2.1$) . . . 55
3.4.2.2 $Fr = 0.31$ ($h/D = 1.5$) . . . 56
3.4.2.3 $Fr = 0.40$ ($h/D = 0.9$) . . . 56
3.4.2.4 $Fr = 0.45$ ($h/D = 0.7$) . . . 57
3.4.2.5 $Fr = 0.53$ ($h/D = 0.5$) . . . 57
3.4.2.6 Power Spectral Density analysis . . . 58
3.4.3 Time-averaged flow field . . . 60
3.4.4 Mean recirculation region . . . 67
3.4.5 Centreline profile . . . 68
3.4.6 Recovery of mean streamwise velocity . . . 70
3.4.7 Gap flux ratio . . . 71
3.4.8 Continuity equation terms analysis . . . 72
3.4.9 Mean kinetic energy . . . 73
3.4.10 Dominant shedding frequency and hydrodynamic coefficients . . . 76
3.5 Closure . . . 79

4 Coherence of the Vortex Shedding Dynamics Shed by a Circular Cylinder in Very Shallow Free-surface Flows Quantified with Proper Orthogonal Decomposition 81
4.1 Aim of the chapter . . . 81
4.2 Summary . . . 81
4.3 Methodology . . . 83
4.4 Case i: Analysis of turbulent structures shed in the cylinder's wake using POD . . . 83
4.4.1 Results and discussion . . . 83

4.4.1.1 Snapshot dependence validation . . . 83
4.4.1.2 Energy contribution of the POD modes . . . 84
4.4.1.3 POD spatial modes . . . 86
4.4.1.4 POD temporal coefficients and associated Strouhal number . . . 87
4.4.1.5 Lissajous curves . . . 89
4.4.1.6 Velocity field reconstruction . . . 91
4.4.1.7 Analysis of the spectral energy decay . . . 94
4.5 Case ii: Impact of RL and LSM on wake characteristics . . . 95
4.5.1 Results and discussion . . . 95
4.5.1.1 Instantaneous flow field . . . 95
4.5.1.2 Energy distribution of the POD modes . . . 97
4.5.1.3 POD spatial modes . . . 98
4.5.1.4 POD temporal coefficients . . . 98
4.5.1.5 Frequency features of temporal coefficients . . . 100
4.6 Closure . . . 100

5 Flow Hydrodynamics around In-stream Leaky Barriers and Potential Sediment Mobilisation 103

5.1 Aims of this chapter . . . 103
5.2 Summary . . . 103
5.3 Case i: Analysis of leaky barriers with inclined designs . . . 104
5.3.1 Computational setup . . . 104
5.3.2 Results and discussion . . . 107
5.3.2.1 Free surface profiles . . . 107
5.3.2.2 Instantaneous flow field . . . 108
5.3.2.3 Time-averaged flow characteristics . . . 112
5.3.2.4 Recirculation region . . . 121
5.3.2.5 Recovery of mean streamwise velocity . . . 122
5.3.2.6 Gap flow ratio . . . 124
5.3.2.7 Decay of the maximum jet velocity . . . 126
5.3.2.8 Bed shear stress . . . 126
5.3.2.9 Hydrodynamic coefficients . . . 132

5.3.3 Leaky barrier design: performance evaluation from an integral hydrodynamic perspective . . . 134
5.4 Case ii: Comparative analysis of leaky barriers with varied longitudinal lengths . 135
5.4.1 Computational setup . . . 135
5.4.2 Results and discussion . . . 137
5.4.2.1 Free surface profiles . . . 137
5.4.2.2 Time-averaged flow characteristics . . . 138
5.4.2.3 Recirculation region . . . 141
5.4.2.4 Potential bed scour . . . 142
5.5 Closure . . . 143

6 Predictive Methods for Estimating Water Depth and Velocity Due to Leaky Barriers 147

6.1 Aim of the chapter . . . 147
6.2 Summary . . . 147
6.3 Methodology . . . 148
6.3.1 Momentum method . . . 149
6.3.2 Leaky barrier afflux method . . . 152
6.3.3 Estimating flow velocity and error metrics . . . 155
6.4 Results and discussion . . . 155
6.4.1 Prediction of upstream water depth and velocity using downstream data . . 155
6.4.2 Prediction of downstream water depth and velocity using upstream data . . 158
6.4.3 Sensitivity of the momentum method to the drag coefficient . . . 161
6.5 Closure . . . 161

7 Conclusions and Outlook 163

Appendices

Appendix A Free-surface tension 170

Appendix B Mesh dependence 171

Appendix C Free-stream turbulence 172

Appendix D Fixed water depth at the inlet 173

Appendix E Upstream Water Depth: Derivation of the Estimation Formula 174

References 178

LIST OF FIGURES

1.1 Sketches by Leonardo da Vinci: (a) water passing a rectangular obstacle; (b) co-existence of eddies with different length scales. Source: (*Leonardo da Vinci Drawings* 2011). 2
1.2 Wake patterns for different values of *Re*. Adapted from (Van Dyke 1982). . . . 3
1.3 Examples of structures interacting with the free surface: (a) submerged pipelines, source: (*agru* 2018); (b) offshore platform, source: (*Offshore Platform Topsides* 2023). 4
1.4 (a) Cumulative global economic (b) and insured losses by peril, 1991–2021, Source: Swiss Re Institute (Bevere and Remondi 2022). 5
1.5 Field photographs of (a) engineered leaky barrier at Killhope Burn (North of England) by the environment agency, source: (*North East project* 2021) and (b) another leaky barrier depicting backwater rise upstream of the dam at Pickering (North East England), source: (*slowtheflow* 2019). 5
1.6 Schematic representation of the flow attenuation process of leaky barriers, depicting the temporal storage of flow upstream of the barrier, subsequent spilling onto floodplains, increased groundwater infiltration and the resulting reduction in downstream flow depths. Figure adapted from (Muhawenimana et al. 2021). 6
1.7 Side view of a three-cylinder configuration for (a) in-line, (b) side-by-side and (c) staggered arrangements. 18
1.8 Distribution of normalised turbulent kinetic energy in a horizontal plane near the bed at $z/H = 0.1$ as computed by (a) free-surface-resolved simulation; (b) rigid-lid simulation (Kara et al. (2015a)). 25
1.9 Contours of normalised spanwise vorticity at $Fr = 0.45$ as computed by (a) rigid-lid simulation and (b) free-surface-resolved simulation. The free surface is depicted as a solid black line (Alzabari et al. (2022)). 25

2.1 A representation of the energy spectrum showcasing the differentiation between the production, inertial, and dissipation ranges. 35

2.2 Two-dimensional depiction of the Cartesian staggered grid. The black-filled symbols within the square boundary represent the neighbours used in the interpolation for a Lagrangian marker (filled-red circle). Pressure nodes are denoted by 'x', x-velocity nodes by '□', y-velocity nodes by '◯', and Lagrangian markers by red circles. ΔV_L refers to the Lagrangian marker volume. 40

3.1 Schematic of the computational domain adopted for the LES with the horizontal cylinder of diameter (D) located at a height G from the bottom surface. The total water depth is denoted by H, while that free-surface elevation overtopping the cylinder is h. The inflow boundary condition with a logarithmic velocity distribution is also indicated. 51

3.2 Vertical profiles of (a) mean streamwise velocity $\langle u \rangle$, (b) turbulence intensity $\langle u' \rangle$, (c) mean vertical velocity $\langle w \rangle$, and (d) turbulence intensity $\langle w' \rangle$ at different locations downstream of the cylinder. Comparison between experimental (symbols) and LES (lines) results. The dashed lines indicate the cylinder position. 53

3.3 Free-surface profiles obtained from the LES for all Fr cases, including experimental values for the case with $Fr = 0.31$, where (a) represents all free-surface profiles together, whilst (b) only shows comparisons of the LES results with the experimental data for $Fr = 0.31$. Vertical dashed lines indicate cylinder position. . 55

3.4 Contours of normalised vorticity behind the cylinder for the case: $Fr = 0.26$, at four instants normalised by the peak frequency $t^* = 2.9$, 3.2, 3.5, and 3.8. The free surface is depicted as a solid-black line. The yellow dots mark the monitoring points for spectral analysis. 56

3.5 Contours of normalised vorticity behind the cylinder for the case: $Fr = 0.31$, at four instants normalised by the peak frequency $t^* = 2.9$, 3.2, 3.5, and 3.8. The free surface is depicted as a solid -black line. The yellow dots mark the monitoring points for spectral analysis. 57

3.6 Contours of normalised vorticity behind the cylinder for the case: $Fr = 0.40$, at four instants normalised by the peak frequency $t^* = 2.9$, 3.2, 3.5, and 3.8. The free surface is depicted as a solid-black line. The yellow dots mark the monitoring points for spectral analysis. 58

3.7 Contours of normalised vorticity behind the cylinder for the case: $Fr = 0.45$, at four instants normalised by the peak frequency $t^* = 2.9$, 3.2, 3.5, and 3.8. The free surface is depicted as a solid-black line. The yellow dots mark the monitoring points for spectral analysis. 59

3.8 Contours of normalised vorticity behind the cylinder for the case: $Fr = 0.53$, at four instants normalised by the peak frequency $t^* = 2.9$, 3.2, 3.5, and 3.8. The free surface is depicted as a solid-black line. The yellow dots mark the monitoring points for spectral analysis. 60

3.9 Plots of the PSD obtained from the vertical velocity fluctuations $\langle u' \rangle$ at six stations downstream of the cylinder along the upper shear layer of the cylinder ($z/D \approx 1.2$) for all simulated cases. 61
3.10 Side elevation contour plots of the LES computed (a-c) streamwise velocity $\langle u \rangle$, (d-f) vertical velocity $\langle w \rangle$, (g-i) streamwise turbulence intensity $\langle u' \rangle$, (j-l) vertical turbulence intensity $\langle w' \rangle$, and (m-o) Reynolds shear stress $-\langle u'w' \rangle$, normalised by the bulk velocity for Fr = 0.26, 0.31 and 0.40. The mean free surface is depicted as a solid-black line. 62
3.11 Side elevation contour plots of the LES computed (a-b) streamwise velocity $\langle u \rangle$, (c-d) vertical velocity $\langle w \rangle$, (e-f) streamwise turbulence intensity $\langle u' \rangle$, (g-h) vertical turbulence intensity $\langle w' \rangle$, and (i-j) Reynolds shear stress $-\langle u'w' \rangle$, normalised by the bulk velocity for Fr = 0.45 and 0.53. The mean free surface is depicted as a solid-black line. 63
3.12 Vertical profiles of normalised vertical Reynolds shear stress $(-\langle u'w' \rangle)/U_0^2$ at different locations downstream of the cylinder for the different simulated cases. The cylinder position is depicted as horizontal dot-dash lines. 64
3.13 Side elevation contour plots of the LES computed turbulent kinetic energy (tke) for all of the simulated cases. The vertical lines mark the locations at which vertical profiles of the mean tke are plotted and shown in Fig. 3.14. The mean free surface is depicted as a solid-black line. 65
3.14 Vertical profiles of (a) turbulent kinetic energy (tke), (b) streamwise velocity fluctuations $\langle u' \rangle$, and (c) vertical velocity fluctuations $\langle w' \rangle$ at six locations downstream of the cylinder along the water depth for all of the simulated cases. The dashed lines indicate the cylinder position. 66
3.15 Comparison of the mean recirculation regions computed using LES for all simulated cases, with contours of the mean streamwise velocity normalised by the bulk velocity. Recirculation length and other characteristics of the recirculation regions, which include the length of the mean recirculation zone (L_R), the transverse spacing between the primary pair (S), the ground bubble height (V), and the distance from the centre of the ground bubble to the centre of the cylinder (B), are overlaid only for the case (b) Fr = 0.31 for simplicity. 67
3.16 Centreline profiles of normalised (a) streamwise velocity $\langle u \rangle$, (b) streamwise turbulence intensity $\langle u' \rangle$, (c) vertical velocity $\langle w \rangle$, and (d) vertical turbulence intensity $\langle w' \rangle$ for all submergence cases. 69
3.17 Progression of velocity deficit ($\Delta\langle u \rangle$) computed from the difference between the upstream profile (x/D = -8) and selected downstream profiles for all of the simulated cases. The horizontal dashed lines indicate the cylinder's position. The vertical line indicates the zero-velocity deficit ($\Delta\langle u \rangle = 0$). 70

3.18 Plots of (a) the variation of the gap flux ratios with gap position and Froude number, and (b) a schematic diagram illustrating the definition of the gap flux ratio and gap position, where q_u represents the upstream flux, q_t and q_b are the fluxes at the top and bottom gaps, respectively. 71
3.19 Contours of the continuity equation terms for all simulated cases, $\partial u/\partial x$ (left-hand) and $\partial w/\partial z$ (right-hand). 72
3.20 Contour plots of the investigated components of MKE, namely (I) the convection of MKE by the mean flow and (II) work due to the pressure gradient for all simulated cases. 74
3.21 Contour plots of the investigated components of MKE, namely (IV) transport of MKE by turbulent stresses and (V) the production term for all simulated cases. . 75
3.22 Plots of (a-e) time history of drag and lift coefficients of the cylinder and (f-j) their corresponding PSD distribution for all simulated cases. 77
3.23 Variation of (a) the drag and lift coefficients and (b) the Strouhal number of the horizontal cylinder as a function of the Froude number. 78

4.1 Sensitivity analysis of the energy contribution when adopting (a) different number of snapshots based on 100 POD modes and (b) increasing POD modes with 900 snapshots. 84
4.2 Comparison of the (a) energy contribution and (b) cumulative value for the 100 first POD modes for the different submergence cases. 84
4.3 First six POD spatial modes obtained for cases with Fr = 0.26, 0.31, 0.40 and 0.45. 85
4.4 Six POD spatial modes obtained for the shallowest case: Fr = 0.53. 86
4.5 Temporal coefficients of the first six POD modes obtained for the cases with Fr = 0.26, 0.31, 0.40, 0.45 and 0.53. 87
4.6 PSD of the temporal coefficients from the first six POD modes obtained for the cases with Fr = 0.26, 0.31, 0.40, 0.45 and 0.53. The dotted-dashed line indicates the Strouhal number (St) frequency associated to the periodic vortex shedding and the dashed line indicates its first harmonic $(2St)$. 89
4.7 The Lissajous plots of the first six POD coefficients for cases with Fr = 0.26, 0.31, 0.45 and 0.53. The linear fit with a circular curve is shown in the first row. . . . 90
4.8 Comparison between the LES (first row of figures) velocity data with those reconstructed with the ROM based on an increasing number of POD modes for Fr = 0.26 (left-hand) and 0.31 (right-hand). 91
4.9 Comparison between the LES (first row of figures) velocity data with those reconstructed with the ROM based on an increasing number of POD modes for Fr = 0.45 (left-hand) and 0.53 (right-hand). 92

4.10 A comparison between the instantaneous velocity obtained from the LES and the ROMs over the time history adopted for the POD analysis for the different Froude numbers. 93
4.11 The mean error plot of the reconstructed velocity (a) over a vertical plane at a single snapshot and (b) at $x/D = 3.5$, $z/D = 1.2$ for all snapshots as a function of the number of POD modes. 93
4.12 PSD of the vertical velocity fluctuation (w') obtained at a point ($x/D = 1.1$ and $z/D = 1.5$) from LES long time series (a–c) and truncated time series from LES and POD-based ROM at $Fr = 0.31$, 0.45, and 0.53. 94
4.13 Contours of normalised vorticity behind the cylinder for the case: $Fr = 0.45$, at four instants normalised by the peak frequency $t^* = 6.5$, 6.9, 7.3 and 7.7. (a-d) RL and (e-h) LSM. The free surface is depicted as a solid-black line. 96
4.14 Comparison of the energy contribution (a) and its cumulative value (b) for the first 100 POD modes. 97
4.15 First eight POD spatial modes obtained for the RL (left-hand) and LSM (right-hand) cases. 98
4.16 Variation of the temporal coefficients of the first eight POD spatial modes for both RL (left-hand) and LSM (right-hand) cases. 99
4.17 PSD of the first two POD coefficients obtained from the RL and LSM cases. The vertical lines indicate the Strouhal number associated with the periodic vortex shedding, namely $St = 0.32$ (dotted-dashed line) and 0.42 (dashed line) corresponding to the RL and LSM cases, respectively. 100

5.1 (a) Schematic of the computational domain adopted in the two-phase LES depicting the main characteristics of a leaky barrier structure. The inflow boundary conditions with a logarithmic approaching velocity profile are also indicated. (b) The structure has a height H_s and a longitudinal length L_s, with vertical inter-cylinder gaps b and a vertical gap between the structure and the bottom wall b_0. H_1 and H_2 represent the mean upstream and downstream flow depths, respectively. The term ΔH refers to the backwater rise, which is calculated as the difference between the upstream and downstream water depths. This structure is composed of a horizontal channel spanning cylinders of diameter D aligned perpendicularly to the flow direction. (c) The leaky barrier is inclined at different angles (γ), where d and u indicate the direction of the barrier inclination in the downstream and upstream directions, respectively. 105
5.2 Vertical profiles of time-averaged streamwise velocity normalised by the bulk velocity $\langle u \rangle / U_0$ at three locations upstream of the leaky barrier. Comparison between experimental (symbols) and LES (lines) results. Horizontal dashed lines indicate the cylinder positions of the barrier. 107

5.3 Free-surface profiles obtained from the LES for (a) downstream-inclined cases and (b) upstream-inclined cases, along with the LES and experimental values of the non-inclined case (S0). Vertical dashed lines indicate the origin of the x coordinates located at the downstream edge of the top log. 109
5.4 (a) The contour of normalised vorticity over a vertical plane at the middle of the spanwise domain length for the non-inclined structure (S0). The free surface is depicted as a solid-black line. (b) The power spectral density (PSD) of the vertical velocity fluctuation (w') obtained at six points downstream of the barrier along the lower shear layer of the bottom cylinder ($z/b_0 \approx 1.0$). The vertical dashed line indicates the Strouhal number (St) equal to 0.373. 109
5.5 Contour plots of (a, c and e) of normalised vorticity over a vertical plane at the middle of the spanwise domain length comparing the downstream-inclined structures (S1d, S2d and S3d). The free surface is depicted as a solid-black line. (b, d and f) PSD of the vertical velocity fluctuation (w') at six points downstream of the barrier along the lower shear layer of the bottom cylinder ($z/b_0 \approx 1.0$). The vertical dashed line indicates the Strouhal number (St). 110
5.6 Contour plots of (a, c and e) normalised vorticity over a vertical plane at the middle of the spanwise domain length comparing the upstream-inclined structures (S1u, S2u and S3u). The free surface is depicted as a solid-black line. (b, d, f) Power spectral density (PSD) of the vertical velocity fluctuation (w') at six points downstream of the barrier along the lower shear layer of the bottom cylinder ($z/b_0 \approx 1.0$). The vertical dashed line indicates the Strouhal number (St). 112
5.7 Vertical profiles of normalised mean streamwise velocities $\langle u \rangle / U_0$ at different locations upstream of the barrier for (a) the S0 case, (b, d and f) the downstream-inclined cases (S1d, S2d and S3d, respectively), and (c, e, g) the upstream-inclined cases (S1u, S2u and S3u, respectively). The dashed lines indicate the positions of the cylinders. 113
5.8 Vertical profiles of normalised mean vertical velocities $\langle w \rangle / U_0$ at different locations upstream of the barrier for (a) the S0 case, (b, d and f) the downstream-inclined cases (S1d, S2d and S3d, respectively), and (c, e, g) the upstream-inclined cases (S1u, S2u and S3u, respectively). The dashed lines indicate the positions of the cylinders. 114
5.9 Side elevation contour plots of the LES computed (a) streamwise velocity, (b) vertical velocity, (c) turbulent kinetic energy and (d) Reynolds shear stress, normalised by the bulk velocity for the S0 case. The vertical lines mark the locations at which vertical profiles of the mean quantities are plotted and shown in Figs. 5.10 and 5.11.115

5.10 Vertical profiles of (a) normalised mean streamwise velocity $\langle u \rangle / U_0$ and (b) vertical velocity $\langle w \rangle / U_0$ at six locations downstream of the barrier. Comparison between experimental (symbols) and LES (lines) results. Horizontal dashed lines indicate the positions of the cylinders. 117
5.11 Vertical profiles of (a) streamwise turbulence intensity $\langle u' \rangle$, (b) vertical turbulence intensity $\langle w' \rangle$, and (c) vertical Reynolds shear stress $-\langle u'w' \rangle$ at different locations downstream of the barrier. Comparison between experimental (symbols) and LES (lines) results. Horizontal dashed lines indicate the positions of the cylinders. . 118
5.12 Side elevation contour plots of the LES computed (a-c) streamwise velocity, (d-f) vertical velocity, (g-i) turbulent kinetic energy and (j-i) Reynolds shear stress, normalised by the bulk velocity for the downstream-inclined cases (S1d, S2d and S3d). 119
5.13 Side elevation contour plots of the LES computed (a-c) streamwise velocity, (d-f) vertical velocity, (g-i) turbulent kinetic energy, and (j-i) Reynolds shear stress, normalised by the bulk velocity for the upstream-inclined cases (S1u, S2u and S3u).120
5.14 Comparison of the mean recirculation regions computed using LES for all simulated cases, with contours of the mean streamwise velocity normalised by the bulk velocity. 122
5.15 Progression of velocity deficit $\left(\Delta\langle u \rangle = \frac{\langle u \rangle - \langle u \rangle_{x/b_0=-10}}{\langle u \rangle_{x/b_0=-10}}\right)$ computed from the difference between the upstream profile (x/b_0 = -10) and selected downstream profiles for (a) the S0 case, (b, d and f) the downstream-inclined cases (S1d, S2d and S3d, respectively), and (c, e, g) the upstream-inclined cases (S1u, S2u and S3u, respectively). The horizontal dashed lines indicate the positions of the cylinders. The vertical line indicates the zero-velocity deficit ($\Delta\langle u \rangle$ = 0). 123
5.16 (a) The variation of the gap flux ratio (F_2/F_1) with gap position and barrier inclination, and (b) schematic diagram illustrating the definition of the gap flux ratio and gap positions (gb_0, gb_1, gb_2, gt), where gb_0 represents the bottom gap, gb_1 represents the lower inter-cylinder gap, gb_2 represents the upper inter-cylinder gap and gt represents the top gap between the top cylinder and the free surface. F_1 represents the flux at the upstream point of x/b_0 = -10, while F_2 represents the flux at the different gap positions. 124
5.17 Decay of local maximum velocity $\langle u \rangle_{\max}$ downstream of barriers relative to depth-averaged initial jet velocity $\langle u \rangle_{b_0}$ in the lower gap region ($0 \leq z/b_0 \leq 1$) with increasing longitudinal distance from the barrier $(x/b_0)^{-0.5}$. The vertical dotted line at x/b_0 = 1 denotes the initial downstream point where the average velocity over the bottom gap is calculated. The vertical dotted line at x/b_0 = 4 denotes the length of the potential core region, after which the maximum jet velocity experiences a similar decay pattern. The dashed-black line indicates the rate of decay scaling with a decay coefficient of 3.0. 125

5.18 Comparison of the wall shear stress τ_w normalised by an initial bed shear stress τ_{w_0} (x/b_0 = -6) for (a) the downstream-inclined barriers and (b) the upstream-inclined barriers, including the values of the non-inclined barrier (S0). The vertical dashed line at $x/b_0 = 0$ denotes the origin of the x coordinates. which represents the downstream edge of the top cylinder in all cases. 127
5.19 Shields diagram of sediment particles movement, giving the dimensionless critical mobility Shields parameter τ_{cr} as a function of the sediment Reynolds number Re_*, Liu (1998). 128
5.20 Modified Shields diagram of sediment particles movement using the dimensionless grain diameter d_*, Julien (1995). 129
5.21 Normalised bed shear stress profiles for the vertical and the inclined barriers to the upstream and downstream directions at (a-b) d_{50} = 0.8 mm, (c-d) d_{50} = 1.0 mm, (e-f) d_{50} = 1.2 mm and (g-h) d_{50} = 1.4 mm. The horizontal black line is the threshold line of motion, where $\tau_w/\tau_c > 1$ depicts possible sediment motion. The vertical dashed line is the origin of the x coordinates, which represents the downstream edge of the top cylinder in all cases. 131
5.22 Plot of the estimated scour length normalised by the bottom gap height (L_{sc}/b_0) for the simulated cases considering four different sizes of sediment particle diameter (d_{50} = 0.8, 1.0, 1.2, and 1.4 mm), plotted with a confidence interval of 10%. 132
5.23 Time-averaged (a) drag and (b) lift coefficients of the top, middle and bottom cylinders for all of the simulated leaky barriers. 133
5.24 Schematic of the computational domain adopted for the LES of a leaky barrier comprising three rows of dowels with equal diameters (D) situated at a height of b_0 above the bottom surface, with a vertical gap of b between rows. The longitudinal length is denoted by L_s, while the barrier's height is H_s. The inflow boundary condition with a logarithmic velocity distribution is also indicated. 136
5.25 Comparison of the mean water-surface elevation (z) normalised by the mean flow depth (H) between experiment (symbols) and LES (line) for the S24 case. The vertical dashed lines indicate the upstream and downstream ends of the leaky structure. 137
5.26 (a) Free-surface profiles obtained from the LES, the vertical dashed lines indicate the downstream edges of the leaky structure; and (b) the calculated backwater rise (ΔH) normalised by the mean water depth (H) for all cases. 138
5.27 Side-elevation contour plots of the LES computed streamwise velocity $\langle u \rangle$ for all of the simulated cases. The vertical lines that are overlaid on the contours indicate the positions where vertical profiles are taken, and are plotted in Fig. 5.28. The free-surface is depicted as a solid-black line. 139

5.28 Profiles of normalised mean streamwise velocity at three selected locations downstream of the leaky barriers. The dotted lines indicate the positions of the cylinders. 139
5.29 Side-elevation contour plots of the LES computed vertical velocity $\langle w \rangle$ for all simulated cases. The free-surface is depicted as a solid-black line. 140
5.30 Contours of normalised turbulent kinetic energy (tke/U_0^2) comparing the different simulated cases. The free-surface is depicted as a solid-black line. 141
5.31 Contours of normalised vertical Reynolds shear stress $(-\langle u'w' \rangle / U_0^2)$ comparing the different simulated cases. The free-surface is depicted as a solid-black line. 142
5.32 Recirculation regions computed using LES for all of the simulated cases, superimposed with contours of normalised mean streamwise velocity. 143
5.33 Normalised bed shear stress profiles for the linear leaky barriers with different longitudinal lengths at d_{50} = 0.8 mm, 1.0 mm, 1.2 mm and 1.4 mm. The horizontal black line is the threshold line of motion, where $\tau_w/\tau_c > 1$ depicts possible sediment motion. The vertical dashed lines indicate the start and the end of the leaky barrier region. 144

6.1 Side-view schematic of the five leaky barrier structures from various cited studies. (a) Single cylinder leaky barrier with varied submergence depth h (Alzabari et al. 2023a). (b-c) Structures with different inclination angles in downstream and upstream directions, respectively (Alzabari et al. 2023b). (d-e) Linear and staggered structures derived from other experimental and numerical studies (Muhawenimana et al. 2021, Müller et al. 2021a,b, Müller et al. 2022, Huang et al. 2022, Alzabari et al. 2023c), where longitudinal length L_S, structure vertical height H_S, and hydraulic conditions were varied. (f) Free surface development near a leaky barrier, showing the locations where upstream water depth (H_1) and downstream water depth (H_2) were measured. 148
6.2 Distribution of normalised mean streamwise velocity profile along the water column just upstream of the leaky barriers for the experimental and numerical setups conducted by Müller et al. (2022), Alzabari et al. (2023c). 151

6.3 Relation based on downstream Froude number, porosity ratio and normalised afflux using measured and simulated data, with the plot of the best-fit equation (6.12). The data set by Alzabari et al. (2023a,b,c) shows the following configurations based on simulated data using LES: (a) a single cylinder with various submergence depths (Alzabari et al. 2023a), (b) three dowel rows in the vertical direction inclined at different angles to both the upstream and downstream directions (Alzabari et al. 2023b), and (c) three dowel rows in the vertical direction with varying dowels along the longitudinal direction (Alzabari et al. 2023c). The experimental data by Huang et al. (2022) comprised leaky barriers with three dowel rows in the vertical direction and 12 dowels in the longitudinal direction studied under different hydraulic conditions. Muhawenimana et al. (2021) and Müller et al. (2021a,b), Müller et al. (2022) conducted experiments involving linear leaky barriers with different longitudinal lengths and structure heights subjected to 80% and 100% bankfull discharges. 153
6.4 Plot of the measured and simulated upstream water depth (H_1) and predicted values using (a) the momentum method, (b) the leaky barrier afflux method, and (c) comparison of the measured and simulated upstream water depths with predictions generated by both the momentum and leaky barrier afflux approaches. . . 156
6.5 Plot of the measured and simulated upstream water velocity (u_1) and predicted values using (a) the momentum method, (b) the leaky barrier afflux method, and (c) comparison of the measured and simulated upstream water velocities with predictions generated by both the momentum and leaky barrier afflux approaches. . 157
6.6 Plot of the measured and simulated downstream water depth (H_2) and predicted values using (a) the momentum method, (b) the leaky barrier afflux method, and (c) comparison of the measured and simulated downstream water depths with predictions generated by both the momentum and leaky barrier afflux approaches. . 158
6.7 Plot of the measured and simulated downstream water velocity (u_2) and predicted values using (a) the momentum method, (b) the leaky barrier afflux method, and (c) comparison of the measured and simulated downstream water velocities with predictions generated by both the momentum and leaky barrier afflux approaches.159
6.8 Plot of the simulated upstream water depth (H_1) and the predicted values using the momentum method with (a) assumed drag coefficient $C_D = 1$ and (b) the LES-computed values of the drag coefficients. 160
6.9 Plot of the simulated downstream water depth (H_2) and the predicted values using the momentum method with (a) assumed drag coefficient $C_D = 1$ and (b) the LES-computed values of the drag coefficients. 160

A.1 Contours of normalised vorticity behind the cylinder for the case: $Fr = 0.53$, at four instants normalised by the peak frequency $t^* = 3.5$, 3.8, 4.2, and 4.4. The free surface is depicted as a solid-black line. 170

B.1 Vertical profiles of mean streamwise velocity $\langle u \rangle$ at the top and mean vertical velocity $\langle w \rangle$ at the bottom, at six locations downstream of the cylinder at $Fr = 0.31$. The data are shown for three different grid resolutions, comparing experimental results (represented by symbols) with LES results (represented by lines). Dashed lines indicate the cylinder's position. 171

C.1 Vertical profiles of normalised time-averaged streamwise velocity $\langle u \rangle / U_0$ at four upstream locations from the Cylinder. Simulations using SEM at TIs of 5% and 10% compared to the baseline case without SEM. The dashed lines indicate the cylinder position. 172

D.1 Comparison of the mean water-surface elevation (z) normalised by the mean flow depth (H) between experiment (symbols) and LES (line) for the S24 case at three streamwise distances from the Inlet to the cylinder position. The vertical dashed lines indicate the upstream and downstream ends of the leaky structure. 173

LIST OF TABLES

1.1 Summary of relevant studies on flow around a circular cylinder, ordered chronologically, including references, Reynolds numbers, parameters (with G/D representing gap ratio, h/D denoting submergence ratio, and Fr indicating Froude number), Type of study (numerical [Num.] and/or experimental [Exp.]), and key findings. 16

3.1 Details of the cases studied including mean water depth (H), submergence depth (h), submergence ratio (h/D), Froude number (Fr), and local Froude number (Fr_h). 51

3.2 Characteristics of the recirculation areas for all submergence cases. All parameters are normalised by the diameter of the cylinder. 68

5.1 Properties of the median diameter of sediment particles (d_{50}) adopted in this research, including the dimensionless grain diameter (d_*), the dimensionless critical Shields parameter (τ_{cr}), the critical shear velocity (u_{*c}) and the critical bed shear stress (τ_c). 130

5.2 Performance evaluation of leaky barrier configurations according to various design criteria. Ratings: 1 = Limited, 2 = Poor, 3 = Good, 4 = Very Good, 5 = Excellent 134

6.1 Details of the data sets including the physical characteristics and hydraulic conditions of the leaky barriers, the diameter of cylinders (D), longitudinal barrier length (L_s), barrier height (H_s), vertical gap (b_0), inter-cylinder gap (b), barrier void ratio ($1 - \phi$, where ϕ is based on the upstream water depth), upstream flow depth H_1, downstream flow depth H_2, upstream Froude number (Fr_1) and Reynolds number (Re_1) based on the cylinder diameter. 150

List of publications

Conference papers

- F. Alzabari, C. A. M. E. Wilson, P. Ouro. 2021. Large-eddy simulation of the free-surface impact on the wake of a circular cylinder. 2nd IAHR Young Professionals Congress,
- F. Alzabari, C. A. M. E. Wilson, P. Ouro. 2022. Large-eddy simulation of the free-surface impact on the wake dynamics of a circular cylinder. Proceedings of the 39th IAHR World Congress, Granada, Spain.10.3850/IAHR-39WC252171192022760.
- F. Alzabari, C. A. M. E. Wilson, P. Ouro. 2023. Large-eddy simulation of flow around leaky barriers in a linear configuration. Proceedings of the 40th IAHR World Congress, Vienna, Austria.

Journal papers

- F. Alzabari, C. A. M. E. Wilson, P. Ouro. 2023. Unsteady vortex shedding dynamics behind a circular cylinder in very shallow free-surface flows. *Computers and Fluids*. 260(12): 105918, 10.1016/j.compfluid.2023.105918.
- F. Alzabari, C. A. M. E. Wilson, P. Ouro. 2023. Large-eddy simulation of flow around leaky barriers in an inclined configuration. *Submitted to Water Resources Research*
- F. Alzabari, C. A. M. E. Wilson, P. Ouro. 2023. Estimating backwater rise and flow velocity in natural flood management instream barriers. *Submitted to Journal of Hydraulic Engineering.*
- F. Alzabari, C. A. M. E. Wilson, P. Ouro. 2023. Hydrodynamic characteristics of flow around a circular cylinder near a free surface. *Under preparation*.

Nomenclature

Abbreviations

CFD	Computational Fluid Dynamics
CFL	Courant-Friedrichs-Lewy
CICSAM	Compressive Interface Capturing Scheme for Arbitrary Mesh
CLSVOF	Coupled Level Set Volume of Fluid Method
DF	Direct Forcing method
DMD	Dynamic Mode Decomposition
DNS	Direct Numerical Simulation
FCT	Flux-corrected Transport Method
IB	Immersed Boundary
IBM	Immersed Boundary Method
LB	Leaky Barrier
LES	Large Eddy Simulation
LMR	Local Mesh Refinement
LS	Level Set
LSM	Level Set Method
LWD	Large Woody Debris
MAC	Marker-and-cell
MPI	Message Passing Interface
NFM	Natural Flood Management
PIV	Particle Image Velocimetry
PLIC	Piecewise Linear Interface Calculation
POD	Proper Orthogonal Decomposition
PSD	Power Spectral Density
RANS	Reynolds Averaged Navier Stokes
RL	Rigid Lid
SG	Specific Gravity
SGS	Sub-Grid Scale
SLIC	Simple Line Interface Calculation
TKE	Turbulent Kinetic Energy
URANS	Unsteady Reynolds Averaged Navier Stokes
VOF	Volume of Fluid

WALE	Wall-adapting Local Eddy viscosity model
WENO	Weighted, Essentially Non-oscillatory scheme

Greek Symbols

Ω_{gas}	Gas domain
Ω_{liquid}	Fluid domain
μ_g	Dynamic viscosity of gas
μ_l	Dynamic viscosity of liquid
ν_t	Eddy viscosity
ν	kinematic viscosity
ω_i	Vorticity in the i-direction
ϕ	Level set signed distance function
ρ_g	Density of gas
ρ_l	Density of liquid
ρ_s	Density of sediment
τ_c	Critical shear stress for incipient sediment motion
τ_w	Wall shear stress
τ_{ij}	SGS stress

Roman Symbols

Fr	Froude number
Re	Reynolds number
C_D	Drag coefficient
C_L	Lift coefficient
D	Cylinder diameter
H_1	Upstream water depth
H_2	Downstream water depth
H_s	Leaky barrier height
L_s	Leaky barrier longitudinal length
U_0	Bulk velocity
V_L	Barrier control volume
V_S	Barrier solid volume
ΔH	Backwater rise
a	Frontal area per jam volume
b_0	Vertical bottom gap
b	Vertical inter-log gap

d_{50} Median sediment grain size

p Pressure

q_1 Upstream flow rate

q_2 Downstream flow rate

u_* Shear velocity

u_1 Upstream velocity

u_2 Downstream velocity

CHAPTER 1

Introduction

1.1 Background

Flow dynamics around cylindrical objects represent a cornerstone of fluid dynamics research, a field dedicated to understanding the movement and interaction of fluids with surrounding objects. For centuries, the complex behaviour of fluids around cylinders has been a subject of great interest and extensive study (Morkovin 1964, Berger and Wille 1972, Williamson 1996). From the spinning rolls of paper in a printing press to the oscillations of deep-sea cables, the effects of flow around cylindrical structures can be observed in many everyday phenomena.

The history of research in bluff body fluid dynamics extends back several centuries. Leonardo Da Vinci was among the pioneering figures who began studying fluid dynamics roughly five centuries ago. Fig. 1.1 shows two of his sketches related to fluid dynamics. The sketch on the left-hand side illustrates a moment when water moves around rectangular obstacles, with vortices forming and shedding at a turbulent wake. The other sketch depicts falling water, which introduced the concept of the co-existence of eddies of varying length scales. This idea of co-existing eddies of different sizes was later formalised by Kolmogorov (1941) and recognised as turbulence cascading. In 1883, Osborne Reynolds conducted his famous experiment, illustrating the transition from laminar to turbulent flow inside a pipe (Reynolds 1883). In this experiment, Reynolds studied the transition of water flow under varying incoming velocities and formulated the Reynolds number. This number is defined as the ratio of inertial forces to viscous forces, given as:

$$\mathrm{Re} = \frac{\rho u L}{\mu} \tag{1.1}$$

Where ρ is the fluid density, u is the incoming flow velocity, L is a characteristic linear dimension, e.g. the diameter for a cylinder, and μ is the dynamic viscosity of the fluid.

The interaction between a single cylinder and fluid flow is especially interesting. As the fluid flows past the cylinder, it does not simply glide smoothly around it. Instead, the flow often breaks into a series of eddies or vortices, creating a phenomenon known as vortex shedding (Bearman and Zdravkovich 1978). For very low Reynolds numbers, there is no separation of the boundary layer, as depicted in Fig. 1.2(a). The vortex shedding arises when the *Re*

of the flow exceeds the critical *Re* for vortex shedding. This critical number lies between 40 and 50. The exact value varies, Williamson (1996) cites 49, while others, such as Triantafyllou and Dimas (1989), indicate about 40. At Reynolds numbers below this threshold, the flow remains steady and a symmetric pair of recirculation bubbles can be observed at the rear of the cylinder (Chen and Jirka 1995). An example of this can be seen in Figs. 1.2(b) to 1.2(d).

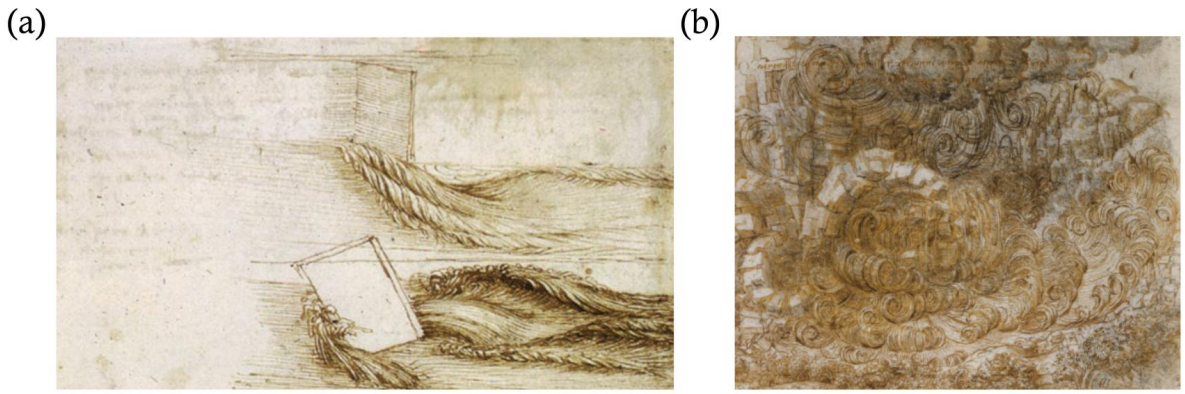

Fig. 1.1 Sketches by Leonardo da Vinci: (a) water passing a rectangular obstacle; (b) co-existence of eddies with different length scales. Source: (*Leonardo da Vinci Drawings* 2011).

When the critical *Re* is exceeded, vortices begin to form and shed from each side of the cylinder alternately. This subsequent pattern of vortices, evident in Figs. 1.2(e) to 1.2(i), is known as a von Kármán vortex street. The vortex street, consisting of what are commonly termed von Kármán vortices, is two-dimensional for Reynolds numbers less than 180. Some three-dimensional effects can be introduced experimentally by altering the end conditions of the cylinder, as described by Williamson (1991).

Gerrard (1966) and Green and Gerrard (1993) provide a detailed description of the vortex-shedding process. For Reynolds numbers exceeding approximately 500, the mechanism of vortex shedding is characterised as follows: a forming vortex remains stationary relative to the cylinder as it grows. Simultaneously, it draws the shear layer from the cylinder's opposite side towards itself. When this shear layer crosses the centreline, it interrupts the upstream supply of vorticity to the expanding vortex, resulting in the shedding of a discrete 'vortex'. The timing of this entire procedure effectively dictates the shedding frequency. However, Green and Gerrard (1993) point out that this mechanism is not directly relevant for lower Reynolds numbers because only a minimal cross flow is observed in the near wake. At these lower Reynolds numbers, vortex shedding is typified by a process where vorticity is divided, Freymuth et al. (1986) describe this phenomenon as 'vortex nipping'.

The vortex shedding from cylinders is not just a captivating visual experience, it also holds significant practical implications. For instance, these vortices can induce vibrations in structures due to the shedding frequency being close enough to the structure's natural frequency (Williamson and Govardhan 2004), which, if not accounted for, can lead to mechanical failures. This makes the study of flow around cylinders crucial for engineering appli-

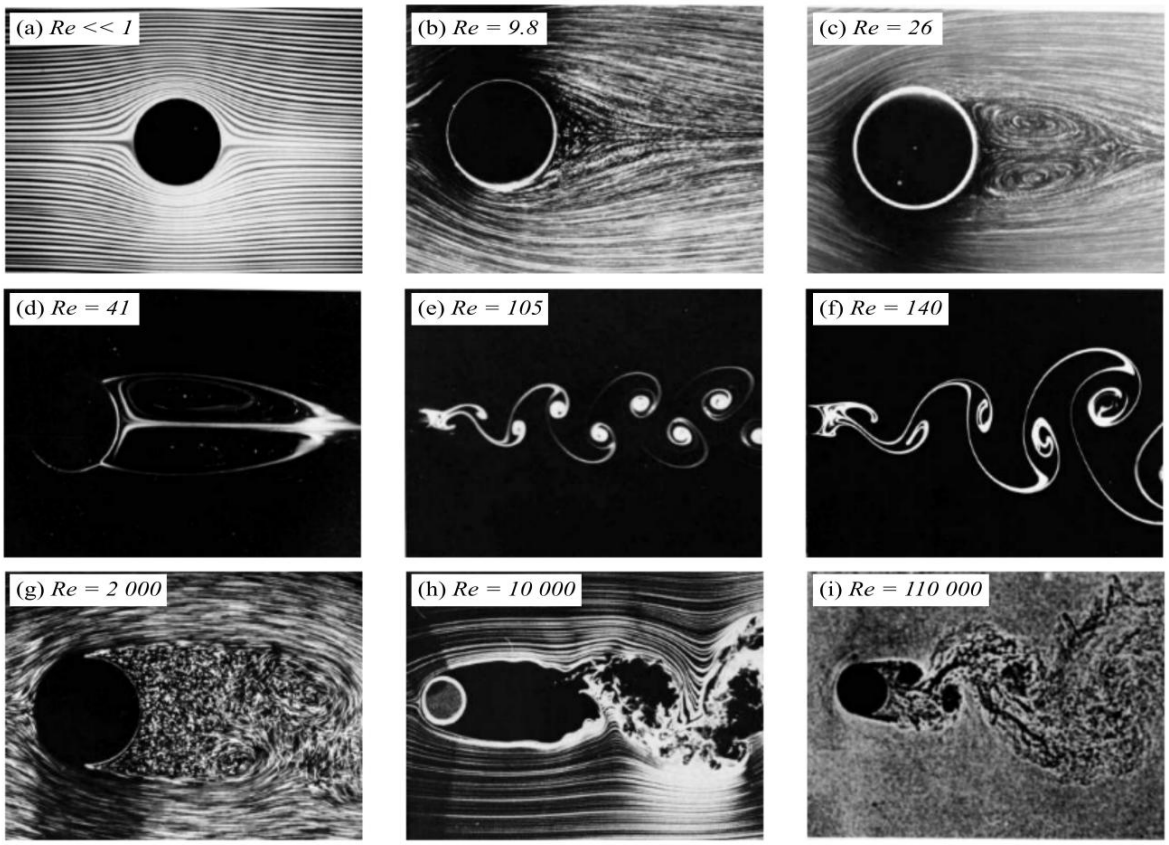

Fig. 1.2 Wake patterns for different values of *Re*. Adapted from (Van Dyke 1982).

cations such as offshore structures, pipelines, or hydraulic structures. Problems with flow-induced vibration are prevalent in many of these engineering applications due to the periodic shedding of von Kármán vortices (Gerrard 1966, Sumner et al. 2004). In the construction and maintenance of sub-sea cables, it is critical to avoid any large vibration that can lead to a structural failure or even to long-term fatigue issues. Pipelines placed on erodible beds can induce a change in the flow dynamics that eventually causes sediment erosion, which eventually leads to scour underneath the pipe, causing the pipeline to become a free-spanning structure likely to suffer from flow-induced loadings (Alper Oner et al. 2008). The understanding of the effects of cylinders in the surrounding environment remains a key topic. Recently, cylinder arrangements have been utilised in complex environments, especially in the construction of woody debris dams for natural flood management (Müller et al. 2022), whose goal is to alleviate flood peaks.

The flow dynamics around cylindrical objects become even more interesting when considering the concept of the free-surface effect. The free surface, typically referring to the interface between a liquid and a gas, e.g. water and air, can introduce additional complexities due to its deformable nature and relative distance to the object of interest. When a cylinder is close to or intersects with a free surface, the vortex shedding and associated flow patterns can be significantly influenced (Sheridan et al. 1995, 1997). As vortices form and shed from the cylinder, they can cause undulations and waves on the free surface. This interaction can

lead to phenomena such as the generation of standing waves, alteration in vortex-shedding frequencies, or even suppression of vortex shedding altogether under specific conditions (Reichl et al. 2005). In practical applications, understanding the interaction between cylindrical structures and the free surface is essential, e.g. in the design of pipelines or offshore structures (Fig. 1.3), where many components may interact with the sea surface.

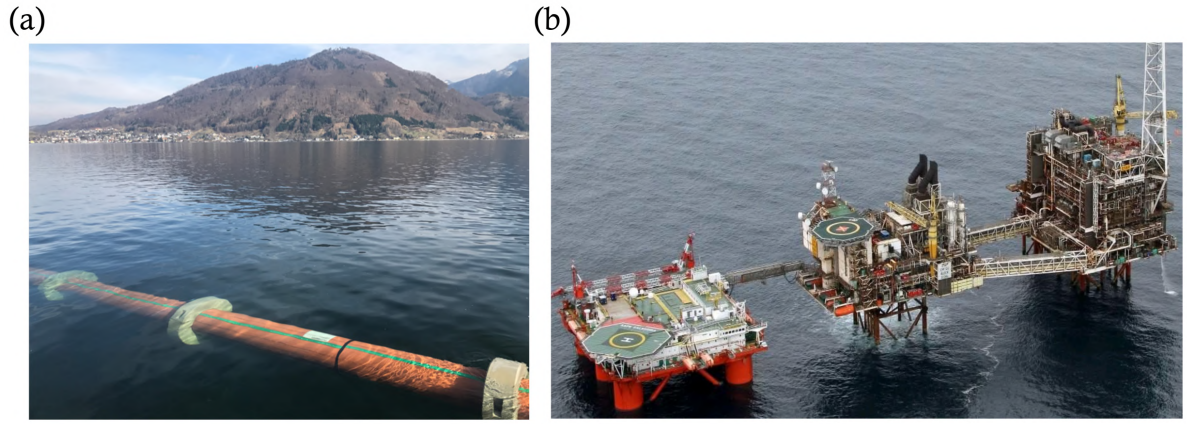

Fig. 1.3 Examples of structures interacting with the free surface: (a) submerged pipelines, source: (*agru* 2018); (b) offshore platform, source: (*Offshore Platform Topsides* 2023).

By transitioning to a macroscopic scale from the study of flow around a single cylinder, the applications of fluid dynamics in broader contexts become apparent. Natural Flood Management (NFM) interventions were recently devised to manage the effects of climate change, particularly in response to natural flooding disasters that result in significant human disruption, economic loss, and casualties (Arnell and Gosling 2016, Dadson et al. 2017). The increasing intensity and frequency of flood events caused by climate change have drastically increased, to the point that Governments worldwide are highly concerned. In 2021, there were over 50 severe flood events worldwide, resulting in economic losses exceeding $82 billion (Bevere and Remondi 2022). Since 1991, major flood events have led to global cumulative economic losses exceeding $1,200 billion (Fig. 1.4). For the purpose of comparison, tropical cyclones resulted in economic losses of over $1,500 billion during the same period, while earthquakes caused approximately $1,100 billion in losses. Insured losses specifically from flood events amounted to around $200 billion (Bevere and Remondi 2022). In response, the Intergovernmental Panel on Climate Change (IPCC) and Paris Agreement participants have urged for considerable investment in infrastructure to ensure future water security (Edenhofer et al. 2014).

Floods have traditionally been managed using engineering measures such as dams, flood walls, flood gates, and storage reservoirs to hold back floodwaters. However, these methods can also have significant negative impacts, such as altering the natural river flow, changing sediment transport regimes, and disconnecting habitats (Tockner and Stanford 2002, McCartney and de la Hera 2004). Therefore, it is crucial, where possible, to explore alternative and more sustainable ecologically-sensitive strategies for flood management that work in parallel

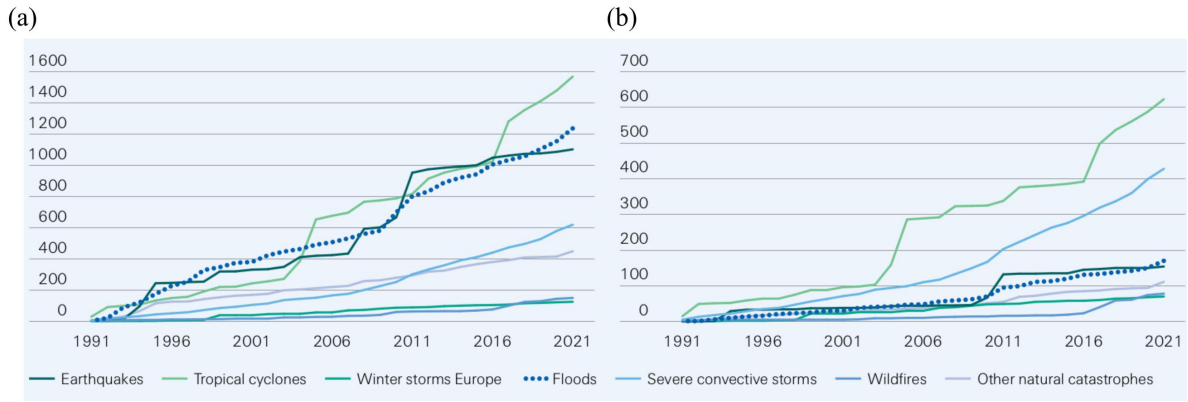

Fig. 1.4 (a) Cumulative global economic (b) and insured losses by peril, 1991–2021, Source: Swiss Re Institute (Bevere and Remondi 2022).

with traditional approaches in managing the effects of climate change.

The Water Criteria of the Climate Bonds Standard advocates for nature-based solutions (NBSs), such as in-stream leaky wood barriers, to improve catchment resilience and decrease dependency on hard engineering (Dadson et al. 2017, Burgess-Gamble et al. 2018). NBSs for flood management are also referred to as Natural Flood Management (NFM) in the UK (Dadson et al. 2017, Lane 2017) and Working with Natural Processes (WWNP) following the 2007 UK summer floods (Pitt 2008). Internationally, these methods are known as nature-based approaches or engineering with nature (Bridges et al. 2018).

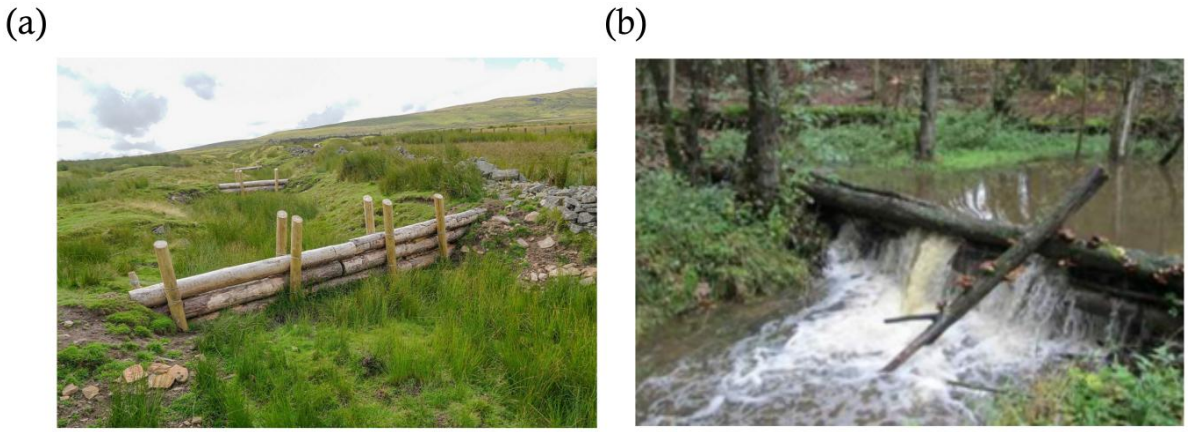

Fig. 1.5 Field photographs of (a) engineered leaky barrier at Killhope Burn (North of England) by the environment agency, source: (*North East project* 2021) and (b) another leaky barrier depicting backwater rise upstream of the dam at Pickering (North East England), source: (*slowtheflow* 2019).

NFM aims to reduce flood risk through small-scale interventions that mimic or work in conjunction with the natural systems (Lane 2017). Examples of NFM techniques include leaky barriers, bunds, storage ponds, scrapes, and swales, and other sustainable drainage approaches (Quinn et al. 2013). NFM not only reduces flood risk but can also provide environmental benefits, such as improving water quality, slowing soil degradation, enhancing habitat, and promoting biodiversity (Roni et al. 2015, Janes et al. 2017, Burgess-Gamble et al. 2018).

Leaky barriers are a form of runoff reduction structure, inspired by beaver dams and large

woody debris (LWD) in riparian rivers (Nyssen et al. 2011). They can be designed to resemble these natural features or take on a more engineered appearance, i.e. mimicking the shape of horizontal cylinders. Leaky barriers are constructed by spanning logs across the full channel width and securing them to the bank with vertical stakes or existing tree stumps (Muhawenimana et al. 2023). A vertical gap beneath the structure is designed to facilitate uninterrupted baseflow and enable aquatic fauna to move freely through the channel (Müller et al. 2022), while diverting excessive water to floodplains during periods of high flow. Fig. 1.5 presents field photographs of typical leaky barriers, providing real-world examples of these designs in action (*slowtheflow* 2019, *North East project* 2021).

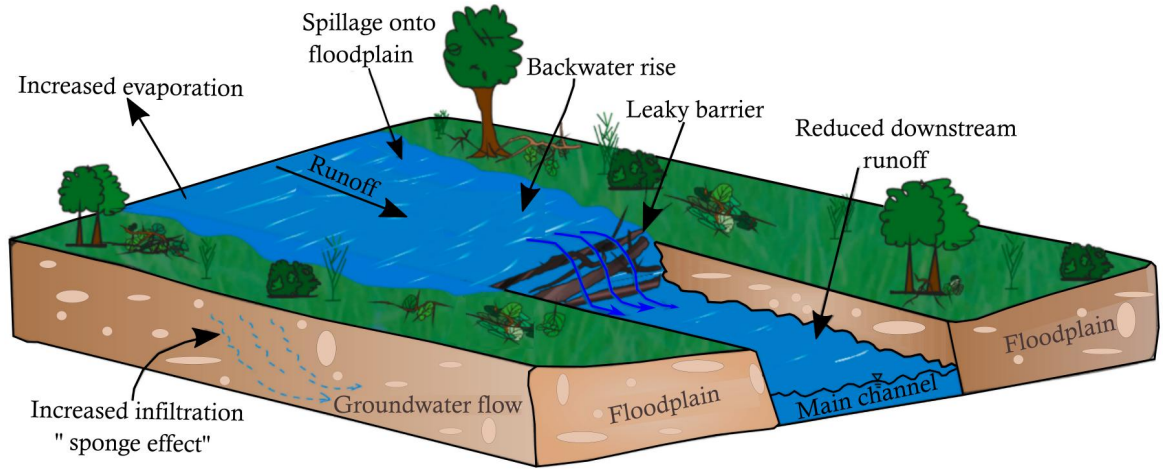

Fig. 1.6 Schematic representation of the flow attenuation process of leaky barriers, depicting the temporal storage of flow upstream of the barrier, subsequent spilling onto floodplains, increased groundwater infiltration and the resulting reduction in downstream flow depths. Figure adapted from (Muhawenimana et al. 2021).

Leaky barriers, which are often engineered from large wood pieces defined as circular logs with a diameter $\geq 0.1\,\mathrm{m}$ (Wohl and Jaeger 2009), have many benefits, including flood mitigation, ecological habitat enhancement, and potential local sediment redistribution (Bouwes et al. 2016, Dodd et al. 2016, Schalko et al. 2019). By intercepting part of the river flow, they create a backwater effect, increasing in-stream and floodplain water storage, vegetation inception, evaporation and ground infiltration. These barriers slow down the upstream velocity and critically reduce the peak flow reaching downstream areas, providing substantial mitigation against flood risks (Estrela et al. 2001, SEPA 2016, Burgess-Gamble et al. 2018) (see Fig. 1.6). The sediment redistribution aspect is especially advantageous for modified rivers that have lost their natural cross-sectional profile due to anthropological activities because they supply sediment to the floodplain.

Leaky barriers, known for their flood management benefits, have limited large-scale application due to cost concerns and an incomplete understanding of their hydrodynamics. Thus, to enable large-scale installation of these natural flood defences, new research is required to enhance the current understanding of their hydro-environmental implications, thereby validat-

ing their implementation. Such advancements could help reduce costs by optimising design performance. Despite the increasing popularity of engineered leaky barriers, there is limited data on their hydraulic performance and design guidance. This lack of comprehensive guidance, with exceptions such as Trust (2016), Burgess-Gamble et al. (2018), Trust (2021), Wren et al. (2022), poses challenges to their effective implementation. Current research efforts are being conducted to evaluate leaky barriers, including studies on the hydrodynamic flow field, sediment transport impacts, water storage potential and how design variations influence their function (Muhawenimana et al. 2021, Müller et al. 2022, Muhawenimana et al. 2023).

Full understanding of the role of engineered leaky barriers requires a comprehension of the hydrodynamics of their components, which are shaped as horizontal cylinders reminiscent of tree branches, especially the effect of the interaction of their wake structures with the free surface. These complex interactions can lead to various flow patterns and vortex formations, which can significantly influence the efficiency and effectiveness of the engineered leaky barriers. By understanding these hydrodynamic interactions, it can be ensured that the barriers not only serve their flood mitigation purpose but also preserve the ecological dynamics of the watercourse.

The numerical tools used to study the hydrodynamics and behaviour of turbulent flows around cylinders must be accurate. With the rapid advances in computing technology, large-eddy simulation (LES) has emerged as a more affordable method compared to direct numerical simulation (DNS) for modelling turbulent flows around cylinders at relatively high Reynolds numbers. However, while LES is more affordable than DNS, it may not be as accurate. Reynolds-Average Navier–Stokes (RANS) remains a widely used method in many industrial applications. However, in specific scenarios such as flow past a cylinder or arrays of cylinders, RANS can overestimate the recirculation length in the wake (Rodi 1997) because of its higher dissipation rate compared to LES. The reliability of unsteady RANS (URANS) models in predicting quasi-periodic vortex shedding behind cylinders is still a topic of investigation, primarily because URANS is most effective when a clear gap exists between large-scale unsteadiness and turbulence, a condition that is not often met.

In this thesis, LES is employed to simulate the flow past cylinders and leaky barriers. Further details on the methods that are utilised can be found in Chapter 2. The next section offers a comprehensive review of the literature, giving special attention to cylinders, leaky barriers, modelling free-surface flows and numerical techniques that account for free-surface deformations. This review is followed by a description of the thesis objectives and structure.

1.2 Literature review

1.2.1 Flow past a circular cylinder and boundary effects

Flow past a circular cylinder in an infinite medium is regarded as one of the classical problems in fluid dynamics and has been extensively investigated over a span of more than 120

years. One of the earliest investigations was conducted by Strouhal (1878), who examined the frequency response of wind blowing over a wire or a string in an Aeolian harp. Many textbooks dedicate substantial attention to this problem, with Tritton (2012) providing just one example. A significant attraction of the circular cylinder is its simple geometry, along with its immediate applicability to engineering problems. The time-varying forces exerted on the cylinder hold immense significance in the design of many structures, including buildings, bridges, offshore structures, vehicles and power generation systems.

Williamson (1996) examined the effect of increasing the Reynolds number on the wake of a circular cylinder. For Reynolds numbers that exceeded 180, the flow field became three-dimensional. Mode A instabilities manifested first at Reynolds numbers ranging from 180 to 230. Beyond 230, Mode B instabilities were observed. These instabilities introduced waviness in the third dimension, with Mode A having a wavelength of 3 to 4 diameters and Mode B approximately 1 diameter. As the Reynolds number continued to increase, Morkovin (1964) described a forward migration of turbulence within the shear layer, accompanied by enhanced three-dimensionality. Williamson (1996) further highlighted that three-dimensional structures on the scale of both the shear layer and the von Kármán vortices emerged when the Reynolds number lay between 1,000 and 200,000. The distance at which vortices formed behind the cylinder, commonly referred to as the formation length, also changed with varying the Reynolds number. Studies by Unal and Rockwell (1988), Lin et al. (1995) and Norberg (1998) indicated that the formation length initially grew from approximately 1.5 diameters to 2.5 diameters for Reynolds numbers between 200 and 2,000, but then decreased as the Reynolds number continued to rise to around 1.25 diameters at a Reynolds number of 10,000.

While the flow past a circular cylinder in unbounded conditions has been thoroughly examined for a wide range of Reynolds numbers (Berger and Wille 1972, Williamson 1996), recent studies on the flow around cylinders have begun to incorporate the impact of asymmetric boundary conditions, particularly near free or fixed surfaces (Reichl et al. 2005). The complex interaction between the cylinder wake and the distortion of the free surface results in a more unsteady flow, which alters the intrinsic properties and large-scale wake patterns that are typically associated with isolated cylinder flows (Blevins 1977). However, the changes in the shear-layers and vortex shedding that can occur when the cylinder is positioned near a deformable free surface have received limited attention to date.

In addition to the Reynolds number that accounts for the turbulence regime, the effects of the free surface lead to the addition of three dimensionless parameters, namely the bulk Froude number ($Fr = U_0/\sqrt{gH}$ with g the gravitational acceleration and H the total water depth), the local Froude number ($Fr_h = U_t/\sqrt{gh}$ with h and U_t denote the free-surface elevation overtopping the cylinder from its top side and velocity at this location, respectively), and the submergence ratio (h/D). The local Froude number is suitable to characterise the effect of the free-surface impact on the flow dynamics shortly downstream of the submerged cylinder (Sheridan et al. 1997).

Previous studies examining the impact of a wall boundary layer on the flow around a cylinder have provided essential insights into the hydrodynamics of flow when the free-surface layer is present. Research on the flow around a circular cylinder positioned near a wall has shown that the gap between the wall and the cylinder, which is expressed as the ratio of the cylinder diameter (D) and the vertical gap (G) between the bottom wall and the cylinder, known as the gap ratio (G/D), is a particularly critical parameter for controlling the flow dynamics. Taneda (1965) investigated the flow past a cylinder close to a no-slip wall at a Reynolds number of 170, focusing on gap ratios of 0.60 and 0.10. For a gap ratio of 0.60, regular vortex shedding was observed. In contrast, at a gap ratio of 0.10, only a single layer of vortices appeared to shed from the cylinder. In the case of the smaller gap ratio, the wavelength of the vortices increased with the distance downstream. After several wavelengths, the wake became unstable and started to break down. This breakdown is believed to refer to the merging of the vortex structures within the wake.

The lift and drag forces acting on a cylinder situated near a plane boundary were investigated by Roshko et al. (1975), considering gap ratios ranging from 0.00 to 6.00. In their experimental study, the boundary layer thickness was half the diameter of the cylinder. The researchers observed that for larger gap ratios, i.e. exceeding 0.60, there was a tendency for the drag to increase as the cylinder approached the wall. Conversely, upon further reduction of the gap ratio, i.e. moving the cylinder closer, a rapid reduction in the drag occurred, reaching its minimum when the cylinder made contact with the wall. This phenomenon was attributed, in part, to the cylinder's movement into a lower-energy boundary layer flow near the wall.

The lift was found to increase as the gap ratio decreased, reaching its peak when the cylinder was in direct contact with the wall. Similar trends were also found by Taniguchi and Miyakoshi (1990), who investigated the variation of the drag and lift forces with increasing boundary layer thickness. For the most part, the trends are similar, while they emphasised the significant impact of the boundary layer on the forces, particularly for small gap ratios.

Bearman and Zdravkovich (1978) investigated the frequency response of flow around a circular cylinder in close proximity to a flat plane boundary, comparing their findings with results from a previous investigation involving two cylinders arranged side-by-side, which had established a solution based on potential flow. On the basis of this analogy, Bearman and Zdravkovich (1978) were able to formulate several predictions about the forces acting on the cylinder and the characteristics of shedding that are likely to be observed. For instance, in cases where the gap ratio exceeded half the diameter of the cylinder, their analysis suggested that the flow would continue to shed normally. Meanwhile, for smaller gap ratios, the boundary layer along the wall would separate at distances both upstream and downstream of the cylinder.

Bearman and Zdravkovich (1978) also discussed the findings of Götkun (1975), whose results were largely in agreement with those of Roshko et al. (1975). Götkun (1975) found that minimal drag occurred when the cylinder was in direct contact with the wall, while maximum

drag (with a drag coefficient, C_D, ranging between 1.4 and 1.5) was observed at a gap ratio of 0.50. Furthermore, Götkun (1975) observed an increase in the shedding frequency as the cylinder was moved closer to the wall, resulting in the Strouhal number peaking at a gap ratio of 0.50. However, the observations of Bearman and Zdravkovich (1978) did not demonstrate a similar increase in the Strouhal number. Instead, they found that the Strouhal number decreased rapidly as the gap ratio decreased. Notably, the transition from a gap ratio of 0.30 to 0.20 marked a significant point of change in this trend. In addition, Bearman and Zdravkovich (1978) indicated that changes in the gap ratio led to shifts in the separation points. Although the separation point closest to the downstream wall shifted, this was typically counterbalanced by an equal shift in the separation point on the other side of the cylinder in the upstream direction.

Angrilli et al. (1982) investigated the influence of the Reynolds number on the flow past a single cylinder near a bottom wall, examining Reynolds numbers ranging from 2860 to 7640. As the gap ratio decreased, they observed an increase in the shedding frequency with the most substantial deviation, approximately 10%, occurring at a gap ratio of 0.50, which was the smallest ratio under examination. This result is similar to that of Götkun (1975), who also identified a peak in the Strouhal number at this specific gap ratio. This agreement is significant because the Reynolds numbers differ by a factor of approximately 40, i.e. Götkun (1975) at around 2×10^5, Angrilli et al. (1982) at roughly 5000. However, the results of Angrilli et al. (1982) deviated slightly from those of Bearman and Zdravkovich (1978), who observed minimal changes in the shedding frequency. Angrilli et al. (1982) proposed that the thickness of the boundary layer on the wall can influence the results. This proposition originated from the fact that the smallest gap ratio examined exceeded the boundary layer thickness by more than twice. While the description of flow behaviour by Angrilli et al. (1982) was limited, they did acknowledge the presence of a wall inducing an asymmetric flow. The mean velocity profile showed augmented flow on the wall side in the near wake. In contrast, reduced flow on the wall side was observed at distances exceeding 2.5 diameters downstream.

Grass et al. (1984) and Taniguchi and Miyakoshi (1990) examined the influence of boundary layer velocity gradients. For Reynolds numbers between 2000 and 4000, Grass et al. (1984) observed regular shedding within gap ratios of 2.00 to 0.75, with slight downstream shifts in separation points on the wall side. Below a gap ratio of 0.50, vortex shedding became intermittent and less energetic. They attributed this to adverse pressure gradients causing detached separation regions on the solid wall. Grass et al. (1984) also proposed that downstream separation zones diverted fluid away from the wall, inhibiting vortex roll-up on the wall side of the wake. Variations in the Strouhal number with gap ratio were influenced by the boundary layer. The gap ratio at which shedding ceased varied with boundary layer thickness. Weakened shedding persisted at a gap ratio of 0.25 for uniform approach flow, but ceased at a gap ratio of 0.50 with a roughened wall boundary (thicker boundary layer).

Lei et al. (1999) conducted an experimental study to examine the impact of a plane bound-

ary on the forces and vortex shedding of a circular cylinder. They focused on Reynolds numbers ranging from 1.30×10^4 to 1.45×10^4. Their findings indicate that the development of the boundary layer significantly influenced the subsequent lift forces acting on the cylinder. Concerning the Strouhal number, the authors observed variations with gap ratio and highlighted the significant role played by the boundary layer in these changes. In contrast to Grass et al. (1984), Lei et al. (1999) suggested that the critical gap ratio at which shedding is suppressed decreased as the thickness of the boundary layer increased.

Price et al. (2002) also investigated the same problem, albeit at a Reynolds number of 1200. Their study yielded significantly larger changes in the Strouhal number, approximately 40% in magnitude. They additionally observed the presence of extra signal frequencies in the wake velocity, which was particularly noticeable at small gap ratios. These added frequencies were attributed to the boundary layer's motion as it separated from the wall downstream of the cylinder. Price et al. (2002) proposed that the suppression of the von Kármán vortex shedding was unlikely to result from the cross annihilation of vorticity between the wall and the cylinder. Their particle-image-velocimetry (PIV) results indicate that oppositely signed vorticities do not cancel each other out. It was suggested that the separation bubbles forming downstream of the cylinder create a free jet, which cancels the vorticity on the side of the cylinder wake near the wall, thereby eliminating vortex shedding, a phenomenon that was observed earlier by Grass et al. (1984).

According to the studies conducted by Lei et al. (1999), Lin et al. (2009), Rao et al. (2013), when $G/D > 1.0$, the wake is dominated by the classical formation of a vortex street, similar to the wall-free case. However, as G/D decreases, the intensity of vortex shedding from the lower side of the cylinder gradually weakens, resulting in an asymmetric wake characterised by a single row of vortices on the upper side of the cylinder (Lei et al. 1999). Further decreasing G/D to a range of 0.2-0.3 suppresses the alternate vortex shedding. The interaction between the shear layers generated by the wall and the cylinder then becomes the primary factor responsible for vortex suppression (Lin et al. 2009). Wang and Tan (2008*a*,*b*) categorised the gap ratio into three regions based on the patterns of vortex shedding at various values of G/D. These regions are as follows: in the wall-effect-free area ($G/D \geq 1.0$), the wake exhibits a resemblance to that of an isolated cylinder; in the intermediate area ($0.3 \leq G/D < 1.0$), the wall effects are significant, leading to the occurrence of asymmetric vortex shedding; and in the vortex-shedding-suppression area ($G/D < 0.3$), vortices are periodically shed from the upper side of the cylinder, resulting in the formation of a one-sided vortex street.

In addition to near-wall effects on vortex shedding, hydrodynamic forces are significantly influenced by G/D values (Lei et al. 2000, Chen et al. 2019, Chen, Ji, Xu and Zhang 2020). As G/D increases from 0.1 to 0.6, the Strouhal number (St) rises. However, beyond G/D of 0.6, St slightly decreases as G/D continues to increase up to 3.0. Buresti and Lanciotti (1992) conducted experiments at Reynolds numbers (Re) ranging from 0.86×10^5 to 2.75×10^5, revealing a non-monotonic trend in mean drag force with varying G/D values, while the mean

lift force experienced a significant drop with increasing G/D. In contrast, Lei et al. (2000) observed that for *Re* values between 80 and 1000, and G/D values ranging from 0.1 to 3.0, both the mean and root-mean-square (RMS) lift forces increased with higher G/D and *Re* values. Ouro et al. (2019) investigated the near-wake dynamics behind a horizontal cylinder at Reynolds numbers between 6,666 and 13,333 for G/D values of 0.5 and 1.0. Their results show that the Strouhal number decreased with increasing G/D and the drag coefficient increased, while both values decreased with the increase in Reynolds number.

The proximity of the cylinder to a free surface under the influence of gravitational acceleration leads to distinct variations in flow behaviour. Yu and Tryggvason (1990) conducted a numerical study of the surface signature of a two-dimensional vortex flow. Their main finding was that the dominant parameter governing surface deformation is the local Froude number (Fr_h). They observed that the surface-vortex interaction could be categorised as either high or low Froude number motion. At small Fr_h, vortices interacted with the free surface similarly to a rigid wall, resulting in minimal surface deformation. Conversely, at larger Fr_h, vortices possessed enough strength to induce significant surface deformation. Yu and Tryggvason (1990) also emphasised that the time scale over which a vortex developed had an impact on the resulting surface deformation.

Miyata et al. (1990) investigated the flow around a circular cylinder near a free surface using a combination of experimental and computational methods. Their study was conducted at a Reynolds number of 4.96×10^4 and a cylinder Froude number of approximately 0.24. They observed distinct changes in flow behaviour as the submergence ratio (h/D) decreased from 0.35. This reduction led to a sharp decline in drag and a significant increase in the Strouhal number. The pronounced increase in the *St* coincided with a visible weakening in the intensity of lift spectra (representing the spectra of the lift forces), accompanied by a broader range of frequencies. Miyata et al. (1990) suggested that shedding at the smaller submergence ratio was less pronounced, implying weaker shedding.

Regarding the forces acting on the cylinder, Miyata et al. (1990) found that lift increased as the submergence ratio decreased. However, they proposed that drag exhibited a bimodal nature, stabilising at a nearly constant value for larger submergence ratios and adopting a different value for smaller submergence ratios. The trend in the lift force variation aligned with the observations presented by Roshko et al. (1975), with both studies noting a similar pattern. In contrast, the trend for the drag force differed slightly: Roshko et al. (1975) reported a gradual reduction in drag with a decreasing gap ratio, whereas Miyata et al. (1990) identified a step-like drag reduction with a decreasing submergence ratio below h/D of 0.35.

Sheridan et al. (1995) examined the flow behaviour of a cylinder in close proximity to a free surface, operating at a Froude number of 0.60 and h/D of 0.45. They observed that at this specific point in parameter space, two viable wake states were present. These states demonstrated limited stability, leading to transitions between them over time, which was referred to as being metastable. The characteristics of these two states resembled those witnessed by

Valluri (1996), who investigated flow past a flat circular disk. In one state, the fluid passing over the cylinder remained attached to the free surface. In the other state, separation occurred. The transitions between states lacked clear periodicity, with Sheridan et al. (1995) noting that shifts occurred spontaneously at a non-dimensional frequency on the order of 10^{-3}.

Sheridan et al. (1997) also conducted experiments to investigate the flow past a circular cylinder close to the free surface at Fr = 0.47–0.72 and $0 \leq h/D \leq 0.75$ as an extension of their previous research. At a submergence ratio of zero, a shear layer forms beneath the cylinder, similar to the shear layer that is observed above the cylinder in near-wall flow. With a small submergence ratio, a jet-like flow structure arises at the cylinder's upper side, descending at an angle and merging with the shear layer originating from the cylinder's lower side. As the submergence ratio increases, the point of mixing progressively moves downstream. The jet-like structure becomes attached to the free surface at an intermediate submergence ratio ($h/D = 0.375$). The angle of the jet is influenced by the bulk Froude number, with larger Fr exerting a greater pull on the jet towards the base of the cylinder. They found that the unsteady interaction of the three separated high-vorticity regions from the free surface, and the top and bottom ends of the cylinder, resulted in a jet-like flow with three different states including attachment to the free surface, to the cylinder and an intermediate state in-between these. Hoyt and Sellin (2000) confirmed some of the findings of Sheridan et al. (1997) and offered additional insights into the time-dependent nature of the flow. Their main finding was the observation of von Kármán vortex shedding at some submergence ratios.

Carberry (2002) conducted a series of experiments at $Fr = 0.166$ and at $Re = 2100$ to investigate the different wake states and force properties as the cylinder approaches the free surface. They observed three distinct wake modes as h/D decreases: a modified von Kármán wake, flow attached to the free surface and a separated jet. For $h/D = 3$, it was found that the cylinder was effectively fully submerged without being influenced by the free surface. Reichl et al. (2003, 2005) numerically investigated the flow past a single cylinder close to the free surface at a fixed Re of 180 for $0.0 < Fr < 0.7$. Their findings revealed a shared mechanism for inhibiting vortex shedding at small gap ratios, irrespective of whether the boundary was a free surface or a no-slip surface. For low Fr, the surface deformations were small, becoming more noticeable when Fr exceeded 0.3. They showed that the Fr_h was critical in an account of free-surface undulations and wave breaking. At large Fr_h, the free-surface distortion is larger and leads to a diffusive flux of vorticity from the induced surface curvature, resulting in a substantially more asymmetric wake downstream of the cylinder.

Kahraman et al. (2012) studied instantaneous and time-averaged flow patterns around a horizontal circular cylinder in shallow flows at Fr = 0.41–0.71 and Re = 1,124–3,374 using PIV. It was revealed that the Froude number was a driving parameter linked to the reattachment position of the separated shear layers to the free surface. Ozdil and Akilli (2015, 2019) used PIV experiments to study flow patterns around a horizontal circular cylinder in shallow water at varying submergence depths. They found that the Reynolds stress and turbulent ki-

netic energy variations are closely correlated with the submergence level.

Bouscasse et al. (2017) conducted two-dimensional simulations in a single-phase flow using the smoothed particle hydrodynamics (SPH) method. Their study focused on a comprehensive flow classification by examining vorticity fields and surface distortions across a wide range of Froude numbers, extending up to 2. They identified a new wake state in which the large meta-vortex in the stagnant recirculating region eventually moved downstream when $Fr \approx 1$. Moreover, they observed the reappearance of von Kármán vortex shedding at extremely high Froude numbers ($Fr \approx 2$). Chu et al. (2018) performed two-dimensional LESs for a submerged circular cylinder. They observed a hydraulic jump behind the cylinder with total suppression of vortex shedding at $Fr \geq 1$. This work was followed by (Moballa et al. 2020), who investigated the transition of the free-surface deformation from regular waves to breaking waves, and suggested the existence of a close relationship between hydrodynamic forces and submergence ratios.

Zhao et al. (2021) conducted LESs for a submerged circular cylinder in a shallow channel flow for $Fr = 0.2$ and 0.6 based on the cylinder's diameter and at $Re = 7{,}550$ to investigate the effects of the free surface distortion on the flow fields and hydrodynamics. While no obvious distortion of the free surface was found at $Fr = 0.2$, they classified the intense free-surface distortion occurring at $Fr = 0.6$ into three categories: a hydraulic jump in the overtopping region, wave generation region near the free surface and a water level recovery further downstream. Zhao et al. (2022) conducted an analysis on the impact of a free surface on the flow around a circular cylinder at $Re = 4.96 \times 10^4$ and h/D from 0.1 to 2.0. They identified three surface deformation patterns: a wake featuring a jet flow, one-sided vortex shedding and free-surface modulated von Kármán vortex shedding. The proximity to the free surface influenced hydrodynamic characteristics. Specifically, when a jet dominated the wake, the mean drag force remained low, and hydrodynamic fluctuations were suppressed. Moreover, the circular cylinder consistently experiences a downward thrust, which increases as the free surface approaches the cylinder.

The related problem of flow around a cylinder of varying cross-sections near a free surface is also relevant to the current research. A series of experiments in a water channel was carried out by Malavasi and Guadagnini (2007) to investigate the interaction between a free surface and a cylinder of rectangular cross-section. Their results revealed that the imposed asymmetrical boundary conditions significantly influenced the average forces and frequencies of vortex shedding. Furthermore, Zhong et al. (2019, 2020) conducted two-dimensional, unsteady Reynolds-Averaged Navier–Stokes simulations of flow past a rectangular cylinder in proximity to the free surface. They examined a wide range of depth-to-length (d/l) and width-to-length (w/l) ratios to illustrate the relationship between variations in flow patterns and force variations. They found that the free surface effects on the flow past rectangular cylinders become significant when $d/l \leq 1.0$. The substantial flow change occurs at around $d/l = 0.6$ and $d/l = 0.9$ for rectangular cylinders with the w/l ratios of 1.0 and 3.0, respectively.

Karmakar and Saha (2020) conducted a numerical study of two-dimensional flow around a square cylinder near a free surface at $Re = 180$ and found a close resemblance between the wake of the square cylinder and that of the circular cylinder, particularly in terms of large-scale vortex structures. Subburaj et al. (2018) conducted two-dimensional flow simulations around an elliptic cylinder situated near a free surface in a laminar flow environment. They examined how the flow characteristics were affected by parameters such as the angle of attack, aspect ratio, submergence depth, and Froude number, where the effect of the free surface on the vortex shedding is significantly influenced by the angle of attack and aspect ratio. Other researchers, such as Liu et al. (2016), Díaz-Ojeda et al. (2019), Attiya et al. (2019), have also investigated the flow around a plate in the vicinity of the free surface. Table 1.1 presents a summary of the relevant studies and their main findings in the study of flow dynamics around a circular cylinder.

Adequate quantification of changes in the development of unsteady turbulent wake dynamics behind cylinders with free or solid wall proximity effects requires the use of advanced techniques, such as proper orthogonal decomposition (POD), which is a reliable and explicit statistical methodology for identifying coherent patterns in transient flows (Berkooz et al. 1993). Other methods of extracting flow information include dynamic mode decomposition (DMD), Koopman mode decomposition, and the Galerkin projection, among many others. POD identifies the modes with the highest energy content and allows us to represent the flow dynamics in a low-dimensional manner (Taira et al. 2017). The use of reduced-order modelling via POD can elucidate the turbulent structures and also save computational time, enhancing the efficiency of numerical models in fluid mechanics (Kevlahan et al. 1994, Ma and Karniadakis 2002, Kostas et al. 2005).

Previous studies have successfully adopted POD to identify the largest scales of motion in cylinder flows. For instance, Rehimi et al. (2008) conducted an experimental study of the impact of wall confinement on the wake formation behind a circular cylinder at Re below 277 using PIV, and employed POD for filtering purposes and to extract the energetic contribution of different modes. Sen et al. (2017) conducted a numerical simulation of two-dimensional laminar flow past a circular cylinder at Re = 100 using a co-counter flow with various fluids to try to suppress vortex shedding by jet injection. They used POD to identify the dominant modes and their respective enstrophy distribution for the vorticity field. Wang et al. (2014) investigated the near wake of a wall-mounted finite-length square cylinder by applying POD to the PIV data, with the main focus on the correlation between flow structures and POD coefficients. Mishra and De (2021) investigated the suppression of vortex shedding using a passive flow control technique at Re = 100-500, and employed POD to quantify its effectiveness, and also to investigate the dominant vortical structures.

An alternative approach based on the Koopman operator was introduced by Rowley et al. (2009) with the aim of revealing the features of vortices that are often buried within a turbulent flow. The infinite-dimensional representation of the Koopman mode can be reduced

and approximated using the DMD algorithm proposed by Schmid (2010). The DMD breaks the dynamical system down into an array of estimated Koopman modes. In contrast to POD, DMD modes are governed by their dynamics rather than energy content. While a POD mode may exhibit a continuous frequency spectrum, each DMD mode is linked to a particular frequency. This distinction is fundamental when comparing the two techniques. DMD can effectively pinpoint dominant frequencies, even for vortices with minimal energy. For instance, a flow structure that holds relatively small energy but maintains strong connections with other structures that share the same frequency is prone to be disregarded by POD analysis, but would be captured by the DMD technique. In a comparative analysis by Wu et al. (2019), it was found that energy is more evenly distributed in DMD, which makes POD the optimal choice for reconstructing the flow when compared to DMD because the latter requires a greater number of modes to capture the same amount of energy.

Table 1.1 Summary of relevant studies on flow around a circular cylinder, ordered chronologically, including references, Reynolds numbers, parameters (with G/D representing gap ratio, h/D denoting submergence ratio, and Fr indicating Froude number), Type of study (numerical [Num.] and/or experimental [Exp.]), and key findings.

Reference	**Reynolds Number**	**Parameters**	**Type of Study**	**Key Findings**
Taneda (1965)	170	G/D = 0.1 and G/D = 0.6	Exp.	Single row of vortices at $G/D = 0.1$, double at $G/D = 0.6$
Roshko et al. (1975)	20000	G/D = 0.00-6.00	Exp.	Increased drag at $G/D > 0.60$, peak lift at $G/D = 0$
Bearman and Zdravkovich (1978)	25000-45000	G/D = 0.0-3.5	Exp.	Vortex shedding suppressed below $G/D < 0.3$, Strouhal number constant above $G/D > 0.3$
Angrilli et al. (1982)	2860-7640	G/D = 0.50	Exp.	Shedding frequency increases as G/D decreases, max discrepancy at G/D = 0.50
Grass et al. (1984)	2000-4000	G/D = 2.00-0.50	Exp.	Regular shedding between G/D = 2.00-0.75, less energetic below G/D = 0.50.
Taniguchi and Miyakoshi (1990)	94000	G/D = 0.1-3.0	Exp.	Fluctuating forces increase at critical G/D, influenced by boundary layer
Miyata et al. (1990)	49600	h/D = 0.0-1.75	Exp/Num.	Drag reduces, Strouhal number increases below $h/D < 0.35$, lift up with lower submergence
Buresti and Lanciotti (1992)	88000-277000	G/D = 0.0-1.5	Exp.	Non-monotonic drag trend, lift drops with increasing G/D.
Sheridan et al. (1995, 1997)	100-10000	Fr = 0.47–0.72, h/D = 0.0–0.75	Exp.	Two wake states identified, free surface vortices dominant over cylinder's

Lei et al. (1999)	13000-14500	G/D = 0.0-3.0	Exp.	Boundary layer affects lift, Strouhal number varies with G/D
Lei et al. (2000)	80-1000	G/D = 0.0-3.0	Num.	Lift regularity and amplitude reduce at lower gap/Reynolds, vortex shedding suppressed at small G/D
Price et al. (2002)	1200-4960	G/D = 0.0-2.0	Exp.	Gap flow suppressed at $G/D \leq 0.125$, onset of vortex shedding at $G/D \geq 0.5$
Reichl et al. (2003, 2005)	180	Fr = 0.0-0.7, h/D = 0.1-5.0	Num.	Wake behaviour changes with surface deformation
Wang and Tan (2008*b*)	12000	G/D = 0.1-1.0	Exp.	Kármán-like shedding for $G/D \geq 0.3$, asymmetry at $G/D \leq 0.6$
Lin et al. (2009)	780-11500	G/D = 0.0-4.0	Exp.	Regular vortex shedding suppressed for $G/D \leq 0.5$
Rao et al. (2013)	25-200	G/D = 0.005-1.0	Num.	Transitions from 2D to 3D flow at $G/D \approx 0.25$
Ozdil and Akilli (2015)	5000	h/D = 0.25-2.0	Exp.	Turbulence correlation with submergence, increased jet flow velocity from h/D = 0.25 to 1
Bouscasse et al. (2017)	180	$h/D = -0.5$-2.5	Num.	Classical shedding absent at low gap ratios, wave-breaking at surface
Chu et al. (2018)	10000	h/D = 0.72-2.5	Num.	Water surface effects are notable at $h/D \leq 1.50$, Strouhal number fluctuates with surface proximity
Chen et al. (2019)	100	G/D = 0.6-3.0	Num.	Non-monotonic trends in hydrodynamic forces with varying G/D
Ouro et al. (2019)	6666-13333	G/D = 0.5 and 1.0	Num.	Vortex generation and wake asymmetry increase with narrow gap G/D = 0.5 and higher Reynolds numbers
Moballa et al. (2020)	150	h/D = 0.5-1.0, G/D = 1.0 and 5.0	Num.	Drag coefficient depends on h/D and G/D, lift influenced by h/D and Fr
Zhao et al. (2021)	7550	Fr = 0.2 and 0.6, h/D = 0.4	Num.	Minimal surface deformation at $Fr = 0.2$, intense distortion at $Fr = 0.6$
Zhao et al. (2022)	49600	Fr = 0.2 and 0.8, h/D = 0.1 and 2.0	Num.	Wake transitions: jet flow, one-sided vortex shedding, modulated and pure Kármán shedding

1.2.2 Leaky barriers and backwater rise

A leaky barrier as a type of NFM measure can be constructed using three horizontal cylinders spanning the main width of the channel, akin to tree branches (Müller et al. 2022, Muhaweni-

mana et al. 2023). This design is of interest to many stakeholders for leaky barriers in flood risk management. Although the hydrodynamics of flow around a single cylinder or a pair of cylinders has been extensively studied (Griffith et al. 2017, Chen, Ji, Xu, An and Zhang 2020), investigations into the flow around three circular cylinders, especially in very shallow free-surface flows, have received less attention.

Fig. 1.7 illustrates some possible configurations of a three-cylinder leaky barrier, which include in-line, side-by-side and staggered configurations. When several cylinders are in close proximity, their mechanical response can be significantly different than when they are isolated. The extent of this influence depends largely on the distance between the cylinders, leading to potential interactions between boundary layers or free shear layers. Zdravkovich (1977) introduced a classification of two-cylinder flow interference in various arrangements, which includes proximity interference, wake interference, and combined interference.

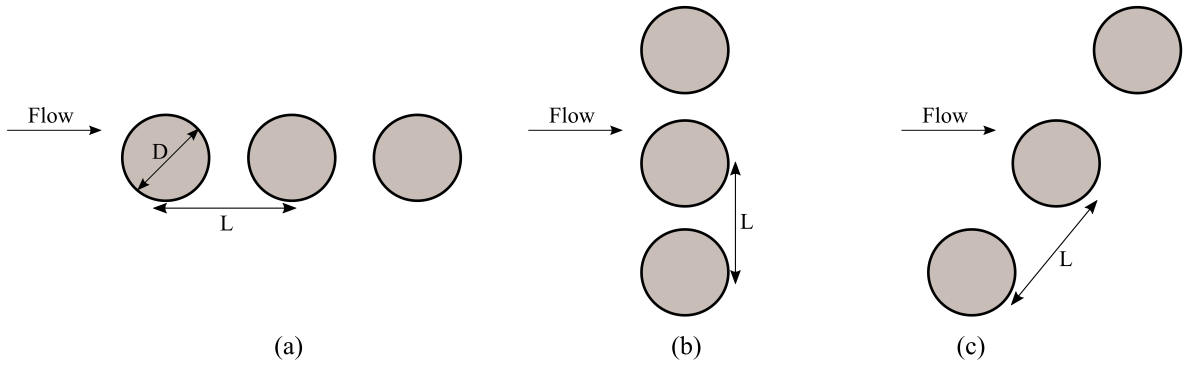

Fig. 1.7 Side view of a three-cylinder configuration for (a) in-line, (b) side-by-side and (c) staggered arrangements.

For the flow around two cylinders in line arrangements, the spacing ratio L/D, where L is the centre-to-centre spacing of the cylinders and D is the cylinder diameter, determines the occurrence of three different flow regimes, namely extended, reattachment and co-shedding flows (Sumner 2010, Alam 2014). The extended-body flow is observed when $L/D < 1.2$–1.8, where the cylinders are close enough for the flow in the gap between them to become stagnant due to the overshooting of free shear layers from the upstream cylinder over the downstream cylinder. In the reattachment flow regime (1.2–$1.8 < L/D < 3.4$–3.8), the shear layers reattach on the downstream cylinder, leading to a quasi-steady flow in the gap. The co-shedding flow regime occurs when $L/D > 3.4$–3.8, where the shear layers alternate in rolling up and down between the cylinders, resulting in significantly unsteady flow in the gap. The influence of the downstream cylinder on the upstream one is only noticeable for L/D ratios below 5.0. However, the upstream cylinder exhibits a significant influence on the flow around the downstream cylinder, even at larger L/D ratios (Papaioannou et al. 2006).

In the side-by-side configuration of two cylinders, the phenomenon of proximity interference occurs when the cylinders are located in close proximity to each other. Sumner (2010) identified five distinct flow patterns that occur in this configuration. For L/D values smaller

than 1.1–1.2, no gap flow exists between the cylinders, and vortices are shed alternately from the free-stream sides of the cylinders, which causes them to behave like a single bluff body (Alam et al. 2003). For intermediate L/D values (1.1–1.2 $< L/D <$ 2.0–2.2), two flow patterns, i.e. the deflected flow pattern and the flip-flopping pattern, appear intermittently. The flip-flopping pattern exhibits different characteristics in low-*Re* laminar flow and high-*Re* turbulent flow.

For the flow around two staggered circular cylinders, Alam and Meyer (2013) identified six different interaction mechanisms between the cylinders, which were characterised by the angle of attack (α) and/or L/D. These mechanisms were boundary layer-cylinder interaction, shear layer or wake-cylinder interaction, shear layer-shear layer interaction, vortex-cylinder interaction, vortex-shear layer interaction, and vortex-vortex interaction. The vortex-cylinder interaction led to a significant fluctuating drag, while the vortex-shear layer interaction produced a high fluctuating lift.

The flow around three cylinders is more complex than that around two, Igarashi and Suzuki (1984) conducted an experimental study on the flow around three cylinders in tandem at $Re = 1.09 \times 10^4 - 3.92 \times 10^4$, and L/D = 1.0–4.0. Six flow patterns and two bistable flow regions were identified due to the dynamic effects of upstream-cylinder shear layers on the downstream cylinders. The flow around three-cylinder configurations, considering various gaps between the cylinders and both side-by-side and tandem arrangements, was numerically investigated by Harichandan and Roy (2010). This study revealed the presence of diverse wake patterns, including in-phase and anti-phase synchronised wake patterns, flip-flopping wake patterns, deflected wake patterns and steady wake patterns. These wake patterns were found to be dependent on the Reynolds number and the gap spacing between the cylinders.

Kang (2004) conducted numerical simulations of laminar flow past three side-by-side cylinders at *Re* = 100. He found that, based on the L/D ratio, the flow patterns could be classified into five distinct types: the single bluff body for $L/D < 1.3$, deflected for $L/D \approx 1.3$, flip-flopping for $1.3 < L/D \leq 2.2$, in-phase for $L/D \approx 2.5$ and modulation for $L/D \geq 3.0$. In the modulation pattern, the vortex-shedding frequency of the central cylinder was observed to be slightly larger than that of a side cylinder and the modulation period was prolonged.

Han et al. (2013) also carried out numerical simulations of the flow past three side-by-side cylinders, but their study spanned a *Re* range of 40—160. They identified eight flow patterns: single bluff body, deflected, flip-flopping, non-identical and identical steady patterns, anti-phase and in-phase patterns, and a combined pattern that integrates the in-phase and anti-phase patterns. In their studies at lower values of *Re*, both asymmetric and symmetric steady patterns were observed. Notably, when the L/D ratio is small, vorticities in the gap shear layers are significantly lower than those in the free-stream shear layers. Conversely, when the L/D ratio is sufficiently large, the three cylinders behave as if they are isolated. In this scenario, the vorticity field and hydrodynamic forces are consistent across all three cylinders.

Yang et al. (2016) studied the flow past three circular cylinders in equilateral-triangular

arrangements at Re = 50–200 from the perspective of vortex-shedding suppression. Their findings reveal that at $\alpha = 0^\circ$ (with one upstream cylinder and two cylinders side-by-side downstream), vortex shedding from the upstream cylinder is suppressed for Re = 100–200. However, when $\alpha = 60^\circ$ (with two upstream side-by-side cylinders and one cylinder downstream), the suppression is noted on the downstream cylinder for $Re \geq 175$. In another study, Zheng et al. (2016) numerically examined the flow past three equidistantly arranged cylinders for $Re = 100$ and 200 with L/D ratios ranging from 1.5 to 7.0. They observed the deflected pattern at $\alpha = 0^\circ$, which is consistent with the findings of Yang et al. (2016). Furthermore, this deflected pattern demonstrated a clear dependence on Re, disappearing at $L/D \geq 2.0$ for $Re = 100$ and at $L/D \geq 3.0$ for $Re = 200$. Bao et al. (2010) conducted a numerical investigation of the same issue for L/D = 1.5–5.0, α ranging from 0° to 60° and $Re = 100$. Their results confirm five flow patterns: single bluff body, deflected, flip-flopping, in-phase and anti-phase. They also deduced that the flow interference between the three cylinders significantly influences the variation of the lift frequency.

In a high Re scenario of 6.2×10^4, Tatsuno et al. (1998) conducted experimental studies on the flow interference between three cylinders, varying α between 0° and 60°, and L/D from 1.39 to 6.93. Their results indicated that when L/D is small (< 2.6), the interference is pronounced, resulting in an asymmetric wake. Conversely, for $L/D \geq 3.5$, the flow interference diminishes, and a symmetric wake emerges. Bansal and Yarusevych (2017) observed a bistable flow pattern at $\alpha = 0^\circ$, $L/D = 1.35$ and $Re = 2.1 \times 10^3$, with a notable absence of gap flow direction switching. They found that the biased direction of the gap flow hinges on the initial flow conditions. This observation agreed with the findings of Lam and Cheung (1988) at Re values between 2.1×10^3 and 3.5×10^3, where the bistable pattern manifested at $L/D \geq 2.29$ for $\alpha = 0^\circ$.

In a recent study by Zhu et al. (2021), the vortex characteristics of flow around three tandem circular cylinders were examined. Their investigation considered gap ratios L/D ranging from 0.5 to 9 at a Re of 160. Four flow patterns were identified: overshoot, continuous reattachment–alternate reattachment, quasi-co-shedding and co-shedding–co-shedding regimes. Their study extensively discussed the corresponding changes in vortex-shedding frequency, force coefficients and the switching of phase lags in fluctuating lifts. Hosseini et al. (2021) analysed the flow states and wake transitions for flows past two and three tandem cylinders at a Reynolds number of 200. They observed a two-row vortex structure when there was a large gap ratio between the two upstream cylinders. However, when a third body was positioned on the wake centreline, occupying most of this two-row structure, it had negligible effects, both upstream and downstream, which they described as 'convectively unstable.' A notable exception was in a region that the authors labelled 'absolutely unstable.' In this region, the third body's placement suppressed vortex shedding from the first cylinder, resulting in the destruction of the two-row vortex structure. A local instability analysis was employed to further clarify these findings.

The effectiveness of large woody debris and engineered leaky barriers in flood attenuation has been quantified using various one-dimensional and two-dimensional hydraulic models that employ geometric and roughness adjustments (Valverde 2013, Geertsemaa et al. 2018, Rasche et al. 2019). However, these models rely on significant approximations and assumptions, and often struggle to accurately represent the hydraulic flow complexity that is induced by these natural flood structures (Manners et al. 2007, Schalko et al. 2018, 2019, Müller et al. 2022). The choice of Manning's coefficient or roughness values to represent a leaky barrier in hydraulic modelling is substantially variable and interdependent on multiple model characteristics, such as the model's spatial resolution. Accurately representing hydraulic effects in detail is only achievable through three-dimensional modelling. However, so far, its application has been limited to straightforward engineered log jams within smaller sub-reach scales (Allen and Smith 2012, Xu and Liu 2017). This is primarily due to significant constraints, such as the creation of meshes for complex large wood features and the computational demands of three-dimensional computational fluid dynamics compared to simpler models. An alternative approach involves the use of a porosity model, which approximates real complex in-stream structures using porous media, to simulate leaky barriers, which can provide similar results to three-dimensional modelling while reducing computational requirements. However, this method may result in the disadvantage of information loss because it may not fully capture all of the complex details and behaviours that are present in the actual system (Xu and Liu 2017, Addy and Wilkinson 2019).

Leaky Barriers create a backwater rise upstream, resulting in slower and deepened water, which enhances channel-floodplain connectivity, and the deposition of sediment and fine particles (Bilby 1981). Equations designed to predict backwater rise due to LWD or engineered leaky barriers have been established through flume experiments and regression analyses based on various experimental setups (Schalko et al. 2018, 2019, Schmocker and Hager 2013, Follett et al. 2021, Huang et al. 2022). These equations account for variables such as the approach flow Froude number, large wood compactness, loose large wood volume, cross-sectional blockage ratio and the longitudinal barrier length. Schmocker and Hager (2013) proposed an empirical equation to characterise the development of backwater rise based on the approach flow Froude number and the total debris volume. They found that the higher the approach flow Froude number, the higher the backwater rise, while the effect of the debris mixture on the backwater rise is comparatively small.

Schalko et al. (2018) proposed an empirical equation to calculate backwater rise resulting from large woody (LW) accumulations. Their study revealed that the magnitude of backwater rise is primarily influenced by the approach flow Froude number, the compactness of LW accumulations and the percentage of organic fine material. Schalko et al. (2019) expanded their 2018 equation to include different accumulation types and noted that movable beds reduce backwater rise compared to fixed beds due to increased scour. Follett et al. (2021) proposed a theoretical model to predict the backwater rise by utilising established sluice gate models

and incorporating a canopy drag law, in contrast to previous studies that modelled log jams as sluices with an empirically determined permeability coefficient (Hankin et al. 2020, Leakey et al. 2020). A recent study by Huang et al. (2022) used the canopy drag model to propose a theoretical method for predicting the upstream water depth based on the momentum equation. Despite the extensive research conducted on the subject, none of the equations studied have demonstrated universal applicability across various hydraulic conditions or settings. Nevertheless, it is important to note that there is no single definitive approach or methodology that can be considered to be the absolute best, as different methods may prove more effective depending on the specific situation being examined.

Equations developed to estimate the backwater rise induced by bridge piers and decks during high flows, known as afflux, can also provide a useful reference for the backwater investigation of leaky barriers. One of the most widely used bridge afflux models is an empirical equation derived from 2600 experiments that considered parameters such as pier shape, width, length, skew angle and flow rate (Yarnell 1934). However, these experiments primarily focused on non-cylindrical piers with a relatively small proportion of cylindrical pier experiments (Yarnell 1934), which are now considered to be the most commonly used shape (Wang et al. 2017). To overcome this shortcoming, equations have been derived that incorporate new parameters that account for cylindrical pier properties (Charbeneau et al. 2001, Suribabu et al. 2011). The values of these parameters were determined through multiple linear regression models. Biery and Delleur (1962) also conducted investigations on backwater analysis for single-span arch bridge models, developing a backwater formula based on the Froude number and the porosity ratio. This formula has since been further optimised in various studies, including Atabay (2008) and Zahang et al. (2021), to expand its applicability to different bridge shapes and hydraulic conditions.

1.2.3 Modelling free-surface flows

Water surface appears in various flows that are significant in engineering hydrodynamics, from the common open-channel flow to shallow submergence coastal flows past marine structures such as tidal stream turbines. These surfaces, which are often referred to as free-surfaces, mark the boundary between the water and the air above. They can deform in response to local flow conditions, including turbulence and bathymetric features. However, deformations caused by turbulence are generally minor when compared to changes in the mean surface position due to the presence of hydraulic structures, ocean waves and non-uniform bed formations.

The equations governing free-surface flow are significantly more complex than those for internal flow. This is due to the additional kinematic and dynamic boundary conditions at the free surface (Hodges and Street 1999, Ferziger and Peric 2002). The kinematic condition, which is hyperbolic in nature, asserts that there can be no convective mass transfer across the

air-water interface. Consequently, the fluid velocity component perpendicular to the surface must match the surface's own velocity. The dynamic boundary condition demands a force equilibrium at the interface. This means that the pressure and viscous forces that are applied by the air and water, respectively, need to be in balance. These boundary conditions introduce new nonlinear terms into the Navier–Stokes equations, which makes their numerical solution significantly more challenging. However, in hydraulics, the dynamic condition is often disregarded. This is based on the assumption that surface tension is negligible and the air-side pressure remains constant.

In the field of computational fluid dynamics, several methodologies are used to manage the free-surface boundary. The simplest is the rigid-lid approximation, which discards free-surface deformations and will be detailed in Section 1.2.3.1. On the more complex end, there are numerical techniques that account for free-surface deformations as the computation advances, e.g. at each time step. These methods are broadly classified into two main categories: interface tracking methods and interface-capturing methods, which are described in Sections 1.2.3.2 and 1.2.3.3, respectively.

1.2.3.1 Rigid-lid approximation

In hydraulics, the predominant method that is used in simulating flows involving water surfaces is the rigid-lid approximation. This method uses a fixed (typically flat) surface or lid to represent the water surface. The specifics of this method involve setting a free-slip boundary condition at the lid. In essence, the simulation mimics a closed conduit with a frictionless condition at the lid. This ensures that the shear stress at the lid and the fluid velocity component perpendicular to it are zero. However, pressure can still vary along a wall, which induces zero shear stress. This is akin to a symmetry boundary condition. Instead of determining the surface height from the local fluid pressure, the problem is reversed: one must compute the pressure based on the pre-established surface height. The momentum equations for free-surface flows replace surface-elevation-gradient terms with pressure gradients. This ensures that the dynamic effects of surface-elevation variations are properly considered in the rigid-lid approximation.

While this method suppresses actual surface deformation, the resulting error in the continuity equation is minimal when the surface deviation is small compared to the local water depth, typically being less than 10% of the depth. Given that many engineering flows, which often have turbulence-induced local surface perturbations, satisfy this condition, the rigid-lid approach has been successfully employed in a large number of studies. This is particularly true of open-channel flows, where rigid-lid LES and DNS have provided valuable understanding on topics such as cylinder flow hydrodynamics (Ouro et al. 2019) and the structure of bed-generated turbulence (Stoesser and Nikora 2008, Bomminayuni and Stoesser 2011).

To evaluate the validity of the rigid-lid assumption, Komori et al. (1993) incorporated sur-

face variations into their computations by applying the kinematic boundary condition. They subsequently compared their findings with results obtained from the rigid-lid simulations conducted by Lam and Banerjee (1992). Their study revealed that deformations in the free surface and the velocities normal to the nearby surface remained remarkably small. This led the authors to conclude that the predicted flow behaviour near the free surface closely corresponds with the outcomes of the rigid-lid simulations. However, it is important to note that when surface fluctuations become significant relative to the local water depth, the potential for errors is anticipated to increase notably. The consensus within the field is that the strict applicability of the rigid-lid approximation is limited to flows that are characterised by low Froude numbers (i.e. $Fr \leq 0.5$), as indicated by Paik and Sotiropoulos (2005) and Koken and Constantinescu (2009).

Kara et al. (2015a) conducted two LESs for flow through the same bridge contraction geometry: one with a rigid-lid boundary and the other using a free-surface capturing algorithm. The bulk Reynolds number was 27,200. Even though the bulk Froude number was relatively low at $Fr = 0.37$, local values reached $Fr = 0.78$ due to the significant constriction the flow faced from the abutment (the channel width to abutment width ratio was 3:1). The results from Kara et al. (2015a) showed that while the first-order statistics and bed shear stresses were strikingly similar between the two simulations, the instantaneous turbulence structure and second-order statistics exhibited substantial differences. Fig. 1.8 illustrates the distribution of normalised turbulent kinetic energy (tke) in a horizontal plane near the bed at $z/H = 0.1$, as derived from both simulations by Kara et al. (2015a). The peak of the high tke is closer to the abutment's tip in the free-surface simulation, unlike the rigid-lid simulation where the peak is observed further downstream. This variation is particularly significant for local scour because near-bed tke represents a fundamental aspect of in the erosion mechanism.

Recently, Alzabari et al. (2022) conducted two LESs for flow over a horizontal circular cylinder at $Re = 13{,}333$ and at a Froude number based on the submergence depth of $Fr = 0.45$. One simulation employed a rigid-lid boundary, while the other incorporated a free-surface capturing algorithm. Their findings revealed that when simulating the free surface, the vortical structures shed by the cylinder cause deformation in the free-surface layer upon interaction, which results in a more rapid loss of coherence of the von Kármán vortices. This phenomenon also leads to an increase in small-scale turbulence near the air-water interface. In contrast, the employment of the rigid-lid approach prevents free-surface deformation, thereby allowing the von Kármán vortices to maintain greater coherence (see Fig. 1.9). In addition, Alzabari et al. (2022) employed POD to thoroughly examine this contrast. They found that the rigid-lid approach could compromise the simulation's accuracy when representing essential turbulent mechanisms.

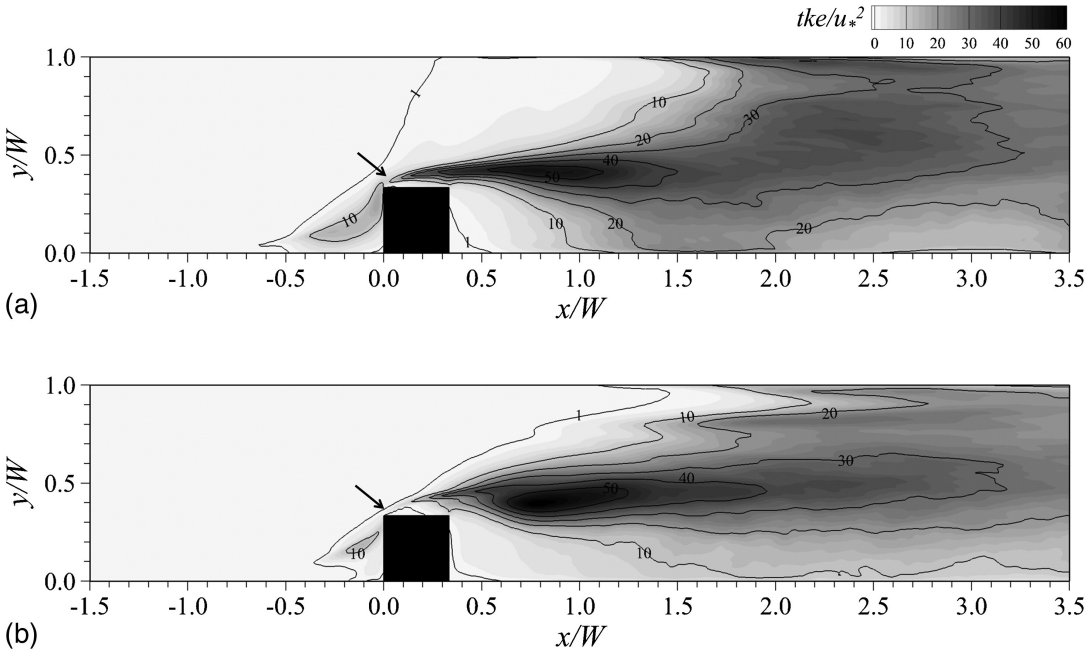

Fig. 1.8 Distribution of normalised turbulent kinetic energy in a horizontal plane near the bed at z/H = 0.1 as computed by (a) free-surface-resolved simulation; (b) rigid-lid simulation (Kara et al. (2015a)).

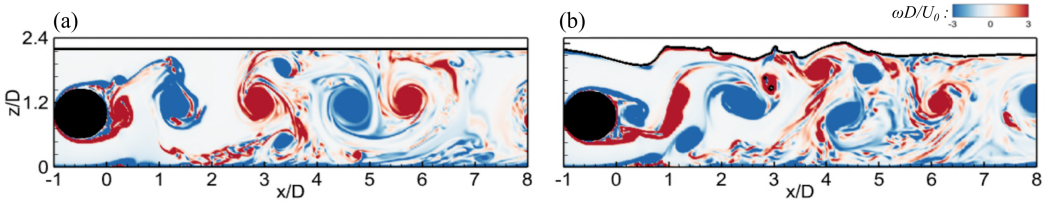

Fig. 1.9 Contours of normalised spanwise vorticity at Fr = 0.45 as computed by (a) rigid-lid simulation and (b) free-surface-resolved simulation. The free surface is depicted as a solid black line (Alzabari et al. (2022)).

1.2.3.2 Interface tracking methods

In interface tracking methods, often referred to as moving mesh methods, the mesh undergoes deformation after every time step to adjust the boundary of the computational domain to the free-surface position, enabling explicit surface tracking. The principal advantages of interface tracking methods stem from the inherent reduction in grid node numbers because no nodes are needed in the air phase and there is an absence of numerical diffusion, which can smooth out the interface in other methods (Chang et al. 1996). While the boundary integral technique is perhaps the most notable interface tracking method (Hou et al. 1994), it is largely unsuitable for flows that are dominated by the viscous Navier–Stokes equations, which makes it inapplicable in hydraulics (Hou et al. 2001).

In interface tracking methods, advances have been made in the field of ship hull hydrodynamics. The primary concern here is the interaction between the viscous boundary layer of the surface-piercing hull and the subsequent surface wave, as studied by Toda et al. (1992) and Longo et al. (1993). Many studies have focused on accurately predicting this interaction

using RANS approaches. For instance, Nichols and Hirt (1973), Farmer et al. (1993) and HC (1996) utilised free-surface height methods, where the free-surface was characterised as a height function. The solution for this function was only loosely coupled, temporally, with the solutions for bulk pressure and velocities. Conversely, Alessandrini and Delhommeau (1996) employed a similar method but solved for the height function and bulk flow simultaneously. Raven and Van Brummelen (1999) and Van Brummelen et al. (2001) successfully implemented an efficient iterative approach for steady and smooth surface waves. However, they observed that the method's efficacy diminishes and eventually breaks down when simulating steeper waves.

Miyata et al. (1987) adopted an interface tracking method using finite differences combined with a subgrid scale (SGS) model for turbulent stresses in simulations of flow past a ship hull where the surface wave profile had achieved a steady state, with Reynolds numbers reaching up to 10^5. In a subsequent study, Miyata et al. (1992) enhanced the accuracy of the method by employing a similar approach with finite volumes, successfully simulating Reynolds numbers up to 10^6.

In the field of hydraulics, Hodges and Street (1999) introduced an interface tracking method within the context of LES, simulating the interaction of waves with a turbulent channel flow. They employed an explicit time-discretisation scheme to progress the free-surface, solving the kinematic boundary condition. They then resolved a Poisson-type equation after each time step to compute a new boundary-orthogonal grid. In their study, the friction Reynolds number $\mathrm{Re}_\tau\,(=u_* H/\nu)$ was comparatively low at $\mathrm{Re}_\tau = 171$, which indicates that the turbulent eddies and the surface deformations that they induced had relatively extensive length and time scales. For friction Reynolds numbers of practical relevance, with considerably smaller turbulent lengths and time scales, recalculating a new mesh would prove prohibitively costly. In fact, Hodges and Street noted that their method would be unsuitable in such scenarios. Aiming to circumvent the need for creating a new mesh after each time step, Fulgosi et al. (2003) applied a mapping scheme that transformed the curvilinear physical space into an orthogonal coordinate system. The authors implemented this technique in a DNS of wind-sheared free-surface deformations.

The effectiveness of interface tracking methods faces a number of limitations in managing complex surface topologies, particularly in scenarios involving three dimensions and the presence of singularities. Typically, these methods encounter challenges beyond the point of singularity occurrence, which necessitates the execution of additional operations to eliminate individual nodes in close proximity to such features, consequently increasing the overall computational cost (Chang et al. 1996).

1.2.3.3 Interface-capturing methods

Unlike interface tracking techniques where the water surface is clearly defined by the mesh boundary, interface-capturing methods do not have this direct representation. Both air and water phases exist on an Eulerian mesh, which requires an algorithm to compute the evolution of the interface between them. Generally, interface-capturing methods are advantageous because they avoid the grid surgery issues that are inherent in interface tracking methods. However, they often face challenges in preserving the thickness of the interface and ensuring mass conservation across it.

Harlow and Welch (1965) first introduced the marker-and-cell (MAC) method. In this method, massless particles, such as tracers, are seeded in the water phase and are passively advected with the flow. One major advantage of the MAC method over many other interface tracking methods is its ability to manage complex surface topologies, such as breaking waves. However, the MAC method does require seeding a large number of particles, which makes it computationally intensive. Consequently, it has mainly been employed for two-dimensional or axis-symmetric flows (Viecelli 1971, Veldman and Vogels 1984, Armenio 1997). However, more recent methods such as those by Tomé et al. (2001), De Sousa et al. (2004) have expanded its use to three-dimensional cases such as tank filling and droplet splashing. A comprehensive review of advancements in MAC techniques can be found in McKee et al. (2008).

Instead of using markers or particles to represent the free-surface, another class of interface-capturing methods employs scalar functions. These functions do not need to align with grid lines and do not carry the significant computational expense that is associated with marker methods. One approach in this category is the volume of fluid (VOF) method that was introduced by Hirt and Nichols (1981). In the VOF method, the liquid phase fraction is calculated by solving a transport equation for the void fraction F. This fraction equals 1 in cells fully submerged in the liquid, 0 in cells completely exposed to the gas, and falls within the range $0 < F < 1$ in cells containing the interface.

Several research groups have proposed variations on Hirt and Nichols's original method, generally aiming to enhance the accuracy of the geometrical representation of the surface and/or the robustness of the advection of the volume fraction. Lower-order schemes, such as first-order upwinding, tend to smear the interface due to numerical diffusion. Meanwhile, high-order methods face stability issues and may result in numerical oscillations (Gopala and Van Wachem 2008). Some adaptations of the method include Hirt and Nichols's original donor-acceptor scheme (Hirt and Nichols 1981), the piecewise linear interface calculation (PLIC) method by Youngs (1982), the simple line interface calculation (SLIC) method by Noh and Woodward (1976), the flux-corrected transport (FCT) method by Boris and Book (1973), the compressive interface-capturing scheme for arbitrary meshes (CICSAM) by Ubbink (1997) and the inter-gamma compressive scheme by Jasak and Weller (1995).

The SLIC and PLIC methods, which both employ geometric rather than algebraic inter-

face reconstruction, have gained popularity, largely due to their relative simplicity and capacity to handle breaking and merging interfaces. However, Gopala and Van Wachem (2008) indicate that SLIC is plagued by high levels of numerical diffusion and limited accuracy. PLIC proves challenging to implement in three dimensions and with boundary-fitted grids. Although CICSAM and the inter-gamma method conserve mass well and maintain a sharp interface, they are highly sensitive to the local Courant-Friedrichs-Lewy (CFL) number.

In spite of the drawbacks of the VOF method, its popularity has steadily risen since its introduction. Thomas et al. (1995) introduced an innovative approach that combined the height function method (Section 1.2.3.2) with VOF. This combination resulted in conservation of both mass and momentum with minimal numerical dissipation. While this method excelled in simulating large surface deformations, the surface slope was bound by a restriction linked to the cell aspect ratio, which makes simulations of breaking waves unfeasible. Later, Shi et al. (2000) applied this method to model turbulent flow in a straight open channel in a relatively poorly resolved LES that was compatible with a standard desktop workstation to prove the applicability of the method within an engineering setting. The turbulence metrics were found to exhibit good agreement with both experimental and DNS data.

Sanjou and Nezu (2010) conducted LES of turbulent free-surface flows past emergent vegetation in compound open channels. While this study did not provide details of the VOF scheme, the results revealed the applicability of surface capturing approaches to LES in complex hydraulic flows. Xie et al. (2014) conducted LES of turbulent open-channel flow over two-dimensional dunes, aiming to replicate the experimental setup by Polatel (2006). Two LES scenarios were employed: one using the rigid-lid approximation, and the other incorporating the CICSAM VOF method to model the free surface. With a bulk Reynolds number set at 28,000 based on mean depth and bulk flow velocity, a relative submergence of 4, defined as the ratio of flow depth to dune height, and a relatively low Froude number of 0.32, the conditions were characterised. A good agreement was found on comparing the mean velocity profiles obtained from both LES runs with the experimental data, although disparities emerged in the turbulence statistics. Moreover, the VOF simulation revealed a noticeable extent of surface renewal in the form of upwelling and drafts.

The effectiveness of the VOF method in managing complex surface configurations that involve both breaking and merging has led to its widespread adoption in studying breaking waves. Although several early studies addressed this issue using RANS approaches (Bradford 2000, Bakhtyar et al. 2009), relatively few instances of LES have been conducted, and most of them are confined to two dimensions (Watanabe and Saeki 1999, 2002, Lubin et al. 2011). However, Christensen (2006) extended the study into three dimensions, although their simulations suffered from inadequate grid resolution.

The level-set method (LSM), which originated in computer graphics, has recently gained popularity as an interface-capturing technique for multi-phase flows. Similar to the VOF method, LSM employs a scalar function instead of Lagrangian particles, thus avoiding the

computational costs that can hinder methods such as the MAC approach. This method was originally proposed by Osher and Sethian (1988) and was developed for computing and analysing the motion of interfaces between two fluid phases in two or three dimensions. In the LSM, the interface is expressed by the zero set of a smooth distance function, denoted as ϕ, defined across the whole spatial region. The conservation equations are simultaneously solved for both the liquid and gas phases, with the interface being advected in accordance with the local velocity vector. The LSM method is an adaptable approach that is capable of computing geometrically complex surfaces, even those involving corners and cusps. It also exhibits robustness in handling rapidly changing topologies. Furthermore, its extension to three-dimensional problems is relatively easy (Chang et al. 1996).

In the field of hydraulics, Yue et al. (2005) employed the LSM in LES to study turbulent open-channel flow over fixed dunes. The relative submergence was at 6.6, a value significantly higher than that considered in the VOF study by Xie et al. (2014). This study revealed that the LSM method accurately and realistically simulated the unsteady free-surface motion. It also highlighted phenomena such as boils, upwelling and downdrafts at the water surface. Suh et al. (2011) investigated flow past a vertical circular cylinder protruding from the water surface using LES. The LSM captured water surface dynamics and indicated that the traditional von Kármán-type vortex shedding was attenuated in the near-surface region, being replaced by smaller vortices.

Kara et al. (2015b) conducted LES of flow through a submerged bridge with overtopping, employing the LSM for free-surface dynamics. The simulations unveiled complex hydrodynamics, featuring a plunging nappe and a standing wave downstream of the bridge. They also revealed horizontal recirculation behind the lateral abutment and vertical recirculation caused by the plunging flow. The simulation results matched well with experimental measurements, particularly concerning water surface deformation. Kang and Sotiropoulos (2015) performed LES of open-channel turbulent flow over a river restoration scheme. They employed the LSM to capture free-surface dynamics on a curvilinear grid. Their method showed good agreement with experimental data for mean velocities and turbulence statistics. Furthermore, it effectively captured complex flow dynamics downstream of the structure, including a standing wave characterised by high near-surface turbulence levels.

The challenge that is commonly associated with front capturing techniques is to maintain interface thickness while ensuring mass conservation (McSherry et al. 2017). In the context of the LSM, the specific problem is that maintaining the status of ϕ as a signed distance function at all times becomes problematic due to the natural distortion caused by advection resulting from the local velocity vector. LSM employs re-initialisation techniques to address this challenge. These techniques entail regular resetting of the ϕ field, ensuring its continuous representation as a signed distance function, while preserving the zero level set. The pioneering re-initialisation technique was introduced by Sussman et al. (1994), followed by modifications proposed by Peng et al. (1999), Russo and Smereka (2000), Sussman and Puckett

(2000), among others. However, the re-initialisation process can lead to numerical errors and introduce numerical oscillations in the free surface (Griebel and Klitz 2017).

In recent years, many efforts have been dedicated to enhancing the mass conservation properties of the LSM through its integration with other techniques, resulting in the development of hybrid methods. An illustrative example of such efforts is provided by Enright et al. (2002), who introduced a particle level-set method (PLSM). This method relied on Lagrangian marker particles to reconstruct interfaces in regions characterised by poor resolution. This study demonstrated that the PLSM showed comparable levels of mass conservation and interface resolution to those achieved by VOF and pure Lagrangian methods, respectively. One particularly promising hybrid methodology that has gained prominence recently is the coupled level-set volume of fluid (CLSVOF) method (Wang, Yang and Stern 2008). Remarkably, this approach has demonstrated its superiority over the PLSM in simulating practical engineering flows (Ménard et al. 2007, Wang et al. 2012, Yu et al. 2019).

1.3 Objectives and thesis structure

The main objective of this research is to provide new insights into the hydrodynamics of horizontal cylinders in free-surface flows. This research seeks to investigate the hydrodynamics of a single cylinder at varying submergence depths and to analyse the nature of the turbulent wake. This research additionally intends to examine in more detail the local hydrodynamics around arrays of horizontal cylinders, assessing their potential to enhance natural flood management measures through various leaky barrier configurations. The goal is to develop and assess methodologies for accurately estimating flow characteristics near leaky barriers in scenarios with limited data availability. The numerical method of LES is employed, with a focus on the influence of free-surface effects on hydrodynamics. By adopting the LSM as an interface-capturing tool, the water surface deformation is simulated to provide a clearer understanding of the free-surface impact on hydrodynamics. The structure of this thesis is outlined as follows:

Chapter 2: This chapter presents the governing Navier–Stokes equations, as implemented in the in-house code Hydro3D, which is followed by the fractional-step method that has been adopted. The use of the immersed boundary method to represent in-stream bodies is then described. The LSM used to track the free surface, and the implementation of surface tension, which aids in preventing the breaking of interfaces and the formation of bubbles within the flow, are then described. Finally, the application of the POD method, which will employed to analyse the flow fields and capture coherent flow structures, is presented.

Chapter 3: LESs of turbulent flow dynamics downstream of a single horizontal cylinder subjected to varying submergence depths are conducted in this chapter. A detailed representation of the hydrodynamics, influenced by free-surface interactions, takes various submergence depths with a fixed close proximity to the bottom wall into account. The impact of increasing

the Froude number based on the submergence depth on vortex-shedding patterns, free-surface profiles, momentum distribution and hydrodynamic coefficients is discussed. A manuscript based on this chapter is currently being prepared for submission, which is tentative title 'Hydrodynamic Characteristics of Flow Around a Circular Cylinder Near a Free Surface' and authored by F. Alzabari, C. A. Wilson and P. Ouro.

Chapter 4: This chpater uses POD to comprehensively analyse the spatio-temporal coherence of cylinder turbulent structures in free-surface flows of varying shallowness. Special attention is given to the dynamics of energy within the dominant von Kármán vortices as the submergence depth changes. Moreover, the correlation between the Froude number and the accuracy of flow field reconstructions, based on different POD modes, is studied, particularly in contexts where the effects of the free surface become more significant. A manuscript based on this chapter has been accepted (30 June 2023) in the *Computers and Fluids* journal, 'Unsteady vortex-shedding dynamics behind a circular cylinder in very shallow free-surface flows' and authored by F. Alzabari, C. A. Wilson, and P. Ouro. This chapter is also part of a manuscript that was published in the proceedings of the 39th IAHR World Congress, Vienna, Austria, 'Large-eddy simulation of the free-surface impact on the wake dynamics of a circular cylinder' by F. Alzabari, C. A. Wilson and P. Ouro.

Chapter 5: This chapter presents LESs to investigate the flow characteristics of several designs of a leaky barrier comprised of multiple cylinders. This research examines the hydrodynamics influenced by both the inclination and length of the barrier. Various angles relative to the upstream and downstream directions are considered, as well as variations in barrier length along the streamwise direction. This research contrasts different barrier configurations, especially with regard to the development of primary and secondary jets. The effects of barrier design on turbulent features, bed shear stress and structural loads are also detailed, shedding light on optimal barrier designs in terms of hydrodynamic efficiency. A manuscript based on this chapter has been submitted to the *Water Resources Research* journal, 'Hydrodynamics of In-stream Leaky Barriers for Natural Flood Management' by F. Alzabari, C. A. Wilson, and P. Ouro. This chapter is also part of a manuscript published in the proceedings of the 40th IAHR World Congress, Vienna, Austria, titled 'Large-eddy simulation of flow around leaky barriers in a linear configuration' by F. Alzabari, C. A. Wilson and P. Ouro.

Chapter 6: Two analytical methodologies have been derived and validated to estimate flow characteristics near leaky barriers (specifically, upstream and downstream depths and velocities), particularly in scenarios where only a subset of these conditions are accessible. One method draws upon fundamental momentum and continuity equations, while the other employs a refined empirical model that is commonly associated with bridge afflux assessments. Leveraging data on leaky barriers from diverse sources, the methodologies are assessed and the outcomes demonstrate the effectiveness of both approaches in predicting flow conditions. A manuscript based on this chapter has been submitted to the Journal of *Hydraulic Engineering*, 'Estimating Backwater Rise and Flow Velocity in Natural Flood Management Instream

Barriers' by F. Alzabari, C. A. Wilson and P. Ouro.

Chapter 7: Conclusion of the thesis and outlook of this research are included in this chapter.

CHAPTER 2

Numerical framework

2.1 Governing equations

The numerical representation of fluid-mechanics phenomena relies on discretisation methods to solve the Navier-Stokes equations. The continuity and momentum equations are derived from Newton's second law ($F = ma$) for fluid motions. In computational fluid dynamics (CFD) research, most cases are studied in four dimensions: three spatial dimensions and one time dimension. Due to the complexity of solving the continuity (Eq. 2.1) and momentum equations (Eq. 2.2), obtaining analytical and direct solutions is challenging. Consequently, these equations are most accurately approximated using a discretised numerical framework. Over the past decades, the increase in available computing resources has driven exponential growth in CFD research (Sotiropoulos 2015), which has made it an invaluable tool in a large number of research and industrial domains. Studies of incompressible flow have predominantly been supported by three main CFD turbulence closures: Reynolds-Average Navier-Stokes (RANS), large-eddy simulation (LES), and direct numerical simulation (DNS).

The Navier-Stokes equations are used to resolve three-dimensional, unsteady, turbulent, and incompressible fluids in a Cartesian rectangular grid. In the LES framework, the continuity and momentum equations are spatially filtered and normalised with the Reynolds number, as follows:

$$\underbrace{\frac{\partial u_i}{\partial x_i}}_{\text{Divergence of velocity}} = 0 \tag{2.1}$$

$$\underbrace{\frac{\partial u_i}{\partial t} + \frac{\partial u_i u_j}{\partial x_j}}_{\text{Acceleration}} = \underbrace{-\frac{1}{\rho}\frac{\partial p}{\partial x_i}}_{\text{Pressure force}} + \underbrace{\nu \frac{\partial^2 u_i}{\partial x_j \partial x_j}}_{\text{Viscous force}} - \underbrace{\frac{\partial \tau_{ij}}{\partial x_j}}_{\text{Shear stress}} + \underbrace{f_i}_{\text{Body force}} + \underbrace{F_{sf}}_{\text{Surface-tension force}} + \underbrace{g_i}_{\text{Gravitational force}} \tag{2.2}$$

where u_i and u_j are the resolved velocity components (where i or $j = 1, 2, 3$ represent the x-, y-, and z-directions, respectively); similarly, x_i and x_j represent the spatial location components in the three spatial directions; ρ is the density of the fluid; p is the resolved pressure; ν is the fluid kinematic viscosity; τ_{ij} is the subgrid-scale stresses; f_i represents external forces calculated using the direct forcing (DF) method proposed by Uhlmann (2005), which imposes

a no-slip condition at the immersed-boundary points comprising the geometry of the bluff body (described in Section 2.3); F_{sf} is the surface-tension force; and g_i is the gravitational acceleration.

The simplest and most straightforward way to describe a flow without any approximations applied in the calculation is achieved through the use of DNS, which calculates the entire spectrum of turbulent scales without the incorporation of any models. DNS numerically resolves all the significant scales of motion down to the Kolmogorov scales, corresponding to the scales accountable for the dissipation of energy in the flow. However, this approach demands significant computational resources, even when dealing with flows characterised by low turbulence, i.e. Reynolds Numbers. LES has emerged as an alternative to DNS, which explicitly computes the energetic flow structures by solving the governing three-dimensional Navier-Stokes equations, while modelling the isotropic small-scale ones via spatial filtering. The filtering is implicit within the adopted numerical grid, where only scales larger than the grid size are resolved. Those scales smaller than the grid cell are addressed by the subgrid scale (SGS) model (Rodi et al. 2013). This filtering assumption is reasonable because the smaller scales are isotropic, which makes them easier to model, whereas the larger scales are more energetic and anisotropic (Stoesser 2014). The LES requirements can be further reduced in Hydro3D using the local mesh refinement (LMR) method, which permits the use of fine grid resolutions in areas of interest and coarser resolutions where such detail is not necessary (Cevheri et al. 2016).

The RANS method filters or averages out fluctuations, resulting in the calculation of only mean flow quantities. The RANS model is the most widely-used mathematical model in industry due to its relatively low computational power requirements. This model does not resolve any turbulence scale; instead, it employs additional turbulence equations, such as the k-ω and k-ε models. These models introduce additional equations to capture the turbulent characteristics of the flow. In cases where the mean flow is unsteady, the method is referred to as URANS and it filters out only the turbulent fluctuations, leaving the lower-frequency unsteadiness of the mean flow (Rodi et al. 2013). This thesis concentrates on the flow around hydraulic structures, which is characterised by large-scale turbulent structures. Given that RANS is unable to accurately capture these flow phenomena, it is not deemed appropriate for this research. LES has gained popularity in this research field due to its balance of accuracy and computational demand, offering a compromise between DNS and RANS.

Throughout this thesis, the in-house Hydro3D code that was initially developed by Stoesser (2001) is the numerical model that is used to perform large-eddy simulations (LESs), which has been validated in a series of challenging hydro-environmental engineering problems such as tidal steam turbines (Ouro and Nishino 2021), flow over bridge abutments (Kang and Sotiropoulos 2015), solitary waves (Christou et al. 2021), free-surface flow over square bars (McSherry et al. 2018, Jalalabadi et al. 2021), rough beds (Bomminayuni and Stoesser 2011, Liu et al. 2017, Nikora et al. 2019), in pipes (Liu et al. 2022), and backward-facing steps (Luo et al.

2023), among many others.

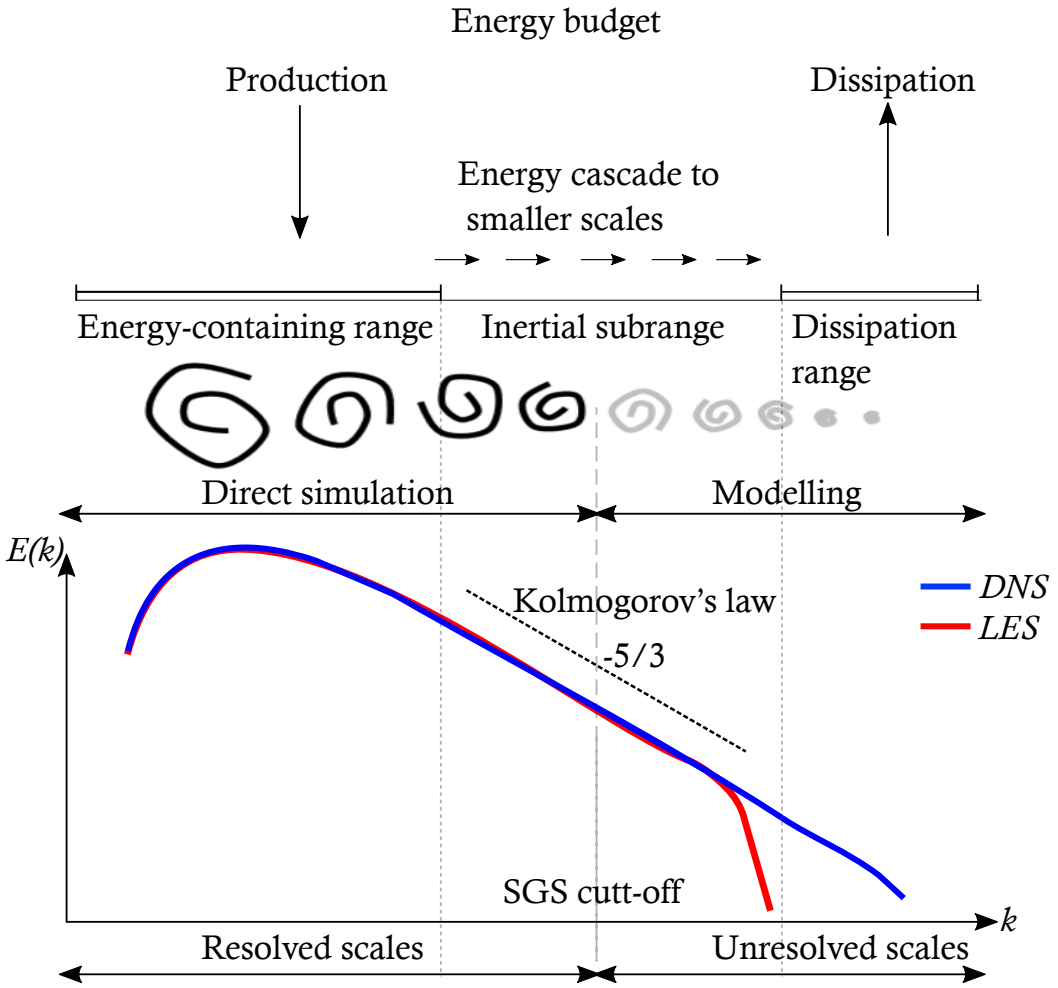

Fig. 2.1 A representation of the energy spectrum showcasing the differentiation between the production, inertial, and dissipation ranges.

The energy production and cascade process for energetic scales are identical for both LES and DNS, but differences can be observed in the spectral distribution of energy near the cut-off wave number (Fig. 2.1). At this point, the SGS model induces significantly faster energy dissipation. Generally, the finer the grid, the smaller the portion of the spectrum that requires modelling. Thus, the capabilities of the SGS model become especially relevant when LES is conducted on coarser grids. Fig. 2.1 presents the typical energy spectrum with three characterised regions: the production range, the inertial subrange that follows the Kolmogorov decay law with -5/3 slope, and the energy dissipation sub-range. These large scales draw energy from the average flow (production range), transferring it to small scales within the energy cascade. At these smaller scales, kinetic energy is withdrawn by the dissipation mechanism (Rodi et al. 2013). In a well-resolved LES, the cutoff vertical dashed line (Fig. 2.1) indicates the separation between resolved and modelled length scales, typically situated within the inertial subrange and preceding the dissipation range. The separation is achieved via spatial

filtering introduced by Leonard (1975). The general rule in LES regarding spatial filtering is that the filter's width is equal to the grid size. Turbulent scales smaller than the grid size are then modelled using a SGS model. In the following equations, the overbar (e.g. $\bar{x}$) denotes a filtered or averaged quantity.

The SGS stress, τ_{ij}, included in the momentum equation (Eq. 2.2), is the unresolved velocity fluctuation, and reads:

$$\tau_{ij} = \tau_{ij}^{a} + \frac{1}{3}\tau_{kk}\delta_{ij} \tag{2.3}$$

the first term τ_{ij}^{a} denotes the anisotropic component, whilst the second term τ_{kk} corresponds to the isotropic component associated with the Kronecker delta δ_{ij}. Hydro3D incorporates the Smagorinsky (Smagorinsky 1963) and Wall-Adapting Local Eddy viscosity (WALE) (Nicoud and Ducros 1999) SGS models. In the standard Smagorinsky SGS model, the turbulent or eddy viscosity (ν_t) is approximated as:

$$\nu_t = (C_s\Delta)^2 \cdot \left|S_{ij}\right|, \quad \text{where } \left|S_{ij}\right| = \sqrt{2S_{ij}S_{ij}} \tag{2.4}$$

$$S_{ij} = \frac{1}{2}\left(\frac{\partial u_i}{\partial x_j} + \frac{\partial u_j}{\partial x_i}\right) \tag{2.5}$$

where C_s represents the Smagorinsky constant, which is set to 0.1 (Rodi et al. 2013), $\Delta = (\Delta x \Delta y \Delta z)^{1/3}$ represents the filter size equivalent to the mesh cell size, S_{ij} denotes the resolved rate of strain derived from the filtered resolved velocities. This artificial viscosity is subsequently used to calculate the anisotropic subgrid stress tensor, as:

$$\tau_{ij}^{a} = -2\nu_t\bar{S}_{ij} \tag{2.6}$$

It is crucial for a SGS model to accurately represent the dissipation of energy because this is the only way for turbulent kinetic energy to be removed from the resolved scales (Davidson 2015). If the dissipation is too high, then it will lead to an artificial increase in diffusive fluxes and result in excessive damping of the resolved scales. Meanwhile, if the dissipation in the SGS model is too low, then it will cause a buildup of energy around the cutoff wavenumber.

In this thesis, the WALE model, introduced by Nicoud and Ducros (1999) is adopted. The WALE SGS model has several advantages compared to the classic Smagorinsky model (Smagorinsky 1963), including:

- Incorporation of both local strain and rotation rates: this allows the model to capture all turbulence structures relevant for the kinetic energy dissipation.
- Automatic reduction of eddy viscosity near walls: the eddy viscosity naturally goes to zero in the vicinity of walls, thus eliminating the need for dynamic constant adjustment or damping functions.

- Ability to reproduce laminar-turbulent transitions: the model produces zero eddy viscosity in pure shear flows, thus allowing for the simulation of the laminar-turbulent transition process.

- Invariance to coordinate transformations: the model is invariant to coordinate translations and rotations and requires only local information, which makes it suitable for LES in complex geometries.

The final consideration is particularly important because the WALE model is perfectly suited for simulations that have non-sharp solid boundaries, such as those performed through the immersed-boundary method (IBM), which is the case in the present research.

The turbulent viscosity in the WALE model is calculated from the resolved velocity-gradients tensor ($g_{ij} = \partial u_i / \partial x_j$) as follows:

$$\nu_t = (C_w \Delta)^2 \frac{\left(S_{ij}^d S_{ij}^d\right)^{3/2}}{\left(\bar{S}_{ij}\bar{S}_{ij}\right)^{5/2} + \left(S_{ij}^d S_{ij}^d\right)^{5/4}} \tag{2.7}$$

where C_w is the constant of the WALE model (assumed to be 0.46, as considered in Cevheri et al. (2016)), $\bar{S}_{ij}$ is the filtered rate of strain tensor, S_{ij}^d is the traceless symmetric part of the square of the velocity gradient tensor $\left(g_{ij}\right)$, presented as:

$$S_{ij}^d = \frac{1}{2}\left(\bar{g}_{ij}^2 + \bar{g}_{ij}^2\right) - \frac{1}{3}\delta_{ij}\bar{g}_{kk}^2 \tag{2.8}$$

The diffusive terms in the Navier-Stokes equations are approximated by second-order central differences, while convective velocity fluxes in the momentum conservation equation and the advection equation from the level-set method (LSM), which will be introduced in section 2.4, are approximated using a fifth-order weighted essentially non-oscillatory (WENO) scheme. The main advantage of the WENO scheme is its capability to achieve the necessary compromise between numerical stability and physical accuracy when simulating two-phase flows (Ouro et al. 2021). According to Rodi et al. (2013), the accuracy and credibility of a code can be established by utilising high-order spatial discretisation schemes, along with sufficiently fine grids.

2.2 Fractional-step method

The spatially filtered Navier-Stokes equations in the LES framework, presented as Eq. 2.1 and Eq. 2.2, are advanced in time through the use of the so-called fractional-step method based on the projection method (Chorin 1968). The main advantage of this technique is the uncoupling of the velocity and pressure computations. The numerical code solves the fluid on a Cartesian rectangular grid that is staggered, with the velocity vectors located in the middle of the cell

faces and the pressure stored in the cell centre. Hence, four different grids are used to compute u, v, w, and p. Fig. 2.2 displays a two-dimensional representation of a staggered grid with uniform grid spacing, along with the Lagrangian markers used in the IBM.

The fractional-step method employs the Helmholtz decomposition to derive the velocity field from two distinct types of vector fields over several computational steps: one representing a steady, continuous stream of fluid without any divergence (solenoidal), and another illustrating fluid motion without any rotation or curl, moving in a straightforward, uniform manner (irrotational). The first step predicts a non-solenoidal or non-divergence-free velocity, $\tilde{u}$, from the explicit computation of convection, diffusion terms, and the pressure term using values from the previous time step. The velocity $\tilde{u}$ at time step t is determined via a low-storage three-step Runge-Kutta scheme, which computes the convective and diffusive terms (Cevheri et al. 2016).

$$\frac{\tilde{\mathbf{u}} - \mathbf{u}^{l-1}}{\Delta t} = \nu \alpha_l \nabla^2 \mathbf{u}^{l-1} - \alpha_l \nabla p^{l-1} - \alpha_l [(\mathbf{u} \cdot \nabla)\mathbf{u}]^{l-1} - \beta_l [(\mathbf{u} \cdot \nabla)\mathbf{u}]^{l-2} \tag{2.9}$$

where $l = 1, 2$, or 3 represents the Runge-Kutta sub-step, and $l = 1$ indicates values from the previous time step $t - 1$. The terms α_l and β_l serve as the Runge-Kutta coefficients and have the following values: $\alpha_1 = \beta_1 = 1/3$, $\alpha_2 = \beta_2 = 1/6$, and $\alpha_3 = \beta_3 = 1/2$.

An additional correction to $\tilde{u}$ is necessary due to the influence of external forces, such as those from Lagrangian bodies. This adjustment aids in obtaining the updated intermediate velocity $\tilde{u}^*$. In this research, the IBM is employed, and its impact on the velocity field is achieved through the forcing term f_i on the right-hand side of Eq. 2.2. Consequently, the corrected predicted velocity field, $\tilde{u}^*$, is updated as

$$\tilde{\mathbf{u}}^* = \tilde{\mathbf{u}} + \boldsymbol{f_i} \Delta t \tag{2.10}$$

This intermediate velocity does not satisfy the solenoidal or divergence-free condition, and therefore a projection scalar function, often referred to as the pseudo-pressure ($\tilde{p}$), is introduced. This pseudo-pressure has no physical meaning but is calculated using the incompressibility condition to ensure the intermediate velocity field meets the divergence-free condition. The pseudo-pressure field is determined in Eq. 2.11 by solving the Poisson equation using an iterative multi-grid technique, given as:

$$\nabla^2 \tilde{p} = \frac{\nabla \cdot \tilde{\mathbf{u}}^*}{\Delta t} \tag{2.11}$$

The pseudo-pressure gradient correction is then used to project the predicted velocity field onto the divergence-free field, deriving the velocity field for the current time step u^t as:

$$\mathbf{u}^t = \tilde{\mathbf{u}}^* - \Delta t \nabla \tilde{p} \tag{2.12}$$

The value of the pressure field at the current time step, p^t, is ultimately calculated based on the value at the previous time step, p^{t-1}, and the pseudo-pressure field, as:

$$p^t = p^{t-1} + \tilde{p} - \frac{\nu \Delta t}{2} \nabla^2 \tilde{p} \tag{2.13}$$

The stability of the model is guaranteed by enforcing the Courant-Friedrichs-Lewy condition (CFL), which demands that the numerical flow speed of $\Delta x/\Delta t$ must be at least as fast as the physical flow speed $|u|$, i.e. $\Delta x/\Delta t > |u|$. To maintain a safe condition, a CFL number, α ($0 < \alpha < 1$), is used as a common conservative practice. The three-dimensional CFL number, α, can be expressed as follows:

$$\Delta t_{\max} \left[\frac{|u|}{\Delta x} + \frac{|v|}{\Delta y} + \frac{|w|}{\Delta z} \right] < \alpha = 1 \tag{2.14}$$

2.3 Immersed-boundary method

The immersed-boundary (IB) method, which was first introduced by Peskin (1972), aimed to develop a technique for simulating heart valves. It was built upon the projection method created by Chorin (1968), which is the basis for the popular fractional-step method. Peskin (1972) formulated a non-body conformal technique that offered an accurate and computationally affordable approach to biomechanical flows, especially in the field of cardiac flows. In over 40 years of development, the IB method has been applied to a wide range of applications, not only in biology but also in fields such as ocean engineering and aerodynamics (Tatsuno and Bearman 1990, Weymouth 2014). The IB method offers an economical and reasonably accurate way to represent solid boundaries within a computational domain. Furthermore, this method is highly adaptable, as it can be combined with any type of mesh, from staggered Cartesian mesh (Hydro3D) to unstructured triangular mesh.

Two primary categories of the IB method can be identified based on body representation: continuum and discrete approaches. The continuum approach represents the body using a continuous geometric description, projecting velocities over the body surface. Typically, this involves classifying Eulerian cells as solid, fluid, or intermediate using techniques such as ray-tracing. Notable examples of this methodology can be seen in the works of Iaccarino (2004) and Kang et al. (2012). On the other hand, the discrete method represents the body using a set of individual Lagrangian points, which collectively form its shape. In the present research, the discrete method is adopted because it offers greater flexibility with complex geometries, ensures detailed capture of fluid behaviour at the interface, and enhances computational efficiency (Mattei et al. 2018). Both the no-slip and pressure conditions are subsequently enforced at each of these Lagrangian markers (L) using a forcing term in the Navier-

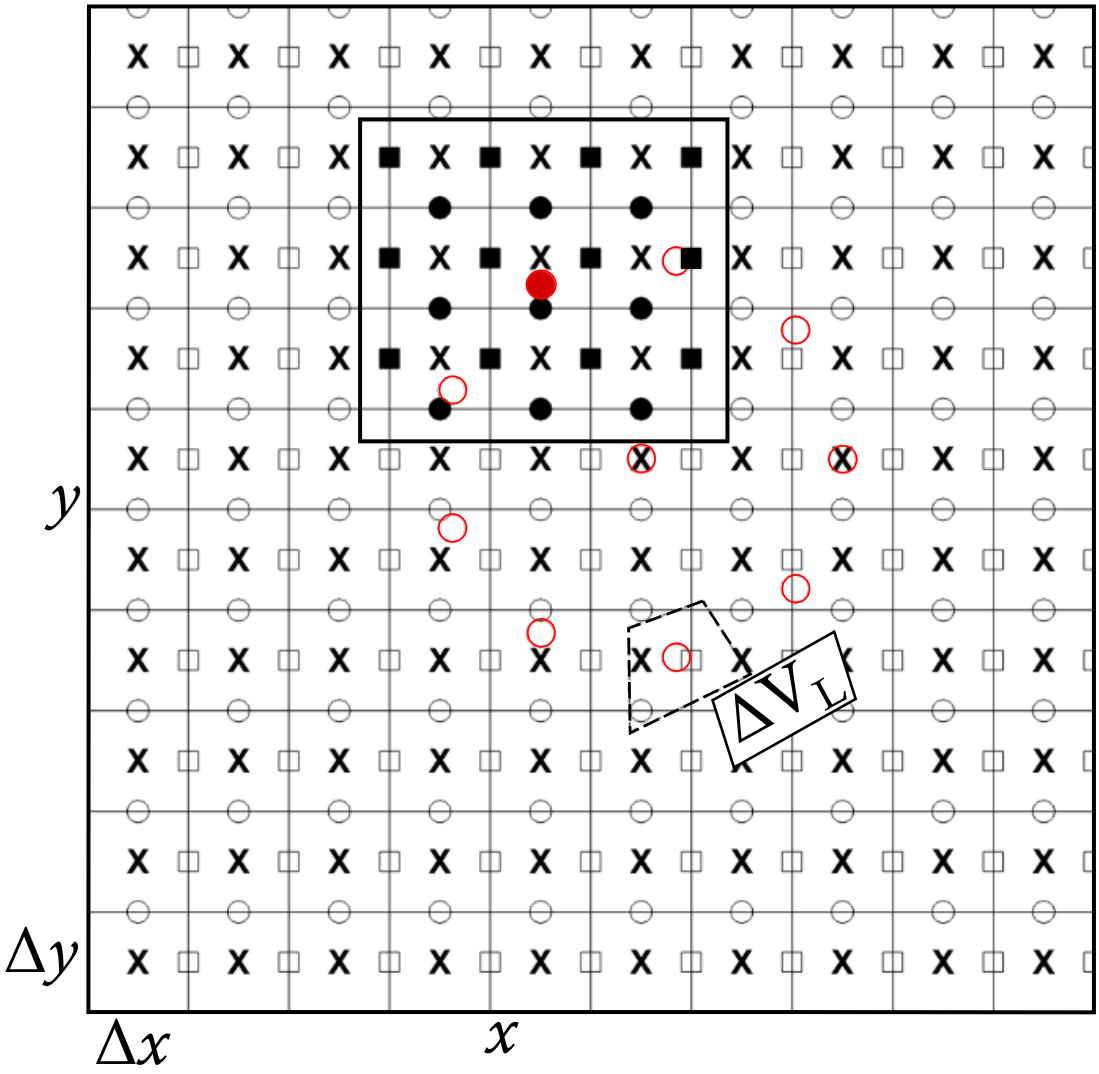

Fig. 2.2 Two-dimensional depiction of the Cartesian staggered grid. The black-filled symbols within the square boundary represent the neighbours used in the interpolation for a Lagrangian marker (filled-red circle). Pressure nodes are denoted by 'x', x-velocity nodes by '□', y-velocity nodes by '◯', and Lagrangian markers by red circles. ΔV_L refers to the Lagrangian marker volume.

Stokes equations (Eq. 2.2). Fig. 2.2 presents a two-dimensional illustration of a staggered grid with uniform grid spacings (Δx and Δy) where the Lagrangian markers are represented by red circles.

There are three different methods to enforce the no-slip condition at the Lagrangian immersed boundary points: 1) Feedback Forcing, 2) Penalty Method, and 3) Direct Forcing. Iaccarino and Verzicco (2003) provided a detailed description of the governing equations for each method. They highlighted that both the Feedback Forcing and Penalty Methods introduced stiffness constraints into the governing equation 2.2, which can significantly increase the computational cost when dealing with complex geometries. Due to these considerations, Hydro3D adopted the direct forcing (DF) method. Based on prior work by Fadlun et al. (2000), Uhlmann (2005) refined the DF method utilising a discrete description. Uhlmann (2005) used delta functions, which were previously applied by Roma et al. (1999) and Pe-

skin (2002), to essentially create a two-way interpolation procedure between Eulerian and Lagrangian cells, facilitating information exchange between fluid and solid frameworks.

Wang, Fan and Luo (2008) provided further improvement by noting that Uhlmann's DF method was unable to fully satisfy the no-slip condition at the boundary because some residual velocities persisted within the solid region. As a result, they introduced the multi-direct forcing (MDF) method, which involves an iterative solution of the DF equations using a multi-correction approach. Meanwhile, Yang et al. (2009) developed an alternative approach to the delta functions, which helps to smooth out force oscillations. Vanella and Balaras (2009) employed moving-least squares (MLS) approximations to construct interpolation functions, which offer the primary advantage of ensuring the partition of unity, whereas delta functions only satisfy this condition if the discrete Lagrangian grid resolution matches the Eulerian mesh (Uhlmann 2005). Pinelli et al. (2010) adapted the reproducing kernel particle method (RKPM), which produces an accurate reconstruction of the interpolation functions. Ouro et al. (2016) introduced the DF-MLS method for applying the IB approach to unstructured meshes.

In the current thesis, the refined version of the DF method by Uhlmann (2005) is used, due to feasible computational effort, adaptability to complex geometries and good numerical stability. Within this method, the solid geometry is discretised into finite Lagrangian markers or points, often referred to as the Lagrangian grid. This collection of points is physically decoupled from the fluid mesh, as the fluid mesh does not conform to the solid's geometry. Instead, as illustrated in Fig. 2.2, these Lagrangian markers are embedded within the fluid mesh. Communication between the solid points and fluid cells is established through the DF equations (detailed below). Using these equations, each Lagrangian marker imposes a desired velocity onto nearby fluid cells through a forcing term, f_i.

The direct forcing method employs a multi-step predictor-corrector approach, which is adapted in the following way: initially, the predicted Eulerian velocities ($\tilde{\mathbf{u}}$) are computed using Eq. 2.9. The delta function (δ) is employed as an interpolation function for transferring $\tilde{\mathbf{u}}$ to the Lagrangian grid from the nearest Eulerian neighbours, n_e (depicted as filled-black symbols in Fig. 2.2), and thus the interpolated Lagrangian velocity, U_L, is acquired:

$$U_L = \sum_{ijk=1}^{n_e} u^*_{ijk} \cdot \delta(x_{ijk} - X_L) \cdot \Delta x_{ijk} \tag{2.15}$$

where x_{ijk} stands for the vector of coordinates for the Eulerian mesh cell ijk, $X_L = (X_L, Y_L, Z_L)^T$ corresponds to the location of the Lagrangian marker L, and $\Delta x_{ijk} = \Delta x \cdot \Delta y \cdot \Delta z$ is the volume of the Eulerian cell. The calculation of the interpolating delta function involves the multiplication of three one-dimensional kernel functions, ϕ, as given:

$$\delta(x_{ijk} - X_L) = \frac{1}{\Delta x_{ijk}} \phi\left(\frac{x_{ijk} - X_L}{\Delta x}\right) \phi\left(\frac{y_{ijk} - Y_L}{\Delta y}\right) \phi\left(\frac{z_{ijk} - Z_L}{\Delta z}\right) \tag{2.16}$$

The reliability of this interpolation technique is dependent on the kernel, which needs to be chosen carefully to avoid large oscillations in the force outputs. Several authors, including Roma et al. (1999) and Peskin (2002), have presented alternative versions of this function. However, these functions can still cause considerable unwanted force oscillations (Lee et al. 2011). Aiming to decrease these oscillations, Yang et al. (2009) applied smoothing to the kernel functions from earlier works, achieving a significant decrease in force oscillations. In the current research, a kernel which uses 64 neighbouring cells is selected because it offers the best compromise between accuracy and computational effort (Ouro et al. 2021).

The second step of the DF method involves calculating the force F_L that each Lagrangian marker needs to apply to the fluid in order to fulfil the no-slip condition at the marker's position. This force term is calculated from the difference between the desired velocity at the marker, U_L^*, and the velocity initially interpolated from the fluid mesh in Eq. 2.15, U_L. When dealing with a static body, the desired velocity at the marker, U_L^*, is zero. This force is given as:

$$F_L = \frac{U_L^* - U_L}{\Delta t} \tag{2.17}$$

The third step involves a reverse process where the Lagrangian force is transferred back to the Eulerian mesh cells to determine the Eulerian force f_i. This backward interpolation of F_L, from the nearest n_L Lagrangian markers to each Eulerian cell, uses the same delta function values from the forward interpolation in Eq. 2.15, and is carried out as follows:

$$f(x_{ijk}) = \sum_{L=1}^{n_L} F_L \cdot \delta(X_L - x_{ijk}) \cdot \Delta V_L \tag{2.18}$$

During the forward interpolation (from Eulerian to Lagrangian), the fluid cell volume Δx_{ijk} is utilised, while the backward process (Eq. 2.18) employs the volume allocated to each of the Lagrangian markers ΔV_L. According to Uhlmann (2005), the DF method demands that the force transferred to the fluid be identical to the one transferred to the solid. The equilibrium condition to achieve is presented in Eq. 2.19, where N_e represents all Eulerian cells subject to the IB method correction. Thus, the Lagrangian volume ΔV_L is nearly equal to Δx_{ijk}.

$$\sum_{ijk=1}^{N_e} f(x_{ijk}) \cdot \Delta x_{ijk} = \sum_{L=1}^{N_L} F_L \cdot \Delta V_L \tag{2.19}$$

In the final corrector step, the predicted Eulerian velocity, $\tilde{u}$, is modified using Eq. 2.10 to obtain the corrected predicted Eulerian velocity, $\tilde{u}^*$, after the IB method correction.

2.4 Level-set method

The LSM that was developed by Osher and Sethian (1988) is adopted to resolve the free-surface between the air and water phases. The LSM employs a level-set signed distance func-

tion, ϕ, with values of $\phi > 0$ denoting water (liquid fraction), while $\phi < 0$ corresponds to air (gas fraction), and it has a zero value at the phase interface. This method is formulated as follows:

$$\phi(x,t) > 0 \quad \text{if } x \in \Omega_{\text{liquid}} \tag{2.20}$$

$$\phi(x,t) < 0 \quad \text{if } x \in \Omega_{\text{gas}} \tag{2.21}$$

$$\phi(x,t) = 0 \quad \text{if } x \in \Gamma \tag{2.22}$$

where Ω_{liquid} and Ω_{gas} denote the fluid domains for liquid and gas, respectively, and Γ is the (air-water) interface. The ϕ function is tracked over time by solving a pure advection equation in addition to the mass and momentum conservation equations:

$$\frac{\partial \phi}{\partial t} + u_i \frac{\partial \phi}{\partial x_i} = 0 \tag{2.23}$$

The numerical stability is disrupted by discontinuities in density and viscosity at the interface because these properties are constant along the particle paths for immiscible fluids. This is avoided by the introduction of a transition zone in which density and viscosity switch smoothly between phases. The transition zone is defined as $|\phi| \leq \varepsilon$, where ε is half the thickness of the interface, which in this research is two grid spacings $(2.0\Delta x_i)$, and, as defined in Kang and Sotiropoulos (2015), it is an adjustable parameter that sets the thickness of the numerical smearing at the interface.

A Heaviside function, $H(\phi)$, accomplishes the transition as follows (Ouro et al. 2021, Christou et al. 2021):

$$\rho(\phi) = \rho_g + (\rho_l - \rho_g) H(\phi) \tag{2.24}$$

$$\mu(\phi) = \mu_g + (\mu_l - \mu_g) H(\phi) \tag{2.25}$$

where ρ_g and ρ_l are the density of gas and liquid, respectively; μ_g and μ_l are the dynamic viscosity of gas and liquid, respectively.

$$H(\phi) = \begin{cases} 0 & \text{if } \phi < -\varepsilon \\ \frac{1}{2} + \frac{1}{2}\left(\frac{\phi}{\varepsilon} + \frac{1}{\pi}\sin(\pi\phi/\varepsilon)\right) & \text{if } |\phi| \leq \varepsilon \\ 1 & \text{if } \phi > \varepsilon \end{cases} \tag{2.26}$$

The LSM is recognised for struggling to conserve mass in highly distorted interfaces due to numerical dissipation from discretising Eq. 2.23 with upwind-biased schemes. Central differencing schemes are unsuitable for this pure advection situation. Therefore, as mentioned previously, a fifth-order WENO scheme is adopted to minimise numerical dissipation. A further challenge with LSM is that ϕ fails to retain the property $|\nabla\phi| = 1$ as time advances due to the inherent nature of the advection equation. Therefore, the LSM is re-initialised to ensure

that this stability criterion is accomplished at every time step, which is essential to maintain mass conservation in the computational domain (Osher and Sethian 1988). A re-initialisation method presented by Sussman et al. (1994) is used, which also contributes to enhancing mass conservation. The re-initialised signed distance function (d) is acquired by solving the partial differential equation as:

$$\frac{\partial d}{\partial t_a} + s(d_0)(|\nabla d| - 1) = 0 \tag{2.27}$$

where $d_0(x,0)$ is equivalent to $\phi(x,t)$, t_a acts as a dummy parameter, and $s(d_0)$ denotes the smoothed signed function, which is given as:

$$s(d_0) = \frac{d_0}{\sqrt{d_0^2 + (|\nabla d_0|\varepsilon_r)^2}} \tag{2.28}$$

This re-initialisation process is carried out within the transition zone over multiple iteration steps, represented by $\varepsilon_r/\Delta t_a$, where ε_r corresponds to one grid space. Modifications to the level set function are only applied to computational cells located at the interface, which eliminates the need to solve the partial differential equation for the entire domain.

2.5 Free-surface tension

A continuum surface force (CSF) model (Yokoi et al. 2016) has been implemented in Hydro3D as a surface-tension model, which is essential to maintain the accuracy of the free-surface simulation when there is significant surface breaking and air trapping the bulk of fluid, forming small droplets and bubbles. The surface-tension force F_{sf}, included in Eq. 2.2, is defined as:

$$F_{\text{sf}} = \sigma k \delta(\phi) n_i, \tag{2.29}$$

where σ is the coefficient of the surface tension ($\sigma = 0.728$), k is the curvature of the interface, and n_i is the unit vector normal to the liquid interface. These are computed as:

$$k = -\nabla \cdot n_i, \tag{2.30}$$

$$n_i = \frac{\nabla \phi}{\|\nabla \phi\|}. \tag{2.31}$$

The smoothed delta function, $\delta(\phi)$, in Eq. 2.29 corresponds to the spatial derivative of the Heaviside function in Eq. 2.26 and reads:

$$\delta(\phi) = \begin{cases} \frac{1}{2}\left(1 + \cos\left(\pi \frac{\phi}{\varepsilon}\right)\right) & \text{if } |\phi| < \varepsilon \\ 0 & \text{otherwise} \end{cases} \tag{2.32}$$

An enhanced method for calculating surface tension is incorporated in the current Hy-

dro3D model, relying on a density-scaled delta function (δ^{scaling}) (Bussmann et al. 2000, Yokoi 2013). This method enhances stability by directing the delta function (δ) towards the fluid with higher density. Thus, the final form of the surface-tension force is calculated as follows:

$$F_{\text{sf}} = \sigma k \delta^{\text{scaling}}(\phi) n_i, \quad \delta^{\text{scaling}} = 2H(\phi)\delta(\phi). \tag{2.33}$$

The derivatives of ϕ are computed using second-order central differences at the centre of the cell, where k, n_i, and $\delta(\phi)$ are also defined. These values are then determined at the cell faces using simple interpolation.

Appendix A, Fig. A.1, demonstrates how air bubbles form in a free-surface simulation without the CSF model, especially under conditions where significant surface breaking and air entrapment occur. This highlights the crucial role of the model in ensuring accuracy.

2.6 Proper orthogonal decomposition

Proper Orthogonal Decomposition (POD), also known as Principal Component Analysis or Karhunen–Loève decomposition, was first introduced in the context of turbulence and fluid dynamics by Lumley (1967). The POD method is a statistical methodology, known for studying events with expected dominant recurrent patterns (Chatterjee 2000) and effectively capturing the dominant modes in turbulent flows (Holmes et al. 1996), is employed to identify and capture the coherent structures within the flow field.

By applying the POD method to data gathered from flow measurements or investigations, one can identify flow patterns that are linked to structures with the highest energy contributions to the flow. However, these structures may not always correspond to coherent flow structures, but rather represent events that statistically contribute the most to the current energy (Kostas et al. 2005). Inputs for the POD method can include the velocity field, the vorticity field (Tang et al. 2015), the pressure field, and flow visualisation data (Brevis and García-Villalba 2011). The following is a brief description of the adopted POD method, for more details the interested reader is referred to Wang et al. (2014) and Sen et al. (2017).

A given spatio-temporal velocity field $w(x_i,t)$ can be decomposed into the mean velocity field and a fluctuating component, such that:

$$w(x_i,t) = \overline{W}(x_i) + w'(x_i,t) \tag{2.34}$$

where $\overline{W}(x_i)$ is the mean flow field, and $w'(x_i,t)$ is the fluctuating component.

The primary objective of the POD method is to optimally represent field data. As this goal is pursued, one inevitably faces the challenge of solving the eigenvalue problem, which involves directly determining the eigenvalues and eigenvectors of the data's covariance matrix. This covariance matrix represents the spatial correlations in the data, and its eigenvalues and eigenvectors provide the POD modes (or eigenmodes) and their corresponding energy con-

tent. However, directly solving the eigenvalue problem for the covariance matrix can be computationally intensive, especially for large datasets. To address this challenge, POD based on a Singular Value Decomposition (SVD) constructed from a set of data-snapshots of the flow-field is employed (Sirovich 1987). This method provides a framework that utilises linear combinations of function space elements, or "snapshots" of the data, to describe the eigenmodes. Through SVD, the snapshot matrix is broken down, and the resulting singular values and vectors are related to the eigenvalues and eigenvectors of the covariance matrix. This offers a computationally efficient alternative to the traditional eigenvalue problem, allowing for the extraction of the necessary information without directly computing the eigenvalues and eigenvectors of the full covariance matrix.

The values of the quantity w are obtained at M different spatial locations (x_i) for N temporal snapshots with equal time interval between them. For the purposes of this discussion, each of these temporal snapshots is denoted by the index n, where n ranges from 1 to N. This allows us to refer to the fluctuating component of the velocity at spatial location x during a specific snapshot as $w'(x,t_n)$. The time-averaged velocity $\overline{W}$ is calculated and then subtracted from each of the instantaneous velocity w values to build the snapshot matrix W of order $M \times N$ from the resulting fluctuating velocity component, which reads:

$$W = \begin{bmatrix} w'(x_1,t_1) & w'(x_1,t_2) & \dots & w'(x_1,t_N) \\ w'(x_2,t_1) & w'(x_2,t_2) & \dots & w'(x_2,t_N) \\ \vdots & \vdots & \vdots & \vdots \\ w'(x_M,t_1) & w'(x_M,t_2) & \dots & w'(x_M,t_N) \end{bmatrix} \tag{2.35}$$

The snapshot matrix W is central to the snapshot POD method, and in typical practice, the eigenvalue problem would be solved directly on this matrix or its autocovariance. The autocovariance matrix C is derived from the matrix transformation $C = W^T W$, where the symbol ^{T} denotes the transpose operator. A set of N eigenvalues (λ^i) and associated eigenvectors (A^i) of the matrix C which satisfy $CA^i = \lambda^i A^i$ are evaluated. The eigenvalues are arranged in a descending order, i.e. starting from the most energetic, and each denotes the mode's energy $(\lambda_1 \geq \lambda_2 \geq \cdots \geq \lambda_N > 0)$, with the sum of all eigenvalues reflecting the total energy. The SVD offers an alternative to this traditional approach. Instead of directly working with the autocovariance matrix, the SVD decomposes the snapshot matrix W into three matrices: U, Σ, and V^T. This decomposition provides direct access to the modes of interest without explicitly computing the autocovariance matrix (Chatterjee 2000).

In this thesis, the Snapshot POD method, which utilises the SVD approach, is employed to decompose the system snapshots into POD eigenmodes, with up to 200 modes selected for this research. The Snapshot POD method via SVD offers computational efficiency particularly when the number of snapshots (N) is much smaller than the spatial resolution (M). The real $M \times N$ matrix W upon SVD is given by $W = U\Sigma V^T$, where U is an orthogonal matrix with range $M \times M$ whose columns are the eigenvectors of WW^T, and V is an $N \times N$ orthog-

onal matrix whose columns are the eigenvectors of $W^T W$ (which is the autocovariance matrix C of the snapshot POD method). Σ is a $M \times N$ diagonal matrix with non-negative real numbers in the diagonal, which are called the singular values of the matrix W, whose entries are the square root of the eigenvalues of $W^T W$ or C. Specifically, the square of each singular value in Σ corresponds to an eigenvalue λ^i. The spatial eigenvectors of C are represented by the columns of U, whilst the temporal eigenvectors are represented by the columns of V, i.e. the i^{th}-column of V is $A^i, i = 1,2,\ldots,N$. The POD spatial modes φ^i are then constructed from the projection of the eigenvector A^i corresponding to the eigenvalue λ^i as:

$$\varphi^i = \frac{\sum_{n=1}^{N} A_n^i w'(x,t_n)}{\left\| \sum_{n=1}^{N} A_n^i w'(x,t_n) \right\|} \tag{2.36}$$

The notation $\| \cdot \|$ is described as $\|R\| = \sqrt{R_1^2 + R_2^2 + \cdots + R_M^2}$. The temporal coefficients a_i, also known as POD coefficients, are calculated by projecting the fluctuating component onto the POD modes, i.e. $a_i^n = \Psi^T w'(x,t_n)$, where $\Psi = \begin{bmatrix} \varphi^1 & \varphi^2 & \cdots & \varphi^N \end{bmatrix}$ represents the spatial modes calculated through Equation 2.36, each column symbolising a specific spatial pattern in the flow field, capturing the dominant, energetic patterns inherent to the flow structures. The individual energy coefficients ζ^i and cumulative energy coefficients η^r, are defined as:

$$\zeta^i = \frac{\lambda^i}{\sum_{i=1}^{N} \lambda^i} \tag{2.37}$$

$$\eta^r = \frac{\sum_{i=1}^{r} \lambda^i}{\sum_{i=1}^{N} \lambda^i} \quad r \leq N \tag{2.38}$$

where ζ^i denotes the fraction of total energy contained in the ith mode and η^r denotes the proportion of the total energy contained in the first r modes.

Following the snapshot POD method, if the first r modes contain the bulk of the total energy of the flow, then a Reduced Order Model (ROM) of the flow can be effectively used to reconstruct the spatial distribution at any selected time step. The reconstructed field (W_r) can then be given by using the time-averaged velocity $\overline{W}$ plus the truncated POD expansion with r number of modes, as follows:

$$W_r(x_i,t) = \overline{W}(x_i) + \sum_{j=1}^{r} a_j(t)\varphi^j(x_i) \tag{2.39}$$

According to Sirovich (1987), the selective POD modes (or r-POD modes) must satisfy at least $\eta^r \geqslant 90\%$. Since the POD modes are ranked according to their energy, the most significant large-scale flow structures (if present in the flow) appear in the first POD modes, which are the most energetic. This arrangement allows for the possibility to reconstruct the flow using only the first few POD modes, thereby capturing the dominant flow features effectively.

2.7 Summary

The numerical framework that is used to resolve the governing equations in the in-house code Hydro3D has been presented. The time advancement using the fractional-step method has been discussed. A direct-forcing IBM, which provides Hydro3D the adaptability to simulate complex geometries, has been explained in detail. The method employed for resolving the free surface and the implementation of free-surface tension in Hydro3D have been discussed. POD as a statistical methodology that can be used to further identify and capture the coherent structures of the flow field has been described.

CHAPTER 3

Hydrodynamic Characteristics of Circular Cylinder Flows in Shallow Conditions

3.1 Aim of this chapter

This chapter focuses on the hydrodynamics of flow past a circular cylinder under varying submergence ratios. Previous numerical studies on this particular problem have primarily examined low Reynolds numbers in the laminar flow regime, resulting in a limited understanding of the problem in a turbulent flow. Moreover, the wake dynamics of a circular cylinder sandwiched between a top free surface and a bottom wall layer with its hydrodynamic coefficients remain to be investigated. This chapter aims to address these gaps, studying the effects of the varying proximity of the free surface to the cylinder with fixed proximity to the bottom wall in turbulent flow conditions.

3.2 Summary

Flow disruptions around circular cylinders have long captured the attention of engineers and researchers due to the implications of von Kármán vortex shedding (Taneda 1965, Williamson 1996). The behaviour and interaction of the shear layers of a circular cylinder near a free surface or solid boundary have garnered significant attention (Subburaj et al. 2018, Ouro et al. 2019). Studies indicate that the flow characteristics in these situations can significantly differ from those typically observed in unconstrained environments (Wang et al. 2021). Furthermore, positioning a cylinder between both a free surface and a solid boundary introduces added complexity to the hydrodynamics of the flow, which poses challenges in various disciplines, such as underwater tunnel construction (Shuping and Qinxi 2019) and flood control infrastructures (Müller et al. 2022). Despite the acknowledged significance of this topic (Chu et al. 2018, Nguyen and Lei 2021, Zhao et al. 2022), several aspects still require further investigation, including the impact of asymmetric boundary conditions and the effects of the distortion of the free surface on the flow fields and hydrodynamics.

In this chapter, LESs of flow past a circular cylinder beneath a free surface are performed. The effects of the submergence depth on the characteristics of the flow field and the hydrodynamic forces generated on the cylinder are discussed. Simulations were conducted at a con-

stant Reynolds number (Re) of 13,333 while varying the Froude number (Fr) based on submergence depth in the range of 0.26 to 0.53. The LES results agreed well with the experimental data for the time-averaged flow quantities, accurately capturing the upwards flow motion that emerged along the lower half of the flow depth due to the near-wall effect. The present investigation revealed that von Kármán vortex streets developed downstream at lower Froude numbers ($Fr \leq 0.31$) and were barely disturbed by the free surface. However, for higher Fr, the shedding of vortices became more disrupted, exhibiting irregular patterns that led to the rapid loss of coherence in large-scale vortices. The distribution of the turbulent kinetic energy indicated that the near wake of the cylinder exhibited zones of high turbulence for all cases, while the longitudinal extent of these zones increased with increasing Fr. At $Fr > 0.31$, the proximity of the free surface to the cylinder causes a significant increase in computed drag and lift coefficients with a negative lift coefficient, indicating an exerting downward thrust on the cylinder. As Fr increases, Strouhal numbers also increase to a 0.30–0.45 range, providing further evidence of the impact of the free-surface proximity on the cylinder wake structure dynamics. Overall, at $Fr > 0.31$, the free-surface proximity has a significant influence on the near-wake dynamics, underlining the necessity to account for the water-surface deformation.

Section 3.3 presents the computational setup. Section 3.4 discusses the impacts of the free surface on the wake dynamics and presents the hydrodynamic coefficients for all Fr. The main findings of this work are provided in Section 3.5.

3.3 Computational setup

The experimental setup described in Muhawenimana et al. (2019) for a horizontal circular cylinder in an open-channel flow is utilised as the basis for this study. The cylinder has a diameter (D) of 0.05 m and is situated at a vertical gap (G) of 0.025 m between the lower edge of the cylinder and the bottom wall, resulting in a gap ratio (G/D) of 0.5. The computational domain shown in Fig. 3.1 measures 1.50 m, 0.24 m, and 0.01 m in the streamwise (x), vertical (z), and spanwise (y) directions, respectively. Whilst studies such as those by Aljure et al. (2017) and Ouro et al. (2019) suggest that a spanwise domain length near $2\pi D$ is optimal for accurately capturing vortical structures in cylinder wakes, in this work, due to the limitations of available computational resources, simulating turbulent flow with LSM proves to be computationally demanding. This has led to the necessary reduction of the spanwise domain length to $0.2D$. This compromise, driven by computational constraints, might affect the representation of three-dimensional turbulent structures. Nonetheless, it remains essential for providing a close view of the impact of varying submergence depths on wake structures. The downstream end of the horizontal cylinder, located $10.5D$ from the upstream inlet, is chosen as the origin of the x-coordinates. Three distinct computational grids (coarse, medium, and fine) containing approximately 5.1, 7.3, and 14.4 million elements respectively, were established to investigate the solution's dependency on grid resolution, as shown in Fig.

B.1 (Appendix B). Although all grids share the same topology, differences arise in the resolution near the cylinder surface and in the vicinity of the air-water interface. To accurately capture the free-surface dynamics and the wake flow structures, the highest mesh resolution is employed. The grid spacing is uniformly distributed throughout the domain with a resolution of $x/D = z/D = 0.01$ in x and z directions, and doubled in the spanwise direction. Therefore, the entire numerical mesh is composed of 14.4 million grid cells, consisting of $Nx \times Ny \times Nz = 3,000 \times 10 \times 480$, where N_{xi} is the number of grid nodes for each spatial direction.

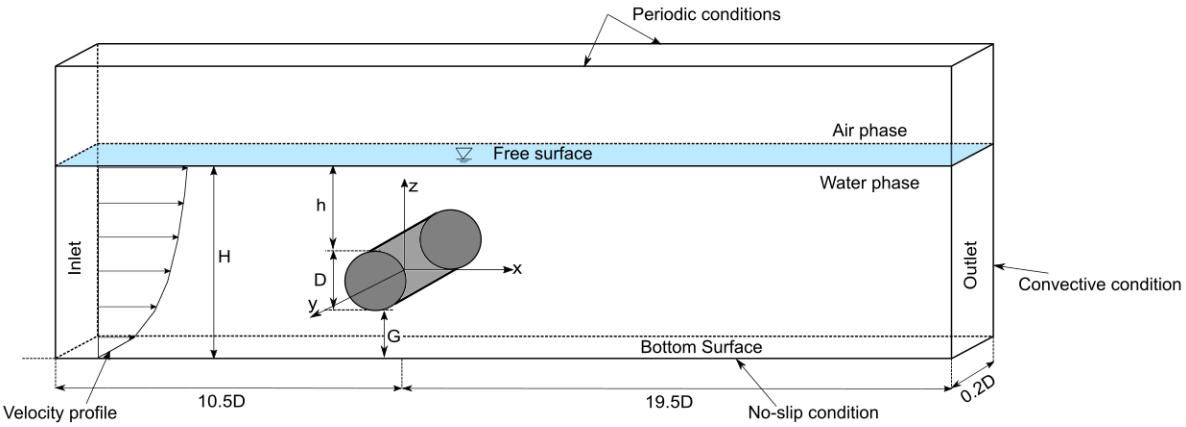

Fig. 3.1 Schematic of the computational domain adopted for the LES with the horizontal cylinder of diameter (D) located at a height G from the bottom surface. The total water depth is denoted by H, while that free-surface elevation overtopping the cylinder is h. The inflow boundary condition with a logarithmic velocity distribution is also indicated.

The bulk velocity (U_0) is equal to 0.2667 m/s, yielding a Reynolds number ($Re = U_0 D/\nu$) of 13,333. The mean water depth (H) is varied to study the free-surface influence on the flow hydrodynamics of the cylinder, which results in different submergence depths (h), where h is determined from the upper end of the cylinder to the free-surface elevation obtained a posteriori in the simulation (Fig. 3.1). The submergence depth varies with the water depth that is in the range of h = 0.025–0.105, resulting in Froude numbers ($Fr = U_0/\sqrt{gh}$) in the range of 0.26–0.53. The details of the water depth, submergence ratio, bulk Froude number, and local Froude number ($Fr = U_t/\sqrt{gh}$, where U_t denotes flow velocity overtopping the cylinder) for the five cases are listed in Table 3.1.

Table 3.1 Details of the cases studied including mean water depth (H), submergence depth (h), submergence ratio (h/D), Froude number (Fr), and local Froude number (Fr_h).

H [m]	h [m]	h/D [-]	Fr [-]	Fr_h [-]
0.18	0.105	2.1	0.26	0.36
0.15	0.075	1.5	0.31	0.46
0.12	0.045	0.9	0.40	0.59
0.11	0.035	0.7	0.45	0.73
0.10	0.025	0.5	0.53	0.89

In the current LES, a mean logarithmic velocity profile is prescribed at the domain inlet

according to a smooth log-law distribution with friction velocity (u_*) equal to 0.033 m/s obtained from the experimental velocity measurements (Muhawenimana et al. 2019), which is defined as:

$$\frac{u(z)}{u_*} = \frac{1}{\kappa} \ln\left(\frac{z u_*}{\nu}\right) \tag{3.1}$$

Here $\kappa = 0.41$ is the von Kármán constant. The consideration of free-stream turbulence is an essential step in representing natural environmental flow conditions. To address the impact of inlet turbulence on wake recovery mechanisms and wake length, two simulations were performed using the Synthetic Eddy Method (SEM) with turbulence intensities (TIs) of 5% and 10%. These simulations were conducted with turbulent length scales set at values equivalent to 40, 5, and 20 grid sizes in the x, y, and z directions, respectively. A comparative analysis with the baseline case, which did not employ SEM, is presented in Fig. C.1 (appendix. C). Notably, the results indicate that using SEM with the performed inlet turbulence intensities had a negligible impact on the developed mean logarithmic velocities upstream of the cylinder, showing negligible differences from the case without SEM. A convective boundary condition is used at the outflow. A no-slip boundary condition is imposed at the bottom boundary and periodic boundary conditions are used in the spanwise direction. The water-surface deformation is calculated by the level-set method and the top of the domain is treated with a slip condition. The time step is variable with a Courant-Friedrichs-Lewy (CFL) condition of 0.2 in order to maintain a stable simulation. All simulations are executed on 200 CPUs and averaging of the flow statistics begins after about four flow-through periods ($T_f = L_x/U_0$, where L_x is the length of the domain) after the initial flow transients have vanished and then continued for about 30–40 flow-through periods to compute mean flow statistics once the flow is fully developed.

3.3.1 Numerical validation

The simulation results are validated in the case of flow around a submerged cylinder at $Fr = 0.31$ from Muhawenimana et al. (2019) to confirm the suitability of the chosen grid size, time discretisation and boundary conditions. The flow profiles in the experiment were measured using an acoustic Doppler velocimeter (ADV), a downward-looking Nortek Vectrino Plus (V.1.31+) at a sampling rate of 200 Hz (Muhawenimana et al. 2019). Profiles of normalised mean streamwise $\langle u \rangle / U_0$ and vertical velocities $\langle w \rangle / U_0$, along with their respective fluctuations, are presented in Fig. 3.2 at six downstream locations from the cylinder.

The vertical profiles of the streamwise velocities show a significant velocity deficit along the cylinder body ($0.5 \leq z/D \leq 1.5$) in the near-wake region ($x/D \leq 1.2$) due to the blockage effects of the cylinder (Fig. 3.2a). In contrast, values of $\langle u \rangle / U_0 > 0$ are observed in the remaining regions along the water column as the approach flow accelerates on the upper and lower sides of the cylinder. Further downstream, the streamwise velocity recovers and ap-

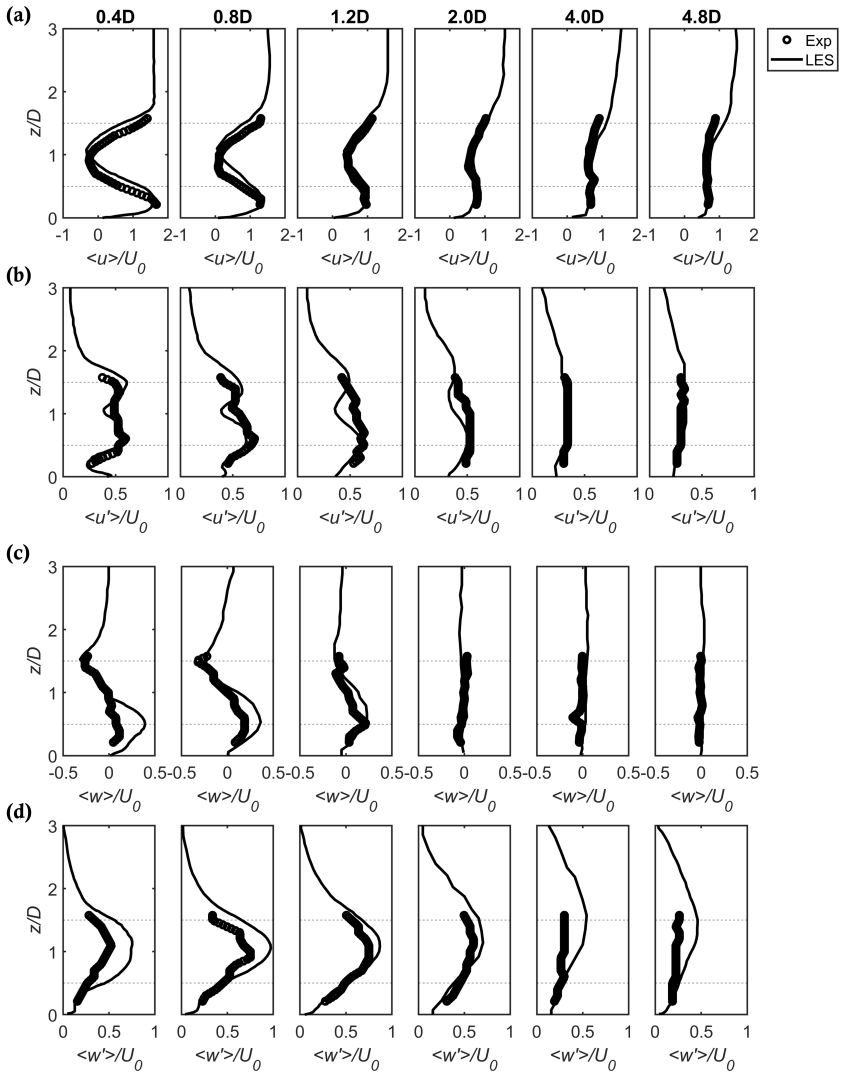

Fig. 3.2 Vertical profiles of (a) mean streamwise velocity $\langle u \rangle$, (b) turbulence intensity $\langle u' \rangle$, (c) mean vertical velocity $\langle w \rangle$, and (d) turbulence intensity $\langle w' \rangle$ at different locations downstream of the cylinder. Comparison between experimental (symbols) and LES (lines) results. The dashed lines indicate the cylinder position.

proaches that of the undisturbed log-law profile encountered upstream of the cylinder, indicating a gradual decrease in the impacts of the obstructed cylinder on mean flow characteristics.

Profiles of $\langle u' \rangle$ exhibit two peaks around the cylinder centre ($z/D = 1$) at locations immediately downstream of the cylinder, i.e. at $x/D \leq 0.8$, which can be ascribed to the unstable formation of the cylinder's shear layers, due to factors such as the proximity of the bottom wall(Fig. 3.2b). Among the two peaks, one is located near the downstream projection of the top side of the cylinder at z/D = 1.5, while the other, more pronounced in peak magnitude, emerges around $z/D \approx 0.5$. This asymmetrical distribution of $\langle u' \rangle$ provides evidence of the bottom wall effect in the development of von Kármán street. These peaks gradually diminish in magnitude at positions further downstream, indicating reduced mixing of turbulent structures and decreased levels of streamwise turbulence intensity compared to nearer downstream regions. The LES results reasonably capture the experimental distributions of $\langle u \rangle$ and $\langle u' \rangle$

over the water depth.

The vertical profiles of the mean vertical velocity $\langle w \rangle$ capture the upwards fluid motion immediately downstream of the cylinder, resulting from the flow acceleration through the lower cylinder gap, as shown in Fig. 3.2c. LES overpredicts the values of $\langle w \rangle$ near the bottom wall immediately behind the cylinder but matches the experimental results well above the cylinder centre ($z/D = 1.0$). Further downstream, the values of the $\langle w \rangle$ gradually recover, showing good agreement with the experimental results along the vertical water depth. For the vertical turbulence intensity $\langle w' \rangle$, the peaks in the near wake are attained along the cylinder centre ($z/D = 1$), but further downstream this peak shifts upwards towards the free surface reflecting the movement of the von Kármán vortices to the region with the highest momentum (Fig. 3.2d). The LES results overpredict the values of $\langle w' \rangle$ immediately behind the cylinder, while they achieve a better match with the experimental results immediately behind the wake bubble ($x/D > 1.2$).

3.4 Results and discussion

3.4.1 Free surface profiles

The free-surface elevation obtained during a previous experimental campaign at $Fr = 0.31$ Muhawenimana et al. (2019) and from the present LES for all submergence levels are presented in Fig. 3.3. For the Fr of 0.31, the experiment and LES show relatively good agreement, while the LES slightly underestimates the drop in the free surface downstream of the cylinder, as shown in Fig. 3.3. As the Fr increases, the water level upstream of the cylinder increases, while featuring a more pronounced drop in the free surface immediately downstream of the cylinder. This drop is almost negligible for the deepest submergence ($Fr = 0.26$).

The water-surface drop behind the cylinder varies between approximately $0.02D$ and $0.16D$ across the different submergence cases, relative to the undisturbed water depth (H). For instance, in the Fr cases of 0.26, 0.31, 0.40, 0.45, and 0.53, the drop level reaches z/H values of 0.999, 0.996, 0.972, 0.938, and 0.924, respectively. The maximum change between two subsequent cases is approximately 3.49%, which is seen between the $Fr = 0.40$ and $Fr = 0.45$ cases, indicating a notable difference after $Fr = 0.40$ in the drop magnitude. Further downstream of the cylinder, the free-surface perturbation gradually diminishes and the water surface appears to be almost flat after a distance of $x/D \approx 6$.

3.4.2 Instantaneous flow field

The characteristics of the instantaneous flow field for all of the submergence cases are discussed, building upon the understanding of the developed air-water interface dynamics. Figs. 3.4–3.8 present the developed vortical structures behind the horizontal cylinder for all cases

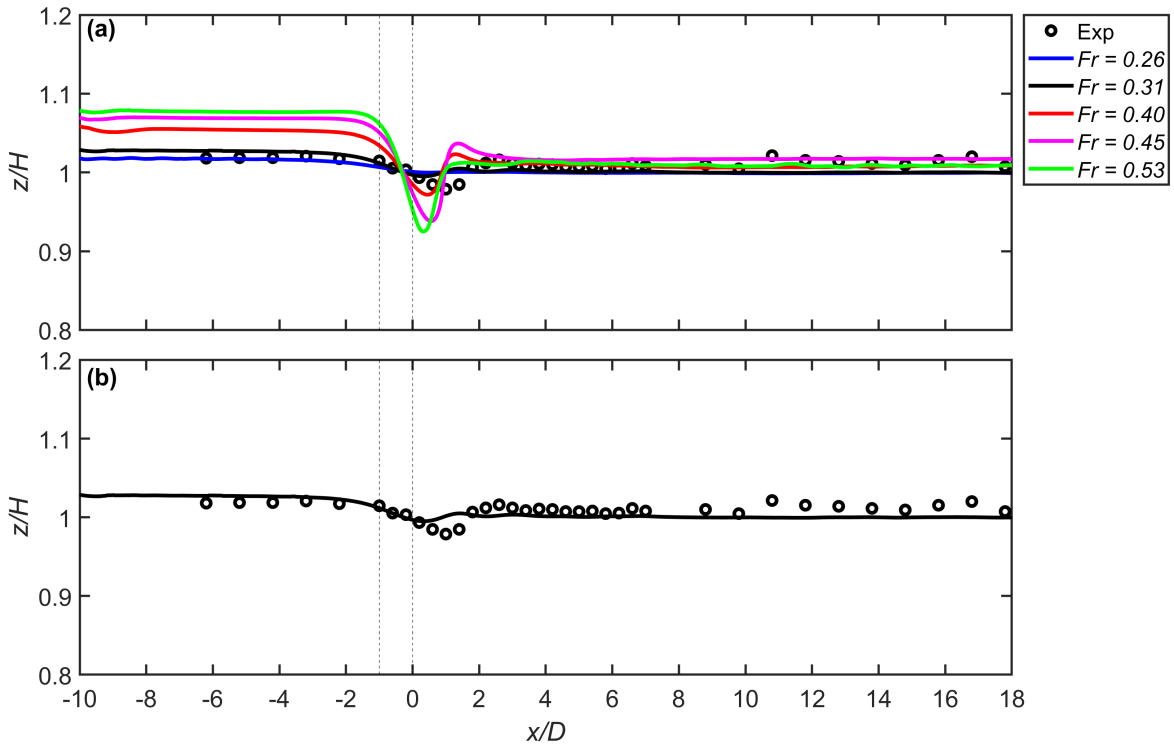

Fig. 3.3 Free-surface profiles obtained from the LES for all Fr cases, including experimental values for the case with $Fr = 0.31$, where (a) represents all free-surface profiles together, whilst (b) only shows comparisons of the LES results with the experimental data for $Fr = 0.31$. Vertical dashed lines indicate cylinder position.

simulated at $Fr = 0.26$–0.53 ($h/D = 2.1$–0.5) during four time instants covering the time range of $t^* = t \cdot f_p \in [2.9, 3.8]$, with t denoting time and f_p is the vortex-shedding frequency, represented with the non-dimensional vorticity $\omega_y D/U_0$, where $\omega_y = \partial u/\partial z - \partial w/\partial x$ is the spanwise vorticity over the xz-plane.

3.4.2.1 $Fr = 0.26$ ($h/D = 2.1$)

The free surface is positioned well above the cylinder, resulting in no noticeable perturbations and thus allowing the von Kármán vortex street to develop freely and be convected downstream (Fig. 3.4). This is similar to the study by Ouro et al. (2019), where the free surface is treated as a shear-free rigid lid. Due to the considered gap ratio of $G/D = 0.5$, the bottom ground limits the generation of the lower shear layer of the cylinder and vortical structures, suppressing the symmetry in the vortex shedding mechanism and leading to a different von Kármán street compared to unbounded cylinder flows (Wu et al. 2004, Aljure et al. 2017).

At the normalised instant of time, $t^* = 2.9$, the von Kármán vortices first move upwards due to the interaction between the ground vortex (GV) and the vortical structure generated behind the cylinder. Coherent von Kármán vortices form in the upper wake region of the cylinder, i.e. $x/D \approx 4$, $z/D > 1$, because of the negligible free-surface effect on the developed vortices. As time progresses to $t^* = 3.2$, these von Kármán vortices continue downstream with the mean flow while preserving their coherence. At $t^* = 3.5$, another vortex shedding cycle

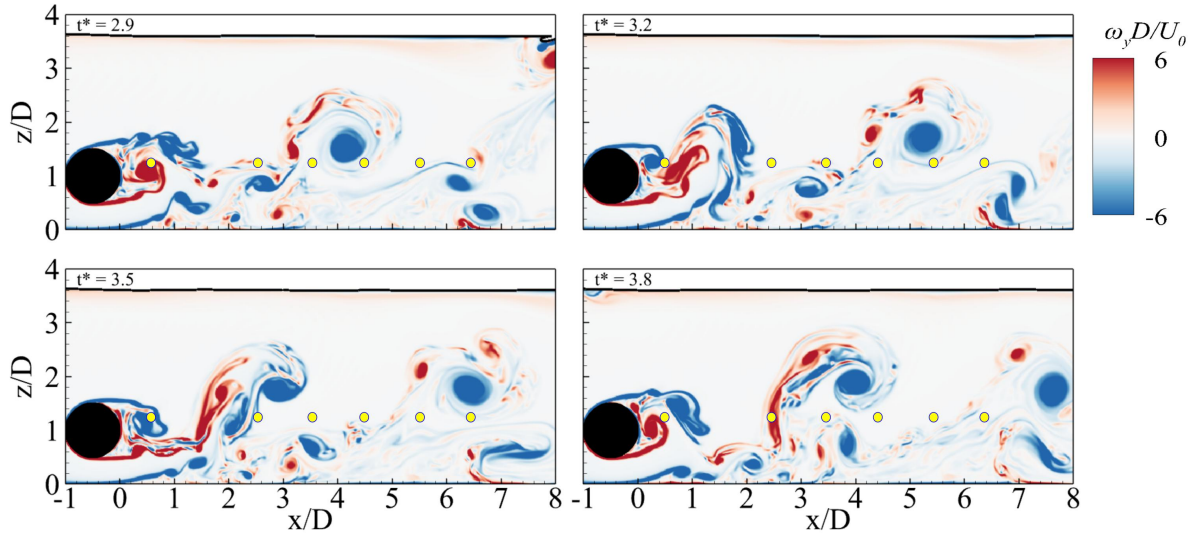

Fig. 3.4 Contours of normalised vorticity behind the cylinder for the case: $Fr = 0.26$, at four instants normalised by the peak frequency $t^* = 2.9$, 3.2, 3.5, and 3.8. The free surface is depicted as a solid-black line. The yellow dots mark the monitoring points for spectral analysis.

occurs in the near-wake region, ascending upwards towards the free surface before continuing its downstream journey in the wake of the pre-existing vortex, as observed at $t^* = 3.8$.

3.4.2.2 $Fr = 0.31$ ($h/D = 1.5$)

Fig. 3.5 shows the vorticity field for the case simulated at $Fr = 0.30$ ($h/D = 1.5$) during the four time instants. Decreasing the water depth to $h/D = 1.5$ leads to a slight influence of the water depth reflected from small free-surface variations, while the von Kármán vortices follow similar trajectories to those at $Fr = 0.26$. Fig. 3.5 shows that at $t^* = 2.9$, the von Kármán vortices first move upwards and then subsequently travel downstream by the mean flow in the direction parallel to the free surface, as seen at $t^* = 3.2$. Advancing in time, at $t^* = 3.5$, the developed vortices reach a maximum vertical height of $z/D \approx 3$ at about seven diameters downstream of the cylinder. Their proximity to the upper boundary of the free-surface can lead to alterations in the wake dynamics when compared to unbounded or lower Froude number scenarios. At $t^* = 3.8$, the vortical structures shed from the lower shear layer are merged with the GV, influencing the dynamics of the vortex generation and shedding, which, in consequence, led to an increasingly pronounced asymmetric wake distribution.

3.4.2.3 $Fr = 0.40$ ($h/D = 0.9$)

As the submergence ratio decreases further to $h/D = 0.9$ ($Fr = 0.40$), the free surface begins to drop shortly downstream of the cylinder (Fig. 3.6). Its proximity to the lee side of the cylinder impacts the vortices being shed. This effect is evident in the vorticity contours shown in Fig. 3.6 at $t^* = 2.9$, where the vortices achieve a vertical height of $z/D \approx 2.4$ shortly after being shed. This proximity to the free surface results in increased fluctuations on the free surface, as demonstrated by the hydraulic jump at $t^* = 3.2$. The coherence of the von Kármán

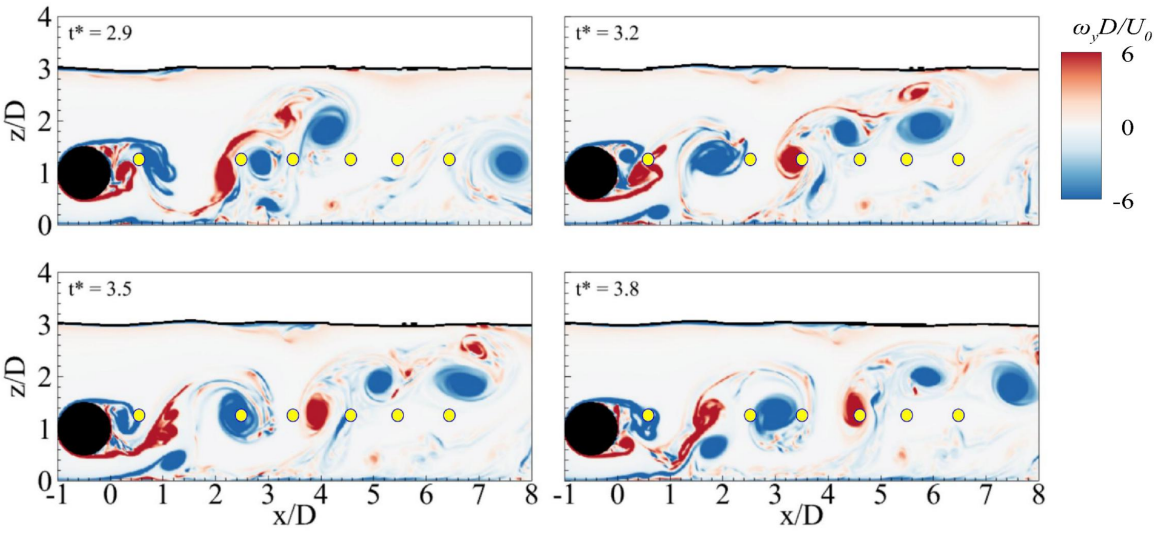

Fig. 3.5 Contours of normalised vorticity behind the cylinder for the case: $Fr = 0.31$, at four instants normalised by the peak frequency $t^* = 2.9$, 3.2, 3.5, and 3.8. The free surface is depicted as a solid -black line. The yellow dots mark the monitoring points for spectral analysis.

vortices dissipates more rapidly at $t^* = 3.5$ compared to instances with lower Fr, especially those near the bottom wall. By $t^* = 3.8$, the vortical structures emanating from the cylinder notably interact with the GV and are then diverted downstream. This behaviour contrasts with conditions at lower Fr, where the vortices tend to ascend upwards towards the free surface after their interaction.

3.4.2.4 $Fr = 0.45$ ($h/D = 0.7$)

Transitioning to a higher Froude number of 0.45 ($h/D = 0.7$), the interaction between the free surface and the wake's vorticity intensifies. Fig. 3.7 shows that at $t^* = 2.9$ and $x/D = 1$, a hydraulic jump occurs due to the extremely shallow water conditions of the overtopping flow. Advancing in time from $t^* = 2.9$ to 3.8, the wake dynamics behind the cylinder exhibit irregular flow patterns. The large-scale vortices at the top become distorted upon interacting with the free surface and subsequently break up into smaller eddies near the air-water interface, while those vortices moving at the bottom of the water column, e.g. GV, dissipate further downstream. Another instance of free-surface breaking occurs at $t^* = 3.8$, reflecting the rapid change in flow dynamics over time.

3.4.2.5 $Fr = 0.53$ ($h/D = 0.5$)

The contours of the vorticity field for the shallowest simulated case with $Fr = 0.53$ ($h/D = 0.5$) reveal significant surface deformation and a direct influence on the development of downstream vortices (Fig. 3.8). At the normalised instant time of $t^* = 2.9$, the surface deformation is quite substantial and the flow acceleration between the cylinder and free-surface layer has a direct impact on vortex formation downstream of the cylinder. The vorticity contours show

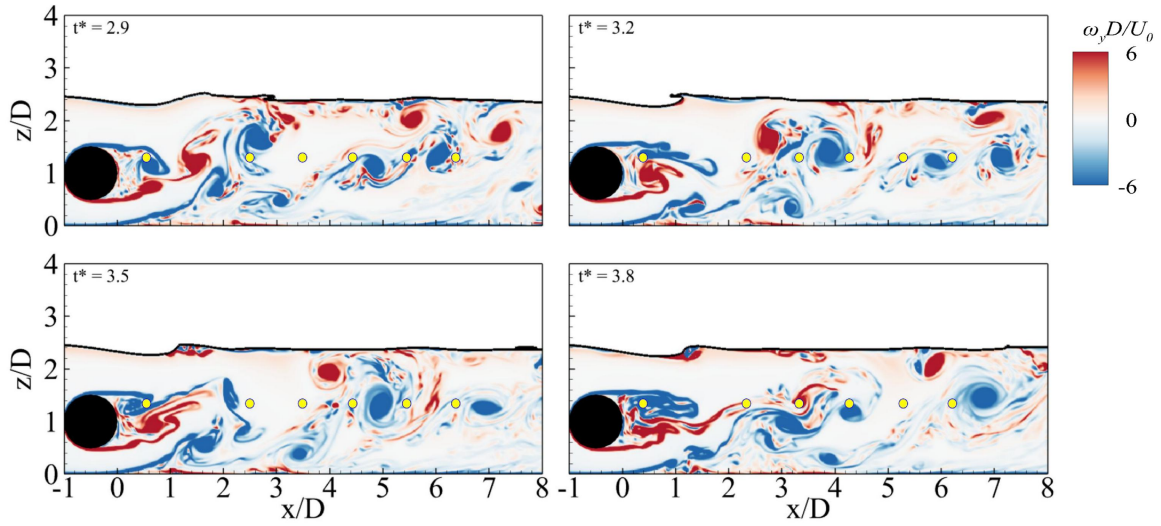

Fig. 3.6 Contours of normalised vorticity behind the cylinder for the case: Fr = 0.40, at four instants normalised by the peak frequency t^* = 2.9, 3.2, 3.5, and 3.8. The free surface is depicted as a solid-black line. The yellow dots mark the monitoring points for spectral analysis.

that the vortical structures lose coherence shortly after being shed, with a hydraulic jump formed due to the very shallow flow over the cylinder. This leads to a marked water-depth drop behind the cylinder compared to its upstream value. Advancing in time at $t^* = 3.2$, the vortices shed in the cylinder wake are seen to merge with the ground vortices before they are diverted upwards approaching the free surface, triggering significant variations in the water depth downstream of the cylinder, i.e. $x/D \approx 3$ (Fig. 3.8). As a consequence of this interaction, the turbulent mixing increases resulting from a higher interaction of the free-surface effects with the bulk flow.

At $t^* = 3.5$, the depression in the water surface behind the cylinder is recovered, allowing the vortices that are shed from the upper side of the cylinder to extend further downstream with a lower interaction with the free surface, which, in consequence, led to increasingly complex flow dynamics far downstream of the cylinder. Moreover, the top shear-layer vortices are not only affected by the vicinity of the free surface but are also amalgamated with the ground vortices. These structures dissipate at a faster rate than those found in deeper flow conditions, making the turbulent wake to become more irregular ($t^* = 3.8$).

3.4.2.6 Power Spectral Density analysis

The Strouhal number ($St = f_p D/U_0$) derived from the shedding frequency values for all cases are determined from the Power Spectral Density (PSD) presented in Figs. 3.9, which are obtained from the vertical velocity fluctuations at six stations downstream of the cylinder in the range of x/D = 0.5–6.5 along the upper shear layer of the cylinder ($z/D \approx 1.2$). The energy peaks in the spectra indicate that high-frequency structures primarily influence the flow, and the frequency of these energy peaks, f_p, identifies the shedding frequency of these structures. Fig. 3.9a shows the spectra of the LES-computed vertical velocity fluctuations at Fr = 0.26

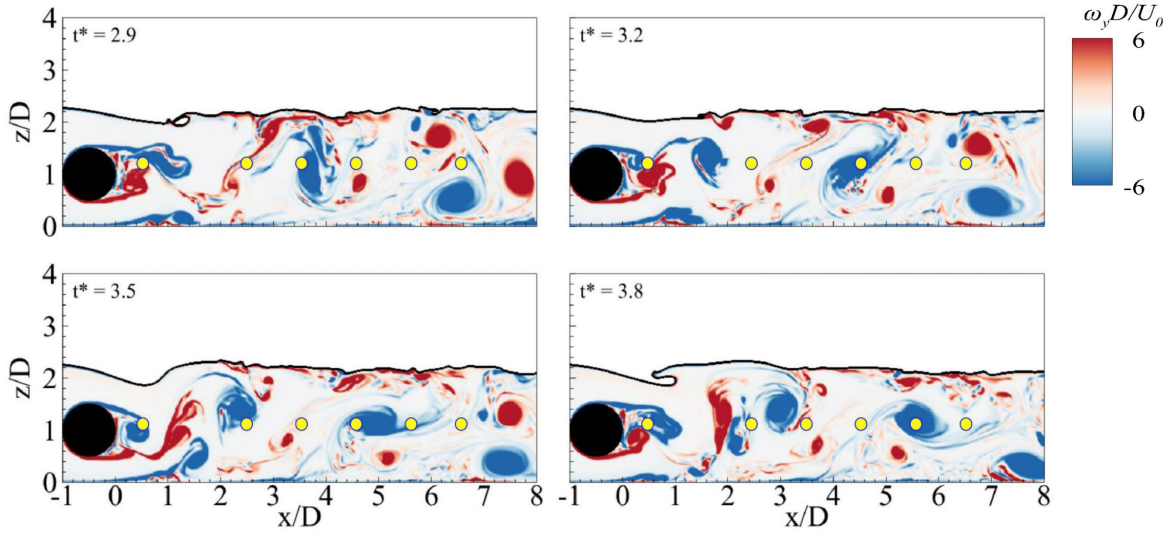

Fig. 3.7 Contours of normalised vorticity behind the cylinder for the case: Fr = 0.45, at four instants normalised by the peak frequency t^* = 2.9, 3.2, 3.5, and 3.8. The free surface is depicted as a solid-black line. The yellow dots mark the monitoring points for spectral analysis.

feature peaks at 0.216, 0.251, 0.311, 0.311, 0.259, and 0.147 for downstream positions with $x/D = 0.5$, 2.5, 3.5, 4.5, 5.5, and 6.5, respectively. The increasing pattern within the range of x/D = 0.5–4.5 can be related to the breakdown of primary vortices and the formation of small-scale vortices, this phenomenon was also described by Zhang et al. (2021). Furthermore, in regions further downstream of the cylinder, there is a notable change in the migratory direction of von Kármán vortices towards the free surface as shown in Fig. 3.4, which can explain the reduction in St monitored at $x/D \geq 5.5$ and $z/D \approx 1.2$.

For Fr = 0.31, the Strouhal numbers associated with the downstream stations predominantly exhibit a value of 0.309, with slight deviations occurring at specific locations (Fig. 3.9b). For instance, at $x/D = 2.5$, there is a marginal increase in St; however, this deviation is minor and quickly followed by a return to the dominant frequency, similar to the slight decrease in St observed at $x/D = 5.5$. These St variations among the downstream stations can be attributed to the complex dynamics of the flow, involving the breakdown of primary vortices, the formation of small-scale vortices, and the movement of von Kármán vortices within the flow domain. At Fr = 0.40, there are distinct characteristics of the Strouhal number at downstream locations, as shown in Fig. 3.9c. Specifically, St varies marginally around 0.36 up to x/D = 2.5. However, at $x/D = 3.5$ and $x/D = 4.5$, there is a marked increase in St, rising to 0.375 and 0.421, respectively. For positions $x/D = 5.5$ and $x/D = 6.5$, St slightly reduces to 0.410 and 0.375, respectively.

At Fr of 0.45, the complexity of flow dynamics increases, which is evidenced by the spectral plot in Fig. 3.9d. This figure shows multiple peaks that are indicative of the unsteady wake of the cylinder, with no clear dominant peak compared to those at lower Fr. At $x/D = 0.5$, the spectral energy peaks at $St = 0.379$, and a marginal increase to $St = 0.385$ is observed at $x/D = 2.5$. Furthermore, there is a significant increase to $St = 0.457$ at $x/D = 3.5$. How-

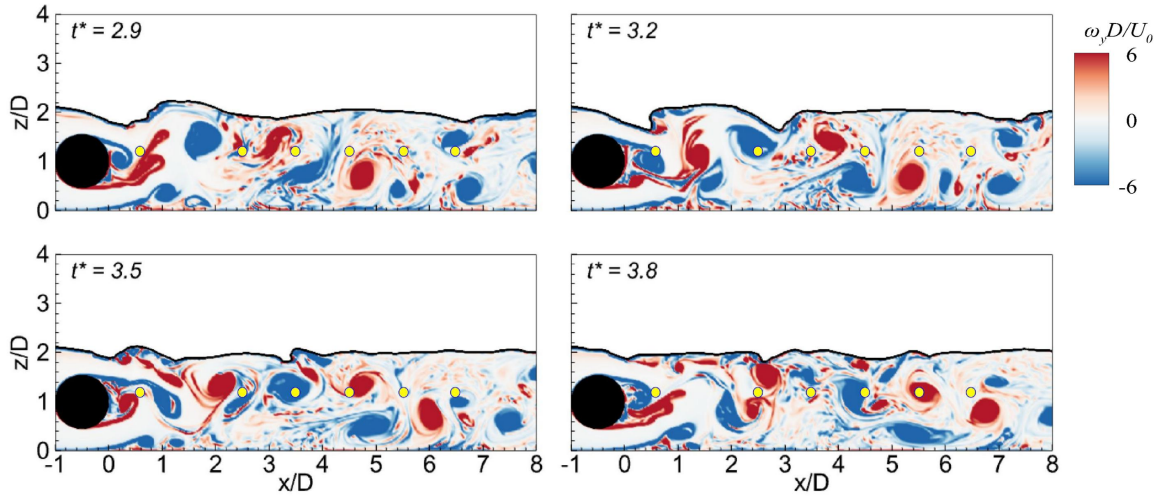

Fig. 3.8 Contours of normalised vorticity behind the cylinder for the case: $Fr = 0.53$, at four instants normalised by the peak frequency $t^* = 2.9$, 3.2, 3.5, and 3.8. The free surface is depicted as a solid-black line. The yellow dots mark the monitoring points for spectral analysis.

ever, a marked decrease in St is observed at $x/D = 4.5$, 5.5, and 6.5, with values of 0.314, 0.229, and 0.229, respectively, suggesting a transition towards more stable flow patterns. Fig. 3.9e shows that at $Fr = 0.53$, the spectral energy peaks at $St = 0.445$ at $x/D = 0.5$, slightly increases to $St = 0.485$ at $x/D = 2.5$, and maintains this value up to $x/D = 4.5$. This constant St indicates a sustained vortex shedding process, which is potentially associated with the breakdown of primary vortices and the continuous formation of smaller-scale vortices. However, a small decrease in St to 0.440 is noted at $x/D = 5.5$, before returning to the initial St of 0.445 at $x/D = 6.5$. For all submergence levels, the spectra of the vertical velocity fluctuations feature a decay slope of $-5/3$ in the inertial subrange that follows the classical Kolmogorov's decay law (Fig. 3.9). This $-5/3$ slope is a key indicator of the von Kármán energy cascade, a fundamental concept in turbulence theory. It represents the transfer of kinetic energy from larger turbulent eddies to smaller scales, ultimately resulting in energy dissipation at the Kolmogorov scale. The consistency of the data in Fig. 3.9 with the $-5/3$ slope highlights the presence of this energy cascade and its role in turbulent energy transfer. However, it is important to note that the complex nature of turbulence can lead to subtle deviations from this classical decay law under specific conditions (Stoesser et al. 2010, Rubinstein and Clark 2017).

3.4.3 Time-averaged flow field

The results of the time-averaged flow developed around the cylinder for the five submergences are shown in Figs. 3.10 and 3.11. The distribution of streamwise velocities represent how the approaching flow impinges on the cylinder, causing acceleration, both over and beneath it, as shown in Figs. 3.10a–c and Figs. 3.11a–b. For cases with $Fr \leq 0.45$, a high-momentum region is observed downstream of the cylinder above the wake ($z/D \geq 1.5$), while a low-momentum region, which is characterised by diminished streamwise velocities, is observed

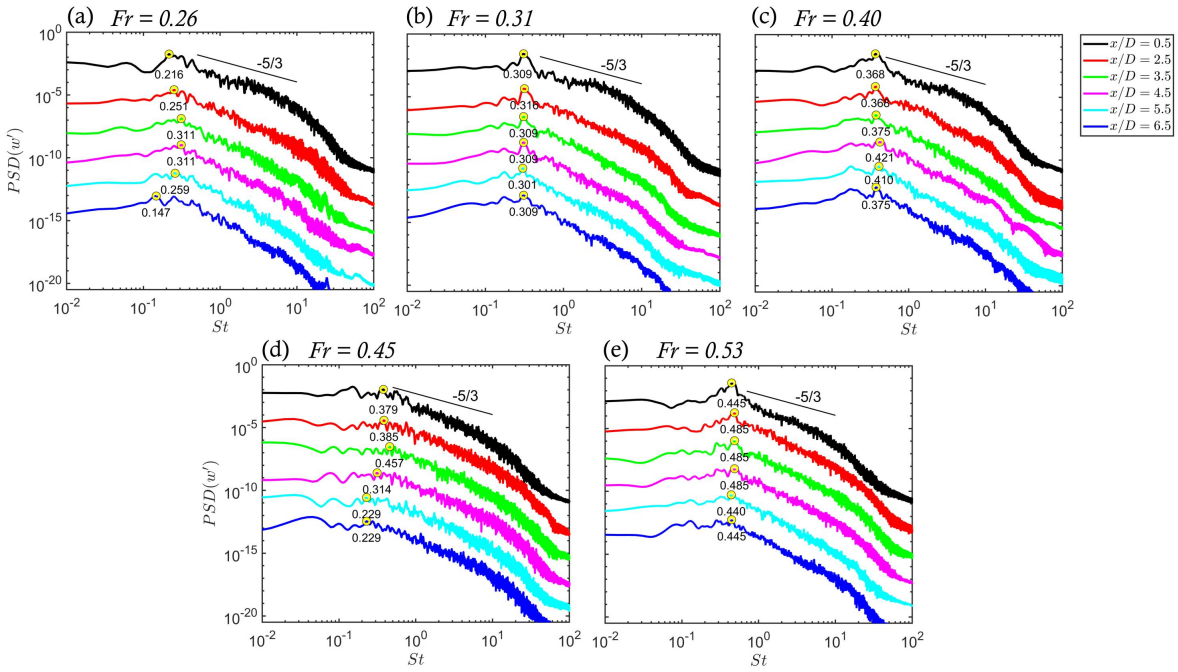

Fig. 3.9 Plots of the PSD obtained from the vertical velocity fluctuations $\langle u' \rangle$ at six stations downstream of the cylinder along the upper shear layer of the cylinder ($z/D \approx 1.2$) for all simulated cases.

on the lower side of the wake ($z/D < 1.0$). However, in the shallowest case of $Fr = 0.53$, the significant free surface deformation leads to the diversion of the flow downwards, resulting in a modification of this distribution. As a consequence, a high-momentum region is located in the mid-wake along the cylinder centre ($z/D = 1$) in the downstream region of the cylinder (Fig. 3.11b).

The contours of time-averaged vertical velocities (Figs. 3.10d–f and Figs. 3.11c–d) reveal the presence of two regions with high vertical velocities around the cylinder body in all cases, denoting a predominant upwards fluid motion. The first region is located upstream above the wake ($z/D = 1.5$) and is caused by the logarithmic distribution of the approaching flow. The second region forms in the lower part of the near wake, and this is attributed to the close proximity of the cylinder to the bottom wall, which leads to fluid acceleration through the vertical gap between the cylinder and the bottom wall. As the Fr increases, the expansion of those high $\langle w \rangle$ regions reduces, a phenomenon attributable to the blockage effect induced by the proximity of the free surface to the cylinder, i.e. $h/D = 0.5$ ($Fr = 0.53$), which constrains the flow, altering fluid dynamics around the cylinder and impacting the high $\langle w \rangle$ regions. Further downstream of the cylinder ($x/D \geq 6$), the distribution of $\langle w \rangle$ can be regarded as independent of the Fr, with almost zero values for all submergence levels.

Figs. 3.10g–i and Figs. 3.11e–f show contour plots of the streamwise turbulence intensities $\langle u' \rangle$ for all Fr cases, revealing the predominantly turbulent nature of the near wake enclosed on the downstream side of the cylinder, lying within the shear layers. Regardless of the free surface impact on the wake dynamics, the proximity of the cylinder to the bottom wall results in an uneven distribution of $\langle u' \rangle$ around the centre of the cylinder wake ($z/D = 1$). The

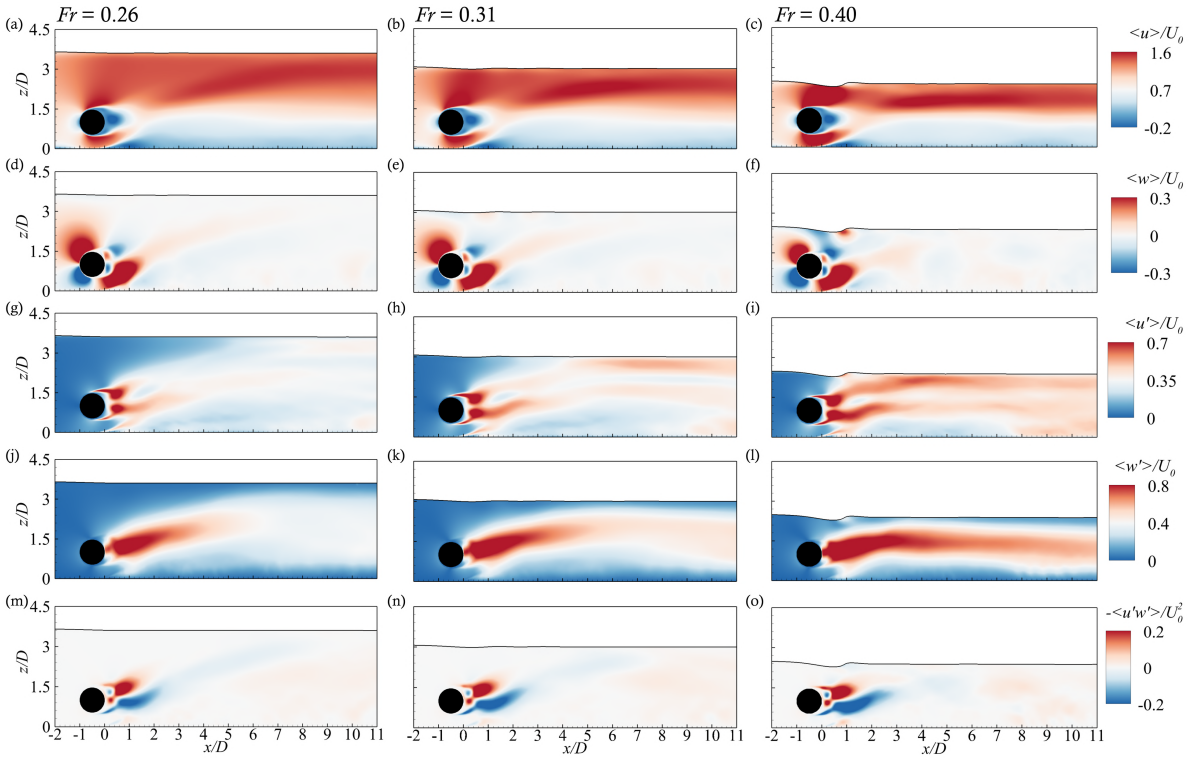

Fig. 3.10 Side elevation contour plots of the LES computed (a-c) streamwise velocity $\langle u \rangle$, (d-f) vertical velocity $\langle w \rangle$, (g-i) streamwise turbulence intensity $\langle u' \rangle$, (j-l) vertical turbulence intensity $\langle w' \rangle$, and (m-o) Reynolds shear stress $-\langle u'w' \rangle$, normalised by the bulk velocity for $Fr = 0.26$, 0.31 and 0.40. The mean free surface is depicted as a solid-black line.

turbulent region below this elevation extends almost twice the length compared to the region higher up in the wake, as a consequence of the interaction between the cylinder-induced near wake and the bottom wall ($0 < x/D < 2$). When the submergence depth decreases to $Fr =$ 0.40, the proximity of the free surface contributes to a higher turbulence intensity on the upper side of the wake, as shown in Fig. 3.10i. For higher Fr, the disturbance increases along the vertical height, which reflects a more turbulent flow. Moreover, For $Fr \geq 0.45$, the sharp deformation of the free surface leads to another region with high $\langle u' \rangle$ values at $x/D \approx 1$, enhancing the turbulence level in the downstream region of the cylinder as shown in Fig. 3.11e–f.

Further asymmetry of the turbulent wake in the downstream direction is evident in the distribution of the vertical turbulence intensities ($\langle w' \rangle$) as shown in Figs. 3.10j–l and Figs. 3.11g–h. The upper wake region shows a larger proportion of high $\langle w' \rangle$, which elucidates how the ground effect considerably alters the generation of dynamic vortex shedding, thereby leading to an asymmetric wake distribution. Conversely, when $Fr > 0.40$, the proximity to the free surface is observed to modify the previously described distribution, resulting in $\langle w' \rangle$ distributions around the cylinder centre ($z/D = 1$) that are almost identical, with an additional contribution from the deformed free surface.

Figs. 3.10m–o and Figs. 3.11i–j show the distribution of vertical Reynolds shear stress ($-\langle u'w' \rangle$) contours for the different submergence cases, revealing the turbulent momentum

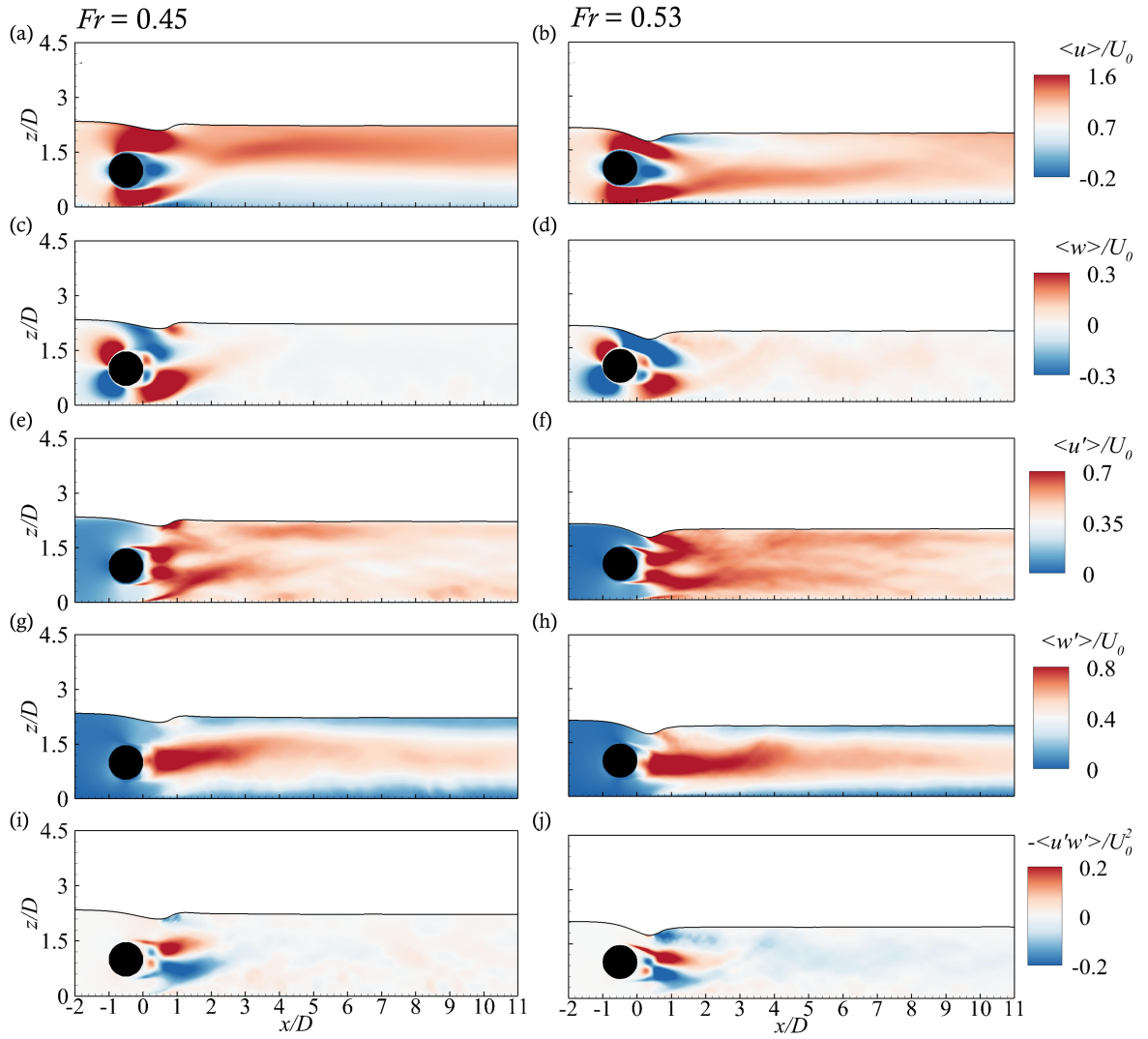

Fig. 3.11 Side elevation contour plots of the LES computed (a-b) streamwise velocity $\langle u \rangle$, (c-d) vertical velocity $\langle w \rangle$, (e-f) streamwise turbulence intensity $\langle u' \rangle$, (g-h) vertical turbulence intensity $\langle w' \rangle$, and (i-j) Reynolds shear stress $-\langle u'w' \rangle$, normalised by the bulk velocity for $Fr = 0.45$ and 0.53. The mean free surface is depicted as a solid-black line.

exchange in the wake of the cylinder. At high submergence ratios ($Fr \leq 0.40$), while flow acceleration from the bottom gap induces a downstream shift in the vertical Reynolds shear stress on the lower side of the cylinder within the near-wake region, the upper side of the cylinder remains unaffected. This suggests that the free surface exerts a minimal influence on altering the vortex shedding dynamics at this location. However, as Fr increases, the proximity of the free surface restricts the longitudinal expansion of regions with $-\langle u'w' \rangle$, pushing their vertical location towards the bottom wall. Moreover, an additional momentum exchange is observed for cases with $Fr \geq 0.45$, mainly due to the presence of a standing wave in the mean free-surface profile, which is more prominent in the shallowest case ($Fr = 0.53$). In general, the contours of $-\langle u'w' \rangle$ imply that the turbulent momentum exchange in the wake remains high until $x/D = 2$ for all submergence depths.

Vertical profiles of $-\langle u'w' \rangle$ at four downstream locations along the water depth are pre-

sented in Fig. 3.12 for the five simulated cases. Fig. 3.12 shows that in the near wake region, i.e. at $x/D = 0.5$, all cases compute similar turbulent momentum exchange values in the bottom half blow the cylinder's centre ($z/D \leq 1.0$) while the values along the top shear layer at approx. $z/D = 0.85$ peak at $Fr = 0.40$. This upper shear-layer maxima of $-\langle u'w' \rangle$ significantly drops at $x/D = 1.5$, with the vertical location of the largest value at $Fr = 0.53$ decreases to $z/D = 1$ due to the influence of the free-surface in the turbulent momentum exchange region. Maximum values of $-\langle u'w' \rangle$ in the lower shear layer at the latter location is again observed at $Fr = 0.40$. Further downstream of the cylinder at $x/D = 2.5$, the vertical Reynolds shear stress distribution varies with the submergence level, with a notable turbulence level decay seen for $Fr \geq 0.31$. Observations at $x/D = 3.5$ and 4.5 show that the largest momentum exchange at cylinder height is for the shallowest submergence.

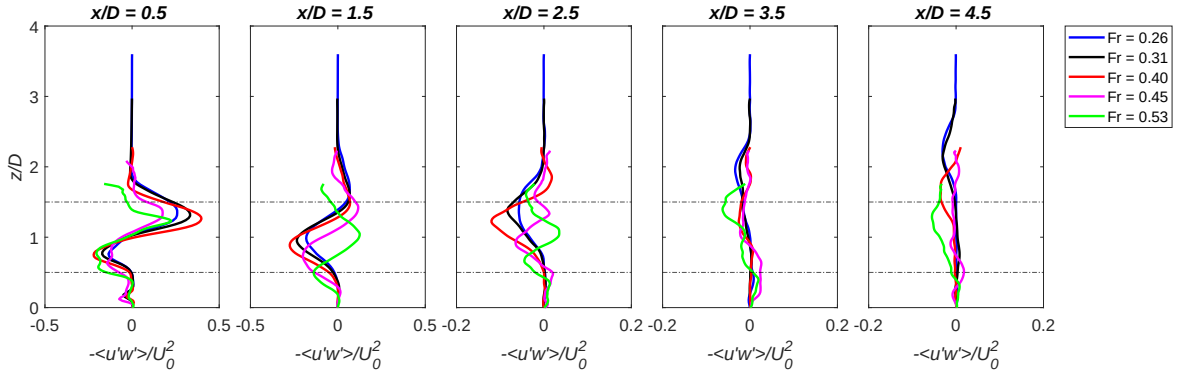

Fig. 3.12 Vertical profiles of normalised vertical Reynolds shear stress $\left(-\langle u'w' \rangle\right)/U_0^2$ at different locations downstream of the cylinder for the different simulated cases. The cylinder position is depicted as horizontal dot-dash lines.

The contours of time-averaged turbulent kinetic energy $\left(tke = 0.5\left(\langle u'^2 \rangle + \langle v'^2 \rangle + \langle w'^2 \rangle\right)\right)$ are shown in Fig. 3.13, where the main contributors to the tke here are $\langle u'^2 \rangle$ and $\langle w'^2 \rangle$, while the contribution from $\langle v'^2 \rangle$ is negligible. Zones of high tke occur immediately downstream of the cylinder along the cylinder height ($0.5 < z/D < 1.5$), reflecting the turbulence in the immediate recirculation zone behind the cylinder. For $Fr \leq 0.31$, an area of high tke extends downstream of the cylinder until $x/D \approx 1.0$. However, as Fr increases, this extends further downstream, reaching about $x/D \approx 3$ for $Fr = 0.53$, with additional contributions induced from the free surface. For the highest Fr cases, high tke dominates the mid-wake region. This is in contrast to lower Fr cases, where the tke levels are more prominent in the upper wake region ($z/D > 1$).

The differences in the mean tke across the five simulated cases are presented in Fig. 3.14a, which shows vertical profiles of tke at six downstream locations along the water depth. Fig. 3.14b and Fig. 3.14c present vertical profiles of the primary contributors to the tke: the streamwise velocity fluctuations $\langle u' \rangle$ and the vertical velocity fluctuations $\langle w' \rangle$, respectively. Fig. 3.14a shows that in the near-wake region ($x/D = 0.5$), all cases exhibit two symmetrical peaks behind the cylinder body, with magnitudes varying independently of Fr, e.g. at $Fr = 0.40$ and

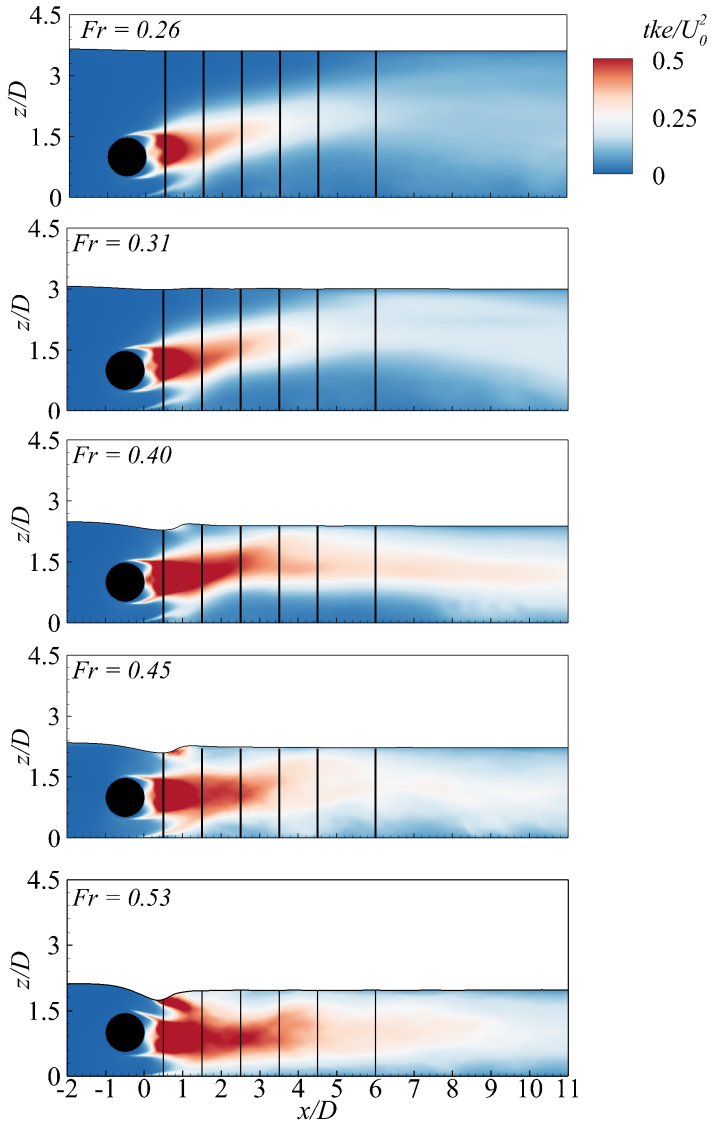

Fig. 3.13 Side elevation contour plots of the LES computed turbulent kinetic energy (*tke*) for all of the simulated cases. The vertical lines mark the locations at which vertical profiles of the mean *tke* are plotted and shown in Fig. 3.14. The mean free surface is depicted as a solid-black line.

0.53, the *tke* reaches values of $tke/U_0^2 > 0.8$, which are larger than those found in other submergence cases. At $Fr = 0.53$, an additional peak value of $tke/U_0^2 \approx 1$ is observed above the cylinder ($z/D \approx 1.8$), resulting from induced free-surface breaking at this shallow condition. At $x/D = 1.5$, the two peaks observed earlier begin to diminish with only one dominant peak remaining. For $Fr \leq 0.40$, this peak is primarily located on the upper side of the cylinder at $z/D > 1$, while for cases with higher Fr, the peak is situated on the lower side at $z/D < 1$. At $x/D = 2.5$, the dominant peaks for $Fr \leq 0.40$ move upwards at around $z/D = 1.5$, while no notable differences are observed for cases with higher Fr. Further downstream, at x/D = 3.5–6.0, the cylinder wake experiences a gradual decay in the *tke* magnitude for all cases.

Fig. 3.14b shows the contribution of the streamwise velocity fluctuations to the *tke* behind the cylinder. This component, which is representative of the flow unsteadiness in the main direction of the flow, exhibits variations depending on the submergence conditions and

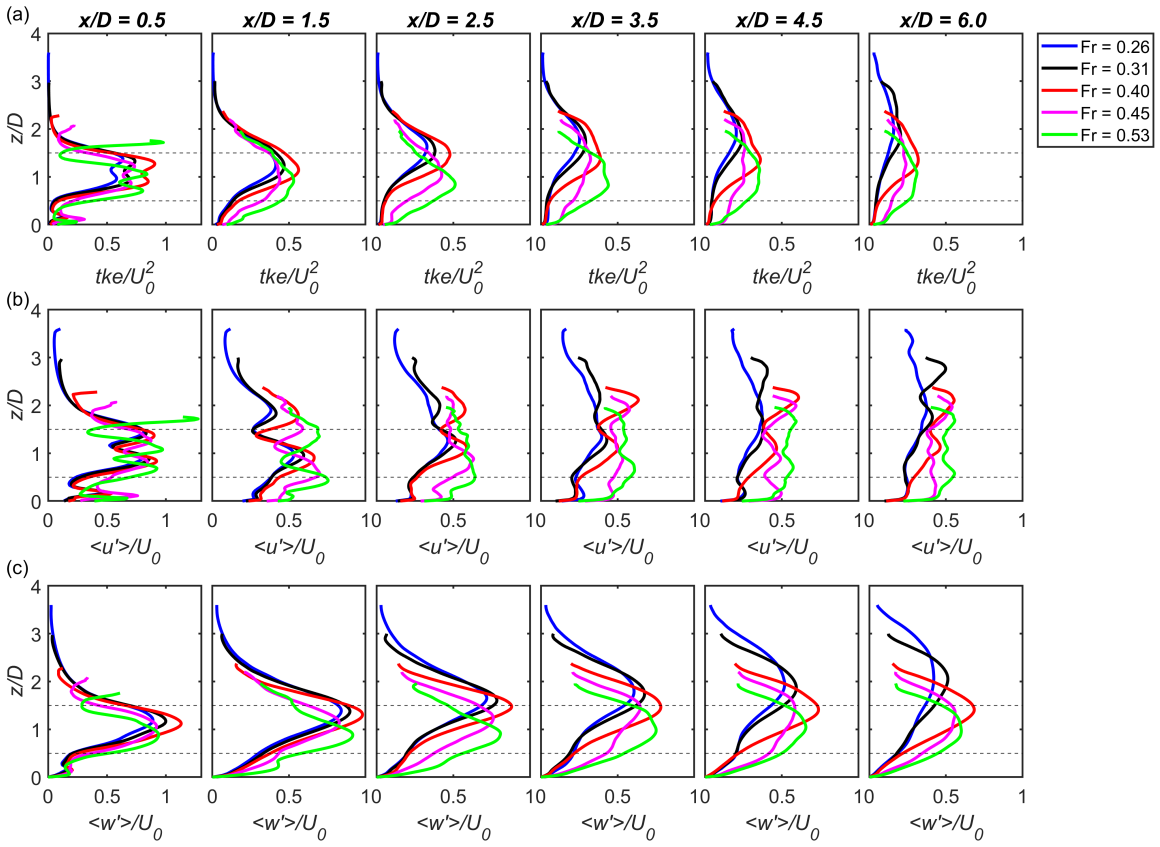

Fig. 3.14 Vertical profiles of (a) turbulent kinetic energy (*tke*), (b) streamwise velocity fluctuations $\langle u' \rangle$, and (c) vertical velocity fluctuations $\langle w' \rangle$ at six locations downstream of the cylinder along the water depth for all of the simulated cases. The dashed lines indicate the cylinder position.

downstream locations. At $x/D = 0.5$, the peaks of streamwise velocity fluctuations exhibit a marginal increase with increasing Fr, as the cylinder wake unsteadiness dominates at this location. Further stations downstream, extending from $x/D > 0.5$ up to six diameters downstream of the cylinder, the level of the streamwise turbulence intensities initially decreases at $x/D = 1.5$ and then its depth-average value remains relatively constant thereafter. This behaviour is especially noticeable for shallow flow conditions ($Fr > 0.31$), where the free surface is substantially deformed, affecting the wake dynamics. When comparing the contributions of streamwise and vertical turbulence intensities to the *tke*, the magnitude of vertical velocity fluctuations peaks at $\langle w' \rangle / U_0 = 1$ for $Fr = 0.40$ when $x/D \approx 1.5$ (as shown in Fig. 3.14c). However, other cases averaged around $\langle w' \rangle / U_0 = 0.8$, which is consistently higher than the streamwise velocity fluctuations, which are approx. $\langle u' \rangle / U_0 = 0.5$. As the flow progresses downstream (for $x/D > 1.5$), $\langle w' \rangle$ generally has a more significant contribution than $\langle u' \rangle$, especially in regions along the vertical height of the cylinder. However, closer to the free surface, at $z/D > 1.5$, the contribution from $\langle u' \rangle$ is greater than $\langle w' \rangle$, indicating a stronger influence of streamwise unsteadiness in that wake region. This varying pattern indicates the distinct roles of both streamwise and vertical fluctuations in the distribution and magnitude of the *tke* downstream of the cylinder.

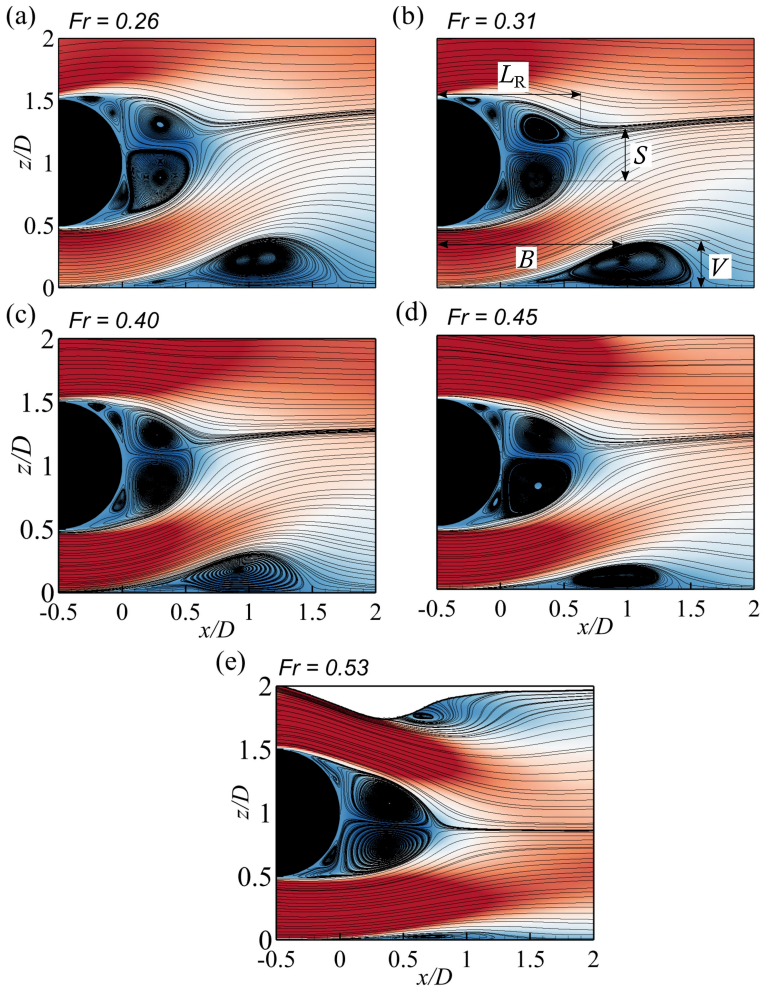

Fig. 3.15 Comparison of the mean recirculation regions computed using LES for all simulated cases, with contours of the mean streamwise velocity normalised by the bulk velocity. Recirculation length and other characteristics of the recirculation regions, which include the length of the mean recirculation zone (L_R), the transverse spacing between the primary pair (S), the ground bubble height (V), and the distance from the centre of the ground bubble to the centre of the cylinder (B), are overlaid only for the case (b) $Fr = 0.31$ for simplicity.

3.4.4 Mean recirculation region

The recirculation regions behind the cylinder for all submergence levels are presented in Fig. 3.15. Despite the influence generated by the free surface at high Fr, the proximity of the cylinder to the bottom wall results in altered wake dynamics (Sarkar and Sarkar 2010). This alteration is noticeable in the asymmetric wake enclosed behind the cylinder, as depicted by the flow streamlines illustrating two asymmetric recirculation cells distributed around the cylinder centre. The lower recirculation core is slightly larger than the upper one, which can be attributed to the influence of a recirculation zone formed close to the bottom wall immediately downstream of the wake bubble ($x/D \geq 0.5$), with its vertical and longitudinal extent varying with increasing Froude number. Other smaller recirculation regions are found downstream of the separation points, bounded by the separated shear layers and the primary recirculation zones for all cases, as shown in Fig. 3.15. At $Fr = 0.53$, a deficit in streamwise

velocity is observed near the free surface due to the downwards deflection of the jet-like flow from above the cylinder, inducing an additional recirculation zone (Fig. 3.15e).

Table 3.2 presents the characteristics of the recirculation zones for all cases, which include the length of the mean recirculation zone (L_R), the transverse spacing between the primary pair (S), the ground bubble height (V), and the distance from the centre of the ground bubble to the centre of the cylinder (B), as outlined in Fig. 3.15b. The length of the recirculation zone (L_R/D) shows a nonlinear relationship with Fr, initially decreasing from 1.087 at $Fr = 0.26$ to 1.042 at $Fr = 0.40$, and then reversing the trend and increasing to 1.212 at $Fr = 0.53$ (Fig. 3.15e). This could be due to the impact of the increasing blockage effect in the highest Fr cases, promoting a larger recirculation zone, as with increasing Fr the distance from the cylinder to the free surface becomes comparable to its distance to the bottom wall. The transverse spacing between the upper and lower recirculation cores of the primary pair (S/D) shows a slight decrease with increases Fr from about $S/D = 0.397$ at $Fr = 0.26$ to $S/D = 0.372$ at $Fr = 0.53$, which can be related to the modification of the separation angles at decreasing submergence depth (Reichl et al. 2005).

Table 3.2 Characteristics of the recirculation areas for all submergence cases. All parameters are normalised by the diameter of the cylinder.

Fr	h/D	L_R/D	S/D	V/D	B/D
0.26	2.1	1.087	0.397	0.384	1.509
0.31	1.5	1.064	0.389	0.361	1.502
0.40	0.9	1.042	0.388	0.318	1.457
0.45	0.7	1.169	0.386	0.202	1.451
0.53	0.5	1.212	0.372	0.074	1.212

The height of the wall recirculation region (V/D) reduces significantly from $V/D = 0.384$ for the deepest flow condition ($Fr = 0.26$) to about $V/D = 0.074$ for the shallowest submergence case, with a notable difference occurring after $Fr = 0.40$. These variations can be traced to the difference in the magnitude of fluid acceleration beneath the cylinder, which impacts the process of generating a wall shear layer and a subsequent separation (Oner et al. 2008). The distance from the centre of the ground feature to the centre of the cylinder (B/D) exhibits a consistent reduction with increasing Fr, with B/D values in the range of 1.509–1.212, indicating a potential relocation of the wall recirculation zone as the submergence depth decreases.

3.4.5 Centreline profile

The longitudinal profiles of mean streamwise and vertical velocities, in addition to turbulence intensities along the cylinder centreline ($z/D = 1$) for all submergence cases, are shown in Fig. 3.16. This shows that as the Fr increases, the streamwise velocity reversal in the attached recirculation area ($x/D < 1$) also increases, characterised by negative streamwise velocity. The peak reversal at $Fr = 0.53$ is $\langle u \rangle = -0.45U_0$, compared to $\langle u \rangle = -0.24U_0$ at $Fr = 0.26$. The

recirculation area ends approximately $1D$ downstream of the cylinder, as indicated by the positive values of $\langle u \rangle$. Downstream of the recirculation region, $\langle u \rangle$ initially increases with the increase in Fr, gradually recovering with $\langle u \rangle / U_0 = 0.7$ at $x/D = 10$ for $Fr = 0.26$ compared to $\langle u \rangle / U_0 = 1$ for $Fr \geq 0.45$.

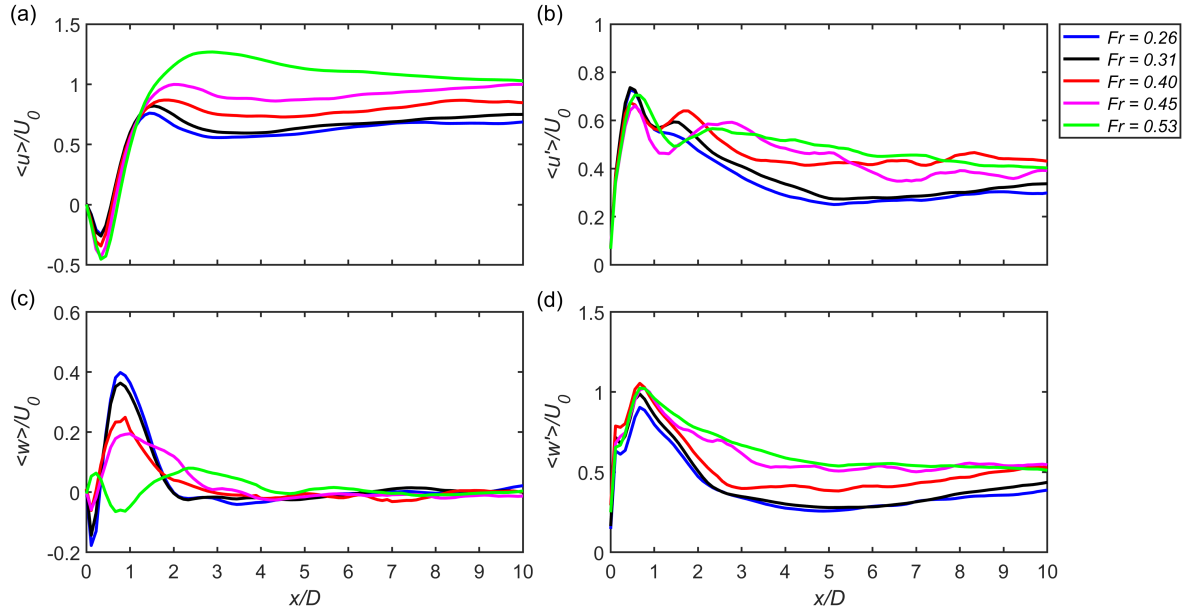

Fig. 3.16 Centreline profiles of normalised (a) streamwise velocity $\langle u \rangle$, (b) streamwise turbulence intensity $\langle u' \rangle$, (c) vertical velocity $\langle w \rangle$, and (d) vertical turbulence intensity $\langle w' \rangle$ for all submergence cases.

Fig. 3.16b shows the evolution of $\langle u' \rangle$, revealing the highest turbulence intensity levels are in the region of the negative streamwise velocity (Fig. 3.16a). The streamwise turbulence intensity progressively decays with increasing downstream distance, with a faster decay evident in deeper flow conditions, i.e. $Fr \leq 0.31$. However, at higher Fr, the free surface proximity induces larger streamwise fluctuations along $z/D = 1$ in the streamwise direction.

The centreline variation of $\langle w \rangle$ in Fig. 3.16c indicate the presence of a peak in positive $\langle w \rangle$ immediately downstream of the cylinder at $x/D = 1.0$, implying a predominant upwards fluid motion. However, this maximum is significantly reduced as Fr increases until a reverse peak of negative $\langle w \rangle$ is achieved at $Fr = 0.53$, indicating downwards fluid motion. The vertical velocities decrease by $3D$ downstream and approach near zero for all submergences at $10D$. Regarding the distribution of vertical turbulence intensity (Fig. 3.16d), the peaks are achieved at $x/D = 1$, ranging from $0.9U_0$ to $1.1U_0$, which are larger than those found for the streamwise turbulence intensities. At 10 diameters downstream of the cylinder ($x/D = 10$), the value of $\langle w' \rangle$ presents a substantial reduction from the initial peaks of approximately 54.55% for $Fr = 0.53$ and 57.78% for $Fr = 0.26$. Specifically, for $Fr = 0.53$, $\langle w' \rangle / U_0$ decays from 1.1 at $x/D = 1.0$ to 0.5 at $x/D = 10$; whereas for $Fr = 0.26$, it drops from 0.9 to 0.38.

3.4.6 Recovery of mean streamwise velocity

The velocity deficit in the streamwise direction $\left(\Delta\langle u\rangle = \frac{\langle u\rangle - \langle u\rangle_{x/D=-8}}{\langle u\rangle_{x/D=-8}}\right)$ between a selected far upstream station ($x/D = -8$) and downstream profiles ranging from $x/D = 0.2$ to $x/D = 15$ is calculated for all of the simulated cases to evaluate the influence of the submergence depth on wake recovery, as shown in Fig. 3.17. In the near-wake region, i.e. at $x/D = 0.5$, all simulations indicate a velocity surplus ($\Delta\langle u\rangle > 0$) along the bottom gap ($z/D < 0.5$) and a velocity deficit ($\Delta\langle u\rangle < 0$) behind the cylinder body from $z/D = 0.5$ to roughly $z/D = 1.5$. At higher water depths, another surge in velocity occurs. The velocity surplus at both positions exhibits an increase with the increase in Fr, unlike the velocity deficit, which shows a negligible difference among the Fr cases.

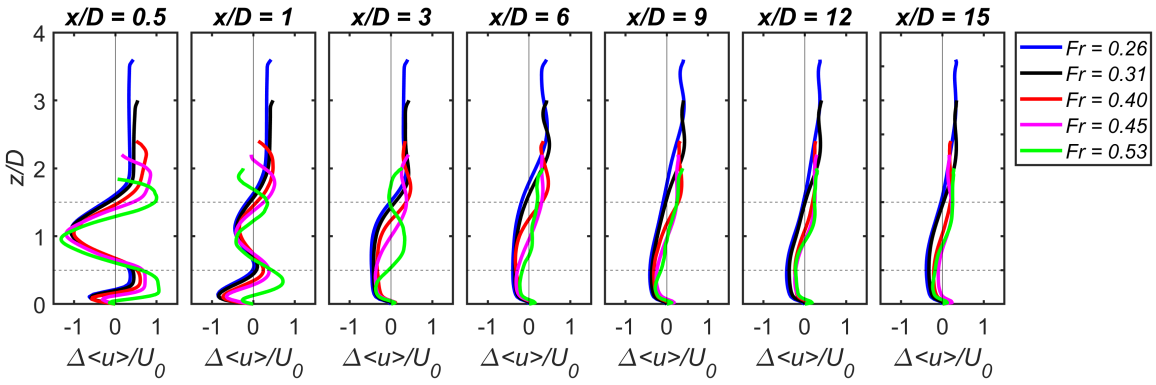

Fig. 3.17 Progression of velocity deficit ($\Delta\langle u\rangle$) computed from the difference between the upstream profile (x/D = -8) and selected downstream profiles for all of the simulated cases. The horizontal dashed lines indicate the cylinder's position. The vertical line indicates the zero-velocity deficit ($\Delta\langle u\rangle$ = 0).

At $x/D = 1$, cases with $Fr < 0.40$ exhibit a velocity deficit along the bottom gap position, while cases with larger Fr still show some velocity surplus, albeit with a lower magnitude when compared to that observed at $x/D = 0.5$. The velocity deficit along the cylinder position gradually decreases, approaching near-zero velocity values ($\Delta\langle u\rangle \approx 0$). At higher water depths, the velocity surplus also reduces, with a slight velocity deficit for the shallowest case (Fig. 3.17).

At $x/D = 3$, all cases exhibit a velocity deficit at $z/D < 0.5$. However, at higher water depths, cases with $Fr = 0.26$ and $Fr = 0.31$ still maintain velocity deficits up to $z/D = 1.5$, in contrast to cases with higher Fr, where they experience velocity surpluses at lower water depths. In particular, at $Fr = 0.53$, a significant velocity surplus is observed almost along the cylinder's position. Moving downstream to $x/D = 6$, the velocity surplus observed at $Fr = 0.53$ is diminished, reflecting a recovered wake with $\Delta\langle u\rangle \approx 0$. At downstream positions between x/D = 9 and 15, the wake almost fully recovers, whilst the velocity surplus at higher water depths $z/D > 1.5$ shows no significant deviation when compared to adjacent profiles.

3.4.7 Gap flux ratio

The flow condition within the cylinder gaps significantly influences the downstream fluid dynamics. Here, gap flux ratios are defined as the ratios of the flow rates at the bottom (q_b) and top (q_t) gaps of the cylinder relative to the upstream flux rate (q_u). The upstream flux (q_u) is determined between the free surface and the bottom wall ($z/D = 0$) at a distance of $8D$ upstream of the cylinder, as shown in Fig. 3.18. The pattern in Fig. 3.18a forms a triangular wedge shape, which illustrates how the flow rates through the top and bottom gaps vary when changing the Fr. The flux ratio of the top gap (q_t/q_u) consistently remains below 1.0, which peaks at $q_t/q_u = 0.81$ for $Fr = 0.26$ and then reduces to $q_t/q_u = 0.76$, 0.64, 0.59, and 0.48 for $Fr = 0.31$, 0.40, 0.45, and 0.53, respectively. This decline corresponds to the gradual increase in the flux ratio of the bottom gap (q_b/q_u) with increasing Fr. The flux ratios of the top and bottom gaps converge as Fr increases, reaching a point of close similarity at $Fr = 0.53$ with values approximately around 0.5 (Fig. 3.18a). This transition in gap flow behaviour and its convergence affects various aspects of the flow, with significant implications for shedding frequency and vortex characteristics downstream, especially in the presence of increased free surface deformation at higher Froude numbers.

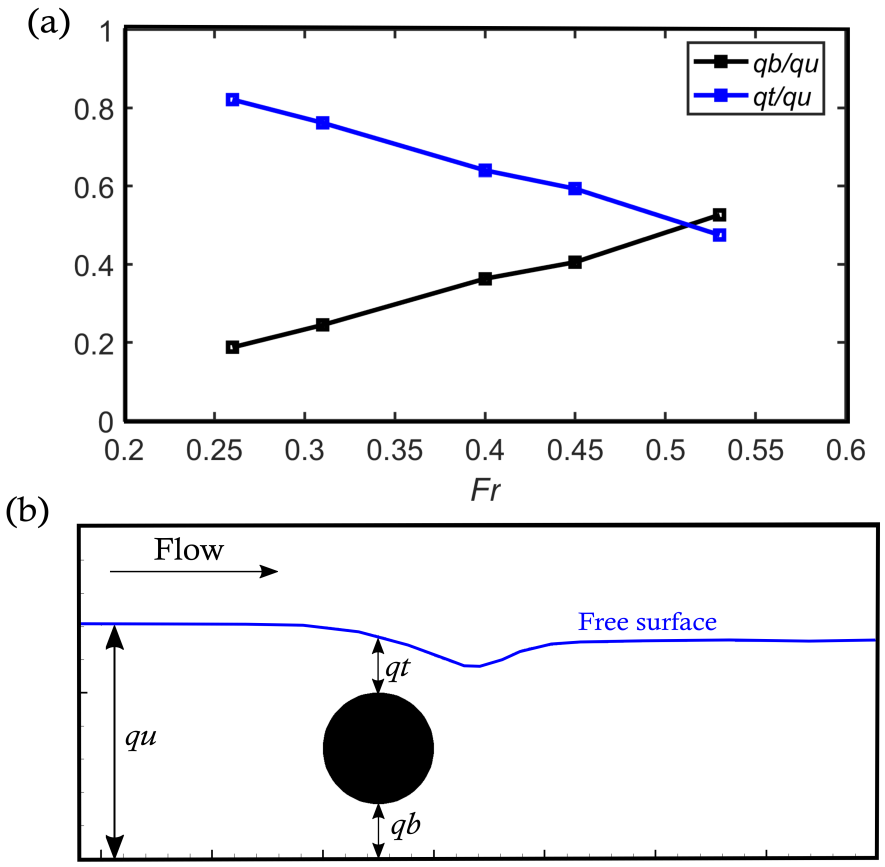

Fig. 3.18 Plots of (a) the variation of the gap flux ratios with gap position and Froude number, and (b) a schematic diagram illustrating the definition of the gap flux ratio and gap position, where q_u represents the upstream flux, q_t and q_b are the fluxes at the top and bottom gaps, respectively.

3.4.8 Continuity equation terms analysis

In an unbounded environment, the mean velocity components present in the following continuity equation are expected to exhibit symmetry with respect to the centreline of the cylinder:

$$\frac{\partial \langle u \rangle}{\partial x} + \frac{\partial \langle v \rangle}{\partial y} + \frac{\partial \langle w \rangle}{\partial z} = 0 \tag{3.2}$$

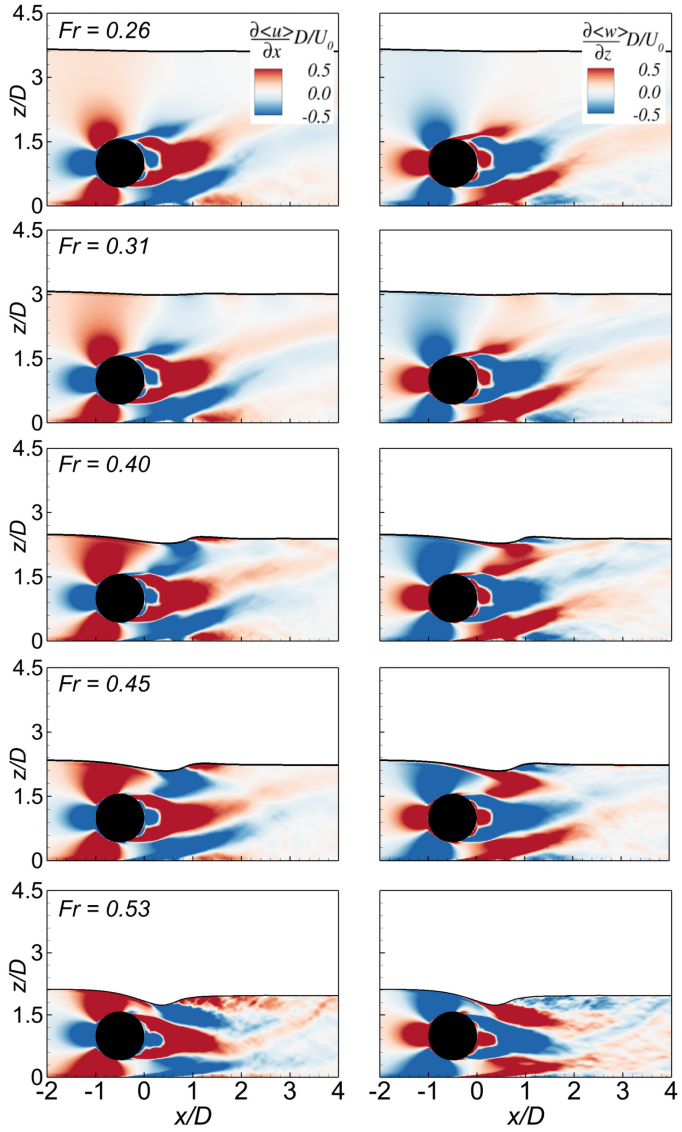

Fig. 3.19 Contours of the continuity equation terms for all simulated cases, $\partial u/\partial x$ (left-hand) and $\partial w/\partial z$ (right-hand).

However, in the cases studied, the proximity of the cylinder to the bottom wall and the free surface is likely to cause deviations from this symmetry. The term $\partial \langle v \rangle/\partial y$ is not considered in this analysis because it is deemed to be much smaller when compared to the other two terms given that the main flow direction is in the xz plane. Fig. 3.19 presents contour plots of the terms $\partial \langle u \rangle/\partial x$ and $\partial \langle w \rangle/\partial z$ for all simulated cases. In all cases, the regions with

the highest rate of change for the mean streamwise velocity are located in the core of the near wake, within the range of $0 < x/D < 2$ and $0.5 < z/D < 1.5$. These regions coincide with those exhibiting the most negative rate of change for the mean vertical velocity because both terms need to counterbalance each other according to Eq. 3.2 to satisfy mass conservation. A region of negative $\partial\langle u\rangle/\partial x$ develops in the gap between the bottom wall and the cylinder, which is indicative of a decrease in the streamwise velocities along the x direction. As the approach flow accelerates on the upper and lower sides of the cylinder, an area with $\partial\langle u\rangle/\partial x > 0$ manifests upstream of the cylinder, while a decrease in $\langle u\rangle$ is evident near the stagnation point.

Furthermore, it is observed that a negative streamwise change of $\langle u\rangle$ develops over the upper shear layer until $x/D \approx 0.5$ for $Fr = 0.26$ and 0.31. This phenomenon diminishes as Fr increases. Whereas, at $Fr \geq 0.40$, another region with negative $\partial\langle u\rangle/\partial x$ emerges from the surface curvature at $x/D \approx 0.8$, which is followed by a small region of positive $\partial\langle u\rangle/\partial x$ attached to the free surface. In the shallowest case, the positive region near the free surface elongates further downstream, while the negative region along the bottom gap becomes narrower when compared to the cases of deeper conditions (Fig. 3.19). A reverse distribution is found for $\partial w/\partial z$ in the near wake of the cylinder for all investigated submergences.

3.4.9 Mean kinetic energy

To understand the dynamics of the mean flow and the driving components behind the process of wake recovery for all submergence cases, the budget of the mean kinetic energy ($K = 0.5\langle u_i\rangle^2$, with $i = 1$) is analysed. The equation is obtained by multiplying the time-averaged streamwise velocity component $\langle u_i\rangle$ by the spatially-filtered momentum equation for mean velocities (Yang et al. 2020), and reads as follows:

$$
\begin{aligned}
0 = & \overbrace{-\left\langle u_j\right\rangle \frac{\partial K}{\partial x_j}}^{I} \overbrace{-\langle u_i\rangle \frac{1}{\rho}\frac{\partial\langle p\rangle}{\partial x_i}}^{II} \\
& \overbrace{+\frac{\partial}{\partial x_j}\left(\nu\langle u_i\rangle \frac{\partial\langle u_i\rangle}{\partial x_j}\right)}^{III} \overbrace{-\frac{\partial\left(\langle u_i\rangle\left\langle u_i' u_j'\right\rangle\right)}{\partial x_j}}^{IV} \\
& \underbrace{-\left\langle u_i' u_j'\right\rangle \frac{\partial\langle u_i\rangle}{\partial x_j}}_{V} \underbrace{-\nu\left(\frac{\partial\langle u_i\rangle}{\partial x_j}\right)^2}_{VI}
\end{aligned}
\tag{3.3}
$$

where $\langle p\rangle$ denotes time-averaged pressure field and $\langle u_i' u_j'\rangle$ are the time-averaged shear stress tensor. Term I is the rate of MKE convection by the mean flow. Term II denotes the mechanical work generated by gradients in the mean pressure field that transports MKE. Term III refers to the MKE transport by mean viscous stresses. Term IV accounts for the transport of MKE by turbulence fluctuations. Term V refers to the destruction of MKE into turbulence,

which is also called the production term in the turbulent kinetic energy equation. Term VI accounts for the viscous dissipation of the MKE.

The production term V in Eq. 3.3 exhibits a negative sign, which can be interpreted as the rate at which MKE is lost from the mean flow and transferred to the turbulent eddies, thus denoting the generation of turbulent kinetic energy. In the current analysis, the viscous terms III and VI are disregarded because the turbulent eddy viscosity becomes negligible at the relatively high Reynolds number of the flow considered (Lopes et al. 2006, Blackman et al. 2017). Figs. 3.20 and 3.21 present the results for all Fr cases with contour of each component in the x- direction (main flow direction). This includes the convection of MKE by the mean flow (I), the transport of MKE due to pressure work (II) and due to turbulent stresses (IV), and the destruction of MKE into turbulent kinetic energy production (V).

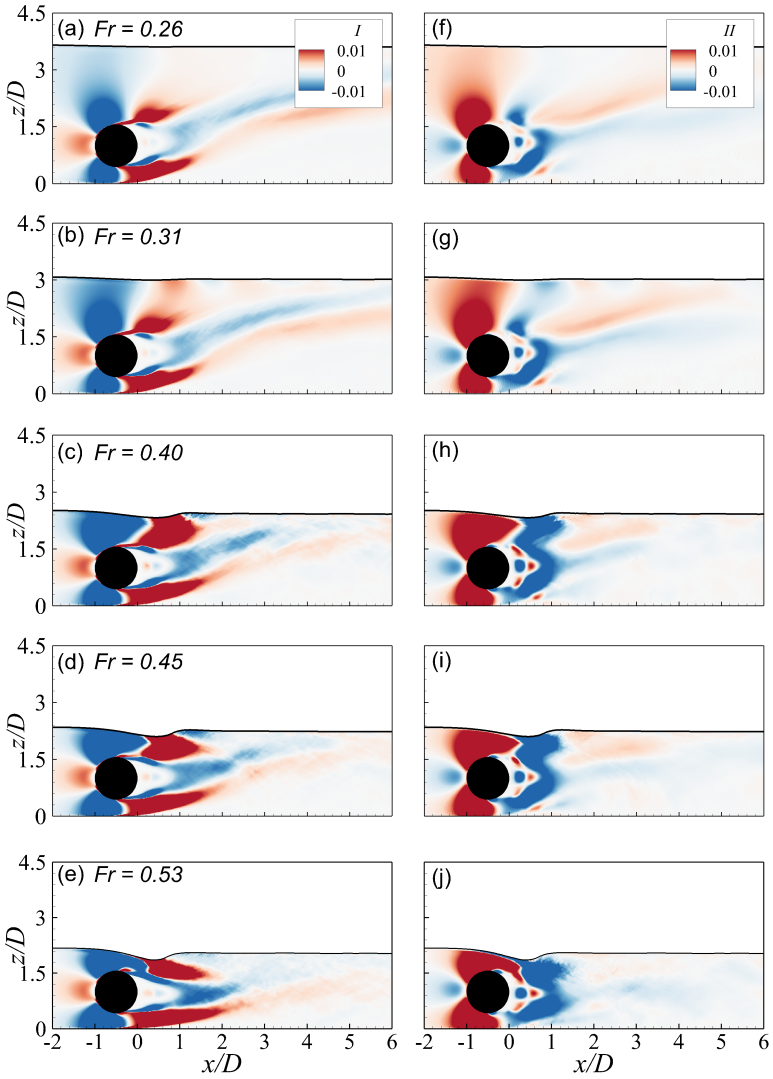

Fig. 3.20 Contour plots of the investigated components of MKE, namely (I) the convection of MKE by the mean flow and (II) work due to the pressure gradient for all simulated cases.

Evaluating each term in the budget equation for MKE allows us to identify the flow mechanisms that predominantly influence its replenishment, loss, and transport over the cylinder

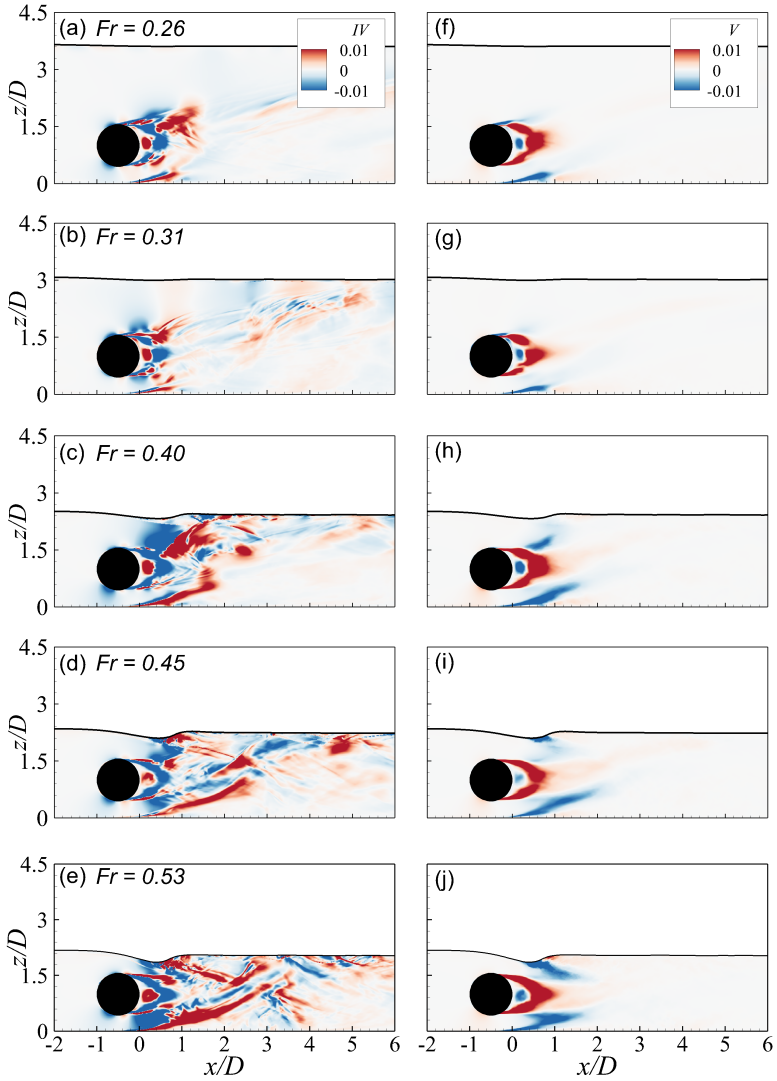

Fig. 3.21 Contour plots of the investigated components of MKE, namely (IV) transport of MKE by turbulent stresses and (V) the production term for all simulated cases.

wake region. Figs. 3.20a–e reveal that upstream of the cylinder, the contours of the convective MKE by the mean flow (I) exhibit values that suggest a loss of MKE on both the upper and lower sides of the cylinder. In contrast, downstream of the cylinder, especially within the separated shear layers, the convective term indicates a strong mechanism for the replenishment and transport of MKE, revealing its highest intensity. For $Fr \geq 0.4$, the region indicating strong replenishment and transport on the upper downstream side begins to detach from the upper shear layer. Instead, near the free surface where there is a significant drop and deformation, a larger region of replenishment occurs. This suggests a more dominant MKE transport mechanism compared to cases with deeper flow conditions. Furthermore, the mechanism contributing to the transport of MKE near the bottom wall appears to extend more downstream as Fr increases, i.e. up to $x/D \approx 2$ when $Fr = 0.53$, as shown in Fig. 3.20e.

The transport of MKE due to pressure work appears to evolve in a reversed pattern to that of the MKE convection driven by the mean flow. This contrasting behaviour is evident across all Fr cases, as shown in Figs. 3.20f–j. The underlying reason for this difference lies in the

pressure dynamics surrounding the cylinder. As the fluid approaches the cylinder, it faces an increasing pressure gradient, which facilitates the transfer of MKE. This phenomenon is reflected by the positive values observed on both the upper and lower sides of the cylinder. Conversely, downstream of the cylinder, there is a reduced transfer of MKE due to pressure work. This reduction is represented by negative values, which are particularly noticeable behind the cylinder and extending along the water column when $Fr \geq 0.4$.

As presented in the contour plots of Figs. 3.21a–e, the spatial distribution of MKE transfer due to turbulence fluctuations (IV) for all cases is quite irregular. Specifically, both positive and negative values of MKE are observed downstream of the cylinder. The reason for such a varied distribution can be traced back to the complex vortical structures that form in the wake of the cylinder as shown in Figs. 3.4–3.8. These vortices do not develop in isolation but instead interact with vortices shed from both the free surface and the bottom wall, and this interaction becomes more pronounced as Fr increases.

Figs. 3.21f–j present contours of the destruction of MKE into *tke* (term V) across all presented cases. These plots indicate that the region immediately behind the cylinder, extending up to approximately $x/D = 1$, is the primary location for the significant loss or depletion of MKE, directly contributing to the production of *tke*. Figs. 3.21f–j reveal regions with a decline in *tke* identified by negative values near the bottom wall and the free surface for cases with high Fr. They can be interpreted as areas with restricted *tke* transport, suggesting reduced turbulent activity. As Fr increases, the reduction in *tke* production at these regions increases.

3.4.10 Dominant shedding frequency and hydrodynamic coefficients

The asymmetric flow field that develops around the cylinder, due to its proximity to the bed, the influence of the free surface, and the upstream-velocity logarithmic distribution, affects the hydrodynamic forces exerted on the cylinder. An investigation of the hydrodynamic properties of the circular cylinder, including the mean drag and lift coefficients and the Strouhal number is conducted. The forces on the cylinder in the horizontal (F_x) and vertical (F_z) directions are directly calculated using the immersed-boundary method (Ouro et al. 2019), and are used to calculate the mean drag (C_D) and lift (C_L) coefficients, as follows:

$$C_D = \frac{F_x}{\frac{1}{2}\rho A U_0^2} \tag{3.4}$$

$$C_L = \frac{F_z}{\frac{1}{2}\rho A U_0^2} \tag{3.5}$$

where A is the cross-sectional area of the cylinder defined as $A = DB$, where B is the cylinder's width (spanwise length). Moreover, the lift acting upon the cylinder includes a hydrostatic contribution due to the presence of gravity. Therefore, this contribution, the buoyancy

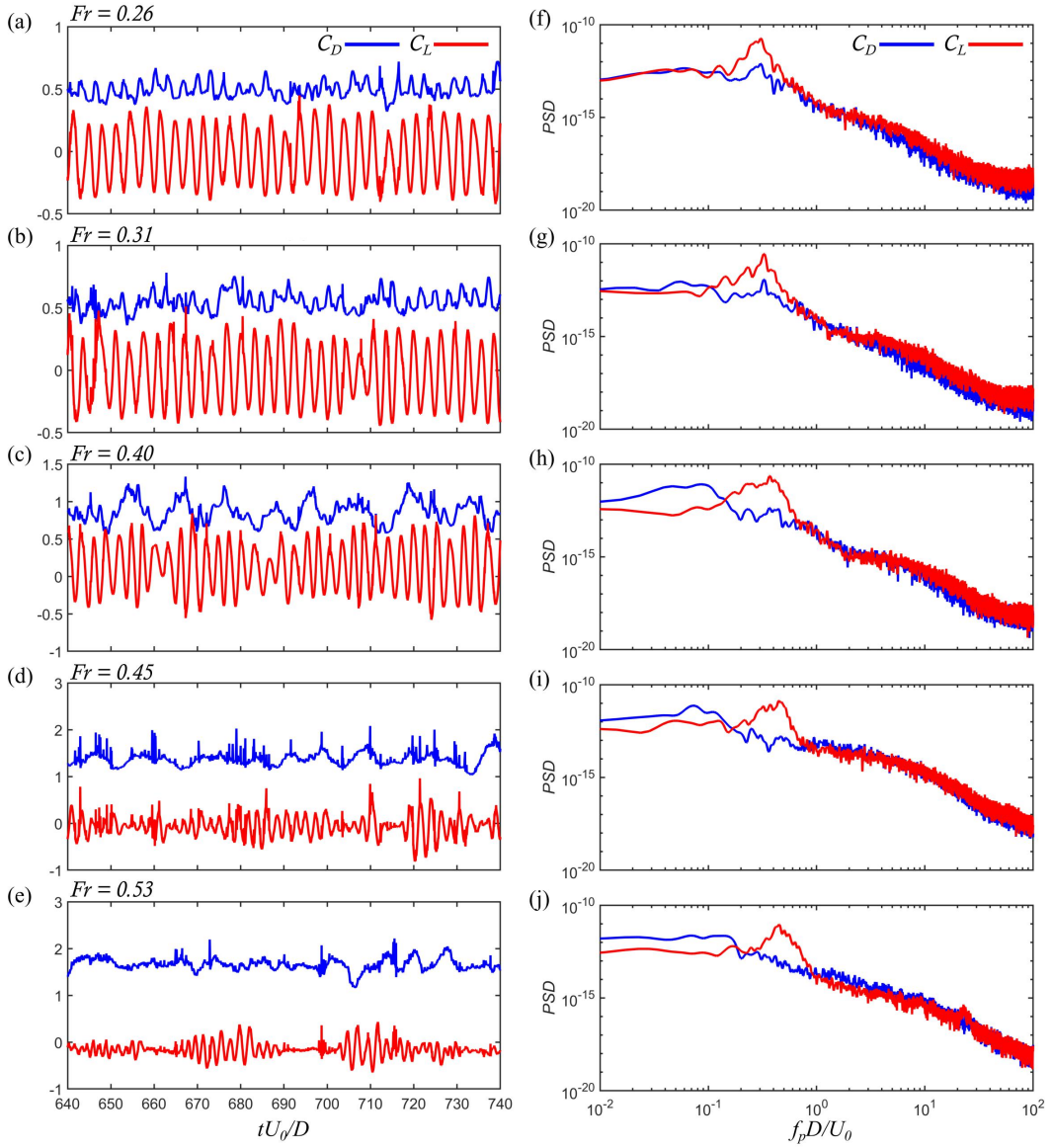

Fig. 3.22 Plots of (a-e) time history of drag and lift coefficients of the cylinder and (f-j) their corresponding PSD distribution for all simulated cases.

force, is subtracted from the calculated lift, as follows:

$$Fz_{\text{actual}} = Fz - Fz_{\text{noflow}} \tag{3.6}$$

where Fz_{noflow} denotes the computed forces with zero inlet velocity.

Fig. 3.22 presents the time histories of the drag and lift coefficients with the corresponding PSD features over an interval of tU_0/D = 640–740 for all simulated cases. In Fig. 3.22a-e, sinusoidal fluctuations are observed in both drag and lift coefficients up to $Fr = 0.40$. The drag coefficient shows a less consistent sinusoidal pattern with a higher amplitude. As Fr increases, the fluctuations in C_D and C_L become increasingly irregular. This irregularity is marked by an increase in the average value of the drag coefficient and a shift towards a larger negative average value of the lift coefficient, most notably at $Fr = 0.53$ as shown in Fig.

3.22e. The irregularity seen with the increase in Fr can be attributed to the proximity of the free surface, which exerts a modulating effect on the behaviour of the force fluctuations (Zhao et al. 2021).

The energy peaks computed from both the drag and lift coefficients for each submergence case are shown in Fig. 3.22f–g. These peaks fall within a range of Strouhal numbers of St = 0.30–0.45, which increases with increasing Fr. The St values are determined by the dominant peak in the lift spectrum. For $Fr \leq 0.4$, this is consistent with what is observed in the drag spectrum, albeit at lower magnitudes. However, as Fr increases, pinpointing distinct energy peaks in the drag spectrum becomes more challenging due to the increasing turbulence in the flow. This is expected as the dynamics of lift are closely tied to vortex shedding (Schewe 1983, Liang and Tao 2018), and the turbulent nature of the flow at high Fr can obscure the periodicity in the drag spectrum, making it harder to identify clear peaks.

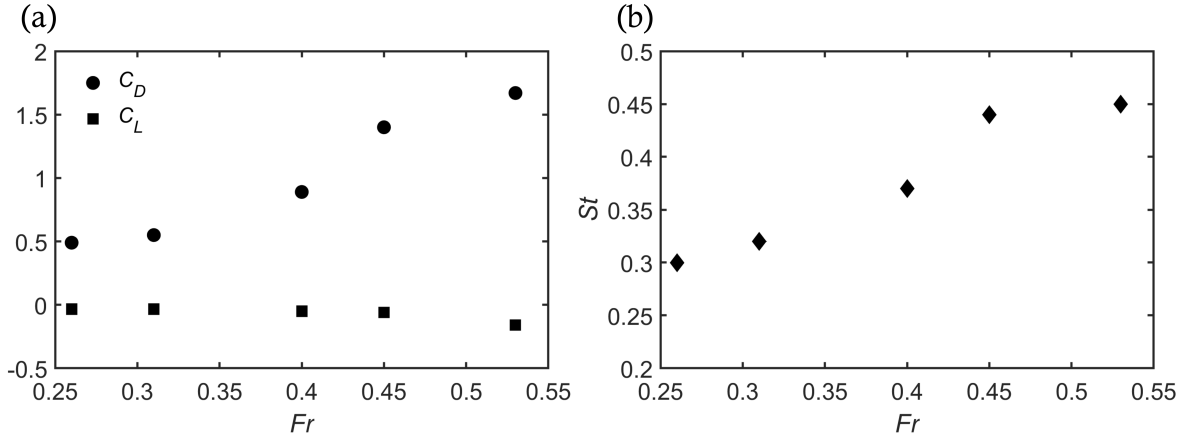

Fig. 3.23 Variation of (a) the drag and lift coefficients and (b) the Strouhal number of the horizontal cylinder as a function of the Froude number.

Fig. 3.23a shows how the drag and lift coefficients undergo significant changes as Fr increases. For instance, at $Fr = 0.26$, C_D is 0.49 and C_L is -0.032, indicating a downward lift coefficient. Moving to a higher Froude number of 0.31, C_D rises to 0.55, while C_L maintains its negative value. At $Fr = 0.31$, the obtained C_D value exhibits a notable difference from the study conducted by Ouro et al. (2019), who considered a shear-free rigid-lid condition to represent the water surface, resulting in a C_D value of 0.41. At $Fr = 0.40$, C_D increases to 0.89, and C_L increases to -0.048. The trend continues with C_D increasing to 1.4 at $Fr = 0.45$, and C_L becoming -0.06. For the shallowest case simulated at $Fr = 0.53$, C_D equal to 1.67, and C_L reaches -0.16, suggesting an even stronger downward lift coefficient, which implies that the cylinder is subjected to a downward thrust with the existence of the free surface. The drag coefficients suggest that as the Fr increases, the object faces greater resistance in the flow. The lift coefficient also indicates the minimal effect of the free surface in cases with deeper flow conditions,i.e. $Fr \leq 0.31$. However, in conditions with shallower flows, the influence of the free surface becomes more pronounced.

Fig.3.23b shows the variation of the Strouhal number with Fr. The observed St at lower

Froude numbers, at $Fr = 0.26$ and $Fr = 0.31$, demonstrates an increase from 0.30 to 0.32. These values are close to the experimental findings by Ouro et al. (2019) for conditions of $G/D = 0.5$ and $Fr = 0.31$, where St was measured to be 0.30. Conversely, the numerical evaluations under rigid surface conditions performed in the same study indicated a lower St value of 0.27. These values at low Fr are significantly higher than the St typically observed in flows around unbounded cylinders, which is approximately 0.21 (Bearman and Zdravkovich 1978). With a further increase in the Fr, a significant increase in the St becomes apparent, reaching its peak at $Fr = 0.53$ with a Strouhal number equal to 0.45. This observation suggests that the configuration of a cylinder bounded by both the free surface and the bottom wall does not suppress vortex shedding in the same way as when the cylinder is positioned near the free surface but sufficiently distant from the bottom wall, as described in the results of Chu et al. (2018). Instead, this configuration induces a higher shedding frequency due to the blockage effect, as it accelerates the fluid along the sides of the cylinder.

3.5 Closure

The nature of the turbulent flow developed behind a submerged horizontal circular cylinder at a fixed gap-to-diameter ratio of 0.5 to a solid bottom boundary for shallow flow conditions at bulk Reynolds numbers of 13,333 is investigated using LES. Results revealed the effect of varying the distances to the free surface on the wake dynamics and the hydrodynamic coefficients of the cylinder. Numerical simulations conducted at five relative submergence levels, ranging from submergence-to-diameter ratios of 2.1 down to 0.5, yielded Froude numbers in the range of 0.26 to 0.53. The LES results showed good agreement with the experimental measurements for the time-averaged flow quantities and water-surface profile at $Fr = 0.31$. At higher Fr, the elevation of the water upstream of the cylinder increased, and the severity of the free surface fluctuations downstream of the cylinder was also enhanced. At Fr of 0.26, the impact from the free surface on the cylinder wake was deemed negligible given that no evident distortion in the free surface occurred in the simulations.

The interaction between the free surface and the wake's vorticity became more pronounced with high Froude number, i.e. $Fr > 0.31$, leading to irregular flow patterns and a more rapid loss of von Kármán vortex street coherence. While the proximity of the cylinder to the free surface affected the wake dynamics, the presence of a small gap between the bottom wall and cylinder had a substantial impact on the generation and shedding of vortices, leading the turbulent wake to become more irregular compared to unbounded cylinder flows or cases with just free-surface proximity. For $Fr < 0.40$, the flow is accelerated both above and below the cylinder, resulting in a higher momentum region above the wake and a comparatively lower one below; this difference diminishes as the Fr increases. In the shallowest cases ($Fr = 0.53$), the plunging flow diverted downwards due to pronounced free-surface deformation, attaining a high-momentum region along the cylinder centre in the streamwise direction.

The proximity of both the free surface and the bottom wall to the cylinder-induced noticeable alterations in the wake dynamics. The length of the recirculation zone exhibited a nonlinear relationship with Fr: initially increasing, then decreasing, and subsequently increasing again at higher Fr values. In addition, the height of the recirculation zone near the bottom wall significantly reduced as submergence decreased, alluding to the modification of fluid acceleration beneath the cylinder. At $Fr = 0.53$, an additional recirculation zone near the free surface became apparent, indicating the considerable effect of the free surface. The contribution of both streamwise and vertical turbulence intensities to the *tke* varied with varying Fr, with the vertical turbulence intensities being larger than their streamwise counterparts. The gap flux ratios, which quantified the relationship between flow rates at the cylinder's top and bottom gaps relative to the upstream flow rate, exhibited a tendency to approach more similar values as Fr increased, reflecting a balancing act between the initially divergent top and bottom flux ratios at deeper flow conditions. The convective transport of mean kinetic energy, influenced by pressure dynamics and turbulence fluctuations, significantly impacted its replenishment and loss, with the variations in Fr affecting its spatial distribution and intensity, particularly near the free surface and the bottom wall.

The presence of the free surface had a significant impact on the hydrodynamic forces generated on the cylinder. In the shallowest submergence case ($Fr = 0.53$), a mean drag coefficient of 1.67 was attained, which is significantly larger than the value achieved with the deepest case ($Fr = 0.26$) of 0.49. At $Fr > 0.31$, the mean lift coefficient began to show a larger downward force on the cylinder, reaching -0.16 at $Fr = 0.53$, which implies that the cylinder is subjected to a downward thrust which increases as the free surface approaches the cylinder. The spectral analysis further revealed variations in the Strouhal numbers, which increased from 0.30 at Fr = 0.26 to 0.45 at Fr = 0.53. This rise suggested alterations in flow patterns due to the close proximity of both the free surface and the bottom wall. These conditions caused greater blockage compared to scenarios where proximity is limited to just one side, which, in turn, weakens or suppresses the von Kármán vortex shedding. This investigation provided evidence of the significant effect of water-surface variations on the cylinder hydrodynamics at high Froude numbers of $Fr > 0.31$.

CHAPTER 4

Coherence of the Vortex Shedding Dynamics Shed by a Circular Cylinder in Very Shallow Free-surface Flows Quantified with Proper Orthogonal Decomposition

4.1 Aim of the chapter

This chapter focuses on the use of POD to investigate the influence of free-surface effects on the cylinder wake downstream. It analyses the variations in these effects based on submergence depths and the numerical methods chosen for the air-water interface. The objective is to identify the core flow mechanisms and obtain a thorough insight into the dynamics of the wake structure under varied conditions.

4.2 Summary

Modelling free-surface turbulent flows is challenging, and there is a need to quantify the impact of the free-surface on the instantaneous wake downstream of cylinders or other submerged structures (Khosronejad et al. 2019). In particular, vortex shedding downstream of a circular cylinder in the vicinity of a boundary, especially a free surface such as the interface between fluid and air, is irregular and exhibits significant spatiotemporal variations, which makes it difficult to extract and analyse the most energetic structures in turbulent flows.

The complex dynamics of unsteady turbulent wakes necessitate the use of advanced methods, such as dynamic mode decomposition (DMD) and proper orthogonal decomposition (POD). DMD and POD, known for their reliability and explicit statistical methodology, identify coherent patterns within transient flows, prioritising modes with the highest energy content and enabling a concise representation of flow dynamics in a low-dimensional framework (Taira et al. 2017). Building on previous research, this chapter employs the widely-used POD technique in the context of cylinder flows for a detailed evaluation of the wake dynamics downstream of the cylinder, specifically addressing the influence of free-surface effects. The popularity of POD in this field is evident in several prior studies. For instance, Rehimi et al. (2008) investigated the impact of wall confinement and utilised POD for filtering purposes; Sen et al. (2017) studied the two-dimensional laminar flow past a horizontal circular cylinder, emphasising the role of POD in isolating dominant modes; Wang et al. (2014) examined the

near wake of a wall-mounted finite-length square cylinder, with the main focus on the correlation between flow structures and POD coefficients. Furthermore, Mishra and De (2021) focused on vortex shedding suppression through passive flow control techniques and applied POD to evaluate effectiveness and identify predominant vortical structures.

In this chapter, POD is employed to analyse the spatiotemporal coherence of turbulent structures shed in the wake of a horizontal circular cylinder with submergence-to-diameter ratios ranging from 0.5 to 2.1. The spatial patterns of the first two POD modes, which contain the most energy, depict the von Kármán vortices. As Fr increases, the energy content of the first pair of POD modes decreases from 56% at $Fr = 0.26$ to 26.8% at $Fr = 0.53$, which happens because large-scale vortices lose coherence more rapidly in shallower conditions. This energy redistribution leads to smaller flow structures to contain a relatively higher energy when Fr is larger. The frequency of the dominating vortex shedding determined from the spectra of the POD temporal coefficients shows that the first two coefficients feature a dominant peak at the von Kármán vortex-shedding frequency. At $Fr < 0.45$, the reconstructed flow field using the first 20 POD modes agrees well with the instantaneous velocities from LES, whereas free-surface effects on the wake dynamics at increasing Fr requires more POD modes to reconstruct the flow field with reduced error.

Furthermore, the wake structures generated downstream of a circular cylinder at $Fr = 0.45$ obtained from two LESs using LSM and RL to represent the air-water interface are discussed to assess how the flow dynamics change depending on the numerical treatment of the free surface. Spanwise vorticity contours show that the coherence of vortical structures is strongly impacted by the water-surface deformation when this is computed with LSM. The coherence of these turbulent structures in the cylinder wake is analysed using the POD method based on the instantaneous turbulent velocity fluctuations. The POD analysis indicates that the first two spatial modes contain most of the energy, irrespective of the free-surface treatment, which corresponds to von Kármán vortices. These have different spatial coherences depending on the air-water surface representation method, e.g. when using the RL, these two first modes account for about 67.7% of the total energy and are more coherent than in the LSM setup in which they account for 42% of the total energy. The spectra computed from the temporal coefficients of the first two POD modes feature a dominant peak for both cases, while the energy content of the spectra diminishes with increasing frequency for the LSM case. This investigation indicates that adopting an accurate free-surface reconstruction method is essential to correctly account for water-surface deformation and turbulent structures in the flow.

Section 4.3 gives a brief overview of the POD methodology. Section 4.4 provides a detailed description of the flow structures, including their POD spatial modes, temporal coefficients, and energy distribution for all Fr cases (Case i). The discussion also covers the reconstructed velocity field using different numbers of POD modes. In Section 4.5, the results of comparing the effects of the assumptions used to prescribe the water surface, obtained by level set and RL methods, on the instantaneous wake characteristics at $Fr = 0.45$ are discussed

(Case ii). Finally, the main findings of this chapter are presented in Section 4.6.

4.3 Methodology

The POD analysis is performed using the LES data obtained at xz-plane at the centre of the computational domain in the transverse y-direction (Fig. 3.1). POD was initially applied to both streamwise and vertical velocity fluctuations obtained from the wake of the circular cylinder but the results obtained using the vertical velocity fluctuation (w') appeared to be more efficient for characterising the energetically dominant modes (Tang et al. 2015). Therefore, only the latter is used in the present POD analysis. The description of the snapshot POD method is presented in Section 2.6. All of the simulated cases in this chapter were performed using the same computational setup that was described in Section 3.3, with simulations being restarted to generate transverse planes at equal time intervals between successive snapshots for the POD analysis.

In Case ii (Sec. 4.5), the numerical results from the LES were generated using a RL approach to represent an undeformed air-water interface, treated as a shear-free rigid lid, at Fr = 0.45. These results are then compared to those obtained when the water surface deformation is calculated by the LSM and the top of the domain is treated with a slip condition at the same Fr.

4.4 Case i: Analysis of turbulent structures shed in the cylinder's wake using POD

4.4.1 Results and discussion

Details of how the instantaneous wake characteristics vary with increasing submergence ratios are analysed in this section using the POD methodology.

4.4.1.1 Snapshot dependence validation

The sensitivity of POD to the temporal duration of the LES velocity dataset is studied by comparing the energy contribution of the eigenvalues as a function of the number of snapshots. Fig. 4.1(a) shows the energy content of the first 100 modes when using 200, 400, 800 and 900 snapshots, for the case at $Fr = 0.26$, at a fixed time step of 0.006 s between two successive snapshots, which is equivalent to approximately two, four, seven and eight vortex-shedding cycles, respectively. The energy contribution of the four datasets show minor variations in the first six POD modes, while differences become more evident after POD mode 15. The energy variation is small when increasing the sampling time from 800 to 900 snapshots, thus a total of 900 snapshots are adopted in the following analysis.

For this selected number of snapshots, 100 POD modes are originally used. However, sensitivity to the number of POD modes used in the snapshot POD decomposition is examined in Fig. 4.1(b), showing the variation of the energy contribution of the first 10 POD modes when

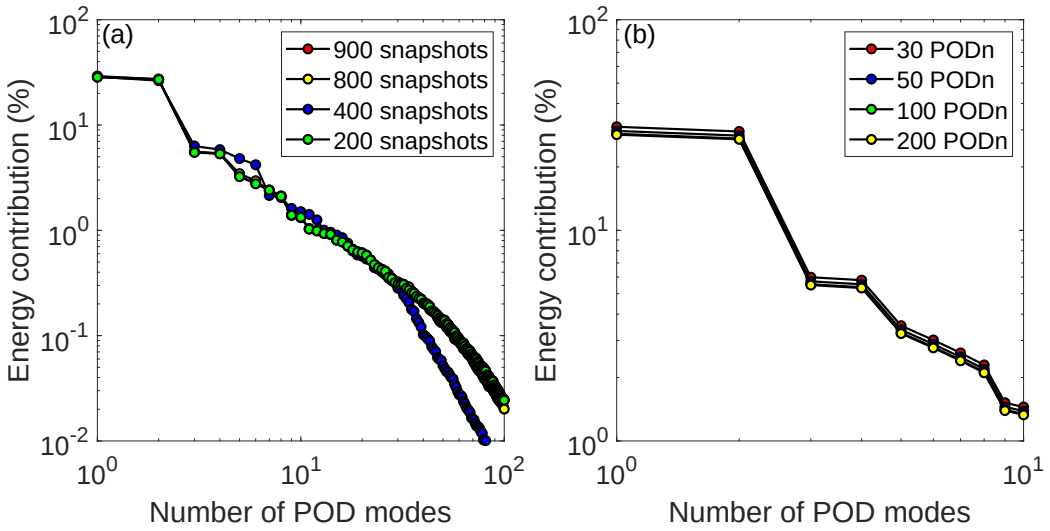

Fig. 4.1 Sensitivity analysis of the energy contribution when adopting (a) different number of snapshots based on 100 POD modes and (b) increasing POD modes with 900 snapshots.

increasing the total number of POD modes from 30 to 200 in the SVD decomposition. Only significant differences in the energy contribution are observed in the first 10 modes, with a slightly larger energy prediction when using 30 POD modes compared to when more modes are used, while almost no significant variations in the relative energy are seen when adopting 100 or 200 POD modes. Hence, 100 POD modes based on 900 snapshots (eight vortex-shedding cycles) are deemed to be adequate to perform the POD analysis for the present study.

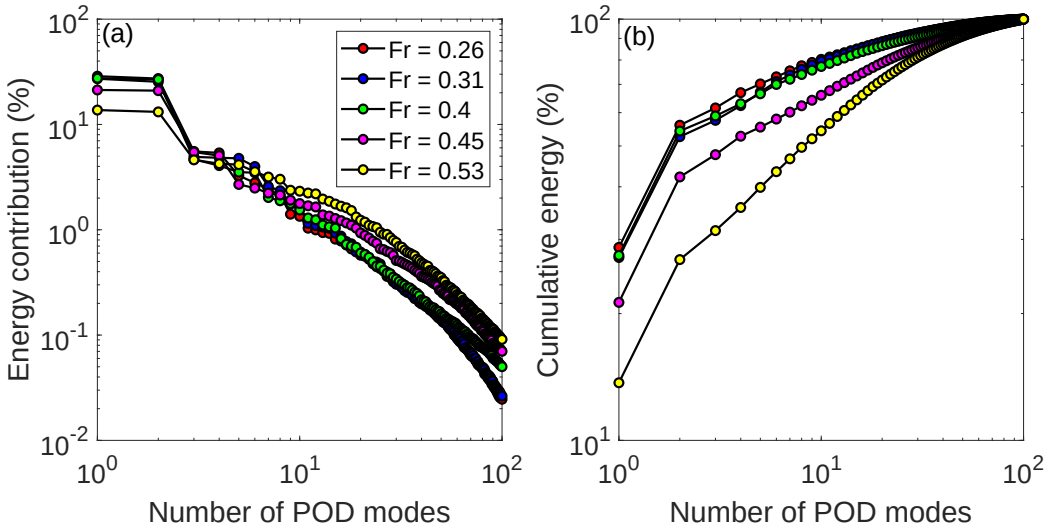

Fig. 4.2 Comparison of the (a) energy contribution and (b) cumulative value for the 100 first POD modes for the different submergence cases.

4.4.1.2 Energy contribution of the POD modes

The relative energy of each POD mode and consequent cumulative energy for the simulations with different Froude numbers is shown in Fig. 4.2. The contribution of POD modes to

the total energy seems to follow a similar distribution among all Fr cases. The first two POD modes have similar relative energy with the largest overall contribution, which happens because they correspond to the energetic large-scale von Kármán vortices shed by the cylinder (as shown in the following section). The energy contained in higher POD modes progressively decreases because they represent the contribution from small-scale turbulent structures (Dipankar et al. 2007, Perrin et al. 2007). As seen in Fig. 4.2 (a), the first two modes account for 56.0%, 52.59%, 54.24% and 42.78% of the total energy for those cases at Fr = 0.26, 0.31, 0.40 and 0.45, respectively, while this notably decreases to 26.8% at Fr = 0.53. This result variation shows that free-surface effects under shallower flow conditions lead to a loss of coherence, or energy, from the dominant von Kármán-like vortices, which directly reduces the energy of the eigenvalues of modes 1 and 2. In all submergence cases, mode 1 has an energy contribution of about 1% larger than mode 2.

Fig. 4.2b compares the cumulative energy for the different Fr cases, which is similar for the deepest conditions at Fr = 0.26, 0.31 and 0.40. Conversely, there are large differences between the shallower conditions at Fr = 0.45 and 0.53, with a noticeable deviation from the other deeper cases as modes 1 and 2 have a lower energy when shallowness increases. Specifically, the first 25 POD modes contain around 80% and 75% of the total energy for the cases at Fr = 0.45 and 0.53, respectively, compared to an average value of 90% found for the deeper cases. This implies that for shallower conditions, more POD modes are required to account for the same amount of energy. This indicates that free-surface effects notably impact the vortex shedding nature behind the cylinder when Fr is larger than 0.4 at the present gap-to-diameter ratio of 0.5 (as shown in Figs. 3.4–3.8).

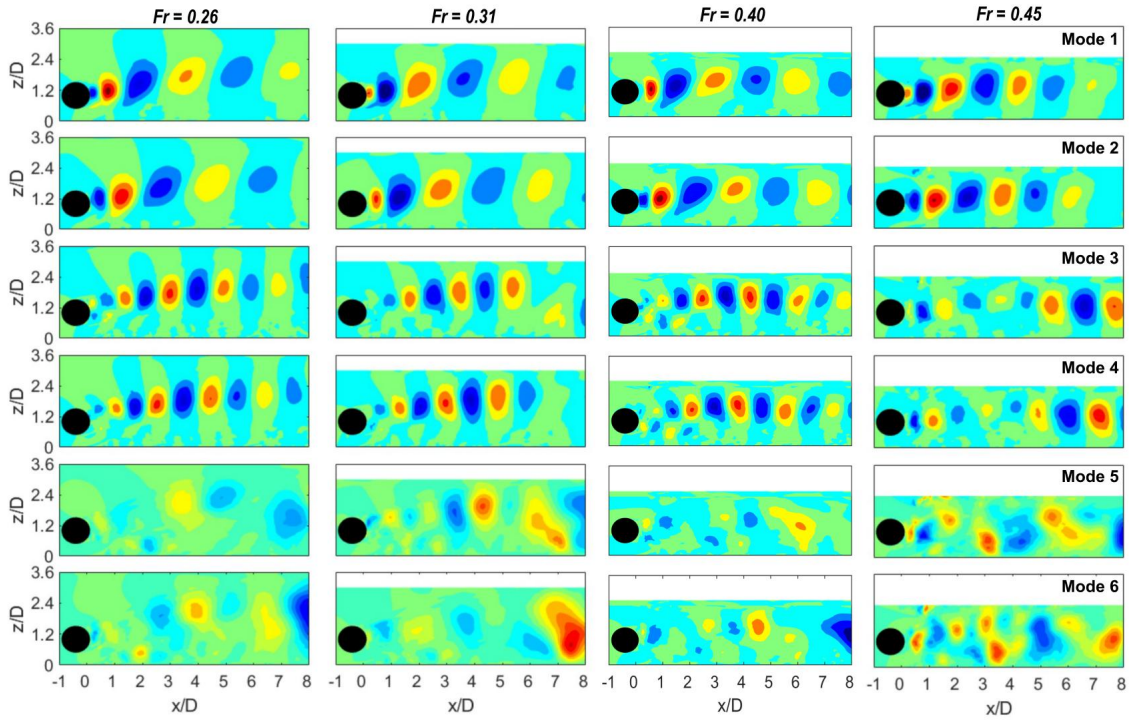

Fig. 4.3 First six POD spatial modes obtained for cases with Fr = 0.26, 0.31, 0.40 and 0.45.

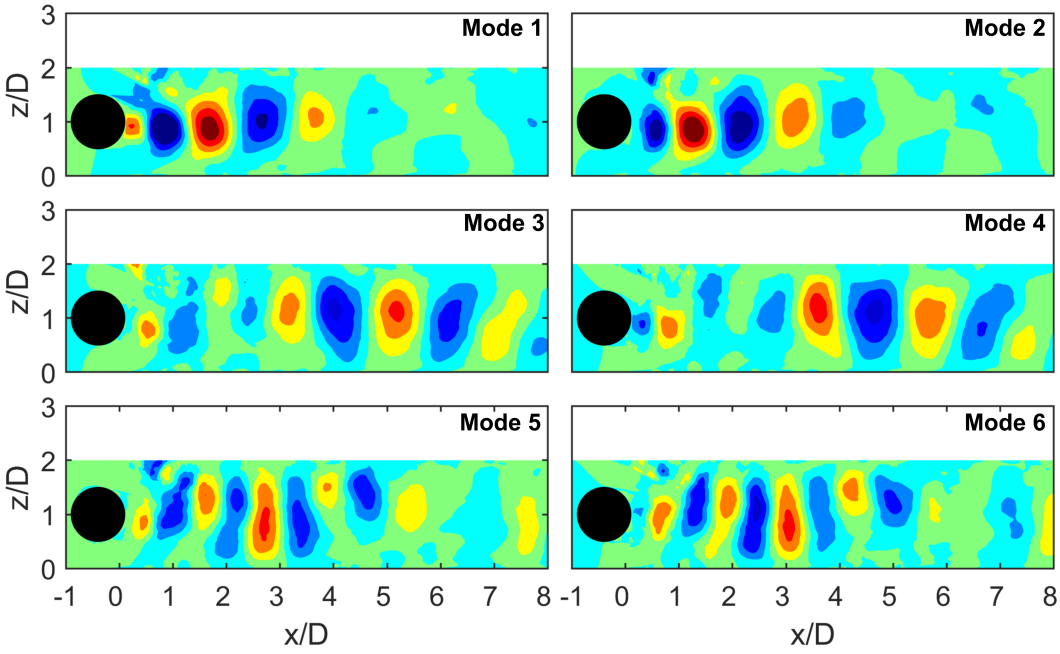

Fig. 4.4 Six POD spatial modes obtained for the shallowest case: $Fr = 0.53$.

4.4.1.3 POD spatial modes

To further quantify the impact of relative submergence on the wake dynamics, the POD spatial modes and corresponding temporal coefficients are analysed. The most energetic POD modes are often paired, i.e. consecutive modes have a similar energy contribution, spatial and temporal modes, only differing by a phase shift (Vitkovicova et al. 2020). This is observed in Figs. 4.3 and 4.4 with the first six POD spatial modes in which modes 1 and 2 are denoted as the pair 1, while pair 2 corresponds to modes 3 and 4, and pair 3 to modes 5 and 6. Irrespective to the submergence level, i.e. Froude number, the coherent regions in the first two modes have similar spatial structures, which capture large-scale flow structures.

For the deeper submergence cases, the observed spatial modes retain a similar distribution to other POD studies for flow behind cylinders (Ribau et al. 2021, Deep et al. 2022), despite the close proximity to the bottom surface affecting the wake dynamics (Ouro et al. 2019). Transitioning to shallower flow conditions impacts the coherence of the most-energetic wake structures, as with increasing Fr the turbulent structures from the first pair of modes decreased in longitudinal and vertical size as there is a limited vertical expansion due to the free-surface proximity.

The second pair of POD modes capture smaller scale flow structures, whose contribution to the overall energy is lower than the first pair (Fig. 4.2). Modes 3 and 4 at $Fr = 0.26$, 0.31 and 0.40 are almost identical, which suggests that the vortex shedding has a negligible impact from the free-surface. Conversely, in the cases at $Fr = 0.45$ and 0.53, this pair of modes losses its spatial coherence with smaller scales in the region closer to the lee-side of the cylinder, while larger structures are observed in the far-wake. The third pair at $Fr = 0.26$, 0.31, 0.40

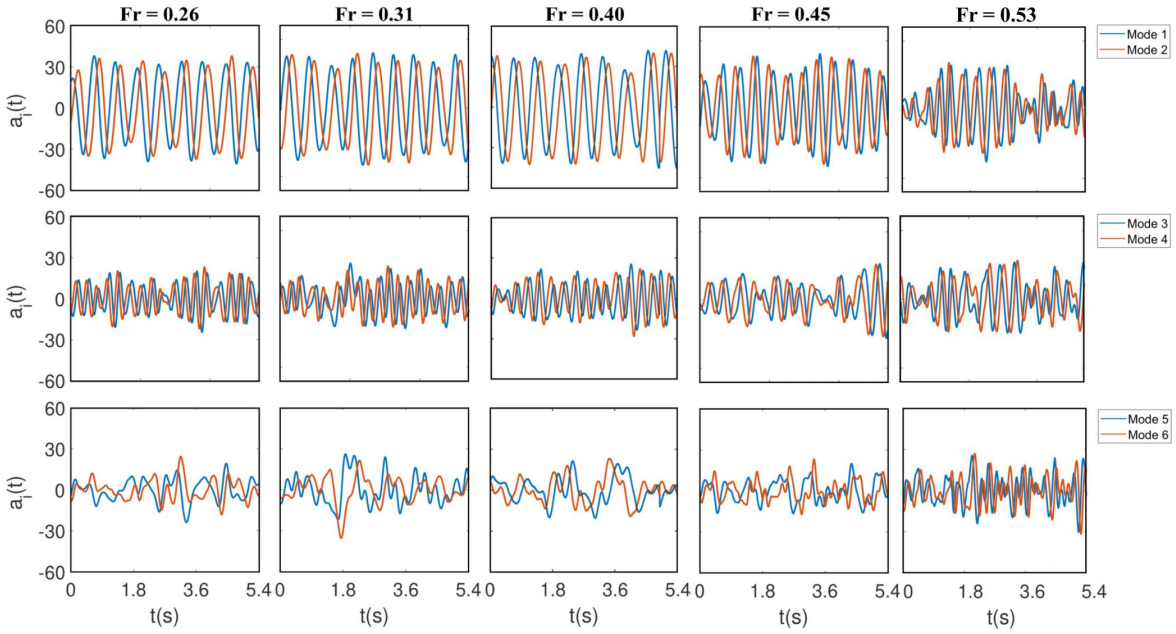

Fig. 4.5 Temporal coefficients of the first six POD modes obtained for the cases with $Fr = 0.26$, 0.31, 0.40, 0.45 and 0.53.

and 0.45 exhibit a less clear spatial distribution capturing a range of flow structures, especially for the deepest flow conditions, which may be attributed to the energy content of these modes. Alternatively, for the $Fr = 0.53$ case, the energy contribution of pairs 1 and 2 is similar, and so are the coherent regions of velocity fluctuations in their POD modes (Fig 4.4). It appears that pair 1 shows coherent structures until a downstream location of $x/D = 4$, after which these vanish, while in pair 2 this pattern is reversed, i.e. coherent regions are seen after $x/D = 4$. The third pair exhibits a rather well-defined distribution when compared to the other cases. These results suggest that the large-scale von Kármán vortices developed in cases with high submergence depths, i.e. at low submergence depth, lose coherence more rapidly due to the free-surface impact.

4.4.1.4 POD temporal coefficients and associated Strouhal number

The temporal coefficients of the six POD modes whose spatial distribution is presented in Figs. 4.3 and 4.4 are now presented in Fig. 4.5 for all submergence cases, which outline the phase difference in the temporal oscillation of the modes within the same modal pair. The temporal coefficients of the first pair exhibit the highest amplitudes when compared to the other two pairs (modes 3 to 6) due to their higher energy contribution and spatial coherence, which can be linked to the large-scale von Kármán vortices. For cases at $Fr = 0.45$ and 0.53, the first pair features a periodic oscillation of the temporal POD coefficients but with an irregular amplitude, especially for the shallowest submergence case. This suggests that the periodic shedding of von Kármán vortices is most impacted by the free-surface for this case. Modes 1 and 2 are out of phase by less than a quarter wavelength for cases with $Fr = 0.26$, 0.31 and 0.40, representing shifted structures in the advection direction by a distance corre-

sponding to their phase difference. However, for higher Fr, modes 1 and 2 exhibit a smaller phase difference and a reversed temporal behaviour when compared to lower Fr, which agrees with their corresponding spatial structures (Fig. 4.3 and 4.4). This again reflects how the free-surface drives the motion of vortical structures downstream of the cylinder.

The second pair of modes also exhibit a sinusoidal shape with a lower, less regular amplitude that is twice the frequency of the first pair at $Fr = 0.26$, 0.31 and 0.40, reflecting harmonics of the von Kármán vortex shedding. Conversely, for higher Froude numbers, the oscillations exhibit a more irregular variation, featuring notable fluctuations in amplitude between high and low values. Irrespective of the submergence level, the temporal coefficients from the third pair of modes show an uneven signal with drastic changes in amplitude, which can be linked to non-periodic flow motions depicted by the uneven spatial correlation of their spatial modes seen in Figs. 4.3 and 4.4. For the shallowest case, the third pair of modes retains some degree of correlation in its frequency to pairs one and two, which is linked to their closer energy content (Fig. 4.2).

Further identification of the relationship between the POD eigenmodes and flow structures is provided with the PSD computed from the first six POD temporal coefficients (Fig. 4.5), which are presented in Fig. 4.6 together with the corresponding Strouhal number for each case. The latter is calculated as $St = f_p D/U_0$, with f_p corresponding to the vortex shedding frequency calculated from the time series of vertical velocities at $x/D = 2.1$, $z/D = 1.5$. The Strouhal numbers associated to cases at $Fr = 0.26$, 0.31, 0.40, 0.45 and 0.53 are 0.29, 0.31, 0.32, 0.41 and 0.48, respectively. The first harmonic at a frequency of twice St is also included in Fig. 4.6. Irrespective of the submergence case, the spectra of the temporal coefficients from the first two modes show a dominant peak that corresponds to the vortex shedding frequency. This indicates that these POD modes represent to the dominant von Kármán vortex shedding. In all cases, the two modes corresponding to the same pair feature an energy peak at a given frequency because they are associated with the same flow structures.

The amplitude of the spectral energy peak at the dominant St frequency reduces for higher POD modes because their energy content is also smaller, with their pattern changing with the submergence level. At $Fr = 0.26$, pair one peaks at St, pair two peaks at $2St$ but pair three does not have a marked peak and its maximum is at a frequency slightly lower than St. Conversely, at $Fr = 0.31$, pair one again peaks at St and pair two at $2St$ but modes 5 and 6 have an increased energy content at lower frequencies, which is almost analogous to the spectral distribution from pair three. The second pair still peaks at $2St$ for $Fr = 0.40$, whereas the third pair has a similar feature of its counterpart at $Fr = 0.26$. When decreasing the submergence depth at $Fr = 0.45$, pairs two and three have a reversed PSD distribution when compared with that at lower Fr cases due to the close energy content of modes in these pairs, as shown in Fig. 4.2. Finally, for the lowest submergence at $Fr = 0.53$, pairs one and two peaks at St, while pair three does at $2St$ but without a defined band of the frequencies.

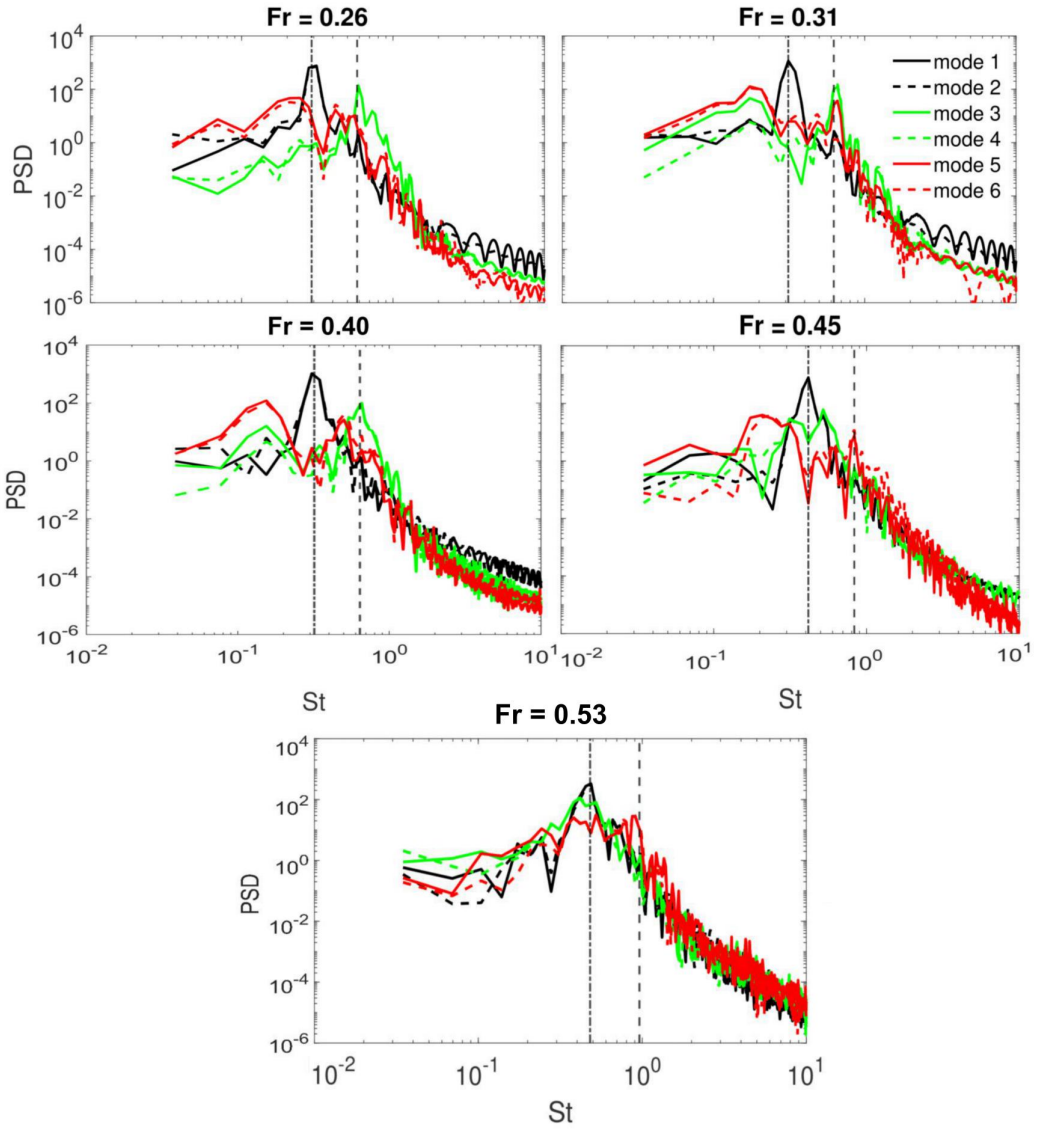

Fig. 4.6 PSD of the temporal coefficients from the first six POD modes obtained for the cases with Fr = 0.26, 0.31, 0.40, 0.45 and 0.53. The dotted-dashed line indicates the Strouhal number (St) frequency associated to the periodic vortex shedding and the dashed line indicates its first harmonic $(2St)$.

4.4.1.5 Lissajous curves

The link between POD modes is provided in Fig. 4.7 with the correlation between the temporal coefficient from the first mode (a_1) with those from modes two to six (a_i), with the exception of the case at Fr = 0.40 (not shown hereafter for brevity). These Lissajous plots depict the phase difference between modes. The first two modes clearly show that the correlation trajectory of a_1–a_2 has a circular shape, which indicates that these modes have a close amplitude and frequency. Such almost linear correlation between coefficients a_1–a_2 allows to fit a representative circle, e.g. using the least squares method, which is depicted by a solid line in Fig. 4.7.

The linear correlation between the first two modes has the lowest errors for cases at Fr = 0.26 and 0.31 when the shedding of vortical structures is more coherent in space at time.

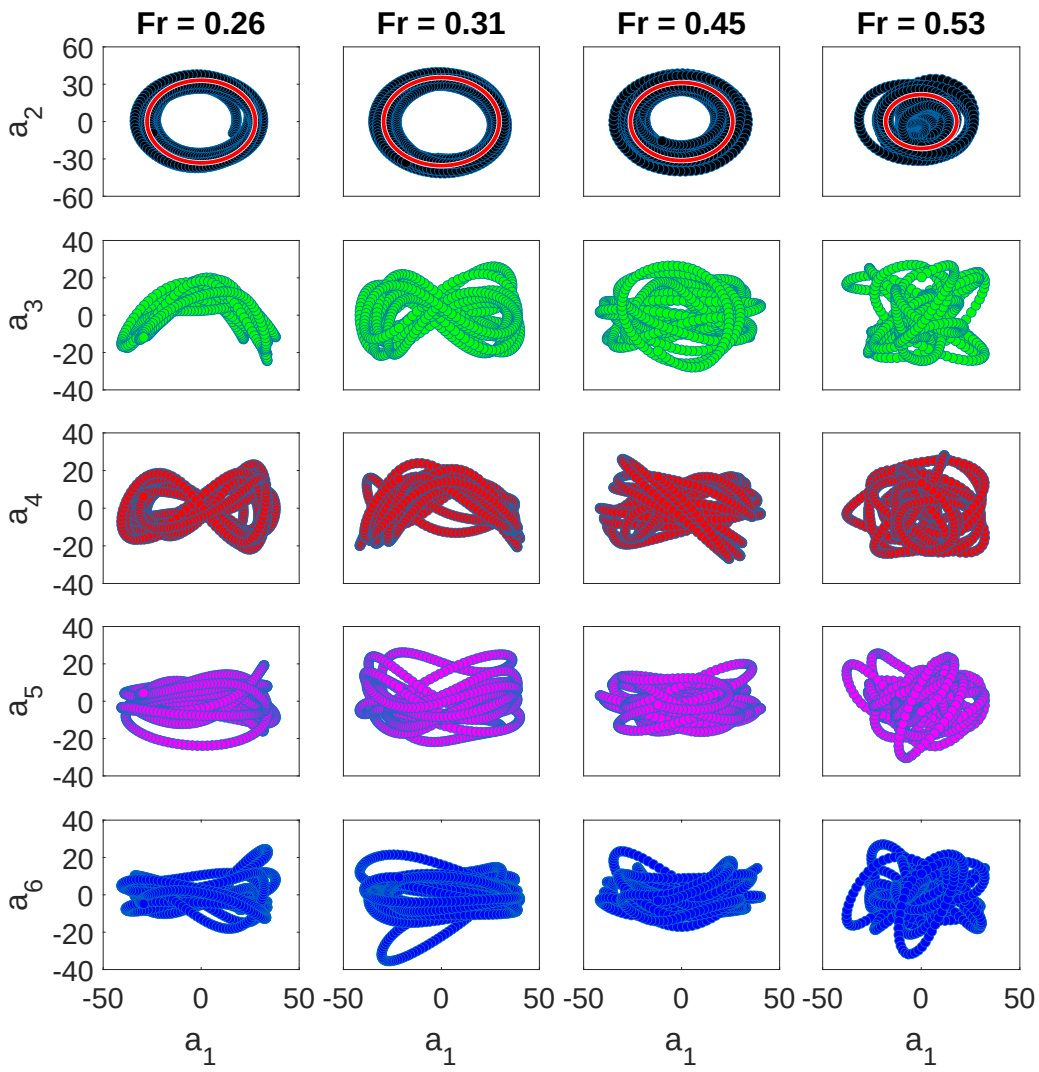

Fig. 4.7 The Lissajous plots of the first six POD coefficients for cases with $Fr = 0.26$, 0.31, 0.45 and 0.53. The linear fit with a circular curve is shown in the first row.

As submergence decreases at $Fr = 0.45$, the a_1-a_2 data points become more scattered and deviated from the fitting circle. For the smallest submergence case, the data exhibit a substantial error from the solid circle as the vortex shedding dynamics are highly altered due to the very shallow flow conditions, which would make the flow field reconstruction difficult if only the first two POD modes were used. The scatter plots of a_1–a_4 at $Fr = 0.26$ and a_1–a_3 at $Fr = 0.31$ (Fig. 4.7) indicate that modes 3 and 4 have half the amplitude and twice the dominant frequency compared to mode 1, paralleling the findings of (Yang et al. 2020). The other trajectories do not exhibit a clear temporal correlation with a dominant frequency. These results can be seen in Fig. 4.6, in which low-energy modes comprise different peaks with lower magnitudes, potentially leading to frequency modulations as suggested by (Papaioannou et al. 2006, Zhang and Zheng 2018).

4.4.1.6 Velocity field reconstruction

A ROM based on the POD spatial modes and temporal coefficients can be built to represent the velocity field in a cost-effective way (Tang et al. 2015, Xia et al. 2018). Given that the ROM accuracy depends on the number of POD modes adopted, the normalised instantaneous velocity (w) and its fluctuation component (w') obtained from the LES (deemed as the true solution) at a given time step and that predicted from the ROM (Eq. 2.39) are shown in Figs. 4.8 and 4.9, adopting the first 2, 10, 20 and 100 POD modes for four submergence cases. The associated absolute error from the ROM-predicted velocity fluctuation compared to the LES value (error = $W_{LES} - W_{ROM}$) is also included.

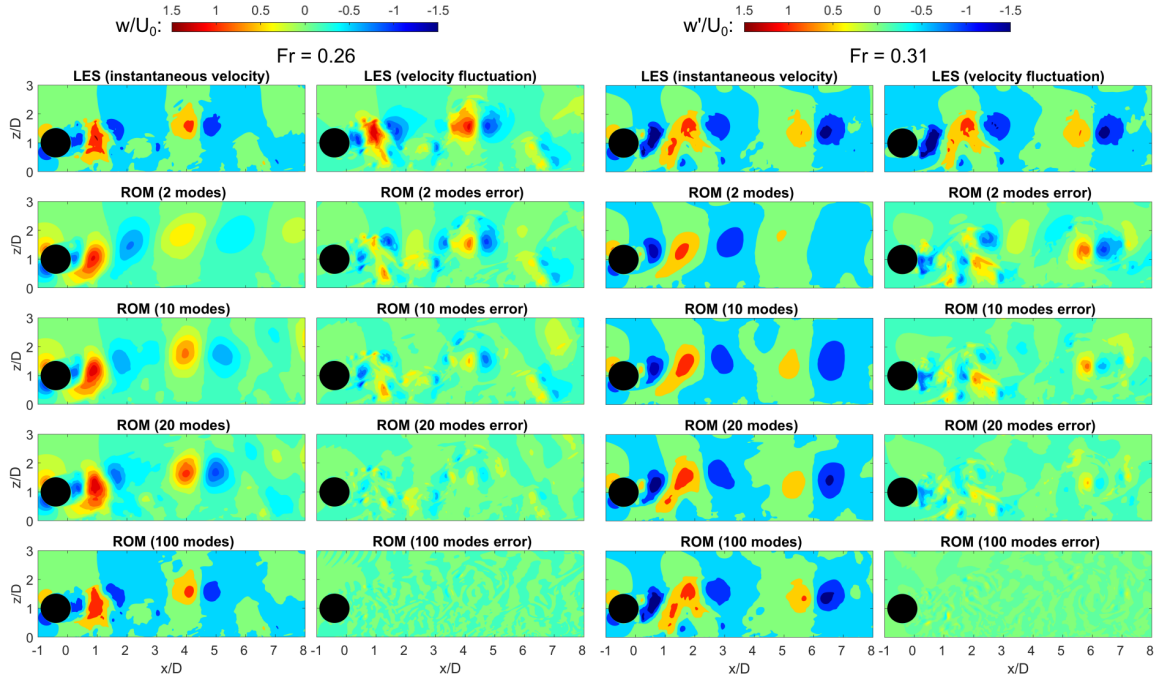

Fig. 4.8 Comparison between the LES (first row of figures) velocity data with those reconstructed with the ROM based on an increasing number of POD modes for $Fr = 0.26$ (left-hand) and 0.31 (right-hand).

The ROM based on the first two modes accounts for the two most energetic modes associated with the von Kármán vortices, which represent a total energy content in the range of 42%-56% for cases with $Fr < 0.53$, and about 27% for the shallowest submergence case (Fig. 4.2). Figs. 4.8 and 4.9 show that adopting two POD modes in the ROM leads to large errors, especially at $Fr = 0.53$, in which the first pair of POD modes provide the lowest energy contribution. Increasing the number of POD modes in the ROM allows to account for flow structures that are less energetic but whose overall energy contribution is not negligible (Fig. 4.2a). When using 20 modes for the ROM, the reconstructed velocity field is close to the LES field for cases with $Fr < 0.45$ because these account for almost 90% of the total cumulative energy contribution (Fig. 4.2b) and less than 80% and 70% for $Fr = 0.45$ and 0.53, respectively. Consequently, the latter cases exhibit larger errors from the 20-mode-based ROM. Adopting 100

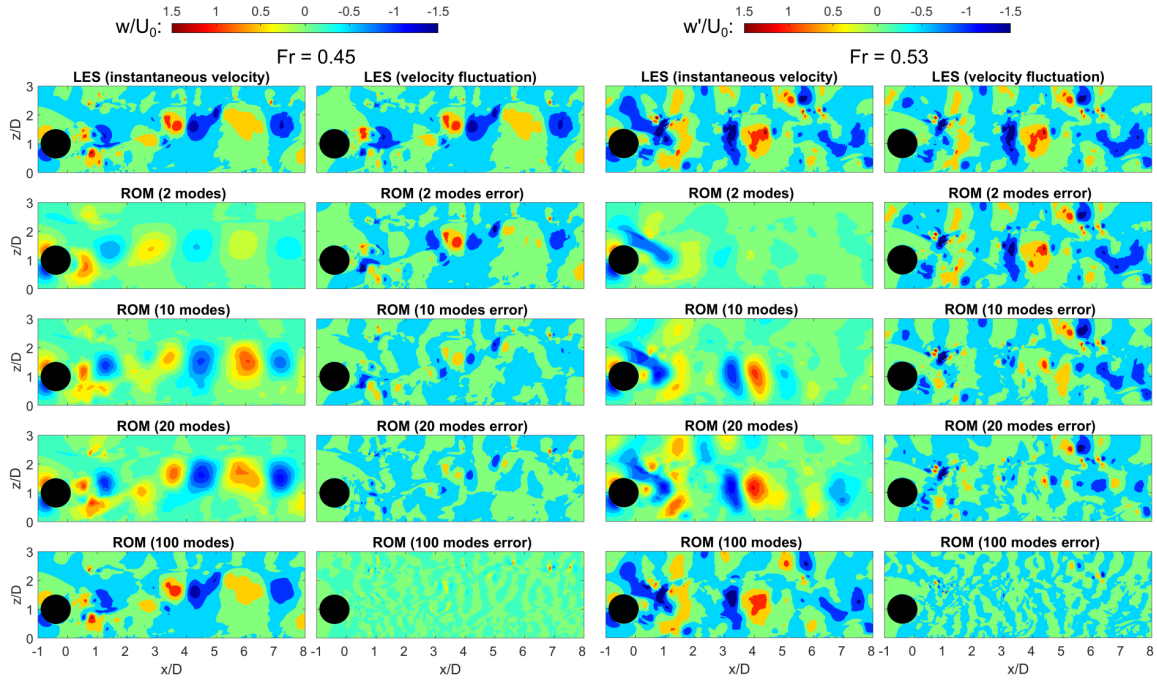

Fig. 4.9 Comparison between the LES (first row of figures) velocity data with those reconstructed with the ROM based on an increasing number of POD modes for $Fr = 0.45$ (left-hand) and 0.53 (right-hand).

modes provides an increased accuracy from the ROM capturing flow structures, both in the near- and far-wakes, leading to a 1% error at $Fr < 0.45$, while a spatially average error of 2% is found for cases at $Fr = 0.45$ and 0.53. This deviation from the ROM accuracy suggests that the impact of the free-surface on the cylinder's wake dynamics can be quantified in the POD analysis by the number of modes that would contribute to, at least, 90% of the energy content. For instance, in the present cases, the reconstruction of the velocity field at $Fr = 0.26$ requires around 20 modes for a cumulative 90% of the total turbulent kinetic energy; while to capture the same amount of energy at $Fr = 0.53$, about 50 POD modes are required. Overall, a ROM based on 100 POD modes provides an excellent agreement with the LES for all cases.

To evaluate the ability of the ROM in reproducing instantaneous velocities over time, Fig. 4.10 shows the instantaneous vertical velocity (w) time series at $x/D = 3.5$, $z/D = 1.2$, i.e. in the upper shear layer of the cylinder in which von Kármán vortices pass through when shed (Ouro et al. 2019), from the LES and those reconstructed using the ROMs with increasing number of POD modes for four submergence levels. Overall, convergence of the ROM predictions is observed when increasing the number of POD modes, requiring almost 100 modes in all submergence cases to capture the low- and high-frequency oscillations of the velocity. Adopting less than 10 modes in the ROM captures the low-frequency oscillations but without an appropriate amplitude, indicating that the contribution from higher POD modes is still required to effectively capture the flow dynamics.

The sensitivity of the ROM to the number of POD modes adopted is presented in Fig. 4.11 with the root-mean-square (rms) error of the reconstructed vertical velocity field at a sin-

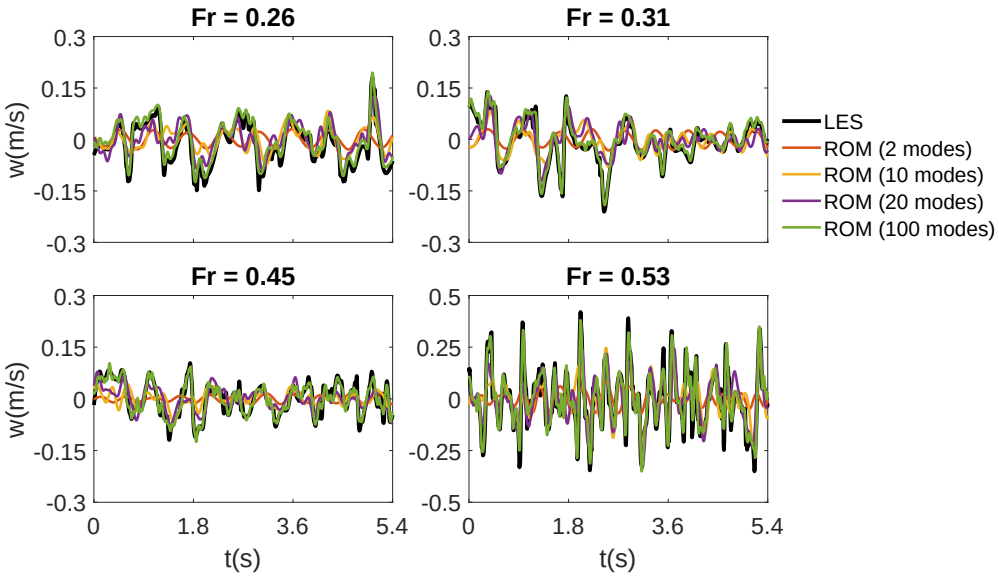

Fig. 4.10 A comparison between the instantaneous velocity obtained from the LES and the ROMs over the time history adopted for the POD analysis for the different Froude numbers.

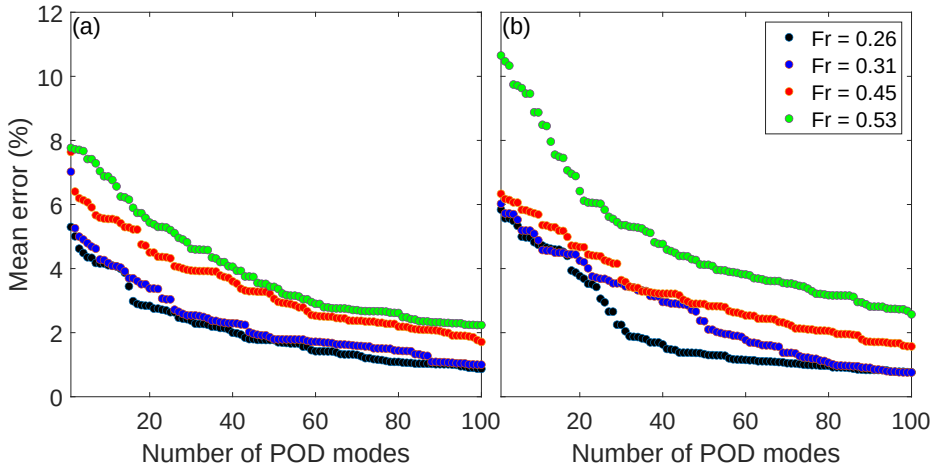

Fig. 4.11 The mean error plot of the reconstructed velocity (a) over a vertical plane at a single snapshot and (b) at $x/D = 3.5$, $z/D = 1.2$ for all snapshots as a function of the number of POD modes.

gle time step over the xz-plane (Figs. 4.8 and 4.9) or at a point over time (Fig. 4.10). The results shown in Fig. 4.11a indicate that at $Fr \leq 0.45$ an appropriate velocity reconstruction can be obtained adopting a small number of POD modes, while a large number of POD modes is required for shallower cases to achieve lower ROM errors. Thus, the wake dynamics at higher Fr are driven by a wider range of flow structures needed to be included in the flow reconstruction. Fig. 4.11b shows the rms of the velocity time series reconstruction at the selected point. For the shallowest case at $Fr = 0.53$, the minimum reconstruction error obtained with 100 POD modes is over 2.5%, while this error value can be attained with approximately 60, 50 and 27 POD modes at $Fr = 0.45$, 0.31 and 0.26, respectively. Note that this point is close to the free-surface in the shallowest submergence (Fig. 3.8) and thus its impact challenges the ability of the ROM to fully capture the instantaneous velocity field. Nevertheless, an error of

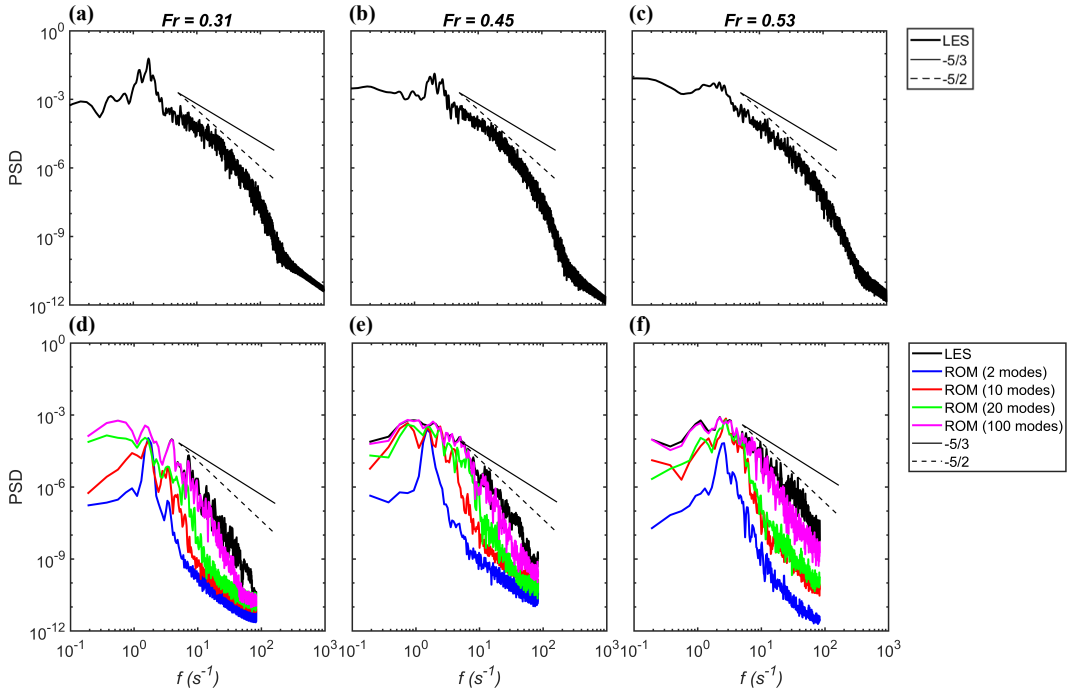

Fig. 4.12 PSD of the vertical velocity fluctuation (w') obtained at a point (x/D = 1.1 and z/D = 1.5) from LES long time series (a–c) and truncated time series from LES and POD-based ROM at Fr = 0.31, 0.45, and 0.53.

1% allows for a very precise reconstruction solution, while an error of less than 3% can be deemed adequate for a low-dimensional ROM (Kuzmina et al. 2021).

4.4.1.7 Analysis of the spectral energy decay

Fig. 4.12 presents an analysis of the PSD computed from vertical velocity fluctuations at a point located at x/D = 1.1 and z/D = 1.5, which is in the cylinder's wake and close to the free-surface, for Fr of 0.31, 0.45 and 0.53. The first set of PSD plots (a–c) is obtained from 48 vortex-shedding cycles computed from the full LES, whereas the second sub-set (d–f) is obtained over a shorter time series of eight vortex-shedding cycles used to construct the ROM based on the first 2, 10, 20 and 100 modes. The spectral analysis in Fig. 4.12a-c exhibits a clear energetic region in the production range corresponding to the energetic eddies emanating periodically from the cylinder over a frequency band close to the shedding frequency. This is most prominent at Fr = 0.31, while less pronounced peaks are observed at higher Fr, suggesting more irregular vortex-shedding patterns (see Figs. 3.5-3.8). At high submergence rates, the inertial sub-range follows the classical $-5/3$ Kolmogorov's slope over a frequency decade up to approximately 20 Hz, after which the decay rate increases with a steeper decay law of $-5/2$. This acceleration in energy decay can be due to excessive dissipation resulting from the distorted free-surface and cylinder proximity to the bottom wall (Stoesser et al. 2010) or even turbulence anisotropy (Rubinstein and Clark 2017). Similar findings have been provided by Zhao et al. (2021) for flow past a cylinder close to a free-surface. At Fr = 0.53, this $-5/2$ slope provides a closer fit to the energy decay over most of the inertial sub-range

and the production range has less energy near the shedding frequency than at $Fr = 0.31$ or 0.45 because the vortices shed have less coherence due to free-surface effects (Fig. 3.8).

Fig. 4.12d–f presents the PSD associated with the truncated time series obtained from the full LES and reconstructed POD modes. As the number of modes increases, the associate energy of the PSD increases, with the ROM using 100 modes collapsing with the LES spectrum over the production range up to a frequency of 20 Hz, when the energy decay starts to accelerate in the full LES (Fig. 4.12a–c). The truncated time series provides valuable insights into the relationship between the increased amplitude in the PSD and the number of POD modes to be adopted for flow field reconstruction, which will be used as a criterion to decide how many modes in a ROM shall be adopted.

4.5 Case ii: Impact of RL and LSM on wake characteristics

This section examines the impact of RL and LSM approaches when employed to represent the air-water interface on the instantaneous wake characteristics using the POD methodology at $Fr = 0.45$. The choice of this Froude number is based on the findings in the previous chapter, where the deformation of the free surface and its effects on the wake dynamics downstream of the cylinder became more pronounced at $Fr > 0.31$.

4.5.1 Results and discussion

4.5.1.1 Instantaneous flow field

The instantaneous flow generated behind a horizontal cylinder from LES using the RL and LSM at four instants in time covering one vortex-shedding cycle is presented in Fig. 4.13, with contours of normalised spanwise vorticity. From the LSM simulations, it is observed that the free surface drops until approximately one diameter downstream of the cylinder, which changes the vertical direction of the vortices. The resolution of the free-surface with the LSM allows to capture the hydraulic jump at approximately $x/D = 0.8$, which is in-phase with the vortex-shedding sequence of the cylinder.

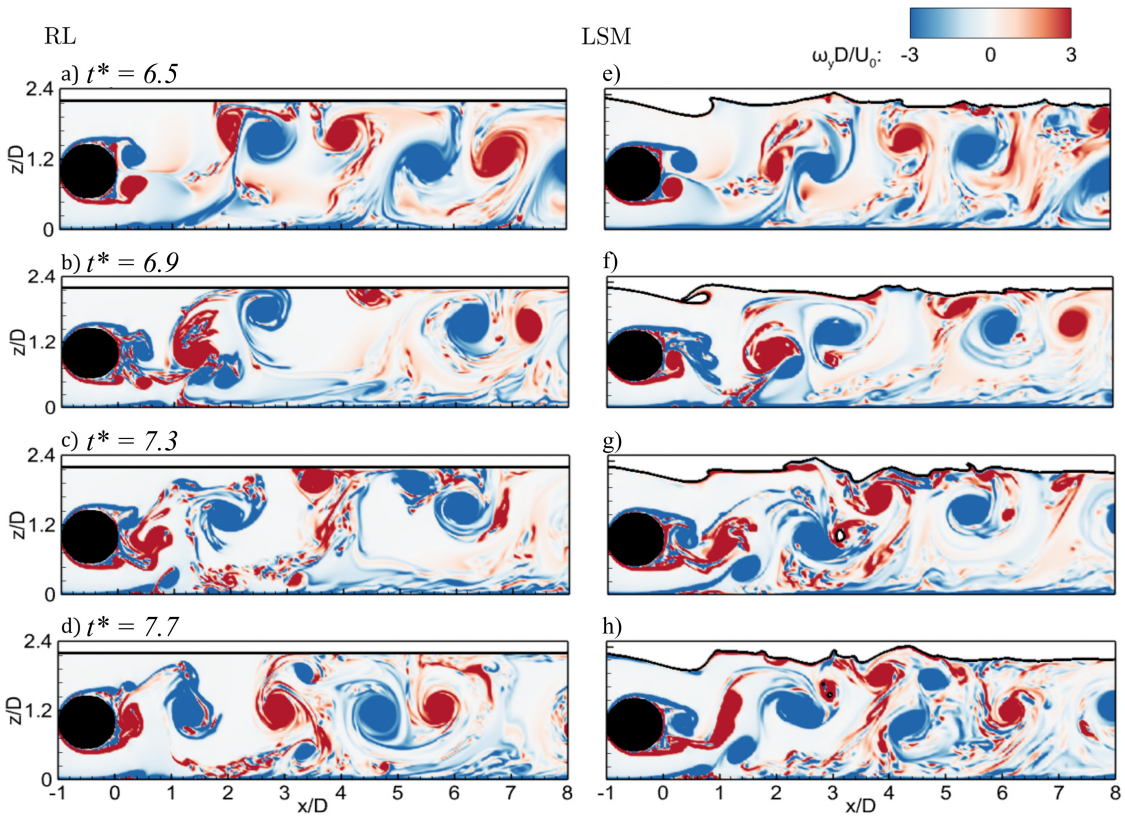

Fig. 4.13 Contours of normalised vorticity behind the cylinder for the case: $Fr = 0.45$, at four instants normalised by the peak frequency $t^* = 6.5$, 6.9, 7.3 and 7.7. (a-d) RL and (e-h) LSM. The free surface is depicted as a solid-black line.

The shear layer developed in the upper side of the cylinder is deflected downwards due to this free-surface effect, while this is not observed in the RL setup (Fig. 4.13a). The proximity of the cylinder to the bottom wall boundary leads to the generation of a high-velocity region underneath it that enables the generation and shedding of a ground vortex, which appears irrespective to the free-surface treatment (Ouro et al. 2019). Fig. 4.13c shows how the shear layer from the bottom surface detaches and interacts with the vortical structures that develop over the bottom shear layer of the cylinder.

In the LES with LSM, the vortical structures shed by the cylinder deform the free-surface layer when they interact with it, which leads to a faster loss of coherence of the von Kármán vortices while increasing the small-scale turbulence near the air-water interface. Conversely, when using the RL approach, the lack of free-surface deformation allows the von Kármán vortices to remain more coherent, e.g. in Fig. 4.13d at a distance of $x/D = 4$–5 the vortex pair is well defined for the RL case, while most of its coherence is lost in the LSM case (Fig. 4.13h). Thus, adopting the RL approach can lead to an underestimation of the vertical wake mixing, which impacts the coherence of the von Kármán vortices. In the following, POD is adopted to reveal how these instantaneous wake characteristics vary between RL and LSM results.

4.5.1.2 Energy distribution of the POD modes

Fig. 4.14 shows the percentual total energy contribution and cumulative value by each POD mode for both RL and LSM cases. Modes one and two have a close magnitude and contribute with most of the total energy with 67.7% and 42.8% in the RL and LSM cases, respectively. This deviation in the energy content estimated from the different methods (Fig. 4.14a) indicates that the RL approach provides the first pair of modes of higher energy, while the interaction of the wake with the free-surface effects resolved with the LSM leads to a reduction in the shedding coherence of the resulting von Kármán vortices. Conversely, the second pair of modes (modes three and four) has a higher associated energy when LSM is used, namely 10.4%, compared to 6.4% when the RL is adopted. Fig. 4.14a shows that the eigenvalues of the remaining POD modes remain constantly higher for the LSM case thanks to the higher vertical mixing (Fig. 4.13), and so small-scale structures are more present in the wake dynamics.

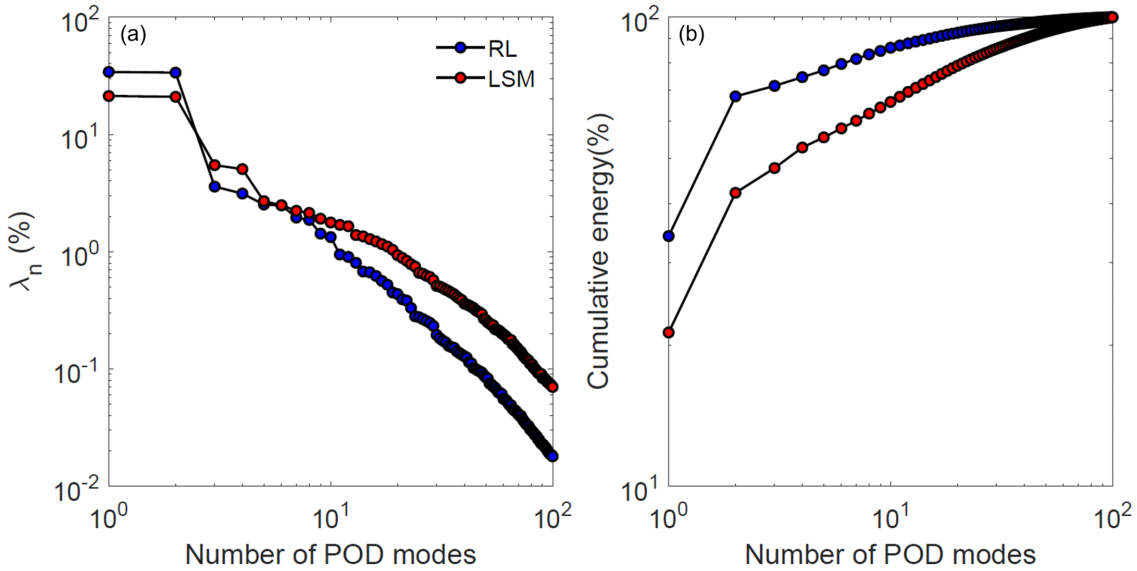

Fig. 4.14 Comparison of the energy contribution (a) and its cumulative value (b) for the first 100 POD modes.

Fig. 4.14b presents a comparison of the cumulative energy for both cases. Due to the uneven energy distribution, especially for the first pair of modes, up to 40 modes are required to yield 90% of the total energy in the LSM case, while only 15 modes are required to attain this cumulated energy threshold with the RL approach. This shows that with LSM, a larger number of modes are required to capture the same amount of energy, and in turn requiring more modes to build an effective reduced-order model based on few number of POD modes (Deep et al. 2022).

4.5.1.3 POD spatial modes

The first eight spatial POD modes that contain the most energetic coherent structures are shown in Fig. 4.15. Each odd POD mode is often paired with the consecutive even mode of comparable energy content (Fig. 4.14a) and similar spatial structures. As can be seen in Fig. 4.15, the first pair of modes, modes one and two, for both RL and LSM cases are paired due to their similar spatial structure and energy contribution. The first pair reveals that the most energetic coherent wake structures for the RL case have a streamwise length equivalent to the cylinder's diameter, while this is reduced when adopting the LSM as the coherent regions get shorter. In both cases, these correspond to the alternating von Kármán vortex shedding.

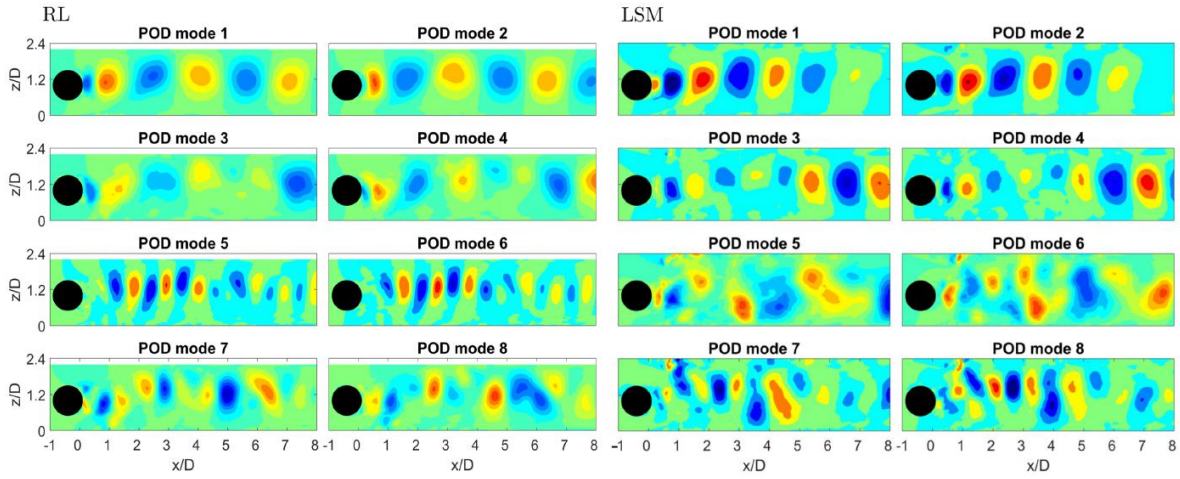

Fig. 4.15 First eight POD spatial modes obtained for the RL (left-hand) and LSM (right-hand) cases.

The vortical structures in the second pair are less energetic than the first pair, containing smaller scale structures. The coherent regions in this pair are notably different, depending on the free-surface approach adopted. With the explicit computation of the free-surface with the LSM, the distribution of coherent regions resembles that from the first pair but with shorter length scale. Conversely, in the RL case, these modes are less coherent thanks to their smaller energy content compared with the LSM results. Even though the energy contribution of the third pair (modes five and six) for both cases has similar levels (Fig. 4.14a), distinctive patterns of the spatial modes are observed, which indicates that these pairs are associated with different flow features. Alternating small-scale vortical structures are present in the RL case, while less coherent vortical structures for the LSM case are seen. It is also noted that as the mode number increases, the distance between the adjacent vortices decreases. The fourth pair exhibits unstructured spatial modes, as is the case of higher POD modes.

4.5.1.4 POD temporal coefficients

Fig. 4.16 presents the time variation of the POD temporal coefficients corresponding to each of the eight modes shown in Fig. 4.15. The temporal coefficients for the first two modes vary with a sinusoidal motion and resemble the natural von Kármán vortex shedding. In compar-

ison to the RL case results, smaller magnitudes and higher frequencies are attained for the LSM, which reflects the weakened strength of the von Kármán vortices when adopting the latter method for the free-surface treatment. Moreover, the temporal coefficients of the first pair exhibit a higher magnitude than the other three pairs due to their higher energy contribution and coherence, which explains why the first two modes represent the large-scale von Kármán vortices. Modes one and two are out of phase by $\pi/2$ rad in their temporal correlation, which agrees well with their slight deviation in the spatial modes (Fig. 4.15).

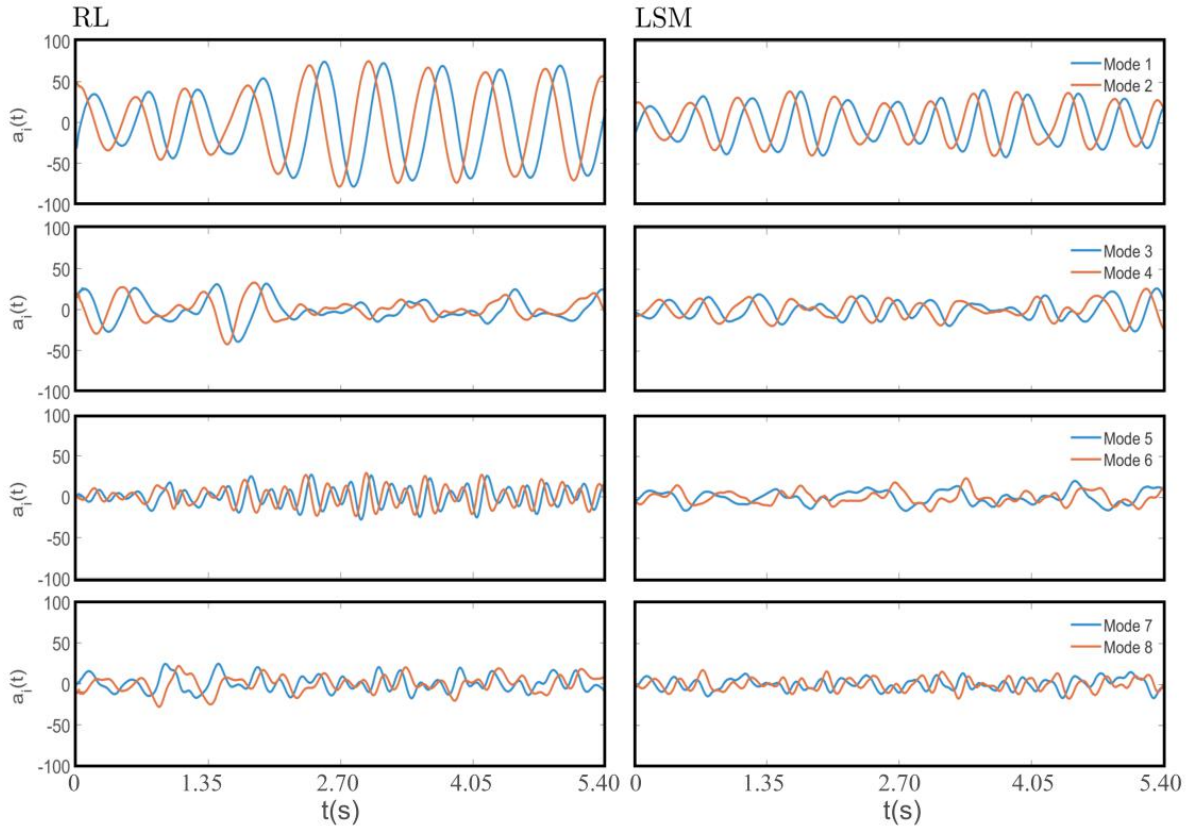

Fig. 4.16 Variation of the temporal coefficients of the first eight POD spatial modes for both RL (left-hand) and LSM (right-hand) cases.

The POD coefficients for modes three and four do not fluctuate in a uniform manner due to the more irregular nature of the vortical structures represented by this pair, as shown in the POD spatial modes in Fig. 4.15. When comparing modes five and six, large differences between both methods are observed. For the RL case, the frequency of the temporal variation is twice that of the first pair, reflecting harmonics of the von Kármán vortex shedding, whereas the sine behaviour for the LSM exhibits an irregular variation and no such harmonics are observed. The temporal coefficients of modes seven and eight for both cases attain an irregular variation representing energetic but less coherent structures.

4.5.1.5 Frequency features of temporal coefficients

A comparison of the PSD distributions corresponding to the POD coefficients of the first two modes for both cases is presented in Fig. 4.17, which can be used to further identify the relationship between the POD eigenmodes and flow structures. The black-dotted lines correspond to the reference Strouhal numbers of $St = 0.32$ and 0.42 obtained in the RL and LSM cases, respectively, which were calculated using the peak shedding frequency obtained from the cylinder's vertical force time series. Linking the St obtained from the POD temporal coefficients and vertical force allows us to identify that the POD mode corresponds to the dominant von Kármán vortex shedding. The spectra of the first two coefficients show a dominant peak, which corresponds to the von Kármán vortex street. The amplitude of the spectra decreases with increasing frequency for the LSM, as shown in Fig. 4.17. This could be related to the fact that the numerical free-surface treatment impacts the width of the wake, e.g. when using a RL the wake width increases, which lowers the frequency. This feature is consistent with previous results in that the shedding frequency reduces as the width of the wake increases (Roshko 1954, Xia et al. 2018).

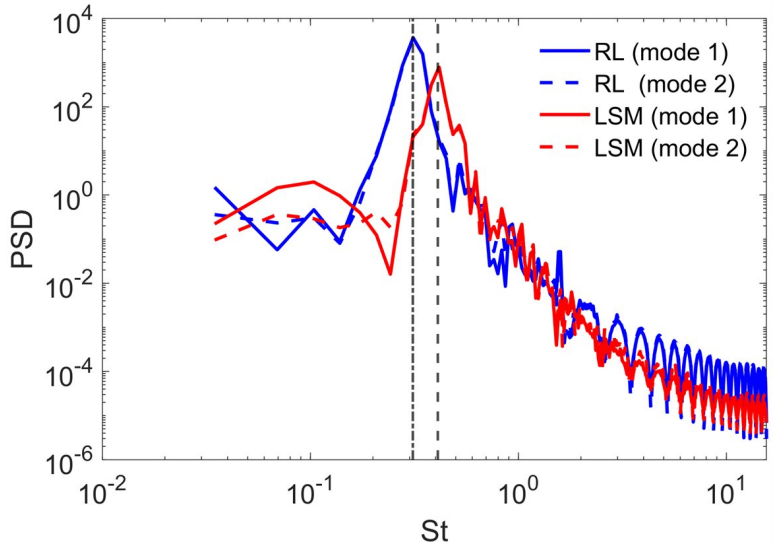

Fig. 4.17 PSD of the first two POD coefficients obtained from the RL and LSM cases. The vertical lines indicate the Strouhal number associated with the periodic vortex shedding, namely $St = 0.32$ (dotted-dashed line) and 0.42 (dashed line) corresponding to the RL and LSM cases, respectively.

4.6 Closure

In this chapter, a POD quantification of the effect of the free surface proximity to the cylinder on wake dynamics is conducted, and the significance of free-surface effects on the hydrodynamics of the cylinder's wake is assessed using two free-surface representation approaches, namely the RL and the LSM. Five different submergence cases with Froude numbers in the range of 0.26–0.53 were considered for a constant cylinder Reynolds number of 13,333 and a bottom gap ratio of 0.5. However, when investigating the effect of the free surface compu-

tation using the level set and RL methods, only the results for a Froude number equal to 0.45 were considered.

In all cases, POD modes were paired because the two consecutive odd-even modes had a similar energy contribution, and POD spatial mode and temporal coefficient patterns. The first two modes contributed with more than 42% of the total energy for cases with $Fr \leq 0.45$, while at $Fr = 0.53$ these eigenvalues reduced their contribution to almost half due to the influence of the free-surface proximity on the coherent structures. The distribution of POD spatial modes revealed that the first two modes feature the same spatial structure, corresponding to large flow structures, irrespective of the Froude number. However, their coherence was altered when transitioning to shallower flow conditions, which led to a loss in coherence of the vortices. The POD temporal coefficients for these first two modes exhibited higher amplitudes when compared to higher POD modes as a result of their larger energy contribution, although the amplitude of the former became more irregular with increasing Fr. This indicates that the free-surface proximity directly impacts the periodic shedding of von Kármán vortices.

The spectra of the POD temporal coefficients of the first pair of modes featured peaks at frequencies corresponding to the dominant structures represented by the Strouhal number, namely at 0.29, 0.31, 0.32, 0.41 and 0.48 for cases with $Fr = 0.26$, 0.31, 0.40, 0.45 and 0.53, respectively. This reveals that the frequency of the flow structures represented by these modes agreed with the von Kármán vortices shed by the cylinder. The correlation between the temporal coefficient of mode 1 against modes 2 to 6 showed that only the first two modes had a linear correlation. As the Froude number increased, this correlation became more scattered, which can be linked to the free-surface effects on the vortex shedding. The velocity fluctuation reconstructed by a ROM using the first 20 POD modes was deemed enough to obtain similar vortical structures to those observed from the original LESs. For the cases at $Fr \geq 0.45$, the ROM based on the first 20 modes still exhibited a relatively large error and required a larger number of modes to take the small-scale structures that improved accuracy into account. Utilising POD modes within the ROM can significantly streamline computational fluid dynamics, particularly in low Froude number scenarios. This approach reduces model complexity and run time, enhancing simulation efficiency whilst maintaining accuracy. In further research, customising the ROM for specific applications and integrating it with advanced technologies such as machine learning could greatly improve its adaptability and efficiency. This positions POD modes in the ROM as a practical tool for real-time analysis and data processing across diverse scientific and industrial fields.

The spectra of the vertical velocity fluctuations from a point in the cylinder's wake exhibited a clear production range with an inertial sub-range following Kolmogorov's -5/3 slope at low Froude numbers, while a steeper -5/2 decay scale was observed for shallower conditions. The spectra from the reduced-order models showed that 100 POD modes effectively reproduce the LES spectrum up to a frequency of 20 Hz, while adopting less modes only captures the energy at the peak shedding frequency.

The presented results in this chapter quantified the impact of the free-surface proximity on horizontal cylinder wake dynamics, especially in the coherence of the turbulent structures identified through an extensive POD analysis compared to LES data. It was found that adopting the RL approach at $Fr = 0.45$ limited the accuracy of simulations in representing the underlying turbulent mechanisms. This highlights the complexity of modelling shallow turbulent flows, which requires advanced simulation techniques to account for free-surface deformations.

CHAPTER 5

Flow Hydrodynamics around In-stream Leaky Barriers and Potential Sediment Mobilisation

5.1 Aims of this chapter

This chapter aims to enhance the understanding of flow dynamics around various designs of leaky barriers using large eddy simulations. Its primary objective is to investigate the influence of barrier configuration on various aspects, including flow features, turbulent characteristics, sediment mobilisation and the structural loads imposed on the cylinders.

The findings of this chapter aim to broaden the application of in-stream leaky barriers, providing valuable knowledge on cylinder design and barrier-induced sediment movement to inform natural flood management and river restoration schemes.

5.2 Summary

Extreme weather events, such as flash floods, have driven the demand for innovative solutions from various entities (Edenhofer et al. 2014, Burgess-Gamble et al. 2018). In response to this urgent call, the Water Criteria of the Climate Bonds Standard have advocated nature-based solutions (NBS), emphasising the use of leaky barriers that are inspired by natural formations, such as beaver dams (Nyssen et al. 2011, Wohl 2013). Leaky barriers are in-stream natural flood management solutions that are designed for peak flow attenuation, where their effectiveness is highly dependent on their design.

This chapter discusses two cases. The first case investigates the flow characteristics around leaky barriers (LB) composed of three cylindrical cylinders. The main configuration of the leaky barrier considered the cylinders to be vertically aligned, with other layouts inclined at 15°, 30°, and 45° in the upstream and downstream directions. Results reveal that the frontal projected blockage area of the LB leads to an increase in the upstream flow depth, with momentum being redirected towards the bottom gap, creating a primary wall-jet, whose peak velocity and coherence varied depending on LB design, however, attained a similar decay downstream. The porous LBs allowed for distinct internal flow paths that generated secondary jets, either diverting momentum upwards or downwards depending on the direction of the barrier inclination, impacting main flow features and turbulent characteristics. Turbulent kinetic en-

ergy and vertical Reynolds shear stress decreased when the barrier was inclined downstream. In the upstream inclination cases, these showed no significant variation, with magnitudes similar to those in the vertical configuration. Bed shear stress decreased with increasing barrier angle, reducing the risk of local scour and sediment mobilisation. The vertical LB achieves the maximum backwater rise at the expense of promoting larger sediment bed mobilisation. Structural loads on the cylinders vary with LB inclination, with drag forces decreasing as barrier angles increase. Hydrodynamic findings, evaluated through five design criteria, show that upstream-inclined designs, particularly with large barrier angles, exhibit improved relative performance compared to other designs.

The second case focuses on the impact of varying barrier lengths in the streamwise direction on free-surface development and wake hydrodynamics. Simulations were conducted for three-row configurations with varying numbers of dowels, i.e. 6, 9, 12, 15, 18 and 24. These numbers correspond to longitudinal lengths (L_s) ranging from 0.05 m to 0.2 m. The results revealed that the longitudinal length distinctly impacts the key flow characteristics. Backwater rise was substantial in S6, minor from S9 to S15, and again pronounced after S15. The wall jet strength varied among cases, with the S9 and S12 designs being weaker than other configurations, as evidenced by their diminished ability to maintain high streamwise velocities along the bottom gap downstream of the barrier. High turbulent kinetic energy regions were identified in analyses of mixing jets along the lowermost cylinders, and there was a clear reduction in these levels as the barrier length increased. The absence of a recirculation core behind the top cylinder was observed for all cases, and the near wake exhibited a large recirculation zone that extended close to the free surface, most prominently for the shortest barrier design. As the longitudinal barrier length increased, it promoted larger sediment bed mobilisation, thereby increasing the risk of local scour. For optimal flood management, designs S6, S18, and S24 exhibit the greatest backwater rise; however, for site sediment management, S18 and S24 are not recommended due to the risk of local bed and bank scouring.

Section 5.3 presents Case i, detailing inclined leaky barriers including the computational setup and the discussion on flow hydrodynamics and structural responses across seven distinct barrier designs. Section 5.4 presents Case ii, which addresses the longitudinal barrier length, providing its computational framework and highlighting the effects of length variations on both upstream and downstream hydrodynamics. Conclusions for both cases are provided in Section 5.5.

5.3 Case i: Analysis of leaky barriers with inclined designs

5.3.1 Computational setup

The experimental setup of Müller et al. (2021b), who studied short porous leaky barriers in lab-scale open channel flow, is adopted and expanded upon to explore additional configurations. The main configuration, referred to as S0 in this study, replicates this experiment

and consists of three rows of horizontal cylinders with a diameter (D) of 0.025 m (Fig. 5.1). These cylinders span the entire width of the main channel and are arranged such that there is a vertical gap (b_0) of 0.05 m ($2D$) from the bottom wall to the lower side of the barrier. Moreover, there is a vertical distance (b) of $0.5D$ between the rows, which allows the flow to pass through the barrier. The leaky barrier has a height (H_S) of 0.1 m ($4D$) and a longitudinal length (L_s) equal to the cylinder diameter. The bulk velocity (U_0) in the experiment was set to 0.29 m/s, resulting in a bulk Reynolds number ($Re = U_0 H/\nu$) of 43500. The mean water depth (H) was 0.15 m, which gives Froude numbers ($Fr = U_0/\sqrt{gH}$) of 0.24.

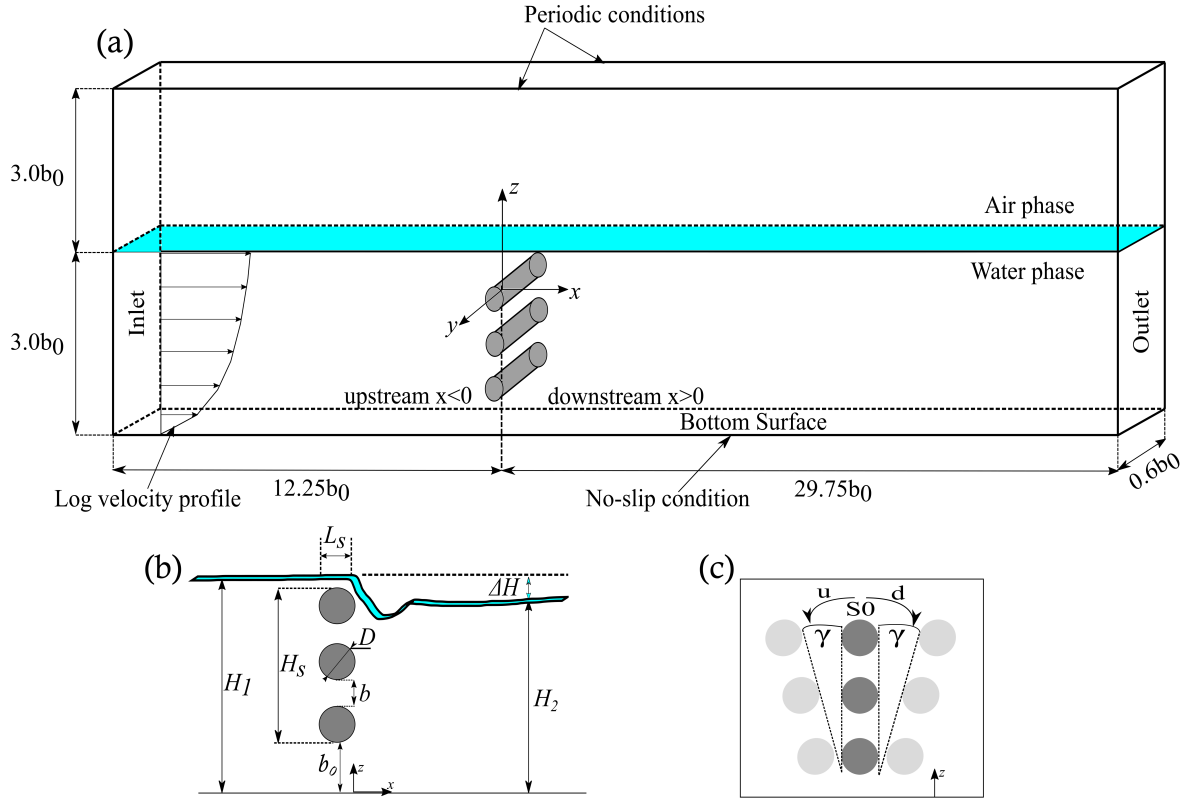

Fig. 5.1 (a) Schematic of the computational domain adopted in the two-phase LES depicting the main characteristics of a leaky barrier structure. The inflow boundary conditions with a logarithmic approaching velocity profile are also indicated. (b) The structure has a height H_s and a longitudinal length L_s, with vertical inter-cylinder gaps b and a vertical gap between the structure and the bottom wall b_0. H_1 and H_2 represent the mean upstream and downstream flow depths, respectively. The term ΔH refers to the backwater rise, which is calculated as the difference between the upstream and downstream water depths. This structure is composed of a horizontal channel spanning cylinders of diameter D aligned perpendicularly to the flow direction. (c) The leaky barrier is inclined at different angles (γ), where d and u indicate the direction of the barrier inclination in the downstream and upstream directions, respectively.

The computational domain, depicted in Fig. 5.1a, has dimensions of 2.1 m, 0.3 m, and 0.03 m in the streamwise (x), vertical (z) and spanwise (y) directions, respectively. The top cylinder is positioned $12.25b_0$ downstream of the upstream inlet, which is considered as the origin of the x-coordinates. Six additional configurations are numerically investigated by varying the angles of the barrier, set at $\gamma = 15°$, $30°$, and $45°$, determined based on the ver-

tical offset from the primary configuration (S0) (Fig. 5.1c) and denoted as S1u, S2u and S3u, and S1d, S2d and S3d, where u and d represent upstream and downstream directions, respectively. For clarity, S1u and S1d are inclined at an angle of 15°, S2u and S2d at 30°, and S3u and S3d at 45°.

In the experimental design conducted by Müller et al. (2021b), geometric scaling was utilised to characterise the physical properties of leaky barriers at Wilde Brook, Corvedale (Shropshire, UK) (Follett and Wilson 2020). The model-to-prototype scale was set at approximately 1:7 (1:6.7), which was determined by considering the bankfull depth, the vertical gap beneath a leaky barrier and the cylinder diameter. The leaky barriers at Wilde Brook exhibited a vertical gap to bankfull height ratio (b_0/H) between 0.333 and 0.5, with a b_0/H ratio of 0.333 maintained in line with the reference model. The barrier model design employed a dowel diameter, D, of 25 mm, representing a field cylinder diameter ranging from 0.17 to 0.33 m. For a better understanding of the field-scale conditions, the Reynolds number and the Froude number are identified, whether the scaling is based on the physical log/gap (Müller et al. 2021b) or the bankfull flow depth (Follett and Wilson 2020). Conforming to the principles of Froude similarity, where the scaling of discharge and velocity follows the formulae $U_{\text{field}} = U_{\text{lab}}\sqrt{\lambda}$ and $Q_{\text{field}} = Q_{\text{lab}}\lambda^{5/2}$, where λ is the scaling factor (1:6.7). Thus, for a leaky barrier characterised by a log diameter of 0.17 m (0.025 m at model scale) and a velocity of 0.77 m/s (0.29 m/s at model scale), the resulting Reynolds number is approximately 130,900, and the Froude number is about 0.60 (Müller et al. 2021b). Alternatively, based on the average bankfull channel depth of $H = 1$ m (0.15 m at model scale), the Reynolds number is 770,000, and the Froude number is 0.25 (Follett and Wilson 2020).

A convective boundary condition is used at the outflow, and a no-slip boundary condition is applied to the bottom boundary. Periodic boundary conditions are used for the spanwise direction. The level-set method is employed to compute the water surface and the top of the domain is treated with a slip condition. The time step is variable, with a Courant-Friedrichs-Lewy condition of 0.2 to ensure numerical stability. The grid is uniform throughout the domain, with a resolution of $\Delta x/D = 0.03$, $\Delta y/D = 0.06$, and $\Delta z/D = 0.024$ in the x, y, and z directions, respectively. The numerical mesh consists of 28 million grid cells, or $N_x \times N_y \times N_z = 2800 \times 20 \times 500$, where N_{xi} denotes the number of grid nodes in each spatial direction. The simulations are executed on 350 CPUs, and each case is simulated for 35 to 40 flow-through periods (T_f) to compute mean flow statistics once the flow is fully developed. In the following, the symbols $\langle\cdot\rangle$ indicate time-averaging operation.

The current LES setup adopts a mean logarithmic velocity profile by setting a smooth log-law distribution at the domain inlet, using a friction velocity (u_*) of 0.01925 m/s, derived from the best-fit of the experimental velocity measurements (Müller et al. 2021b):

$$\frac{u(z)}{u_*} = \frac{1}{\kappa}\ln\left(\frac{zu_*}{\nu}\right) \tag{5.1}$$

Here $\kappa = 0.41$ is the von Kármán constant.

To assess the appropriateness of using this mean logarithmic velocity profile at the inlet, Fig. 5.2 presents vertical profiles of normalised mean streamwise velocity $\langle u \rangle / U_0$ at three stations upstream of the leaky barrier (S0), comparing LES with the experimental data. The LES results exhibit a generally consistent agreement with the experimental results. At x/b_0 = –4.0, the $\langle u \rangle$ distribution is almost uniform along the water depth, while profiles closer to the upstream edge of the leaky barrier ($x/b_0 >$ –4.0) show an increase of $\langle u \rangle$ along the bottom gap ($z/b_0 \leq 1$), while there is a reduction in $\langle u \rangle$ at higher water elevations ($z/b_0 > 1$) due to the vertical obstruction of the barrier and mass conservation, which causes the incoming flow to accelerate through the large gap beneath the structure.

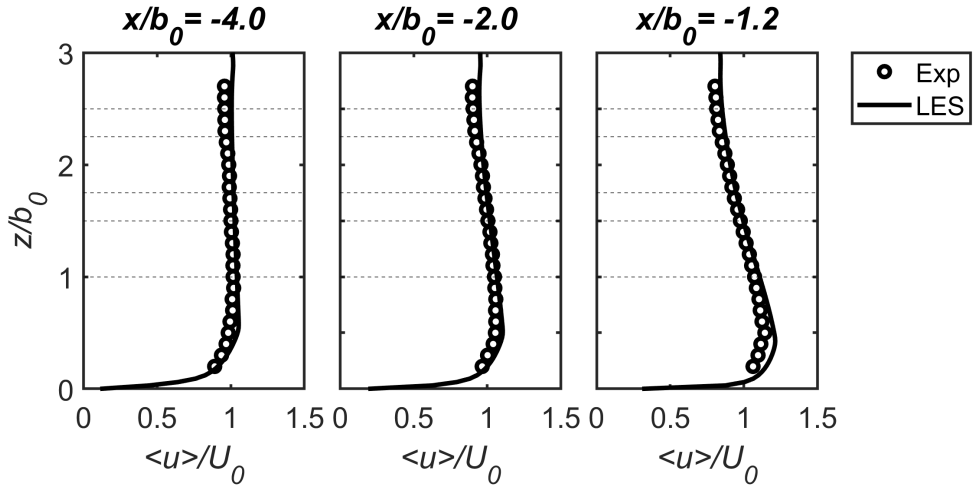

Fig. 5.2 Vertical profiles of time-averaged streamwise velocity normalised by the bulk velocity $\langle u \rangle / U_0$ at three locations upstream of the leaky barrier. Comparison between experimental (symbols) and LES (lines) results. Horizontal dashed lines indicate the cylinder positions of the barrier.

5.3.2 Results and discussion

This section will present the hydrodynamic characteristics of seven leaky barrier configurations. This includes examining the free-surface profiles, instantaneous flow field, time-averaged nature of the flow, recirculation regions, recovery of mean streamwise velocity, gap flow ratio, decay of the maximum jet velocity, potential bed scour and hydrodynamic coefficients.

5.3.2.1 Free surface profiles

The time-averaged water-surface profiles obtained during a previous experimental campaign for the vertical barrier (Müller et al. 2021b) and from the present LES for different leaky barrier configurations are presented in Fig. 5.3. The development of the free surface that results from the incident of the oncoming flow with the porous obstructions is classified into three distinct regions: (i) the backwater rise region ($x/b_0 < 0$), which is characterised by gradually

varied flow conditions; (ii) the water-surface drop region ($x/b_0 \approx 0$), where there is a sudden decrease in water depth that results from the flow backing up very close to the upstream edge of the barrier, which then undergoes significant acceleration that causes a considerable drop in the water surface; and (iii) a transition region that extends between the water-surface drop and undisturbed downstream regions.

Fig. 5.3 shows that the longitudinal extent of the transition regions varies across cases. The end of the transition region corresponds to the downstream location where the slope of the mean water depth is nearly flat. For instance, in the S0 case and cases with the smallest angle (S1u and S1d), the downstream recovery region begins after a transition region of approximately $12b_0$, while this is at about $6b_0$ in the S2u and S3u cases. Conversely, for the S2d and S3d cases, the transition region extent is approximately $18b_0$ (Fig. 5.3).

Although the free-surface data that were obtained from the measurements and the LES for the non-inclined barrier (S0) exhibits a good agreement, the LES seems to slightly overestimate the experimental data at the positions of the drop in the free surface and in the transition region downstream of the barrier ($0 \leq x/b_0 \leq 5$). The results show that increasing the barrier's angle to either upstream or downstream directions leads to a decrease in the backwater rise, which can reduce the incidence of overbank flow (Nisbet et al. 2015, Burgess-Gamble et al. 2018, Muhawenimana et al. 2023). Furthermore, the magnitude of the free surface drop varies with the angle of barrier, i.e. a flatter inclination corresponds to a smaller drop. Fig. 5.3b shows that in comparison to the S0 layout, S1u exhibits a lower backwater rise and a higher water depth in the region immediately downstream ($x/b_0 \leq 10$), while the difference between S0 and S1d is negligible, as shown in Fig. 5.3a. These differences between the S1u and S1d cases compared to the S0 case are associated with the direction of the flow through the inter-cylinder gaps of the barrier, which will be shown later. For instance, in the upstream-inclined cases, the flow is forced to move upwards towards the free surface.

5.3.2.2 Instantaneous flow field

The turbulent flow fields and vortex shedding developed behind the leaky barriers for all of the simulated configurations are shown in Figs. 5.4, 5.5, and 5.6. These figures present contours of normalised spanwise vorticity over the xz-plane, along with the power spectral density computed from the vertical velocity fluctuations at six points downstream of the barriers over the lower shear layer of the bottom cylinder ($z/b_0 \approx 1.0$). Fig. 5.4a presents the instantaneous flow structure of the S0 case, revealing that the proximity to the free surface creates a disturbance that narrows the wake behind the top cylinder and affects the separation of the shear layers. This causes the upper shear layer to deflect downwards and merge with the lower shear layer, which inhibits the formation of roll-up shear layer vortices. Meanwhile, the shear layers formed along the sides of the lowermost cylinders have less influence from the proximity to the free surface. They can roll up and generate vortices in the near wake

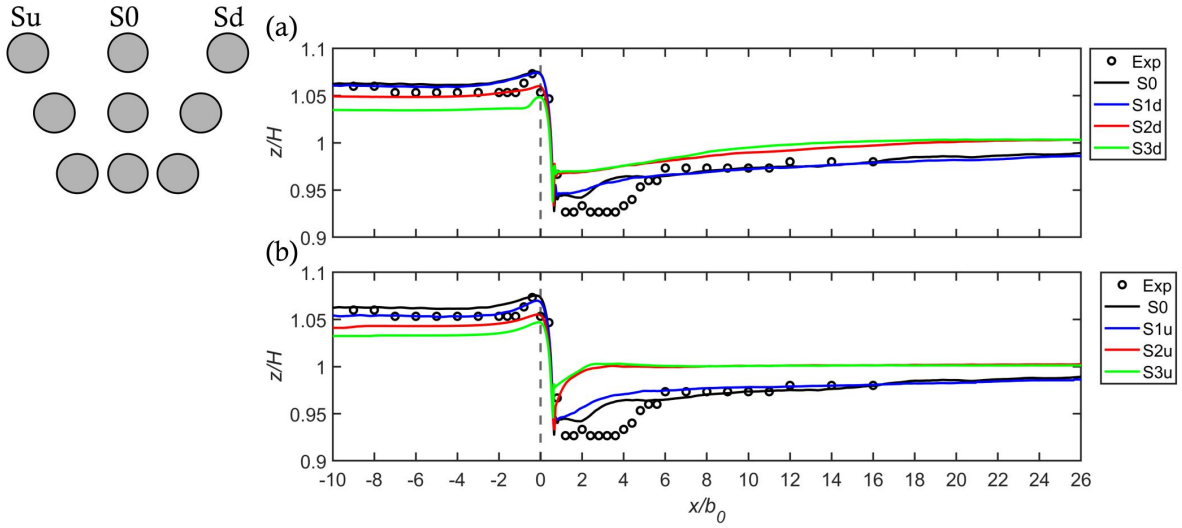

Fig. 5.3 Free-surface profiles obtained from the LES for (a) downstream-inclined cases and (b) upstream-inclined cases, along with the LES and experimental values of the non-inclined case (S0). Vertical dashed lines indicate the origin of the x coordinates located at the downstream edge of the top log.

before merging with the deflected shear layers from the top cylinder within the region of $1 \leq x/b_0 \leq 2$. These vortices interact with each other and combine the wakes into a wider one, a phenomenon known as vortex and vortex interaction regime (Alam and Meyer 2013). Eventually, this results in the vertical location of the merged shed vortices being shifted towards the bottom wall at approximately $x/b_0 \approx 3$. The von Kármán vortices lack spatial coherence shortly downstream of the barrier. However, within the range of $6 \leq x/b_0 \leq 7$, coherent turbulent structures emerge because they are less affected by the merging of vortices observed at closer downstream positions.

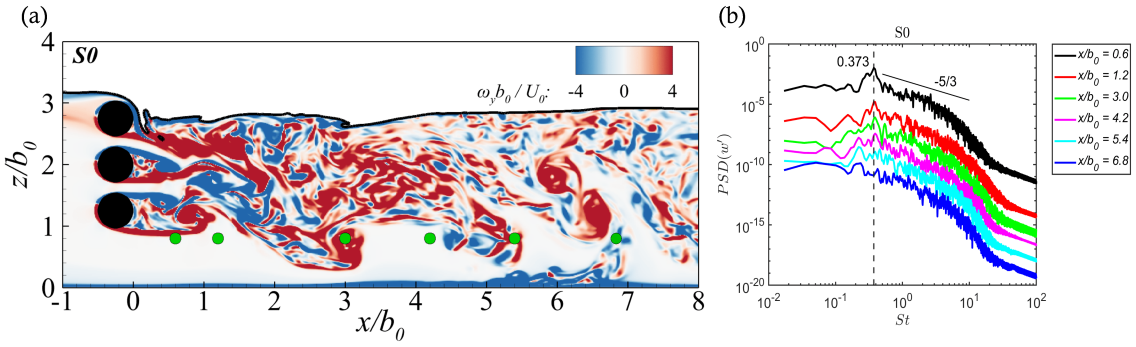

Fig. 5.4 (a) The contour of normalised vorticity over a vertical plane at the middle of the spanwise domain length for the non-inclined structure (S0). The free surface is depicted as a solid-black line. (b) The power spectral density (PSD) of the vertical velocity fluctuation (w') obtained at six points downstream of the barrier along the lower shear layer of the bottom cylinder ($z/b_0 \approx 1.0$). The vertical dashed line indicates the Strouhal number (St) equal to 0.373.

The proximity interference, e.g. when the cylinders are located close to each other, has an effect on the vortex-shedding behaviour. This interference can impact aspects such as the frequency of vortex shedding or the phase synchronisation between the von Kármán vortex

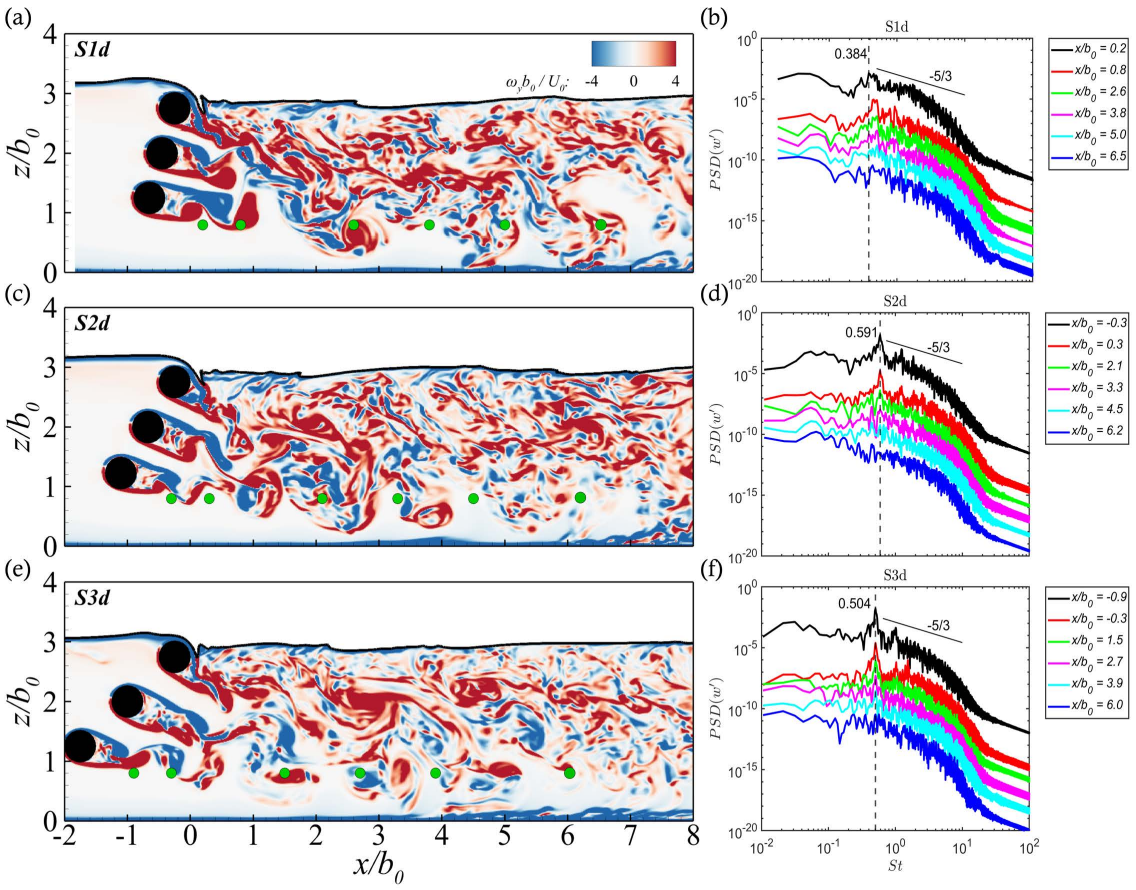

Fig. 5.5 Contour plots of (a, c and e) of normalised vorticity over a vertical plane at the middle of the spanwise domain length comparing the downstream-inclined structures (S1d, S2d and S3d). The free surface is depicted as a solid-black line. (b, d and f) PSD of the vertical velocity fluctuation (w') at six points downstream of the barrier along the lower shear layer of the bottom cylinder ($z/b_0 \approx 1.0$). The vertical dashed line indicates the Strouhal number (St).

street (Meneghini et al. 2001). Fig. 5.4b shows that the spectra of the LES vertical velocity fluctuations feature peaks at frequencies indicating the vortex-shedding frequency represented by the Strouhal number, namely at $St = 0.373$, up to $x/b_0 = 4.2$. However, the energetic peaks in the spectra deviate from this characteristic frequency when computed at positions further downstream, exhibiting multiple peaks with the most energetic at $St = 0.221$. The reduction in St corresponds to a large vortex originating from the merging of the von Kármán vortices, exhibiting greater spatial coherence and lower frequency. The classical $-5/3$ Kolmogorov's slope (black line) characterises the decay of energy in the inertial subrange.

In the S0 case, the interactions between the shear layers and the development of downstream wake vortices are primarily influenced by the proximity interference, the downstream-inclined cases exhibit further complexity to the flow dynamics downstream of the barrier due to the combined effect of both the wake and proximity interferences, as shown in Figs. 5.5a, 5.5c and 5.5e. Wake interference occurs when the wake of one cylinder is affected by the wake of another cylinder. Here, the separated free shear layers generated by the top cylinder interact with the von Kármán vortex formation of the lower cylinders, as shown in Fig. 5.5a

for the S1d case ($x/b_0 \approx 1$). As the barrier angle increases, the occurrence of this interference is delayed to positions further downstream. This delay allows the shear layers of the lowermost cylinders to freely roll up and generate vortices in the near wake, before they interfere with each other when $x/b_0 > 1$. Fig. 5.5e shows how the von Kármán vortices for the S3d configuration detach and move closer to the bottom wall in comparison to the other cases, which results in a faster loss of coherence of the shed vortices as they travel further downstream.

Fig. 5.5b illustrates that the S1d barrier exhibits a vortex-shedding frequency at $St = 0.384$, evaluated at the nearest sampling point of $x/b_0 = 0.2$, which does not significantly differ from the S0 case. However, for sampling points located further downstream of the barrier, the frequency of the high-energy spectra peaks increases, reaching $St = 0.454$ at $x/b_0 = 0.8$ and peaking at $St = 0.506$ for $x/b_0 = 2.6$, 3.8, and 5.0. At $x/b_0 = 6.5$, the frequency decreases again to approximately $St \approx 0.454$, accompanied by multiple peaks at both lower and higher Strouhal numbers. For barriers with greater inclinations, there is an increase in St of the dominant peaks in the spectra compared to the S1d configuration. In the S2d case, the St reaches approximately 0.591 at $x/b_0 = -0.3$, while in the S3d case this is 0.504 at $x/b_0 = -0.9$, as identified in Figs. 5.5d and 5.5f, respectively. In the S2d case, the spectral peaks appear to shift to lower frequencies as the downstream distance increases ($x/b_0 > 3.3$) at $St \approx 0.438$. In contrast, the S3d case exhibits the same dominant frequency for most downstream positions, except at the furthest point ($x/b_0 = 6$), where multiple peaks are observed without a clearly defined dominant peak, which is likely to be due to a loss of coherence of the large-scale vortices (Fig. 5.5f). Moreover, the spectra of the vertical velocity fluctuations for the downstream-inclined cases feature a decay slope of $-5/3$ in the inertial sub-range.

Fig. 5.6a shows that despite the upstream inclination of the S1u setup, the merged vortices in the near wake of the barrier continue to feature a downwards movement at $x/b_0 = 2$. Furthermore, the small-scale vortices in the near downstream region at $z/b_0 > 2$ tend to converge and then be convected downstream. They gradually descend and eventually reach the bottom wall at $x/b_0 = 4$–5. In the S2u case, significant deformation of the free surface occurring behind the top cylinder hinders the development of its shear layers, their combination and interaction with others, as shown in Fig. 5.6c. This causes the vortices that are shed from the middle and bottom cylinders to travel upwards towards the free surface shortly after being shed, which triggers substantial variations in water depth downstream of the barrier. When the barrier is largely inclined to the upstream direction, the wake interference becomes less apparent. The S3u case demonstrates a negligible interaction between the shed vortices in the near wake region ($x/b_0 \leq 3$), as shown in Fig. 5.6e. Therefore, compared to the upper water column where the developed vortices decay faster near the free surface, the vortices in the lower wake region exhibit some spatial coherence and are convected downstream with the flow, i.e. $x/b_0 = 2.7$ and 5.0.

Fig. 5.6b shows that for $x/b_0 \leq 5.8$, the dominant characteristic frequency for the S1u

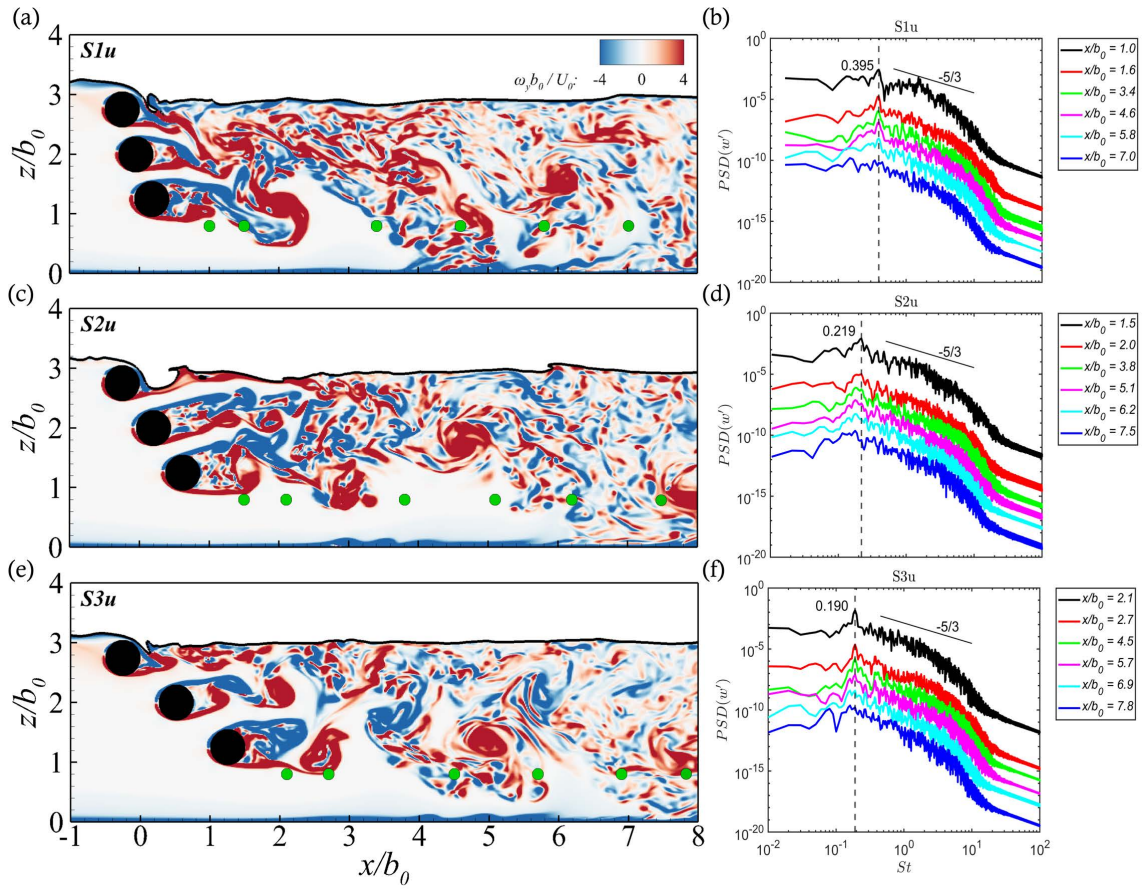

Fig. 5.6 Contour plots of (a, c and e) normalised vorticity over a vertical plane at the middle of the spanwise domain length comparing the upstream-inclined structures (S1u, S2u and S3u). The free surface is depicted as a solid-black line. (b, d, f) Power spectral density (PSD) of the vertical velocity fluctuation (w') at six points downstream of the barrier along the lower shear layer of the bottom cylinder ($z/b_0 \approx 1.0$). The vertical dashed line indicates the Strouhal number (St).

case is at $St = 0.395$, which slightly differs from the $St = 0.373$ in the S0 layout. Figs. 5.6d and 5.6f show that there is a significant decrease in the dominant frequency for cases with larger angles towards the upstream direction. Specifically, the St values are 0.219 and 0.190 for the S2u and S3u cases at $x/b_0 = 1.5$ and 2.1, respectively. This reduction can be attributed to the decreased flow variations in the lower wake region ($z/b_0 < 1$) compared to cases with a leaky barrier inclined to the downstream direction. The characteristic frequency for the S2u case at $St = 0.219$ remains constant until $x/b_0 = 2.0$, after which it decreases to $St = 0.178$. In contrast, the dominant frequency in the S3 case remains constant until $x/b_0 = 5.7$. Beyond that point, the spectrum's shape becomes broad-band and a primary frequency cannot easily be identified. For all upstream-inclined cases, the $-5/3$ decay law is also evident, corresponding to the decay of the energetic eddies in the inertial sub-range.

5.3.2.3 Time-averaged flow characteristics

The upstream flow is first characterised. The velocity profiles in both the streamwise and vertical directions are examined for all cases and presented in Figs. 5.7 and 5.8, respectively. Fig.

5.7 shows that as proximity to the barrier increases, the flow is diverted towards the lower gap of the structure ($0 \leq z/b_0 \leq 1$), manifesting in a high streamwise velocity at this position. The maximum streamwise velocity along the bottom gap at the nearest upstream profile exhibits slight variations among the cases due to the positioning of the cylinders in relation to the incoming flow. For instance, in the downstream-inclined cases at $x/b_0 = –2.5$, the peak values range between $\langle u \rangle / U_0 = 1.05–1.11$. Conversely, in the upstream-inclined cases at $x/b_0 = –1.0$, the peak values range between $\langle u \rangle / U_0 = 1.11–1.28$.

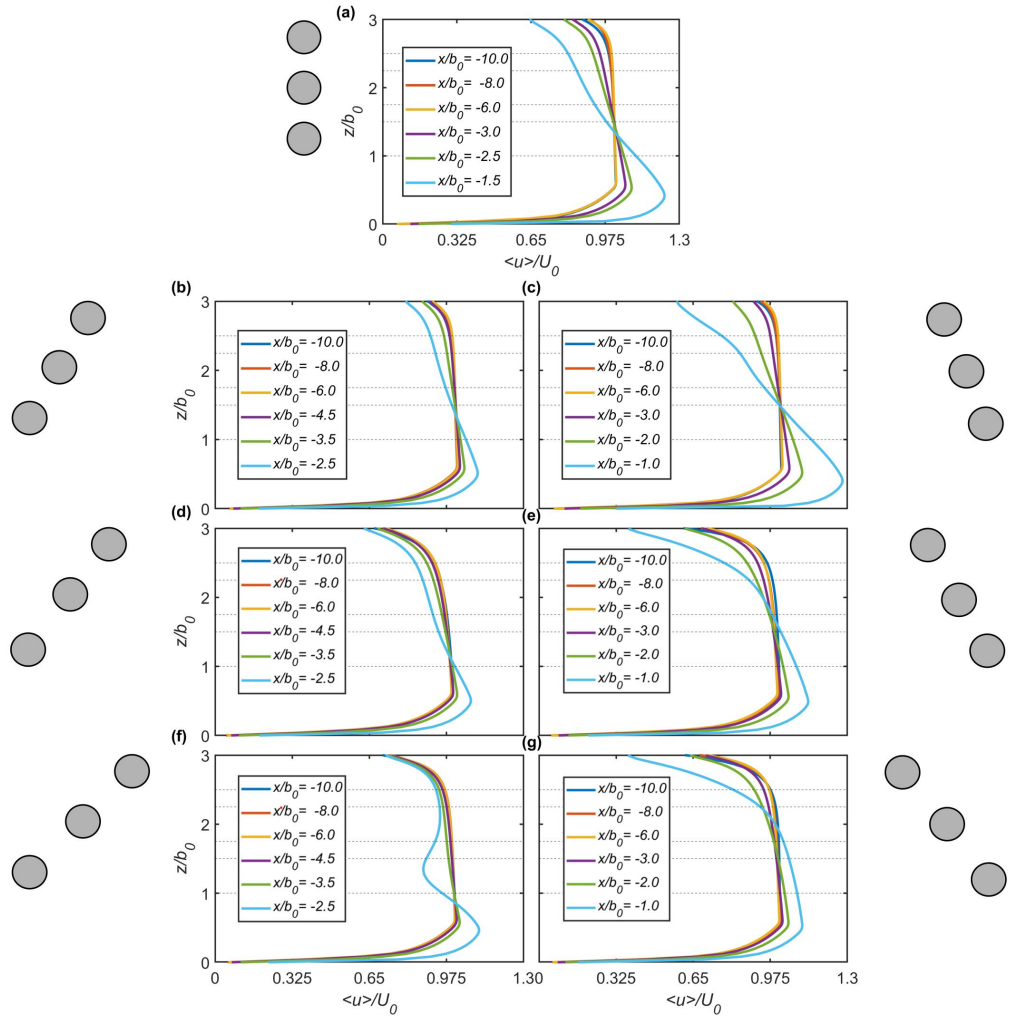

Fig. 5.7 Vertical profiles of normalised mean streamwise velocities $\langle u \rangle / U_0$ at different locations upstream of the barrier for (a) the S0 case, (b, d and f) the downstream-inclined cases (S1d, S2d and S3d, respectively), and (c, e, g) the upstream-inclined cases (S1u, S2u and S3u, respectively). The dashed lines indicate the positions of the cylinders.

At $z/b_0 > 1$, the streamwise velocities tend to decrease with increasing z, with a larger reduction for stations closer to the barrier compared to those further upstream. Near the free surface, at $x/b_0 = –1$ and $z/b_0 = 3.0$, the S1u configuration exhibits a mean streamwise velocity of $\langle u \rangle / U_0 = 0.6$, in contrast to the lower value of $\langle u \rangle / U_0 = 0.4$ that can be observed in the more inclined S2u and S3u designs (Figs. 5.7c, 5.7e, 5.7g). The downstream-inclined barriers also exhibit a decrease in the streamwise velocities but at a smaller rate. For instance, at

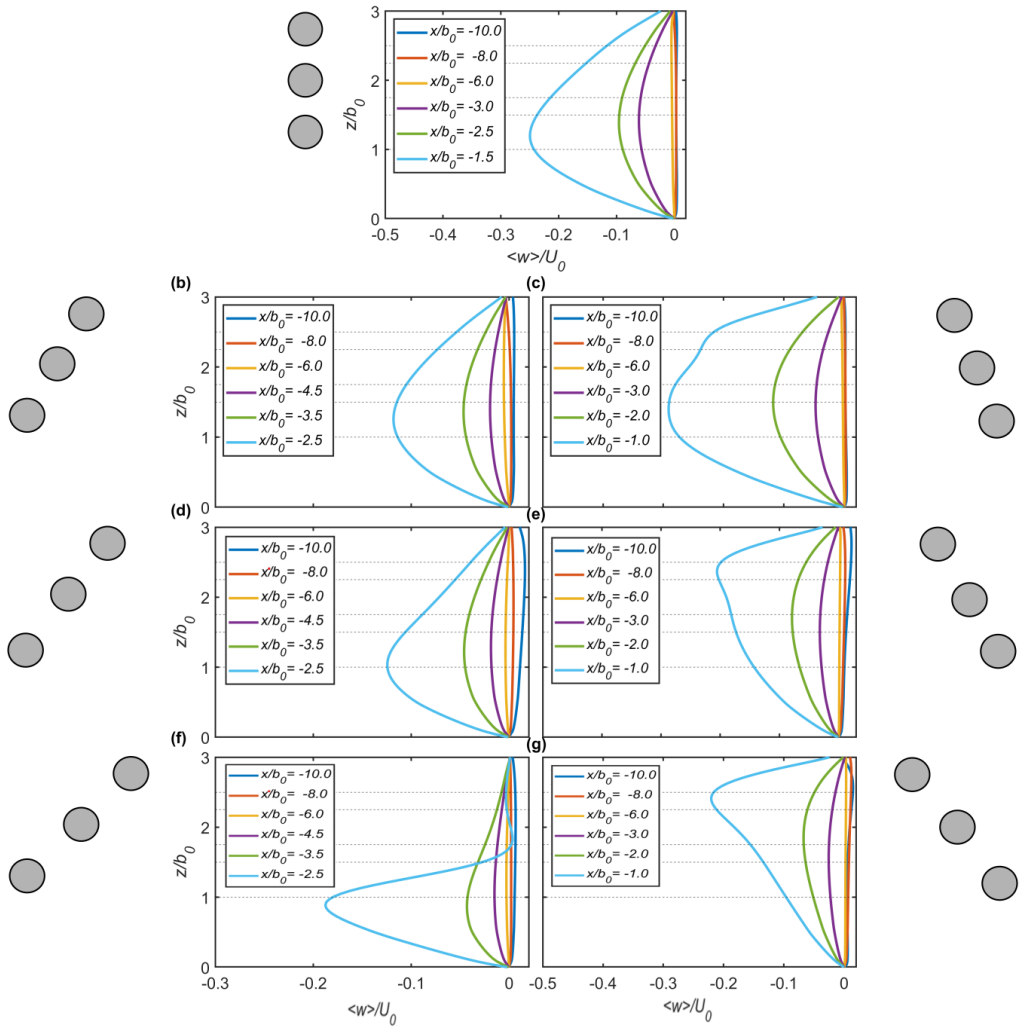

Fig. 5.8 Vertical profiles of normalised mean vertical velocities $\langle w \rangle / U_0$ at different locations upstream of the barrier for (a) the S0 case, (b, d and f) the downstream-inclined cases (S1d, S2d and S3d, respectively), and (c, e, g) the upstream-inclined cases (S1u, S2u and S3u, respectively). The dashed lines indicate the positions of the cylinders.

x/b_0 = –2.5 and z/b_0 = 3.0, for the S1d layout $\langle u \rangle / U_0$ = 0.8, which reduces to about $\langle u \rangle / U_0$ = 0.7 for the S2d and S3d designs (Figs. 5.7b, 5.7d, 5.7f). Overall, the reduction in the $\langle u \rangle$ magnitude that is associated with inclining the barriers to either direction over the backwater region can benefit the catchment by increasing water storage, enhancing ground infiltration and reducing downstream flood levels, benefits discussed also by (Burgess-Gamble et al. 2018, Muhawenimana et al. 2023).

Fig. 5.8a shows that the vertical velocity profiles ($\langle w \rangle$) for locations near the barrier ($x/b_0 >$ –6) in the S0 case exhibit elevated magnitudes and a parabolic shape. The $\langle w \rangle$ profile shows that the maximum magnitude is attained along the centre of the lowest cylinder at z/b_0 = 1.25 and corresponds to a region of downward fluid motion, as indicated by $\langle w \rangle = -0.25 U_0$ at x/b_0 = –1.5. Moving further upstream of the barriers ($x/b_0 \leq$ –6), there is a substantial decrease in the magnitudes of $\langle w \rangle$, gradually converging towards nearly zero values as the effect from the barriers vanishes. In the S1d case, the distribution of $\langle w \rangle$ along the water column closely re-

sembles that of the S0 case, albeit with a reduced peak value of $\langle w \rangle / U_0 = -0.12$ (Fig. 5.8b). The greatest downward flow velocity in the S2d case is almost similar to that of S1d, although its position is slightly shifted to a lower vertical height at $z/b_0 = 1$. With a maximum vertical velocity of $\langle w \rangle / U_0 = -0.19$ in the S3d layout, there is a noticeable shift of its position further downwards ($z/b_0 < 1$), as shown in Fig. 5.8f. Moreover, the S3d case features a faster reduction in the magnitude of $\langle w \rangle$ at higher water depths of $z/b_0 > 1.5$ compared to the other configurations, whereas in the other cases the reduction occurs gradually as the proximity to the free surface increases.

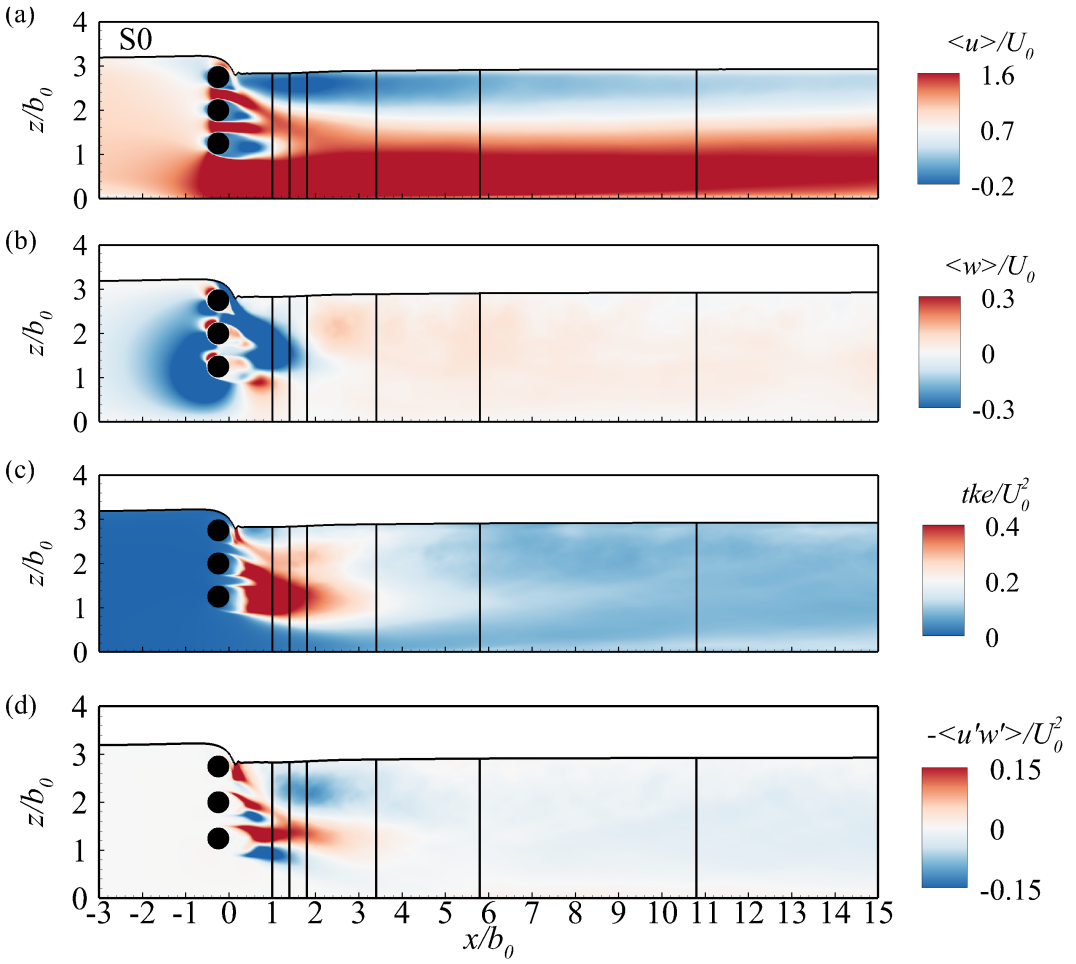

Fig. 5.9 Side elevation contour plots of the LES computed (a) streamwise velocity, (b) vertical velocity, (c) turbulent kinetic energy and (d) Reynolds shear stress, normalised by the bulk velocity for the S0 case. The vertical lines mark the locations at which vertical profiles of the mean quantities are plotted and shown in Figs. 5.10 and 5.11.

The profiles of $\langle w \rangle$ in the upstream-inclined cases (Figs. 5.8c, 5.8e and 5.8g) exhibit a reversed pattern compared to the downstream-inclined barriers. At $x/b_0 = -1$, the upstream profiles for the S2u and S3u cases show an upward shift in the position of the maximum downward flow velocity ($z/b_0 \approx 2.25 - 2.5$) with a peak vertical velocity of $\langle w \rangle / U_0 \approx -0.2$. In contrast, the S1u case reaches a peak magnitude of $\langle w \rangle / U_0 \approx -0.3$ at a similar vertical position as the S1d case but with a higher $\langle w \rangle$ at greater water depths compared to the S1d case.

These differences between inclined barrier layouts in both directions can be attributed to the alteration in the positioning of the cylinders in relation to the point of initial flow impingement. Further upstream for all cases ($x/b_0 < -3$), the $\langle w \rangle$ decreases along the water column, which indicates a reduced influence from the obstructed barrier compared to profiles closer to it.

The results of the time-averaged flow hydrodynamics developed for the S0 case are shown in Fig. 5.9 along the channel centre-line plane, i.e. at $y/b_0 = 0.3$. Fig. 5.9a shows that a high-momentum jet forms beneath the barrier, which is characterised by a significant increase in mean streamwise velocities. This jet exhibits characteristics similar to a modified wall jet (Ead and Rajaratnam 2002) or the flow beneath engineered or naturally formed logjam (Beebe 2000) in terms of maintaining its maximum velocity until a certain downstream distance before commencing a rapid decay, as explained later in Sec. 5.3.2.7. Behind the leaky barrier at $z/b_0 > 1$, the streamwise velocities gradually diminish, becoming significantly reduced closer to the free surface. The inter-cylinder gaps of the barriers allow for distinct internal flow paths, generating secondary jets, known as offset jets, which influence near wake decay and turbulent mixing (Wang and Tan 2007). Fig. 5.9a shows how these parallel offset jets deflect downwards and then converge with increasing downstream distance, until they eventually merge with the main wall jet in the range of $x/b_0 \approx 2$–3.

Fig. 5.9b presents the contours of time-averaged vertical velocities, revealing two distinct regions of high negative vertical velocities that indicate the downwards motion of the flow. The first area with high negative <*w*> is situated upstream of the barrier along its lower part ($z/b_0 < 2$), which results from the vertical obstruction caused by the barrier. The second region is adjacent to the lee side of the barrier, extending from the free surface downwards and further to regions along the upper shear layer of the lowest log, reflecting the downwards motion of flow overtopping the barrier and the flow penetrating the structure through the inter-cylinder gaps. In contrast, a small region of positive vertical velocities is found downstream of the leaky barrier, in close proximity to the bottom log, which indicates the upwards vertical motion of the flow. This upwards motion is a result of the fluid accelerating through the vertical gap between the barrier and the bottom wall.

Fig. 5.9c presents the contours of the time-averaged turbulent kinetic energy (*tke*) distribution, revealing a prominent area of high *tke* in the near field wake along the middle and bottom cylinders until $x/b_0 \approx 2$. This region indicates the high turbulence in the immediate recirculation zones behind the cylinders, which coincides with low streamwise velocity values presented in Fig. 5.9a. The evolution of the shear layers shed from the cylinders and the interaction of the secondary jets downstream of the barrier are the main contributors to these high levels of the *tke* (Fig. 5.9c). Fig. 5.9d shows the distribution of the vertical Reynolds shear stress ($-\langle u'w' \rangle$) with higher values observed along the upper side of the bottom log, which indicates a greater momentum exchange between the flow over the bottom cylinder and the near wake compared to that with the flow moving under the log. Likewise, the middle cylin-

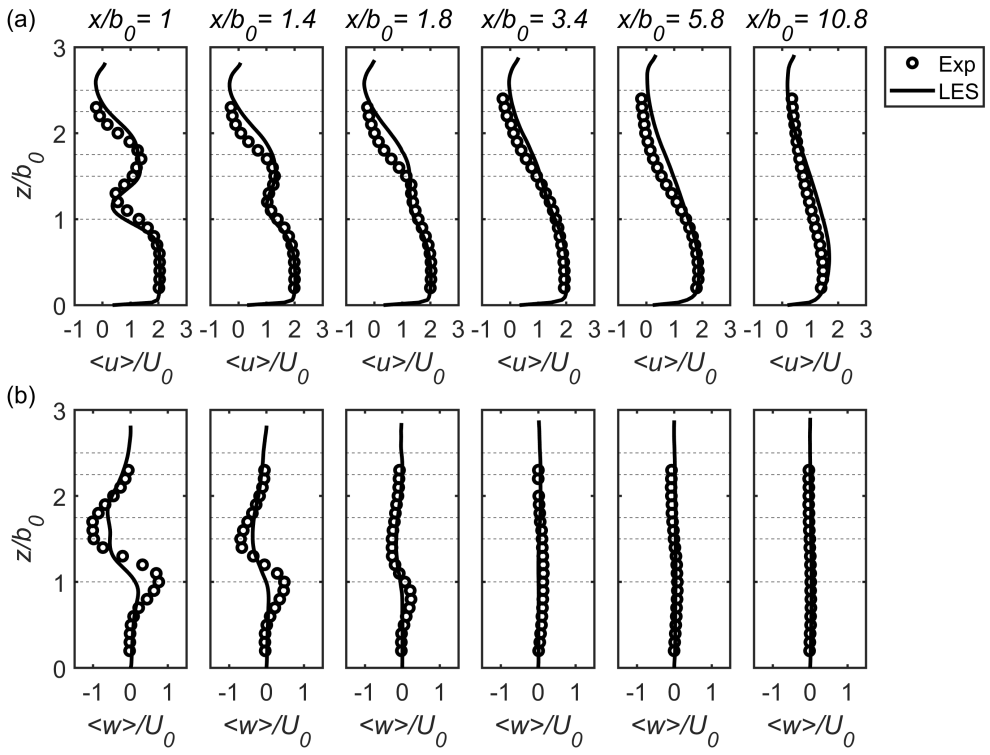

Fig. 5.10 Vertical profiles of (a) normalised mean streamwise velocity $\langle u \rangle / U_0$ and (b) vertical velocity $\langle w \rangle / U_0$ at six locations downstream of the barrier. Comparison between experimental (symbols) and LES (lines) results. Horizontal dashed lines indicate the positions of the cylinders.

der shows a similar pattern, albeit with lower levels of $-\langle u'w' \rangle$, which indicates a reduced momentum exchange compared to the bottom log. The top cylinder exhibits a weak momentum exchange. Moreover, an additional area of high turbulent momentum exchange is found below the free surface at $1 \leq x/b_0 \leq 3$.

Vertical profiles of mean streamwise $\langle u \rangle$ and vertical $\langle w \rangle$ velocities at six locations downstream of the S0 case obtained from the experiment (Müller et al. 2021b) and the LES are shown in Fig. 5.10. In the near wake ($x/b_0 \leq 1.4$), the profiles feature a high-momentum region that expands from the bottom bed into the upper region of the barrier's wake ($z/b_0 \geq 1$), as shown in Fig. 5.10a. The distribution of $\langle u \rangle$ agrees well between the experimental and the LES results, especially along the bottom gap ($z/b_0 < 1$). At $x/b_0 = 1$, the streamwise velocity along the bottom cylinder height ($1 < z/b_0 < 1.5$) initially decreases due to the effect of the log's wake. It subsequently increases along the lower inter-cylinder gap ($1.5 < z/b_0 < 1.75$). This is the signature of the secondary jet, whose velocity is smaller in comparison to that of the primary jet present at the bottom gap. Above $z/b_0 > 1.75$, the streamwise velocity experiences another decrease, followed by a slight increase at greater water depths ($z/b_0 \approx 2.75$), which is influenced by the proximity to the free surface. As the downstream distance increases, the disturbance caused by the barrier's wake gradually reduces, and the agreement between the experimental and the LES results continues.

The distribution of vertical velocity at the selected downstream stations (Fig. 5.10b) reveals a predominant upwards fluid motion along the lower side of the lowest cylinder ($z/b_0 =$

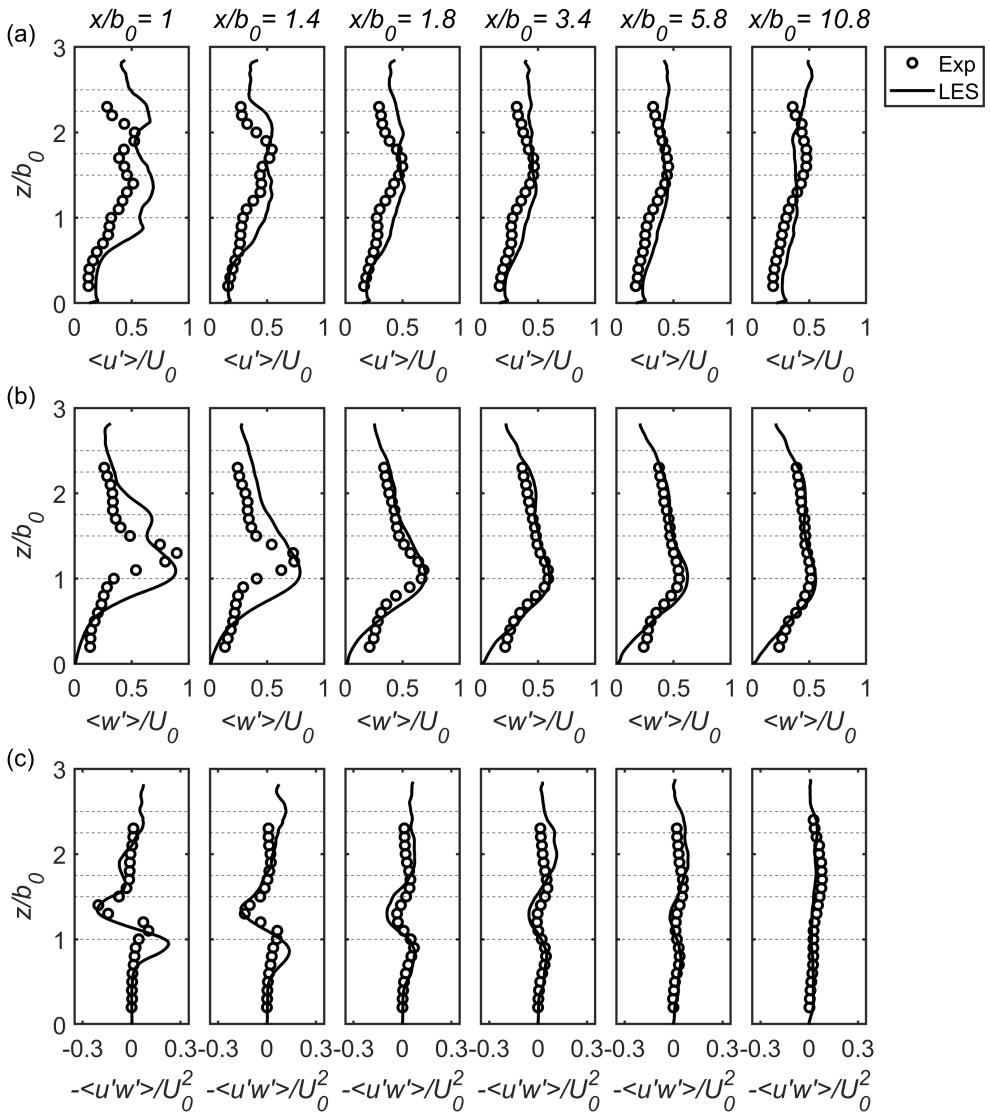

Fig. 5.11 Vertical profiles of (a) streamwise turbulence intensity $\langle u' \rangle$, (b) vertical turbulence intensity $\langle w' \rangle$, and (c) vertical Reynolds shear stress $-\langle u'w' \rangle$ at different locations downstream of the barrier. Comparison between experimental (symbols) and LES (lines) results. Horizontal dashed lines indicate the positions of the cylinders.

1) in the near wake ($x/b_0 \leq 1.4$), whereas a downwards motion is apparent along the lower inter-cylinder gap ($1.5 < z/b_0 < 1.75$). At $x/b_0 \leq 1.4$, the peak $\langle w \rangle$ values are underestimated by the LES, but further downstream these differences gradually diminish. Fig. 5.11 shows the distributions of time-averaged second-order statistics, including $\langle u' \rangle$, $\langle w' \rangle$, and $-\langle u'w' \rangle$, at six positions downstream of the barrier. At positions closer to the barrier ($x/b_0 \leq 1.4$), Fig. 5.11a reveals that the LES distribution of $\langle u' \rangle$ exhibits higher values than the experiment between $1 < z/b_0 < 2.75$. Beyond $x/b_0 = 1.4$, the variation in the distribution of $\langle u' \rangle$ along the water column reduces, accomplishing a better agreement between the LES and the experimental data.

The vertical turbulence intensity profiles near the structure ($x/b_0 \leq 1.4$) indicate that the maxima of $\langle w' \rangle$ are attained along the height of the lowest cylinder (Fig. 5.11b), with a

slight downwards shift in the peak position observed in the LES data compared to the experiments. At $x/b_0 \geq 1.8$, both the experimental and LES results attain the peak $\langle w' \rangle$ at a height of $z/b_0 \approx 1.0$, demonstrating a better agreement along the whole water column compared to closer downstream locations. The maxima $\langle w' \rangle$ shift in the downstream region is a consequence of the von Kármán vortices travelling downwards to the region with the highest momentum (Fig. 5.11b). At $x/b_0 \leq 1.4$, the vertical profiles of the $-\langle u'w' \rangle$ exhibit peak positive values at $z/b_0 = 1$, indicating upwards turbulent momentum exchange, while negative peak values are noted along the upper shear layer of the lowest cylinder at $z/b_0 \approx 1.5$, indicating downwards turbulent momentum exchange (Fig. 5.11c). With the exception of the LES overprediction of the peak values of $-\langle u'w' \rangle$ in the near wake at $x/b_0 \leq 1.4$ and $z/b_0 \approx 1$, the experimental and LES data demonstrate good agreement in the remaining regions along the water depth and at further downstream positions.

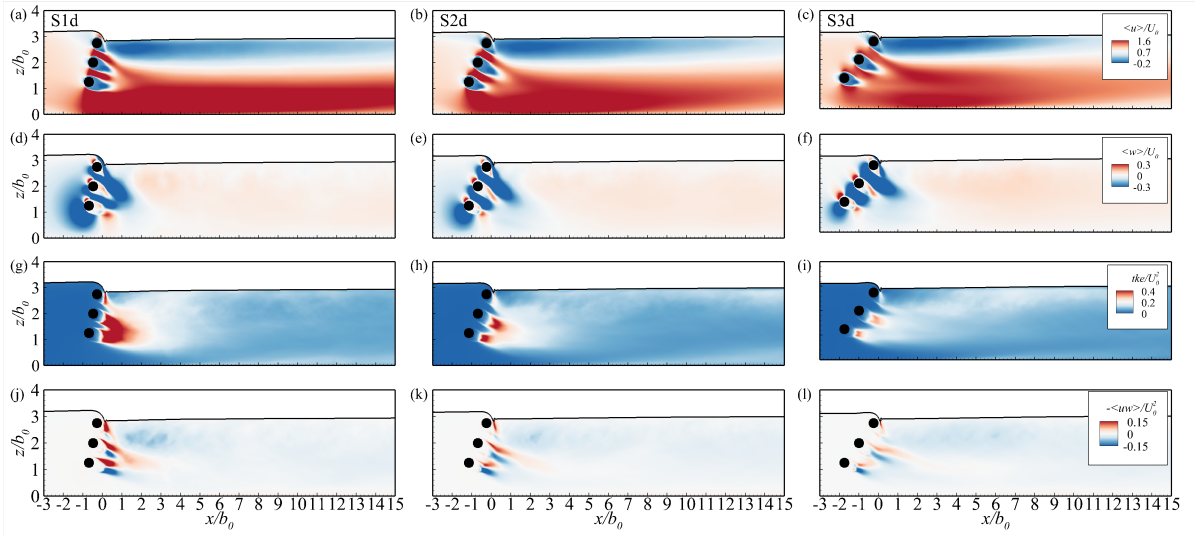

Fig. 5.12 Side elevation contour plots of the LES computed (a-c) streamwise velocity, (d-f) vertical velocity, (g-i) turbulent kinetic energy and (j-i) Reynolds shear stress, normalised by the bulk velocity for the downstream-inclined cases (S1d, S2d and S3d).

Figs. 5.12a–c show the streamwise velocity contours in the downstream-inclined cases. In the S1d case, no significant changes are observed compared to the S0 case, while in the S2d and S3d cases the magnitudes of the streamwise velocity remain relatively high downstream before exhibiting a notable reduction at far downstream positions ($x/b_0 \geq 10$). For instance, at $x/b_0 = 10$, the maximum $\langle u \rangle$ along the bottom gap decreases as the angle of barrier increases, with $\langle u \rangle / U_0 = 1.8$, 1.5 and 1.3 for S1d, S2d and S3d, respectively. Furthermore, the increase in the angle of barrier results in a decrease in the magnitude of $\langle u \rangle$ within the inter-cylinder gaps, with average values of $\langle u \rangle / U_0 = 1.9$, 1.7, and 1.5 for the S1d, S2d and S3d barriers, respectively. The downstream-inclined cases also exhibit a significant decrease in $\langle u \rangle$ close to the free surface, which is mainly due to the diverted fluid motion towards the bottom downstream region of the barrier.

The downstream-inclined cases do not exhibit significant changes in the downstream re-

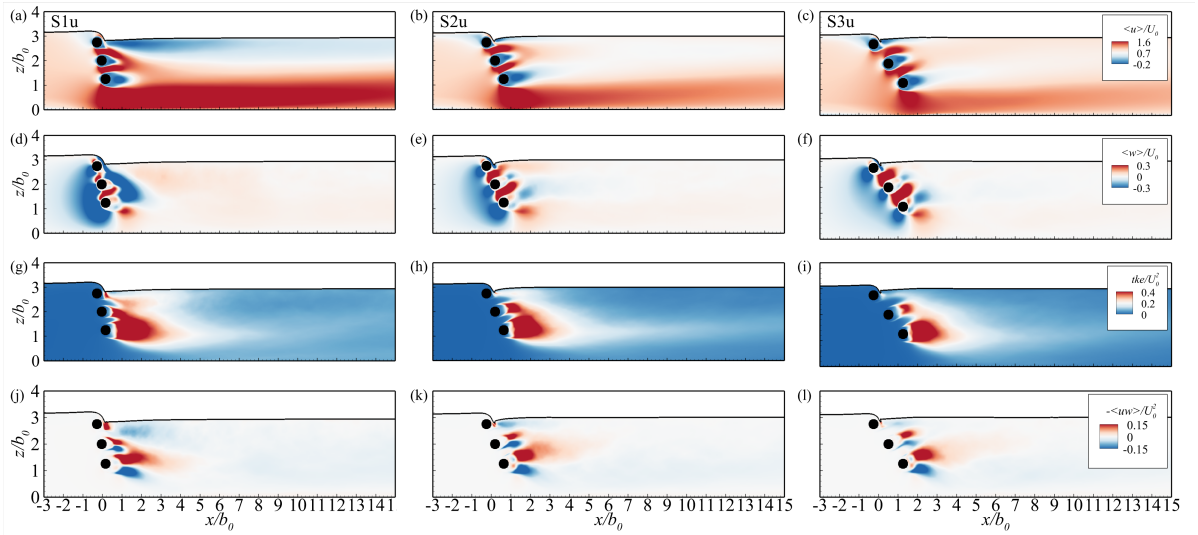

Fig. 5.13 Side elevation contour plots of the LES computed (a-c) streamwise velocity, (d-f) vertical velocity, (g-i) turbulent kinetic energy, and (j-i) Reynolds shear stress, normalised by the bulk velocity for the upstream-inclined cases (S1u, S2u and S3u).

gions of the negative $\langle w \rangle$, although these regions become detached or separated from each other as the angle of barrier increases (Figs. 5.12d-f). Furthermore, shrinkage occurs in the region of the negative $\langle w \rangle$ located upstream of the barrier's lower side as the angle of the barrier increases. Figs. 5.12g-i present the mean turbulent kinetic energy, revealing that the downstream-inclined case S1d exhibits an almost similar *tke* distribution and magnitude to the non-inclined case (S0). However, the *tke* levels significantly reduce as the angle of barrier increases (S2d and S3d). Similarly, the levels of the vertical Reynolds shear stress (Figs. 5.12j-l) decrease as the angle of the barrier increases.

In the upstream-inclined cases, the increase in the angle results in a decrease in the magnitude of streamwise velocities (Figs. 5.13a-c), implying a shorter longitudinal extent of the region dominated by high $\langle u \rangle$ compared to the other cases. This decrease originates from the redirection of flow through the inter-cylinder gaps in an upwards direction, thereby limiting the influence of the formed secondary jets on the bottom region ($z/b_0 < 1$). In contrast to the downstream-inclined cases shown in Figs. 5.12a-c, where the $\langle u \rangle$ near the free surface is reduced in downstream regions, the upstream-inclined cases exhibit an increase in $\langle u \rangle$ as the barrier angle increases. Figs. 5.13d-f presents the contour plots of the time-averaged vertical velocities, which shows that increasing the angle of the cylinder structure towards the upstream direction results in an upwards fluid motion through the inter-cylinder gaps of the barrier.

Figs. 5.13g-i show that the upstream-inclined cases exhibit a highly turbulent wake, mainly along the heights of the middle and bottom cylinders, until $x/b_0 = 2$, followed by a region between $2 < x/b_0 < 6$, where the turbulence decays. As the barrier angle increases towards the upstream direction, the magnitude of *tke* within these regions remains notably high. This is in contrast to the significant reduction observed when the barrier angle increases towards the

downstream direction (Fig. 5.12g-i). Figs. 5.13j-l show that, regardless of the barrier angle, the behaviour of the vertical Reynolds shear stress behind the lowermost cylinders remains consistent across the upstream cases and the differences in the $-\langle u'w' \rangle$ magnitudes between cases are negligible.

5.3.2.4 Recirculation region

The cylinders of the leaky barriers create recirculation zones of various scales immediately downstream, characterised by low streamwise velocities, as shown in Fig. 5.14. The recirculation zone behind the top cylinder exhibits just one recirculation core enclosed on the lower side of the log, while the upper recirculation core is affected by the proximity to the free surface and the overtopping flow that plunges downstream of the cylinder edge. In contrast, in the recirculation zones behind the other cylinders, both the upper and lower cores of the recirculation appearing almost symmetrical in relation to the centre of the log.

Fig. 5.14 shows that the recirculation zones exhibit a downwards inclination when the barrier is inclined in the downstream direction, while an upwards inclination can be observed with upstream-inclined barriers. The direction of the barrier inclination, along with the proximity effects of the adjacent cylinders, leads to variations in the length of the recirculation zones behind the cylinders. For instance, the mean recirculation length (L_r/b_0) behind the lowest cylinder is larger in the S1u, S2u and S3u cases compared to the S1d, S2d and S3d cases, with differences of approximately 15% observed between the 15-degree inclined cases (S1d and S1u) and differences exceeding 50% in cases with higher angles, where the L_r/b_0 ratios are 0.91, 1.24 and 1.01 for the S1u, S2u and S3u cases, respectively, and 0.77, 0.52 and 0.50 for the S1d, S2d and S3d cases, respectively.

The flow diverted through the inter-cylinder gaps of the barrier towards the lower downstream region ($z/b_0 \leq 2.5$), moving away from the free surface, creates a flow pattern that leads to an extended recirculation zone near the free surface, as shown in Fig. 5.14 for the non-inclined case and the downstream-inclined cases. However, when the barrier is inclined upstream, the recirculation zone shrinks in the S1u case and nearly disappears in the S2u and S3u cases due to the upwards flow through the inter-cylinder gaps, resulting in higher streamwise velocities near the free surface. As the downstream angle of the barrier increases, the large recirculation zone narrows and elongates in the streamwise direction, leading to a reduced width of the recirculation zone. This narrowing is accompanied by a shift in the centre of the recirculation zone towards the free surface layer. This shift is indicated by the values of the centre positions changing from $z/b_0 = 2.24$ for the S1d case to $z/b_0 = 2.30$ and 2.35 for the S2d and S3d cases, respectively.

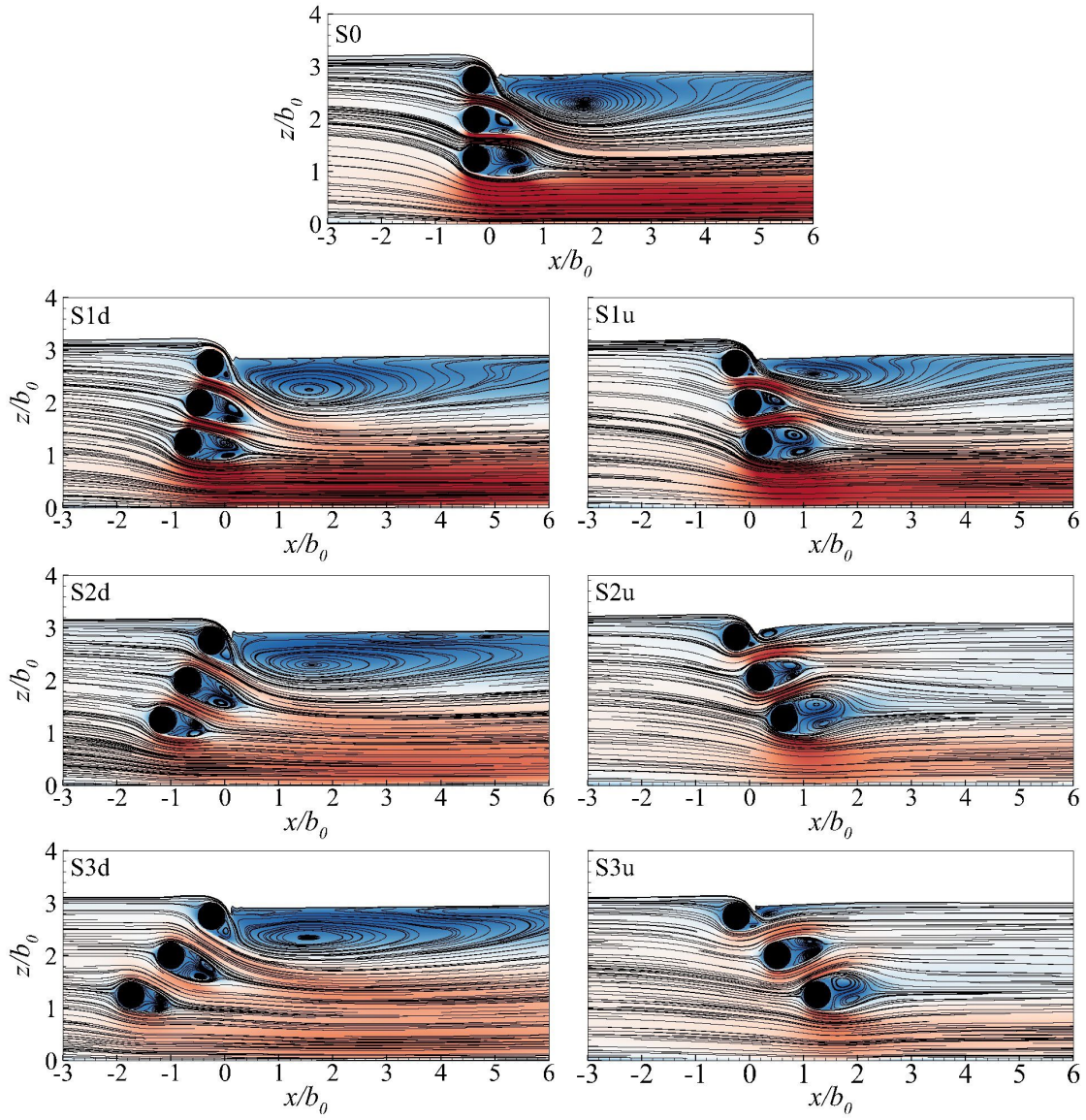

Fig. 5.14 Comparison of the mean recirculation regions computed using LES for all simulated cases, with contours of the mean streamwise velocity normalised by the bulk velocity.

5.3.2.5 Recovery of mean streamwise velocity

The velocity deficit in the streamwise direction $\left(\Delta\langle u\rangle = \frac{\langle u\rangle - \langle u\rangle_{x/b_0=-10}}{\langle u\rangle_{x/b_0=-10}}\right)$ between a selected far upstream station ($x/b_0 = -10$) and downstream profiles ranging from $x/b_0 = 2$ to $x/b_0 = 29$ is calculated for all of the simulated cases to evaluate the influence of the structural design on wake recovery, as shown in Fig. 5.15. All of the leaky barriers initially show a velocity surplus ($\Delta\langle u\rangle > 0$) along the bottom gap ($z/b_0 < 1$) due to the high-momentum flow exiting underneath the barriers. The S2u and S3u cases demonstrate a more pronounced difference between the first downstream profile ($x/b_0 = 2$) and subsequent profiles, indicating a faster rate of wake recovery compared to the other cases.

In the upper wake region ($z/b_0 \approx 1.5$–2.5), all cases exhibit a velocity deficit ($\Delta\langle u\rangle < 0$) due to low mean streamwise velocities, while for the S2u and S3u cases the deficit begins at

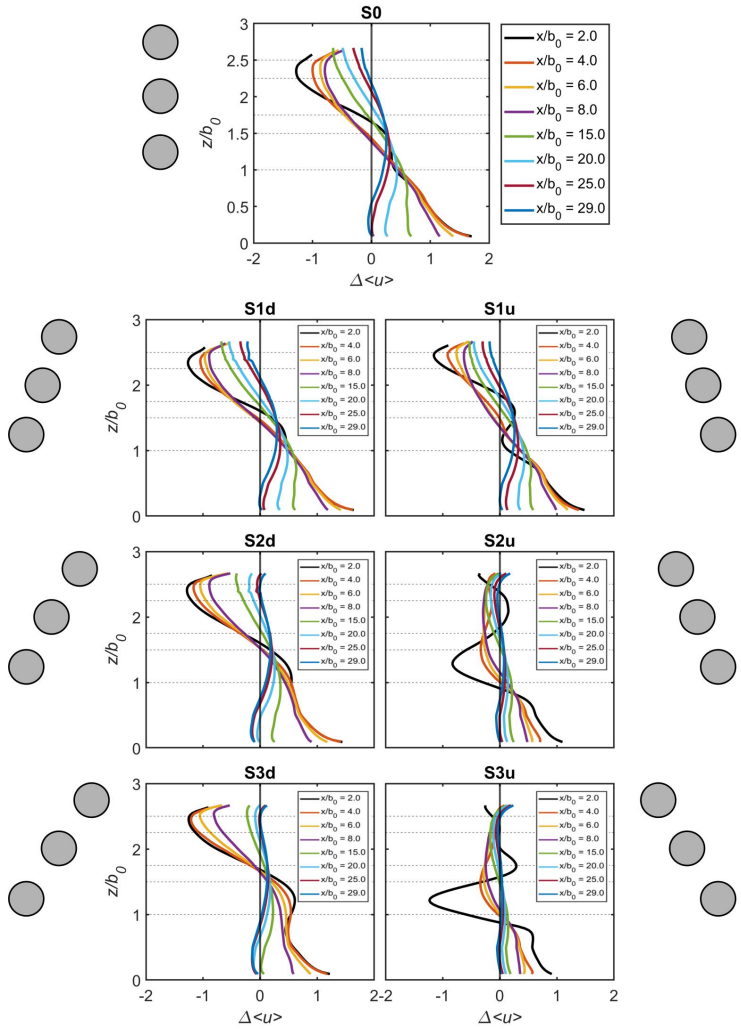

Fig. 5.15 Progression of velocity deficit $\left(\Delta\langle u\rangle = \frac{\langle u\rangle - \langle u\rangle_{x/b_0=-10}}{\langle u\rangle_{x/b_0=-10}}\right)$ computed from the difference between the upstream profile (x/b_0 = -10) and selected downstream profiles for (a) the S0 case, (b, d and f) the downstream-inclined cases (S1d, S2d and S3d, respectively), and (c, e, g) the upstream-inclined cases (S1u, S2u and S3u, respectively). The horizontal dashed lines indicate the positions of the cylinders. The vertical line indicates the zero-velocity deficit ($\Delta\langle u\rangle$ = 0).

a lower vertical height of $z/b_0 \approx 1$, as shown in Figs. 5.15e and g. At $z/b_0 > 2$, the S0, S1d and S1u cases show a similar pattern of $\Delta\langle u\rangle < 0$ in downstream profiles, suggesting that the streamwise velocity does not fully recover within this range for these cases. However, in the S2d case, wake recovery begins at $x/b_0 \geq 25$, gradually leading to a nearly zero-velocity deficit ($\Delta\langle u\rangle \approx 0$). The S3d case features a faster recovery in its wake, with the velocity deficit approaching $\Delta\langle u\rangle \approx 0$ at $x/b_0 = 20$. In contrast, the upstream-inclined cases (S2u and S3u) exhibit a streamwise velocity recovery that is closer to the barrier ($x/b_0 > 8$) and throughout the water column (Figs. 5.15e and g). Hence, a relationship between the extent of the transition region (Fig. 5.3) and the rate of wake recovery can be inferred, which implies that a faster wake recovery coincides with a shorter transition region.

5.3.2.6 Gap flow ratio

The flow developed through barrier gaps significantly influences the downstream dynamics of the barrier. To gain a better understanding of the flow rate at each gap, an analysis of the time-averaged flow rate is conducted, focusing on calculating the gap flux ratio, which is defined as the ratio between the flow rate through the gap (F_2) and the mean incoming flow rate (F_1). Fig. 5.16a presents how the gap flux ratio (F_2/F_1) correlates with the change in barrier inclination at each gap position. The F_1 calculations are performed between the mean free-surface level and the bottom wall, specifically at a distance of $10b_0$ upstream of the barrier. For F_2, the calculations are done vertically along each gap, including gb_0 (bottom), gb_1 (lower inter-log), gb_2 (upper inter-log) and gt (top between the top cylinder and free surface), as illustrated in Fig. 5.16b. The gap flux ratios at the bottom gap (gb_0) exhibit the highest values among all gaps, ranging approximately from $F_2/F_1 = 0.47$ to 0.61. Conversely, the flux ratios at the inter-cylinder gaps, gb_1 and gb_2, show negligible differences between cases and contribute to an average total of 32% of flow passing through these gaps. Although variations in the flux ratios exist between cases at the top gap, the gap flux ratio is minimal compared to the ratios at the other positions, with a maximum ratio of $F_2/F_1 = 0.24$ for the S3d case.

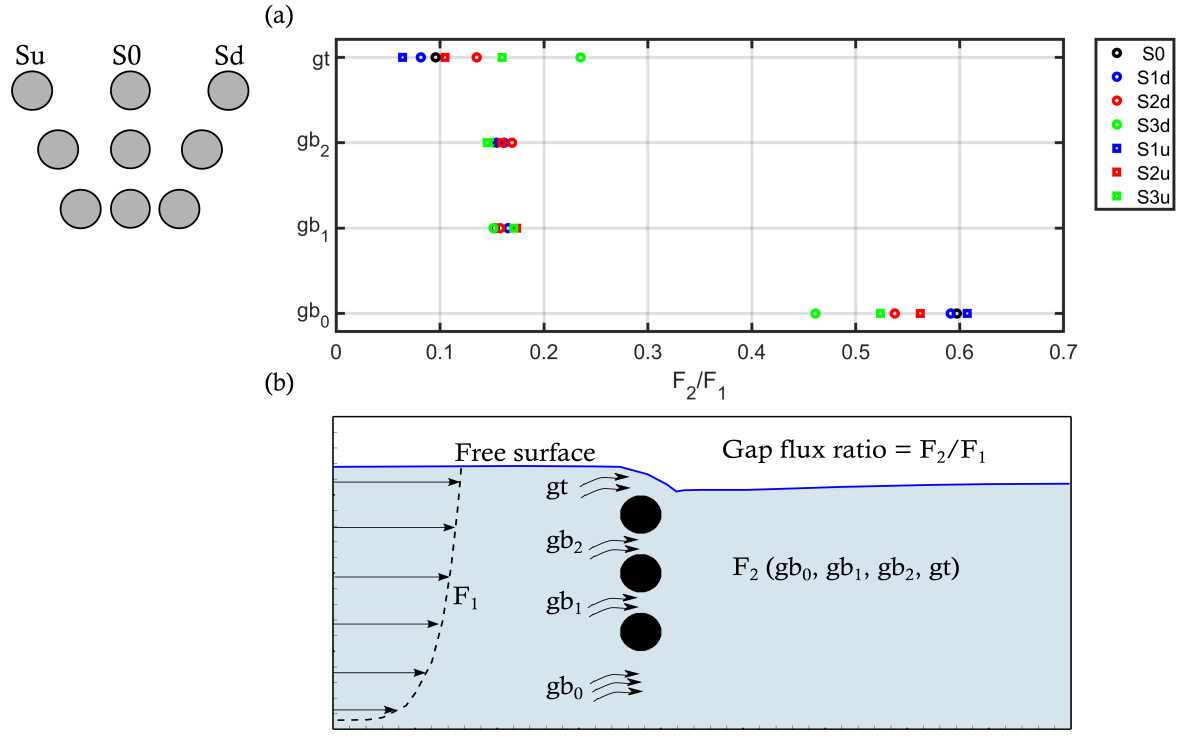

Fig. 5.16 (a) The variation of the gap flux ratio (F_2/F_1) with gap position and barrier inclination, and (b) schematic diagram illustrating the definition of the gap flux ratio and gap positions (gb_0, gb_1, gb_2, gt), where gb_0 represents the bottom gap, gb_1 represents the lower inter-cylinder gap, gb_2 represents the upper inter-cylinder gap and gt represents the top gap between the top cylinder and the free surface. F_1 represents the flux at the upstream point of x/b_0 = -10, while F_2 represents the flux at the different gap positions.

The flux ratio gb_0 decreases as the angle of the barrier increases in both upstream and

downstream directions, with the reduction being greater for the downstream-inclined cases than the upstream-inclined cases. For instance, the flux ratio for the downstream cases reduces by approximately 22% from 0.59 for S1d to 0.46 for S3d, compared to a reduction of approximately 15% from 0.61 for S1u to 0.52 for S3u. The flux ratios of the bottom gap can be correlated with the initiation of the high-momentum jet formed beneath the structure, where a larger flux ratio indicates a stronger initiation of the jet, while a smaller flux ratio corresponds to a weaker jet. The minimal variations in the flux ratios at the inter-cylinder gaps between the barriers can likely be attributed to their narrow width gaps, which are smaller than the bottom gap. This is anticipated to result in an analogous strength in the initiation of the offset jets across all cases. Varying the angles of the barrier in both directions affects the elevation of the free surface at the top of the barrier, leading to alterations in the width of the flow route at the top gap and differences in the magnitudes of flow velocity. The flux ratios of the top gap for all cases show smaller values than the values at gb_2, except for the S3d and S3u cases, which exhibit larger flux ratios. The flux ratio at the top gap position reflects the proportion of incoming flow overtopping the barrier. The flux ratio at the top gap is inversely proportional to the flux ratio at the bottom gap for all inclined cases, as presented in Fig. 5.16a.

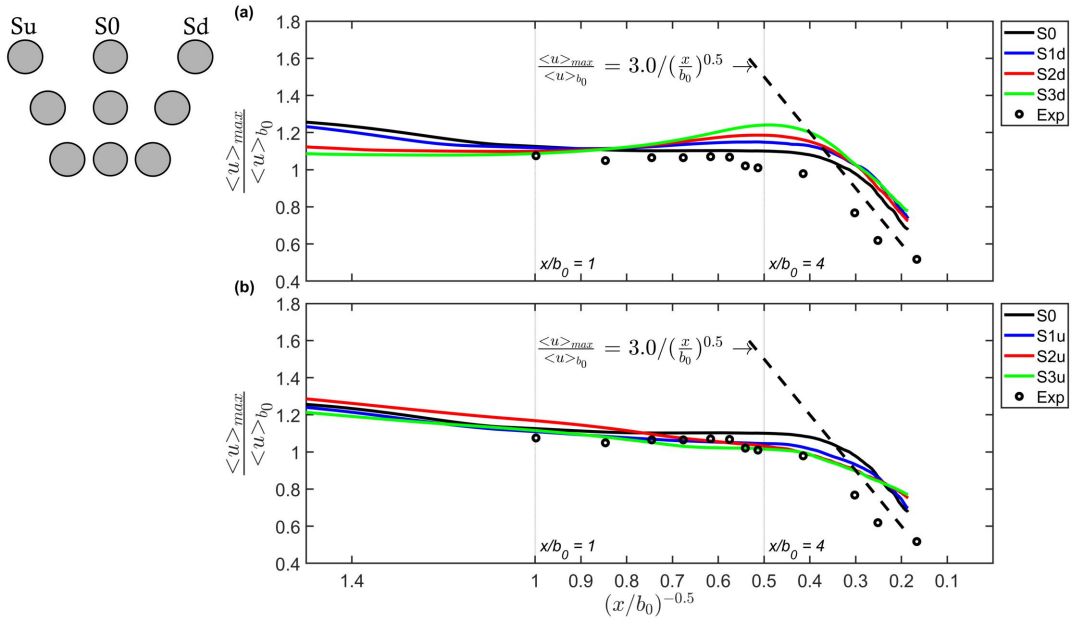

Fig. 5.17 Decay of local maximum velocity $\langle u \rangle_{\max}$ downstream of barriers relative to depth-averaged initial jet velocity $\langle u \rangle_{b_0}$ in the lower gap region ($0 \leq z/b_0 \leq 1$) with increasing longitudinal distance from the barrier $(x/b_0)^{-0.5}$. The vertical dotted line at $x/b_0 = 1$ denotes the initial downstream point where the average velocity over the bottom gap is calculated. The vertical dotted line at $x/b_0 = 4$ denotes the length of the potential core region, after which the maximum jet velocity experiences a similar decay pattern. The dashed-black line indicates the rate of decay scaling with a decay coefficient of 3.0.

5.3.2.7 Decay of the maximum jet velocity

The maximum streamwise velocity ($\langle u \rangle_{\max}$) and the velocity profile of the flow coming out of the bottom gap vary based on the barrier's angle, but it has a self-similar pattern of decay as the longitudinal distance from the barrier increases. Fig. 5.17 shows the decay of $\langle u \rangle_{\max}$ in the lower gap region ($0 \leq z/b_0 \leq 1$), relative to the depth-averaged velocity $\langle u \rangle_{b_0}$ at an initial downstream location ($x/b_0 = 1$) over the bottom gap region with increasing longitudinal distance from the barrier $(x/b_0)^{-0.5}$. The scaling of the maximum velocity decay in this region is described by a relationship expressed as $\langle u \rangle_{\max}/\langle u \rangle_{b_0} = C_{wj}(x/b_0)^{-0.5}$, where C_{wj} represents the decay coefficient of the wall jet (Wu and Rajaratnam 1995). In the range of $1 < x/b_0 < 4$, there is no notable decay of the maximum jet velocity for the vertical barrier from the LES and experiment, which shows maintained values of $\langle u \rangle_{\max}$ that are close to the value at the point nearest to the barrier ($x/b_0 = 1$). Ead and Rajaratnam (2002) define this region ($1 < x/b_0 < 4$) as the potential core region where the maximum jet velocity remains close to the initial value. However, in the potential core region, the values of $\langle u \rangle_{\max}$ demonstrate an increasing pattern for the downstream-inclined cases, with a notable increase beginning at $(x/b_0)^{-0.5} \geq 0.8$ and with values surpassing those observed in the S0 case (Fig. 5.17a). This pattern can be attributed to the influence of the downwards fluid motion through the upper gaps towards the bottom wall (Fig. 5.12). In contrast, the upstream-inclined cases experience a notable decrease in the values of $\langle u \rangle_{\max}$ beyond this position within the potential core region. The average maximum velocity over the range of $1 < x/b_0 < 4$, relative to the depth-averaged velocity at the initial downstream point, $\langle u \rangle_{\max}/\langle u \rangle_{b_0}$ = 1.10, 1.14, 1.16, 1.18, 1.06, 1.08 and 1.04 for barriers S0, S1d, S2d, S3d, S1u, S2u and S3u, respectively.

Further downstream, beyond the potential core region ($x/b_0 > 4$, $(x/b_0)^{-0.5} > 0.5$), the maximum velocity experiences a reduction from the initial value $\langle u \rangle_{b_0}$, which can be attributed to the loss of momentum caused by the mixing of the jet with the surrounding flow. At $x/b_0 = 4$, there is a significant change in the rate of decay for all cases, as shown in Fig. 5.17. The position of this change at $x/b_0 = 4$ is comparable to the values observed for free jets and offset jets (Bhuiyan et al. 2011). However, it is lower than the corresponding values for plane wall jets at $x/b_0 = 6$ (Albayrak et al. 2008). A decay coefficient denoted as $C_{wj} = 3$ is found to fit the decay pattern at $x/b_0 > 4$, as illustrated by the dashed-black line in Fig. 5.17. However, there is a slight deviation from the scaling decay rate at the S2u and S3u barriers, showing a flatter decay compared to the other cases. This flatter decay can be attributed to these cases exhibiting a larger decay at closer distances to the barrier ($x/b_0 < 4$) compared to the others.

5.3.2.8 Bed shear stress

The increase in near-bed velocity in the vicinity of a leaky barrier is likely to enhance bed shear stress, thereby increasing the risk of local scour and sediment mobilisation both upstream and downstream of the structure (Beebe 2000, Lagasse et al. 2010). This process can

be further exacerbated by the upstream vertical flow diversion and the resultant high-momentum flow beneath the barrier (Figs. 5.7–5.8). Bed shear stress ($\tau_w = \mu\,(\partial\langle u\rangle/\partial z)$) is determined from the first grid cell off the bottom wall ($z = \Delta z$) for all cases, with results presented in Fig. 5.18. In the vicinity of the barrier, $-2 < x_{b_0} < 2$, the maximum bed shear stress varies the most among cases and increases with a decreasing barrier angle in either direction. The vertical barrier S0 induces the highest relative bed shear stress. Peaks in τ_w relative to an initial bed shear stress τ_{w_0} are found at x/b_0 values of 0.05, -0.34, -0.81, -1.44, 0.45, 0.91 and 1.12 for the S0, S1d, S2d, S3d, S1u, S2u and S3u cases, respectively. Correspondingly, the values of τ_w/τ_{w_0} are 11.2, 10.6, 10.0, 6.8, 10.5, 9.3 and 6.7. For all cases, the peak in bed shear stress is observed at around the location of the bottom log. Regardless of the direction of barrier inclination, there are slight variations in the maxima of τ_w between cases with the same angle, i.e. S1d and S1u.

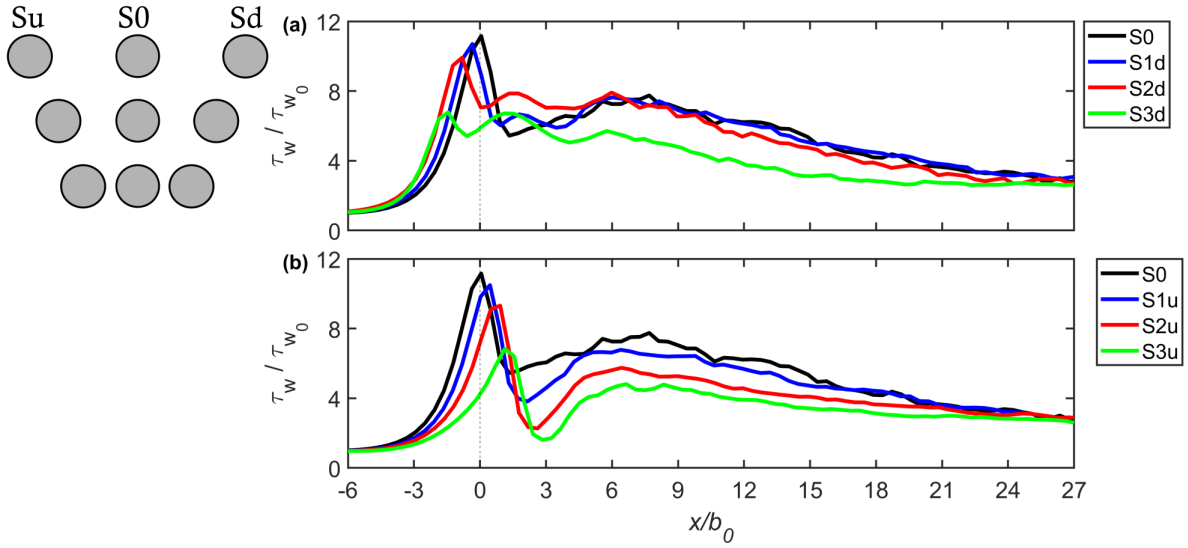

Fig. 5.18 Comparison of the wall shear stress τ_w normalised by an initial bed shear stress τ_{w_0} (x/b_0 = -6) for (a) the downstream-inclined barriers and (b) the upstream-inclined barriers, including the values of the non-inclined barrier (S0). The vertical dashed line at x/b_0 = 0 denotes the origin of the x coordinates. which represents the downstream edge of the top cylinder in all cases.

For the upstream configurations, the τ_w/τ_{w_0} in Fig. 5.18b indicates a marked decrease in bed shear stress magnitude immediately downstream of the barrier for all cases; for instance, this decrease is observed at $x/b_0 \approx 3$ for the S3u configuration. Moreover, as the streamwise distance from the barrier increases, there is a subsequent additional rise in τ_w/τ_{w_0}, with a peak at downstream location $x/b_0 \approx 6$. This increase is observed in the region where the secondary jets can interact with the main wall jet (Fig. 5.13), and this behaviour is attenuated for the barrier layout with a flatter inclination. Further downstream from this location, all cases exhibit a gradual decrease until they converge to an approximate value of $\tau_w/\tau_{w_0} = 2.8$ at around $x/b_0 = 27$.

The Shields parameter is commonly used to determine the threshold of sediment transport based on mean flow and sediment characteristics (Shields 1936). The riverbed is stable

with no sediment movement when the flow is below the threshold criteria. When the flow exceeds the threshold conditions, the boundary sediment is entrained in the flow, causing sediment movement. Shields (1936) collected experimental data on sediment initiation of motion and bedload transport and published the Shields diagram utilising a dimensionless parameter to represent the initiation of sediment motion as a function of the boundary Reynolds number, which is impacted by viscosity and sediment size. Fig. 5.19 shows the Shields diagram, which illustrates the relationship between the dimensionless critical Shields parameter, defined as:

$$\tau_{cr} = \frac{u_{*c}^2}{(SG-1)gd_{50}} = \frac{\tau_c}{(SG-1)\rho g d_{50}} \tag{5.2}$$

with the sediment Reynolds number defined as,

$$Re_* = \frac{u_{*c} d_{50}}{v} \tag{5.3}$$

where τ_{cr} is the dimensionless critical mobility Shields parameter, u_{*c} is the critical shear velocity, τ_c is the critical shear stress, v is the kinematic viscosity, d_{50} is the median diameter of the sediment particle, g is the acceleration due to gravity, ρ is the density of the fluid, and SG is the specific gravity of the sediment which typically ranges from 2.60 to 2.80, though this can vary based on the mineralogical composition. For instance, quartz, which is common in many sediment mobilidasation studies, has a SG around 2.65.

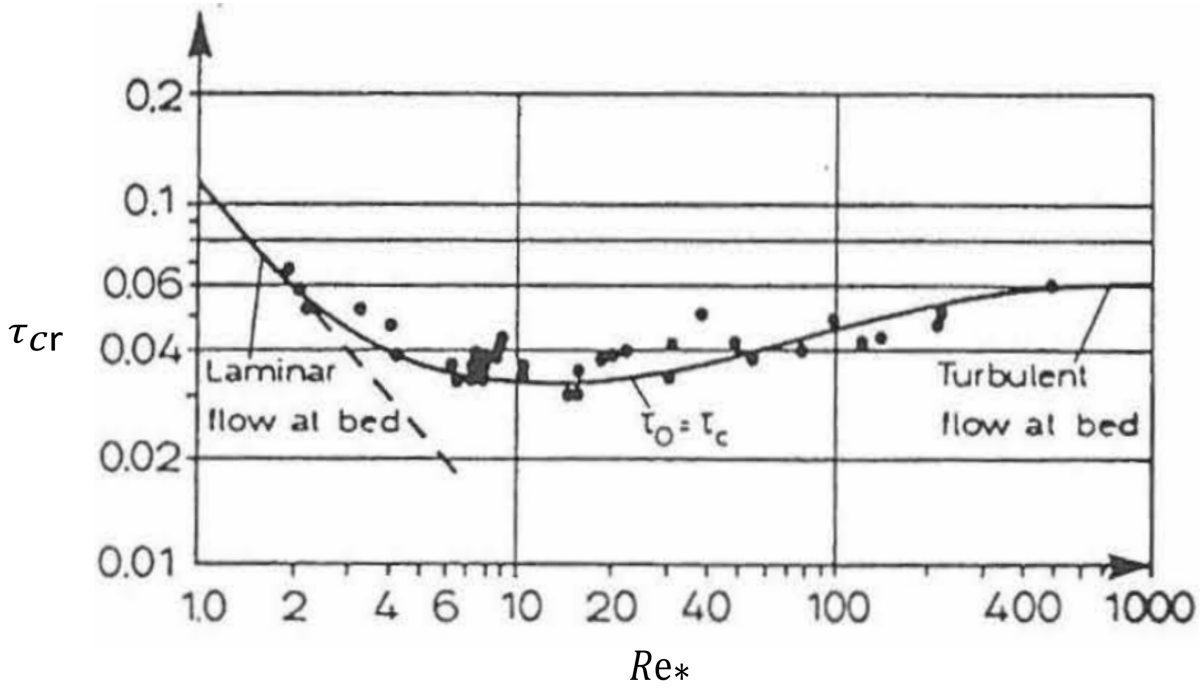

Fig. 5.19 Shields diagram of sediment particles movement, giving the dimensionless critical mobility Shields parameter τ_{cr} as a function of the sediment Reynolds number Re_*, Liu (1998).

As explained by Liu (1998), the Shields diagram presented Fig. 5.19 has three distinct regions corresponding to different flow-sediment interaction situations:

- **Hydraulically smooth flow for** $Re^* \leq 2$: d_{50} is much smaller than the thickness of the viscous sublayer. Grains are embedded in the viscous sublayer, and hence, τ_{cr} is independent of the grain diameter.
- **Hydraulically rough flow for** $Re^* \geq 500$: The viscous sublayer does not exist and hence, τ_{cr} is independent of the fluid viscosity. τ_{cr} has a constant value of 0.06.
- **Hydraulically transitional flow for** $2 \leq Re^* \leq 500$: Grain size is of the same order as the thickness of the viscous sublayer. There is a minimum value of τ_{cr} of 0.031 corresponding to $Re^* = 10$.

The Shields diagram was later modified by many other researchers, including Yalin and Karahan (1979), Julien (1995), Buffington (1999) and Sturm (2001). For instance, Julien (1995) pointed out the difficulty of applying the Shields diagram due to the presence of the critical shear velocity in both axes of the diagram. Therefore, a new variable was used in the horizontal axis instead of the Reynolds number. Fig. 5.20 shows the relation between the critical Shields parameter on the y-axis and the new variable on the x-axis, which is the dimensionless grain diameter, given by:

$$d_* = \left(\frac{(SG-1)gd_{50}^3}{\nu^2} \right)^{\frac{1}{3}} \tag{5.4}$$

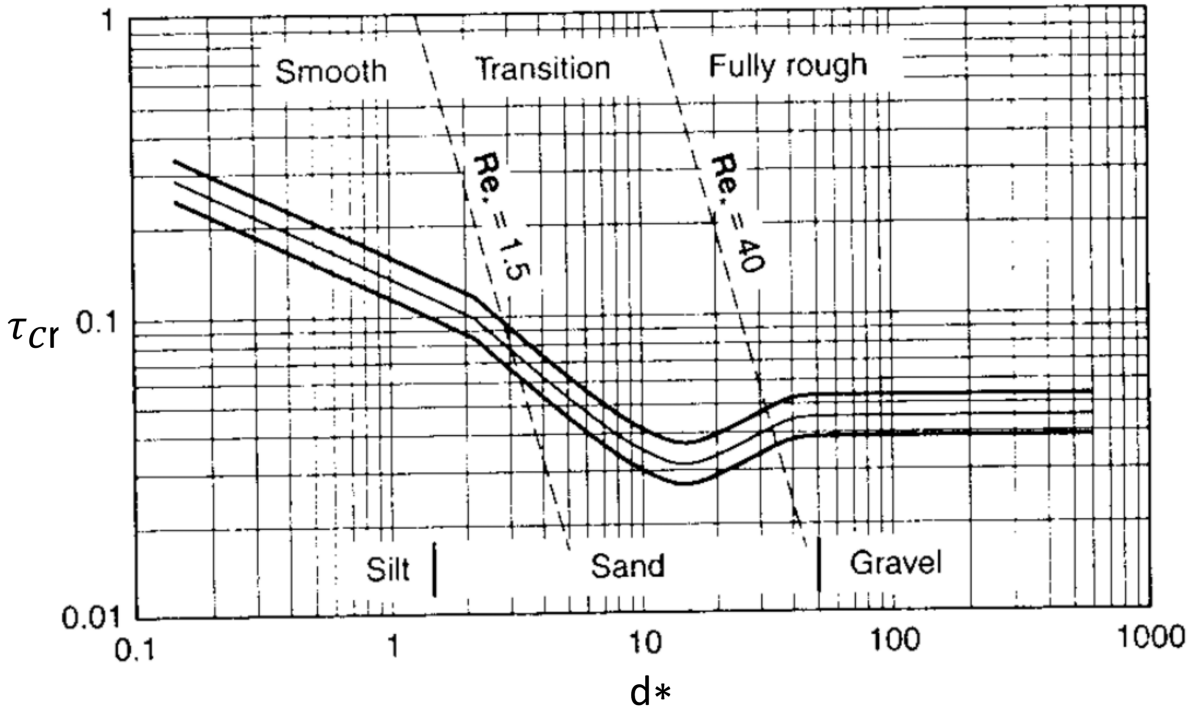

Fig. 5.20 Modified Shields diagram of sediment particles movement using the dimensionless grain diameter d_*, Julien (1995).

Using the calculated value of d_*, the critical Shields parameter (τ_{cr}) is determined from Fig. 5.20, which indicates the critical shear velocity, u_{*c}, for the initiation of sediment motion, defined as follows:

$$u_{*c} = \sqrt{\tau_{cr}(SG-1)gd_{50}} \tag{5.5}$$

then, the critical bed shear stress can be determined as

$$\tau_c = \rho u_{*c}^2 \tag{5.6}$$

where u_{*c} varies with varying d_{50} (Julien 1995).

Alluvial rivers can be broadly categorised into two types based on the median diameter of their sediment particles (d_{50}). Sand-bed streams typically have a d_{50} ranging from 0.0625 mm to 2 mm, while gravel-bed streams range from 2 mm to 64 mm (Hey and Thorne 1986, Bunte 2001). In this context, a scale for NFM streams was established using a model-to-prototype ratio of 1:10, which was derived from the geometric scaling of bankfull depth and cylinder diameter. Following sediment transport scaling guidelines (Pugh 2008), the sand grain sizes were adjusted to conform to Froude scaling, ensuring a settling velocity consistent with the Froude law. This is similar to the work conducted by Müller et al. (2021a), where river and barrier model designs were based on the geometric scaling of four length scales characterising the physical properties of the stream and the presence of leaky barriers at Wilde Brook, Corvedale, Shropshire, UK (Follett and Wilson 2020). For prototype values of d_{50} ranging from 8 mm to 14 mm, the corresponding model values, utilising a 1:10 model-to-prototype scaling, fall within the range of 0.8 mm to 1.4 mm. These values are utilised in the calculation of the Shields parameter, which serves as an indicator of sediment movement. Table 5.1 lists the properties of the sediment used in this research. Fig. 5.21 presents profiles of bed shear stress normalised by the critical bed shear stress, where zones of $\tau_w/\tau_c > 1$ are indicative of potential sediment entrainment activities.

Table 5.1 Properties of the median diameter of sediment particles (d_{50}) adopted in this research, including the dimensionless grain diameter (d_*), the dimensionless critical Shields parameter (τ_{cr}), the critical shear velocity (u_{*c}) and the critical bed shear stress (τ_c).

d_{50} [mm]	d_*	τ_{cr}	u_{*c} [m/s]	τ_c [N/m^2]
0.8	20.237	0.029	0.020	0.382
1	25.296	0.031	0.022	0.502
1.2	30.355	0.035	0.026	0.670
1.4	35.414	0.037	0.029	0.843

The smallest sediment size ($d_{50} = 0.8$ mm) exhibits the largest scour pool length and potential scour depth, seen in Figs. 5.21a-b. As the sediment size increases, the longitudinal extent of the scouring decreases and is solely in the vicinity of the structure ($-2 < x/b_0 < 2$), which is clearly evident in Figs. 5.21c-h. With the increase in the angle of barrier in either direction, the longitudinal extent of the downstream region susceptible to sediment motion

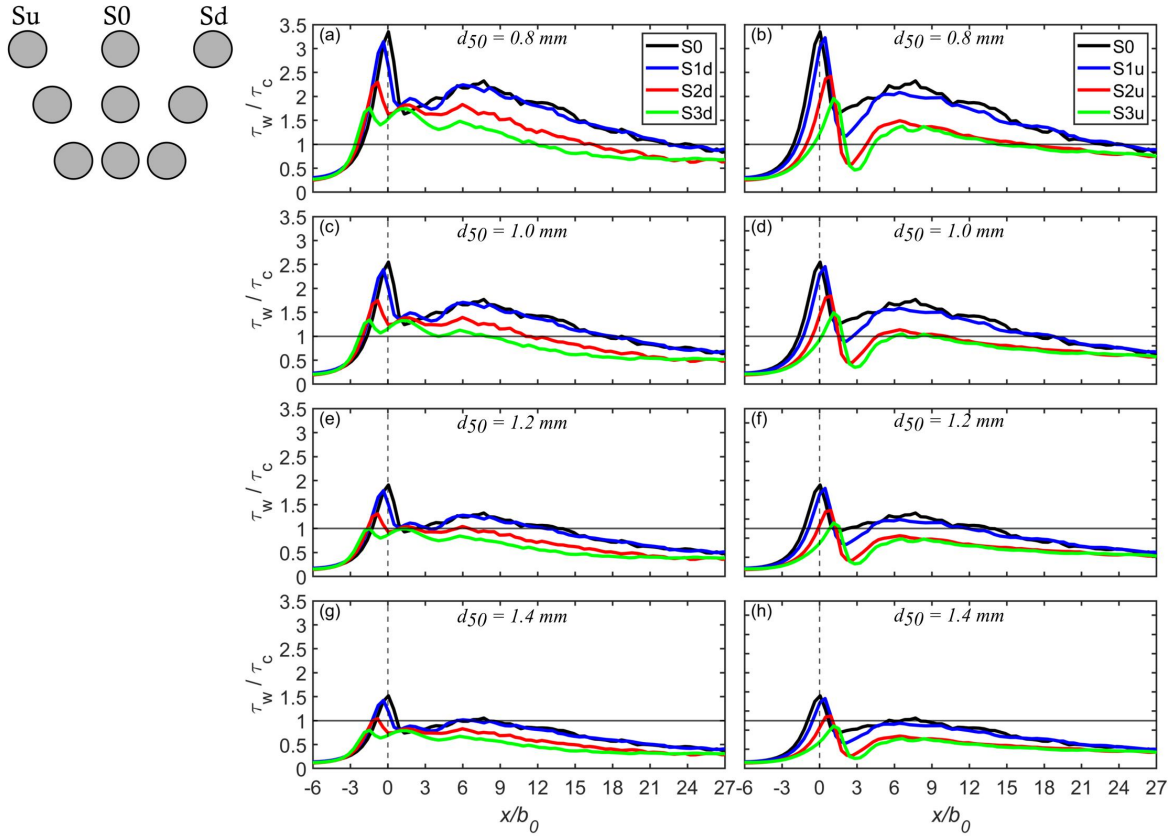

Fig. 5.21 Normalised bed shear stress profiles for the vertical and the inclined barriers to the upstream and downstream directions at (a-b) d_{50} = 0.8 mm, (c-d) d_{50} = 1.0 mm, (e-f) d_{50} = 1.2 mm and (g-h) d_{50} = 1.4 mm. The horizontal black line is the threshold line of motion, where $\tau_w/\tau_c > 1$ depicts possible sediment motion. The vertical dashed line is the origin of the x coordinates, which represents the downstream edge of the top cylinder in all cases.

($\tau_w/\tau_c > 1$) reduces and it is likely that scour depth also reduces. For a sediment size of $d_{50} = 0.8$ mm, the downstream region prone to sediment motion extends up to $x/b_0 = 23$ in the S0 case. However, for the flattest inclination towards the downstream direction (S3d), this extent is shortened to $x/b_0 = 13$. This trend of reduced longitudinal extent of sediment motion continues as the sediment size increases. For S3d and S3u cases with d_{50} = 1.4 mm, no bed erosion will occur, while all other cases will exhibit limited bed erosion (Figs. 5.21g-h).

Scour length (L_{sc}) is determined when the bed shear stress values exceed the values of the critical shear stress, as shown in Fig. 5.21, with Fig. 5.22 presenting the calculated scour length for all simulated cases across four distinct sediment particle diameters, each with a confidence interval of 10%. The 10% margin was chosen based on uncertainties in the selection of the Shields parameter. The original Shields diagram exhibits a clear range of variation, illustrating the variability in critical shear stress values necessary for the incipient motion of sediment particles (Shields 1936). Several factors contribute to this variability, including grain size, bedform features, flow properties, bed roughness, and channel gradient (Shields 1936, Buffington and Montgomery 1997, Church et al. 1998, Shvidchenko and Pender 2000). Moreover, in this research, when employing the velocity gradient method to calculate bed shear

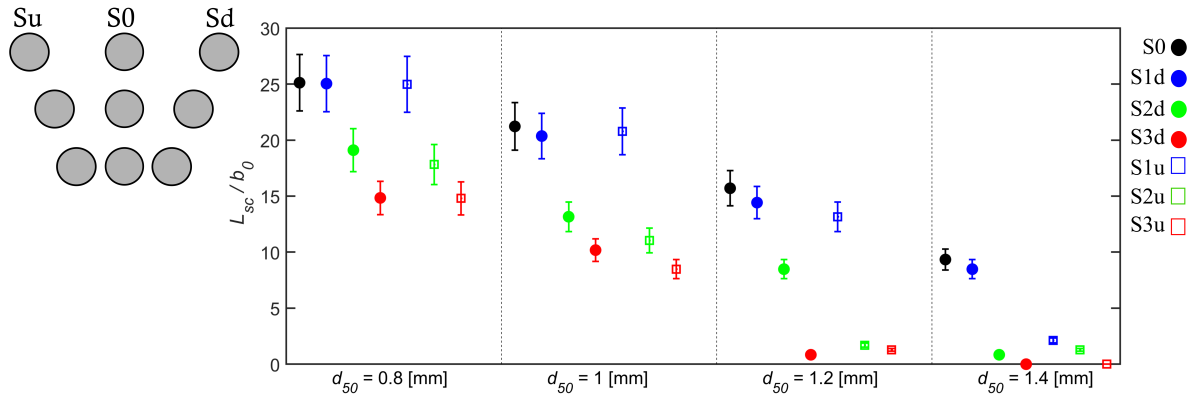

Fig. 5.22 Plot of the estimated scour length normalised by the bottom gap height (L_{sc}/b_0) for the simulated cases considering four different sizes of sediment particle diameter (d_{50} = 0.8, 1.0, 1.2, and 1.4 mm), plotted with a confidence interval of 10%.

stress, the one-dimensional nature of the approach can pose challenges in determining an accurate average bed shear stress, given that the flow is three-dimensional.

For the barrier cases, the finest sediment with a $d_{50} = 0.8$ mm exhibits the greatest scour length, which decreases as the d_{50} value increases. For instance, the non-inclined barrier has an estimated scour length of approximately 1.3 m for a sediment size of $d_{50} = 0.8$ mm, decreasing to about 0.5 m for $d_{50} = 1.4$ mm. In general, the increase in the angle of barrier in either direction results in smaller scour lengths, with the upstream-inclined barriers exhibiting further smaller values compared to the downstream-inclined barriers. For instance, at $d_{50} = 1$ mm, differences in scour lengths are noted between S2u and S3u versus S2d and S3d, with the latter two being greater (Fig. 5.22). However, the S3d and S3u cases exhibit no scour development at $d_{50} = 1.4$ mm.

5.3.2.9 Hydrodynamic coefficients

The hydrodynamic forces experienced by the cylinders are influenced by the presence of an asymmetric flow field that develops around them, which is a consequence of the cylinders' proximity to each other, their closeness to the bottom wall and the free-surface layer, as well as the logarithmic distribution of upstream velocity. The forces acting on the cylinders, namely in the horizontal and vertical directions, are directly calculated using the forces obtained from the immersed boundary method. These forces are then employed to calculate the drag and lift coefficients, as previously described in Section 3.4.10.

Fig. 5.23 presents the drag and lift coefficients determined for each barrier cylinder in all layouts. The average drag coefficients on the top, middle and bottom cylinders are the largest for the non-inclined barrier, with values of C_D = 2.1, 2.2 and 1.7 respectively. These values decrease as the angle of the barrier increases in either direction (Fig. 5.23a). However, the differences in the mean drag coefficients on all cylinders between the inclined-upstream and inclined-downstream cases are small, showing a maximum difference of 16% between S2d and S2u. For the S0, S1d, S1u and S2u cases, the mean drag coefficients on the middle cylin-

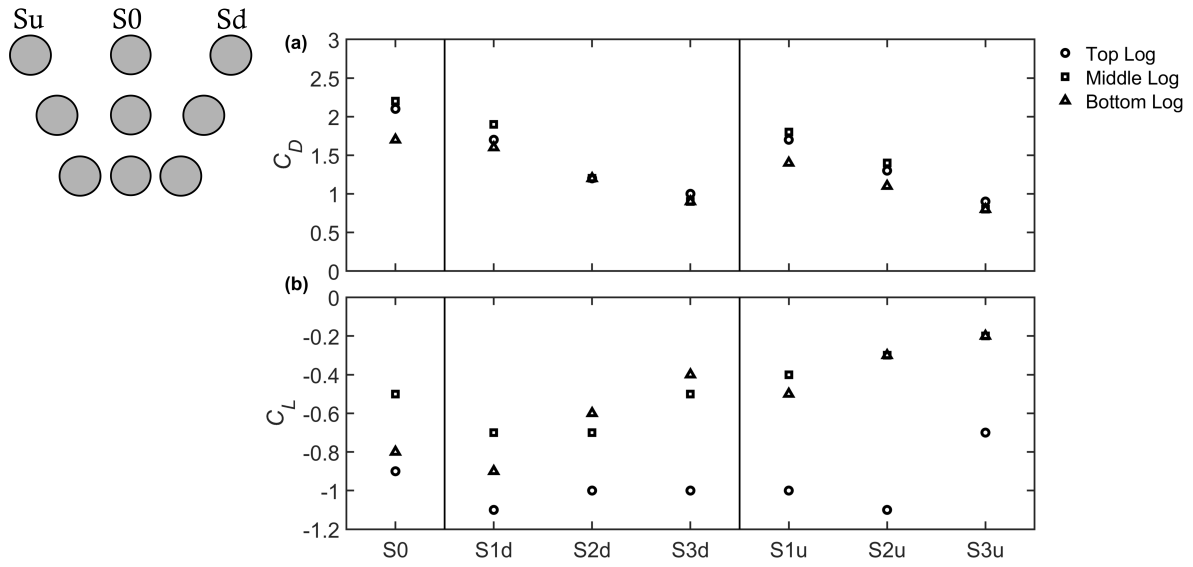

Fig. 5.23 Time-averaged (a) drag and (b) lift coefficients of the top, middle and bottom cylinders for all of the simulated leaky barriers.

der are larger than those on the other cylinders, whereas for the S3d and S3u layouts the top cylinders experience the largest drag force. For the S2d case, the mean drag coefficients on all cylinders are similar. In all cases, the bottom cylinder consistently exhibits smaller drag coefficients compared to the other cylinders. This is due to the fact that the blockage effect is larger for the top and middle cylinders than for the bottom log. In addition, the top and middle cylinders are influenced by both the free surface and the secondary jets, affecting the separation of the shear layers behind them. This, in turn, leads to an asymmetric pressure distribution around the cylinders, and consequently an increase in their drag coefficient (Chu et al. 2018).

Fig. 5.23b reveals that with the close placement of the top cylinder to the free surface, the lift coefficients in all cases reach their maximum value compared to those at the other cylinders, indicating a downward force on the top cylinder ranging from $C_L = –0.7$ to $C_L = –1.1$. For the S0, S1d and S1u configurations, the lift coefficients on the middle cylinder are smaller than those on the other cylinders, which can be attributed to the shielding effect of the other cylinders on the middle cylinder (Tong et al. 2015). With the increase of barrier angle, there is a lessening of the shielding effect, showing smaller lift coefficients on the bottom cylinder than that on the middle log. However, for the S2u and S3u cases, there are no differences in the lift coefficients between the middle and bottom cylinders, with mean values of $C_L = –0.3$ and –0.2, respectively. When comparing the lift coefficients of the middle and bottom cylinders between the upstream and downstream-inclined cases, a noticeable difference becomes apparent. In the downstream-inclined cases, the mean lift coefficients of the middle and bottom cylinders exhibit larger downward forces compared to the upstream-inclined cases. This discrepancy suggests that in the upstream-inclined cases, there is resistance to the downward thrust on these cylinders as the flow through the structure is diverted towards the free surface

due to the direction of barrier inclination.

5.3.3 Leaky barrier design: performance evaluation from an integral hydrodynamic perspective

The seven distinct leaky barrier configurations that are simulated are assessed based on five identified performance aspects. The first aspect to be evaluated is backwater rise, which is a key consideration for well-designed leaky barriers, because this aims to improve channel-floodplain connectivity and water storage, and promotes infiltration into the ground (Collins et al. 2012, Schalko et al. 2019, Muhawenimana et al. 2023). The second aspect to be evaluated in barrier design is to achieve a faster wake recovery, which reduces potential disturbances to aquatic environments or structures, i.e. additional barriers or infrastructure (Bisson and Vvondzei 2003, Reich 2003, Müller et al. 2022). The third performance criterion is the extent of recirculation occurring near the free surface, which induces turbulence and can challenge local aquatic fauna by hindering fish navigation and obstructing migratory patterns (Castro-Santos 2005). This turbulence can also lead to lateral bank erosion, posing risks of instability and potential failure, particularly for unprotected or unvegetated banks (Zhang et al. 2020). The fourth aspect to consider is the potential for bed scour. A proper design of a leaky barrier should prioritise minimising scouring because this alters the surrounding channel hydrodynamics and bank morphology (Dixon and Sear 2014, Wohl and Iskin 2022). Finally, leaky barrier design should also focus on limiting the magnitude of the total force exerted on cylinders because this is essential for maintaining the barrier's structural integrity under varying hydrodynamic conditions (Gippel et al. 1996).

Table 5.2 Performance evaluation of leaky barrier configurations according to various design criteria. Ratings: 1 = Limited, 2 = Poor, 3 = Good, 4 = Very Good, 5 = Excellent

Leaky Barrier Design	**Backwater Rise**	**Wake Recovery**	**Recirculation Adj.**	**Potential Bed Scour**	**Structural Loads on cylinders**	**Total**
S0	5	3	2	1	1	12
S1u	4	4	3	2	2	15
S2u	3	5	4	4	3	19
S3u	2	5	4	5	5	21
S1d	5	3	2	1	2	13
S2d	3	4	1	3	4	15
S3d	2	4	1	5	5	17

Table 5.2 presents an evaluation of the seven leaky barrier configurations, assessed across these five key design criteria: backwater rise (Fig. 5.3), recirculation adjacent to the free surface (Fig. 5.14), wake recovery (Fig. 5.15), potential bed scour (Fig. 5.18, Fig. 5.21 and Fig. 5.22) and structural load on cylinders (Fig. 5.23). The scores for each criterion range from 1 to 5, with 5 indicating the best performance. It is essential to clarify that this scoring methodology combines quantitative analysis (assessing data such as flow rates and structural loads)

and qualitative engineering judgement (interpreting data based on experience). While aiming for objectivity, the reliance on professional expertise and judgement inherently introduces subjectivity, which is carefully counterbalanced with empirical evidence for a thorough evaluation of each design.

Configurations S0 and S1d score 5 in backwater rise but S0 achieves a total low score of 12, which indicates suboptimal performance in other categories, whereas the S1d configuration obtains a slightly higher total score of 13, which is primarily due to a diminished structural load on the cylinders. Both the S1u and S2d barriers yield a total score of 15, with their performance varying across individual criteria. For instance, S1u demonstrates a 'Very Good' rating (4 out of 5) in backwater rise and wake recovery, despite comparatively lower performance in other aspects. Meanwhile, S2d achieves a rating of 4 (out of 5) in wake recovery and structural load on cylinders and a 3 in backwater rise. With a total score of 19, the S2u case achieves a score of 5 in wake recovery and scores of 4 in both recirculation adjacent to the free surface and potential bed scour, significantly contributing to its overall performance. In comparison to the S2u design, the S3u configuration improves the performance in bed shear stress and structural loads but induces less backwater rise, ultimately achieving the highest mark of 21. Despite the lower total score of 17 for the S3d configuration compared to its counterpart inclined to the upstream direction, the S3d barrier performs with a rating of 5 in potential bed scour and structural load on cylinders, which is similar to the rating of those aspects at the S3u barrier.

Overall, the upstream-inclined configurations outperform their downstream counterparts, particularly those with flatter inclination, such as the S3u design. Consequently, when assessing the effect of leaky barrier design, it is clear that when a leaky barrier is designed to achieve maximum backwater rise, this leads to a decreased performance in essential criteria, and vice versa.

5.4 Case ii: Comparative analysis of leaky barriers with varied longitudinal lengths

This section will discuss six additional leaky barrier designs each varying in barrier length in the streamwise direction.

5.4.1 Computational setup

The experimental setup of Müller et al. (2021b) who studied long porous leaky barriers in lab-scale open channel flow is adopted and expanded upon by investigating various other barrier designs, with the main configuration, S24, replicating the original experiment and featuring a linear barrier with a longitudinal length (L_s) of 0.2 m (Fig. 5.24). This barrier comprises three rows of horizontal cylinders with a diameter (D) of 0.025 m that spans the full channel width. It maintains a vertical gap (b_0) of $2D$ from the bottom wall to the lower side of the barrier and a vertical distance (b) of $0.5D$ between the rows, allowing flow through the barrier. Five

additional configurations are numerically investigated by varying the longitudinal length of the barrier: S6 (0.05 m), S9 (0.075 m), S12 (0.1 m), S15 (0.125 m) and S18 (0.15 m). The term "Si" denotes the number of dowels in each configuration.

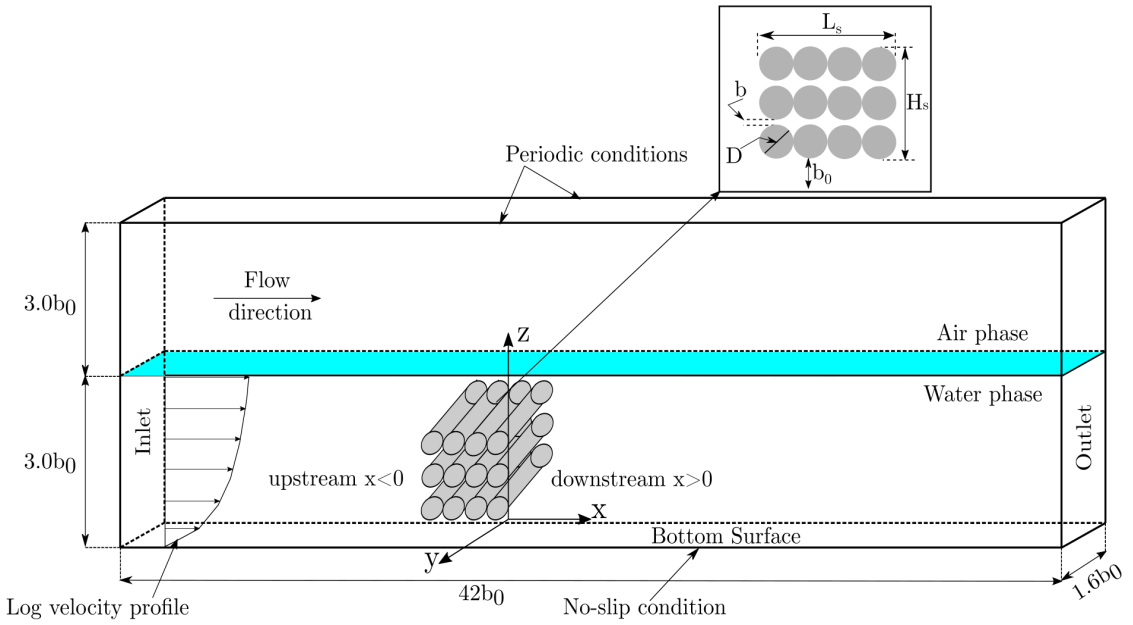

Fig. 5.24 Schematic of the computational domain adopted for the LES of a leaky barrier comprising three rows of dowels with equal diameters (D) situated at a height of b_0 above the bottom surface, with a vertical gap of b between rows. The longitudinal length is denoted by L_s, while the barrier's height is H_s. The inflow boundary condition with a logarithmic velocity distribution is also indicated.

The computational domain shown in Fig. 5.24 spans 2.1 m in the x-direction (streamwise), 0.08 m in the y-direction (spanwise), and 0.3 m in the z-direction (vertical). The origin of the coordinates is chosen as the downstream end of the leaky barrier from the upstream inlet. The mean flow depth (H) and bulk velocity (U_0) are equal to 0.15 m and 0.28 m/s, respectively, resulting in a Reynolds number ($Re = U_0 D/\nu$) of 7000 and Froude number ($Fr = U_0/\sqrt{gH}$) of 0.23. The grid is uniform throughout the domain, with a resolution of $\Delta x/D$ = $\Delta z/D$ = 0.025 and $\Delta y/D$ = 0.06. The time step is variable with a CFL condition of 0.2 to maintain numerical stability. For the boundary conditions, a mean logarithmic velocity profile is adopted at the inlet according to a smooth log-law distribution with a friction velocity of 0.019 m/s, a convective condition is used at the outlet, a no-slip condition is imposed at the bottom of the domain and periodic conditions are set at the lateral sides. The LSM calculates the water-surface deformation, with the top of the domain treated as a slip condition. All of the simulations are executed on 1400 CPUs, and flow statistics averaging commences after approximately four flow-through periods (T_f) once the initial flow transients have vanished. The process continues for about 40 flow-through periods to calculate mean flow statistics once the flow is fully developed.

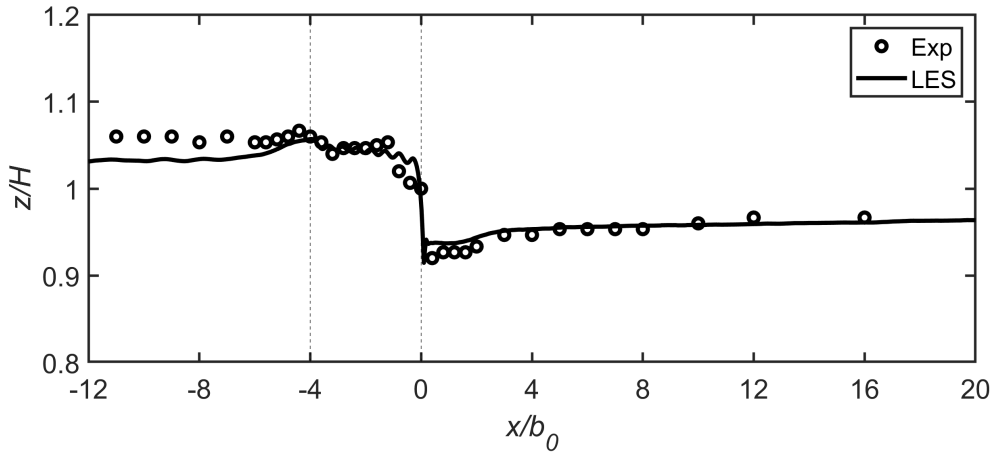

Fig. 5.25 Comparison of the mean water-surface elevation (z) normalised by the mean flow depth (H) between experiment (symbols) and LES (line) for the S24 case. The vertical dashed lines indicate the upstream and downstream ends of the leaky structure.

5.4.2 Results and discussion

5.4.2.1 Free surface profiles

The free-surface elevation results from a prior experimental study for S24 (Müller et al. 2021b) and those obtained from the current LES for the same S24 scenario are presented in Fig. 5.25. Both the experimental data and LES results for S24 show good agreement. The LES effectively captures the drop in the free surface immediately downstream of the S24, as well as the free-surface patterns in the region further downstream. However, the LES slightly underestimates the water depth upstream of the leaky barrier. The simulated free-surface profiles for the cases S6, S9, S12, S15, S18, and S24 are shown in Fig. 5.26a, illustrating the change in the free surface profile with varying L_s. In all cases, the water level is elevated upstream of the leaky barrier, experiences a marked drop immediately downstream and then shows a gradual recovery further downstream of the barrier. Distinct surface ripples, originating from the top edge of the barrier and extending its length, are especially evident in the range $-1 < x/L_s < 0$ and are more pronounced for larger barrier lengths. When comparing the mean water elevations for the various cases at a specific upstream location, i.e. at $x/L_s = -2$, the shortest barrier length (S6) exhibits the highest upstream water depth. In other words, the highest backwater rise, ΔH (defined as $\Delta H = H_1 - H_2$, where H_2 is calculated from a point further downstream after the free surface is recovered), is $0.44D$ mm for the S6 case, while the lowest rise of $0.32D$ mm is identified for the S9 design. This variation is further illustrated in Fig. 5.26b, which shows the calculated backwater rise normalised by the mean water depth in relation to the longitudinal length of the barrier. Cases between S9 and S15 show negligible differences. Fig. D.1 (appendix D) illustrates the development of the free surface at three different streamwise distances from the inlet to the position of the cylinders. This visualisation is intended to ensure that there are no adverse effects on the free surface development due to the proximity of the upstream inlet or due to the constrained water surface to a fixed depth at the inlet.

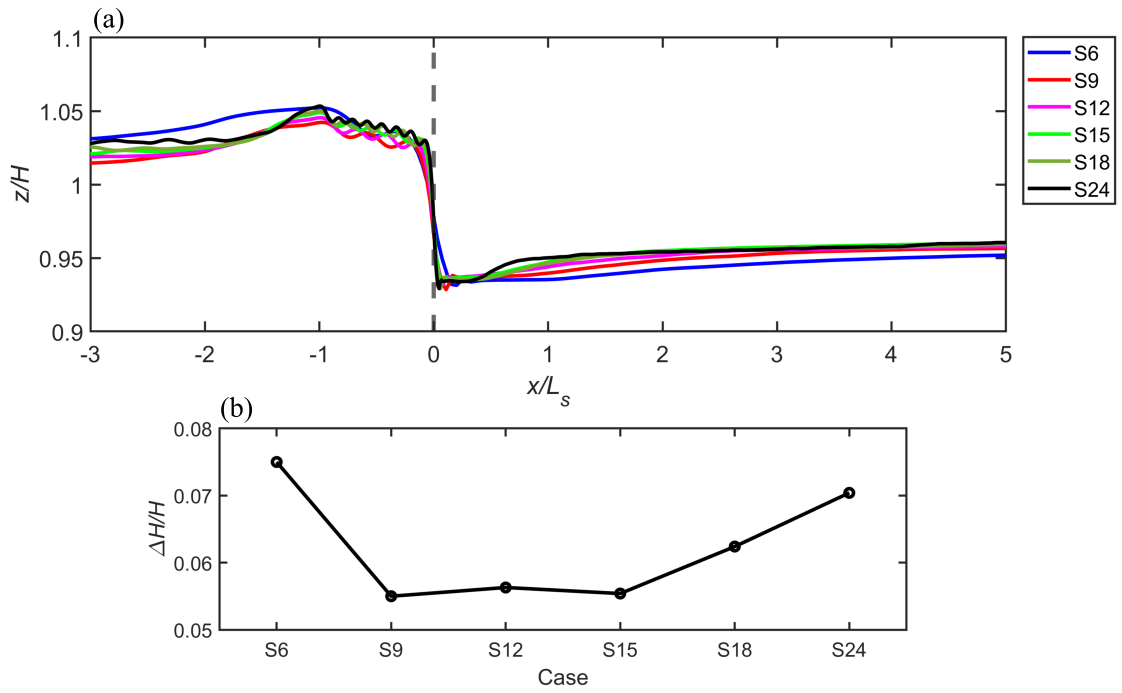

Fig. 5.26 (a) Free-surface profiles obtained from the LES, the vertical dashed lines indicate the downstream edges of the leaky structure; and (b) the calculated backwater rise (ΔH) normalised by the mean water depth (H) for all cases.

5.4.2.2 Time-averaged flow characteristics

The contours presented in Fig. 5.27 show the time-averaged streamwise velocity for all of the leaky barriers along the channel centre-line plane at $y/b_0 = 0.8$, which provides evidence for how the approaching flow impinges on the barriers and subsequently accelerates over, through and beneath them. Beneath the barrier, and in the downstream region along the bottom gap where $z/b_0 < 1$, a high-momentum area is present. This condition is attributed to the fluid undergoing acceleration as it passes through the bottom gap, leading to the formation of a wall jet. This acceleration is capable of inducing scouring effects that alter the sediment distribution, as sediment is eroded from areas surrounding the leaky barrier and subsequently deposited in regions further downstream of the barrier (Aamir and Ahmad 2016). At higher water depth $z/b_0 > 1$, a low-momentum region is featured, specifically near the free surface. Areas of high streamwise velocities are also evident between the cylinders, suggesting the formation of secondary or offset jets, which are seen to deflect downwards towards the bottom wall for all cases and later merge with the main wall jet at a further distance downstream of the barrier (Fig. 5.27).

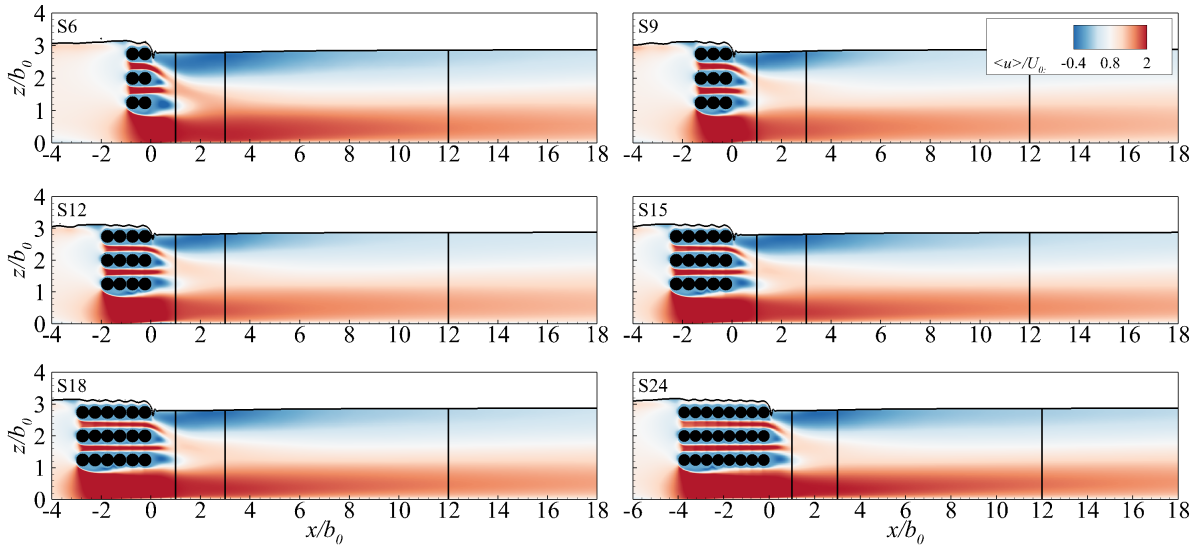

Fig. 5.27 Side-elevation contour plots of the LES computed streamwise velocity $\langle u \rangle$ for all of the simulated cases. The vertical lines that are overlaid on the contours indicate the positions where vertical profiles are taken, and are plotted in Fig. 5.28. The free-surface is depicted as a solid-black line.

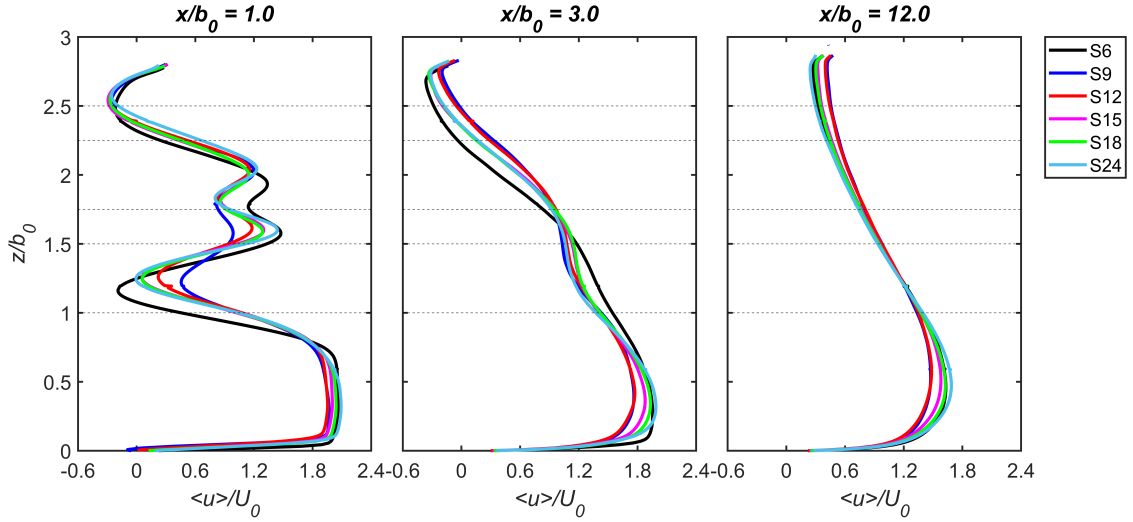

Fig. 5.28 Profiles of normalised mean streamwise velocity at three selected locations downstream of the leaky barriers. The dotted lines indicate the positions of the cylinders.

Among the cases, differences in the streamwise velocities are examined through vertical profiles of $\langle u \rangle$ taken at three downstream locations from the barriers (specified as $x/b_0 = 1.0, 3.0,$ and 12.0), as shown in Fig. 5.28. At $x/b_0 = 1.0$, pronounced normalised streamwise velocities are observed along the bottom gap where $z/b_0 \leq 1$. In this region, the S6 and S24 cases feature almost similar magnitudes, while the S9 and S12 cases have the least pronounced values. Further downstream along the bottom gap, specifically at $x/b_0 = 3$ and $x/b_0 = 12$, the streamwise velocities decrease. The differences between the cases become more pronounced, with S9 and S12 consistently showing the lowest velocities. This indicates the weakest development of the wall jet.

At $x/b_0 = 1.0$, a significant reduction in the streamwise velocities is observed downstream

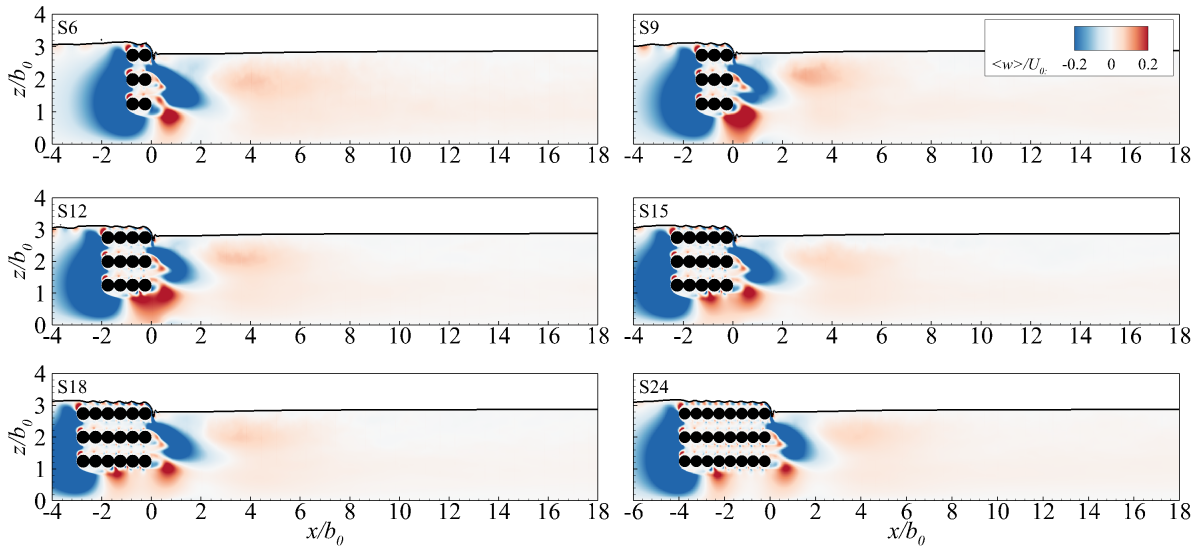

Fig. 5.29 Side-elevation contour plots of the LES computed vertical velocity $\langle w \rangle$ for all simulated cases. The free-surface is depicted as a solid-black line.

of the lowest row ($1.0 < z/b_0 < 1.5$), due to the obstruction of the cylinders at this position. This reduction is not seen behind the middle row of the cylinders ($1.75 < z/b_0 < 2.25$), which can be attributed to the effects of the downwards fluid motion through the inter-cylinder gaps. Along the lower inter-cylinder gap ($1.5 < z/b_0 < 1.75$), there is a noticeable increase in the $\langle u \rangle$ magnitude, contrasting with the region behind the upper inter-cylinder gap ($2.25 < z/b_0 < 2.5$), where the flow is deflected towards the bottom wall. This latter region is characterised by high vertical velocity, which will be discussed later. At $x/b_0 = 3.0$, the velocity deficit behind the lowest row recovers in all cases, with the S6 case showing the highest streamwise velocities. However, the S6 case exhibits the lowest streamwise velocities at greater water depths compared to the other cases. At $x/b_0 = 12$, all cases exhibit a quicker flow recovery, with the S9 and S12 cases being the closest to reaching full recovery ($\langle u \rangle / U_0 \approx 1$), especially at higher water depths $z/b_0 > 1.5$ (Fig. 5.28).

Fig. 5.29 shows the contours of time-averaged vertical velocities, revealing two distinct regions characterised by negative vertical velocities indicating a downwards fluid motion. The first region is located upstream of the leaky barrier, while the second is primarily found along the upper inter-cylinder gap of the barrier. This second region explains the reduction in streamwise velocities shown in Fig. 5.28, reflecting the behaviours of the offset jet. Furthermore, an area exhibiting high vertical velocities is observed downstream of the barrier, close to the bottom row, as illustrated in Fig. 5.29. This phenomenon arises from the wall effect, where the fluid accelerates through the gap between the barrier and the bottom wall. For longer barriers, specifically those of $L_s > 0.1$ m, e.g. S15, the extent of the positive vertical velocities region reduces, forming two smaller regions along the lower side of the bottom row.

The complex behaviours of fluid motions, which move both upwards and downwards, can lead to significant turbulent fluctuations downstream of the leaky barrier. Fig. 5.30 illustrates contours of turbulent kinetic energy (tke), highlighting a region with elevated tke levels

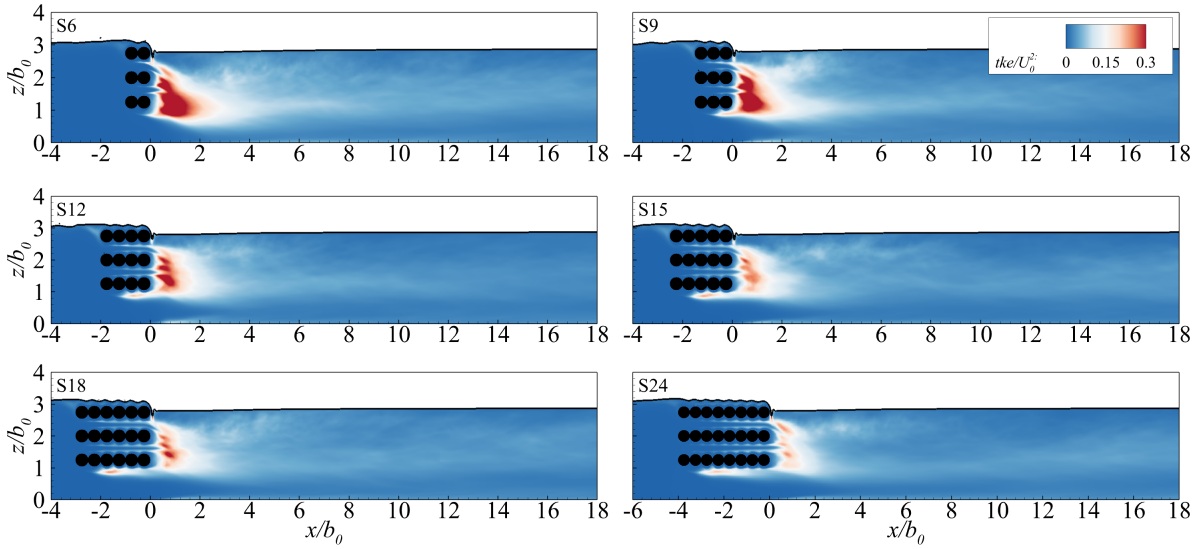

Fig. 5.30 Contours of normalised turbulent kinetic energy (tke/U_0^2) comparing the different simulated cases. The free-surface is depicted as a solid-black line.

downstream of the barrier, predominantly along the lowermost cylinders and most profoundly along the lowest row. This region manifests a common characteristic of mixing jets. Fig 5.30 shows that as the barrier length in the streamwise direction increases, a notable reduction in the *tke* levels occurs within this region.

Fig. 5.31 presents contours of vertical Reynolds shear stress $(-\langle u'w'\rangle)$, which reflects turbulent momentum exchange downstream of the barrier. The results reveal that the highest momentum exchange occurs behind the lowest row, with higher values of $-\langle u'w'\rangle$ below the row than above it. For shorter barrier lengths, regions with high levels of vertical Reynolds shear stress are pushed closer to the bottom wall. Conversely, as the barrier length increases, the highest $-\langle u'w'\rangle$ region does not approach the bottom wall and maintains its orientation in the x-direction. Furthermore, another region of turbulent momentum exchange is observed downstream of the middle row, but with lower $-\langle u'w'\rangle$ values and smaller extents compared to that emanating from the bottom row. The distribution and magnitude of the vertical Reynolds shear stress exhibit negligible differences among cases with barrier lengths greater than 0.1 m ($>$ S12). Furthermore, the close proximity of the free surface to the leaky barrier induces an additional contribution to momentum exchange near the free surface. This can be attributed to the variation in the free-surface dynamics and the alteration in the direction of fluid motion downstream of the barrier, as previously discussed. Notably, this effect is most pronounced for the S9 configuration, as shown in Fig. 5.31.

5.4.2.3 Recirculation region

Recirculation zones that occur in regions with a low-momentum inner wake are shown in Fig. 5.32. These zones unveil two recirculating cells formed behind the bottom and middle cylinders. The distribution of these cells is asymmetrical around the log's centre, with the upper cell being smaller due to the effect of the downwards deflection of the offset jets. The recir-

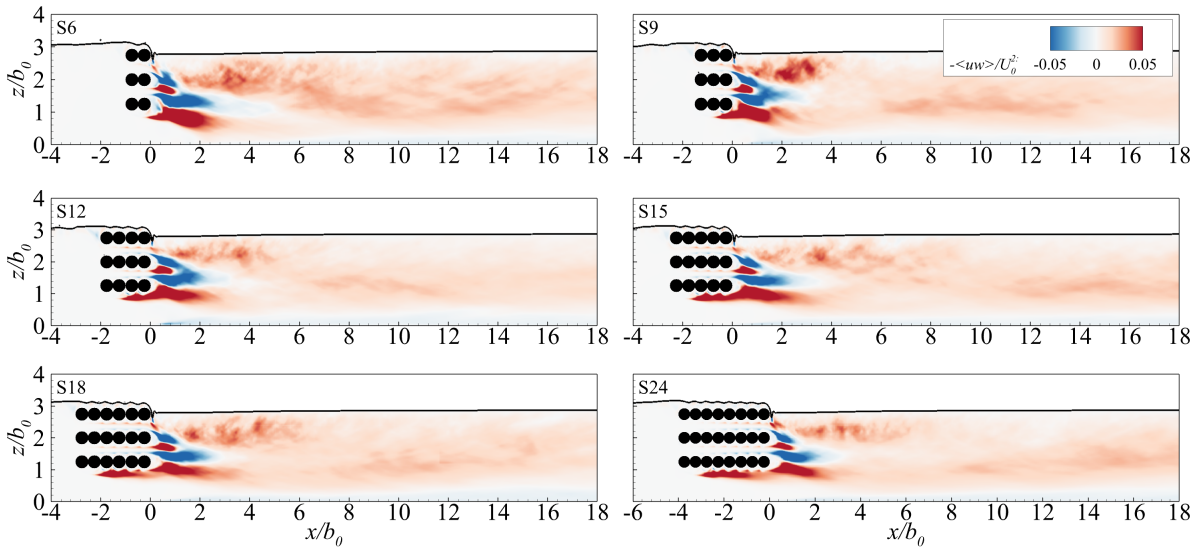

Fig. 5.31 Contours of normalised vertical Reynolds shear stress $(-\langle u'w'\rangle/U_0^2)$ comparing the different simulated cases. The free-surface is depicted as a solid-black line.

culating cells behind the bottom cylinder extend more in the streamwise direction than those behind the middle cylinder for all cases. This distinction is particularly noticeable for the S6 case. However, no recirculation core forms behind the top cylinder because it is inhibited by the impact of the significant drop in the free surface immediately downstream of the leaky barrier.

Downstream of the leaky barrier, a large recirculation zone forms, attached to the free surface. This is due to the downwards motion of the flow overtopping the barrier and the acceleration of the flow through it, leading to low streamwise velocities near the free surface. The length of this recirculation zone is determined by the point of flow convergence in the upper wake region, which sets the boundary of the velocity deficit region. In the S6 case, the recirculation length is approximately $6b_0$, whereas for the S9 and S12 designs it reduces to about $4b_0$, while falling within the range of $4b_0$–$6b_0$ for the other designs. In addition, all of the cases feature another small recirculation zone positioned between the large recirculation region and the free-surface layer, immediately downstream of the barrier (Fig. 5.32).

5.4.2.4 Potential bed scour

Vertical flow diversion upstream and the resulting high-momentum flow beneath leaky barriers are assumed to increase bed shear stress, potentially raising the risk of pit formation and particle mobilisation if the bed shear stress exceeds the critical shear stress. Similarly to what was discussed before in Section 5.3.2.8, values of $d_{50} = 0.8\text{mm} - 1.4\text{mm}$ are used in calculating the Shields parameter. Fig. 5.33 presents profiles of bed shear stress normalised by the critical bed shear stress, where zones of $\tau_w/\tau_c > 1$ are indicative of potential sediment entrainment activities. The region susceptible to sediment motion begins at the upstream edge of the leaky barrier and reaches a peak in the middle of the leaky barrier region for cases with

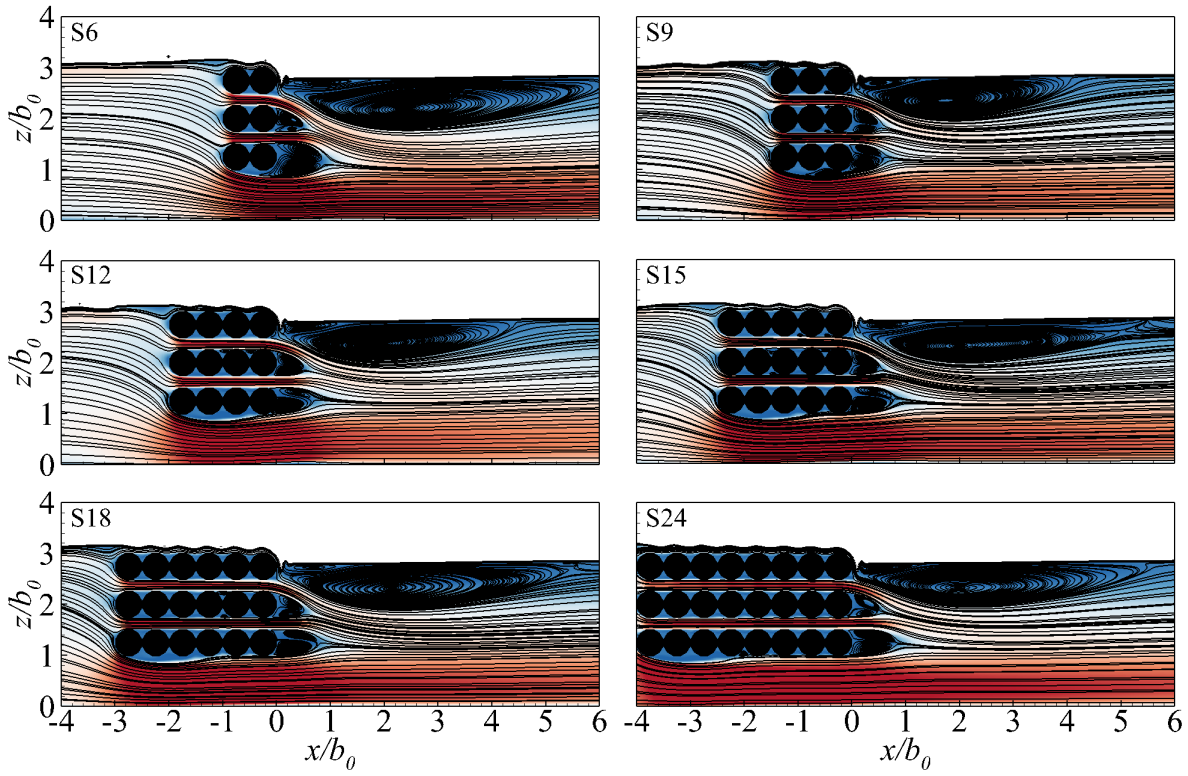

Fig. 5.32 Recirculation regions computed using LES for all of the simulated cases, superimposed with contours of normalised mean streamwise velocity.

short barrier lengths, specifically in the S6 case. As the barrier length increases, the peaks are reached before the middle region is attained. Subsequently, they begin to decrease and, in cases where $L_s > 0.075$ m (greater than S9), no sediment motion is indicated in the downstream region of the leaky barrier.

The smallest sediment size, $d_{50} = 0.8$ mm, exhibits the largest magnitude of areas prone to sediment motion. For $d_{50} = 0.8$ mm, the peak values of τ_w/τ_c are 1.85, 1.91, 1.98, 2.03, 2.06 and 2.26 for barrier lengths S6, S9, S12, S15, S18 and S24, respectively, which indicates that the potential scour depth increases with increasing barrier length. As the sediment size increases, the likelihood of sediment movement reduces, as evident in Fig. 5.33. For the largest sediment size studied, $d_{50} = 1.4$ mm, potential sediment entrainment is only apparent for the longest barrier length, S24. Overall, these results indicate that increasing the longitudinal length of the leaky barrier leads to an increase in the risk of local scour and sediment mobilisation.

5.5 Closure

Large eddy simulations using the level set method are performed on different designs of leaky barriers, covering two primary cases examined in this chapter. In the first case, flow around leaky barriers (LB) composed of three circular cylinders was investigated. The main LB configuration considered vertically aligned cylinders, with other layouts inclined at $\gamma = 15°$, 30°,

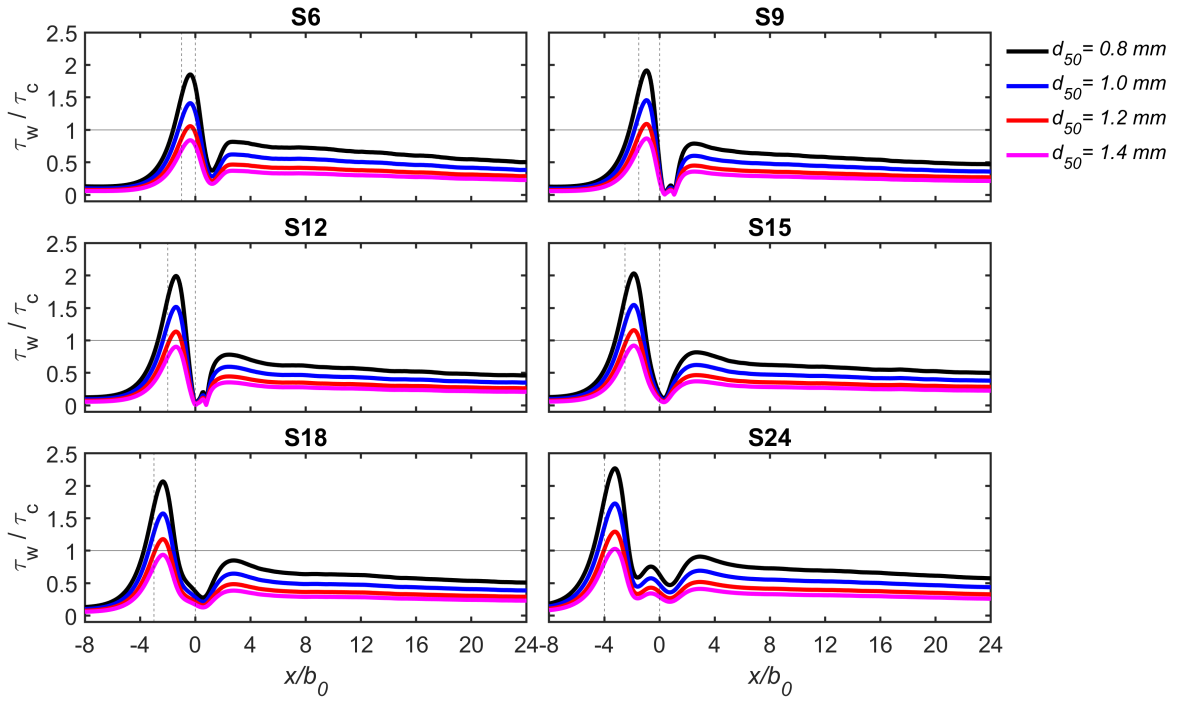

Fig. 5.33 Normalised bed shear stress profiles for the linear leaky barriers with different longitudinal lengths at d_{50} = 0.8 mm, 1.0 mm, 1.2 mm and 1.4 mm. The horizontal black line is the threshold line of motion, where $\tau_w/\tau_c > 1$ depicts possible sediment motion. The vertical dashed lines indicate the start and the end of the leaky barrier region.

and 45° in both upstream and downstream directions. The simulations were conducted at a Reynolds number of 7,250 based on the cylinder's diameter and bulk velocity, and for when the barrier crest is overtopped. The LES results were validated for the main configuration where cylinders were vertically-aligned (S0), showing good agreement with the experimental results for time-averaged flow quantities and free surface elevation. The simulation successfully captured the streamwise and vertical velocities, their time-averaged fluctuations, and variation in the free surface layer and high-momentum jet underneath the barrier.

For all barrier configurations, the close proximity of the upper cylinder to the free surface affects the flow separation over the shear layers, which converge and deflect downwards, resulting in an interaction with shear layers generated from the adjacent mid log, increasing the unsteadiness and coherence of the turbulent wake. Increasing the angle of the barrier towards the upstream direction resulted in reduced longitudinal extent of regions with high streamwise velocities along the bottom gap height and increased streamwise velocities in downstream regions near the free surface compared to the other cases. In addition, upstream-inclined barrier designs (S1u, S2u, S3u) resulted in high upward velocities through the inter-cylinder gaps of the barrier. This is in contrast to the downstream-inclined designs (S1d, S2d, S3d), where vortices shed travelled predominantly downwards towards the streambed. Increasing the angle of the barrier in the downstream direction resulted in a distinct reduction in both turbulent kinetic energy and vertical Reynolds shear stress.

The inclination of the barriers significantly impacted the flow dynamics, with implica-

tions on the formation of recirculation zones downstream of the leaky barrier, wake recovery, and the gap flux ratio. Both vertically-aligned and downstream-inclined barriers developed a large recirculation zone near the free surface. However, upstream inclination of the barrier, particularly in the S2u and S3u cases, limited the formation of this recirculation zone. Barrier designs with flatter inclinations upstream (S3u) demonstrated quicker wake recovery and an earlier return to near-zero velocity deficit in the far wake compared to cases with greater angles in the downstream direction. Variations in the gap flux ratio revealed that flattening the barrier inclination in both directions (S3u, S3d) resulted in differences in the fluxes at the bottom gap and between the upper cylinder and the free surface, while negligible differences were found in the inter-cylinder gap fluxes.

In assessing how leaky barrier design influenced bed shear stress, flatter barrier designs (S3u, S3d) resulted in a decrease in peak bed shear stress in the vicinity of the structure, effectively diminishing the scour potential and reducing the scouring pool region underneath the barrier and immediately downstream. The structural load on the cylinders was influenced by the cylinder configuration, and as the cylinders were arranged in a flatter configuration (angle increased), the drag and lift coefficients decreased. The top cylinder exhibited a larger downward force compared to the other cylinders due to its proximity to the free surface.

The findings of the first case give new insight into leaky barrier hydrodynamics and barrier design. The results indicate that to maximise backwater rise a leaky barrier design with cylinders aligned in the vertical plane is advantageous to an inclined design. If the risk of local bed and bank scouring needs to be limited and considered in light of site sediment management goals and site-specific conditions (e.g. steep bed slope) then scour risk can be mitigated by the utilisation of an upstream- or downstream-inclined barrier design. To achieve a balance between optimal flood mitigation and sediment management, an upstream-inclined configuration offers the best hydrodynamic performance. In natural flood management schemes consideration needs to be given to a strategy that integrates aspects of these design elements in working towards sustainable solutions which are sensitive to the stream and catchment setting.

In the second case, the effect of the longitudinal length of the leaky barrier spanning from 0.05 m to 0.2 m on wake characteristics and the flow field is discussed. The simulations were conducted at a Reynolds number of 7,000 based on the cylinder's diameter and bulk velocity. The results revealed distinct variations in water-surface profiles, with the backwater rise being the highest in the S6 case. Conversely, it was the smallest for cases between S9 and S15, but increased again with the extension of the barrier's longitudinal length. Streamwise velocities revealed the interaction between the flow and the leaky barrier, leading to phenomena such as the wall jet and offset jets formed by high-velocity flow through these gaps. Notably, the S9 and S12 designs exhibited lower streamwise velocities along the bottom gap compared to the other cases, suggesting a less prominent wall jet formation.

Analysis of the time-averaged vertical velocities revealed two regions characterised by the

upwards and downwards fluid motions along the lowermost cylinders, which coincide with the region of high turbulence levels. The magnitude and distribution of these effects were notably influenced by the barrier lengths. For instance, as the barrier length increased, the turbulent kinetic energy levels decreased, indicating a reduction in mixing jets with the increase in barrier length. The vertical Reynolds shear stress patterns revealed areas of turbulent momentum exchange, with the most pronounced exchange observed behind the bottom row, showing negligible differences between cases of larger barrier length, i.e. $L_s > 0.1$ m. Multiple recirculation zones were observed, all enclosed by the cylinders except for one large recirculation zone that formed downstream of the barrier, near the free surface. Behind the top log, the plunging flow and its proximity to the free surface inhibited the recirculation zones. The length of the near-surface recirculation zone was largest for the S6 design, while the S9 and S12 designs had the least extensive ones.

In assessing the impact of varying barrier lengths on bed shear stress, an increase in barrier length corresponded to an increase in bed shear stress and potential scour depth. Based on the current hydrodynamics results, several key insights emerge that can guide stakeholders in designing leaky barriers and facilitate the wider use of NFM in flood risk management. The longitudinal length of the leaky barrier is pivotal in determining the behaviour and interactions within the fluid system. Designs such as S6, S18, and S24 exhibit maximum backwater rise compared to the others. This is optimal for flood management because the increased backwater acts as temporary storage, helping to delay and reduce downstream flood peaks, promotes sediment deposition which can help in restoring and nourishing eroded areas, and can also facilitate groundwater recharge, enhancing local water supplies. However, the latter designs (S18 and S24) are not advised if the risk of local bed and bank scouring needs to be limited.

CHAPTER 6

Predictive Methods for Estimating Water Depth and Velocity Due to Leaky Barriers

6.1 Aim of the chapter

This chapter addresses a significant knowledge gap in quantifying the hydraulic impact of leaky barriers on both structural and reach scales, which has long hindered the ability to incorporate NFM schemes into broader flood risk management strategies. To address this, hand-calculation methods are introduced to estimate water depths and velocities induced by a given leaky barrier design. These methods are expected to enhance understanding of the impact of leaky barriers on backwater rise, water storage, and velocity reduction and to help in the design of effective water management strategies.

6.2 Summary

Several analytical equations based on experimental data aim to predict backwater rises associated with leaky barriers (Schmocker and Hager 2013, Schalko et al. 2019, Follett et al. 2021). These equations consider many variables, including the approach flow Froude number, wood compactness, wood volume, blockage ratio and barrier length. However, despite the research efforts on this subject so far, none of the equations studied have demonstrated universal suitability across diverse hydraulic conditions or settings. Nevertheless, it is important to note that there is no definitive approach or methodology that can be considered the absolute best, as different methods may prove more effective depending on the specific situation being examined. A thorough understanding of the hydraulics of leaky barriers is necessary to fully assess their impact on the river flow environment.

This chapter introduces and compares two methods for estimating the flow depth and velocity upstream or downstream of leaky barriers, in situations where only one of the conditions is already known. The first method is based on the momentum and continuity equations, while the second method adopts a modified empirical relation previously used for estimating bridge afflux. These direct methods are validated using experimental and simulated data sets from the literature, covering Reynolds numbers ranging from 4,800 to 14,000. The predicted upstream and downstream water depths and velocities for both methods showed a good agree-

ment with the observed and simulated values, with a maximum mean relative error (MRE) of approximately 0.04 and lower deviations in the leaky barrier afflux model compared to the momentum-based method. The results show that while both approaches can be reliably used to infer water depth and velocity around engineering wood structures, predicting upstream values from downstream data yields less error. These models will inform design tools for flood risk management.

Section 6.3 presents the methodologies for predicting upstream and downstream water depths and velocities in an open channel with a leaky barrier. Section 6.4 presents the results and discusses the accuracy of these methodologies. Section 6.5 presents the main findings and outlines several limitations for further consideration.

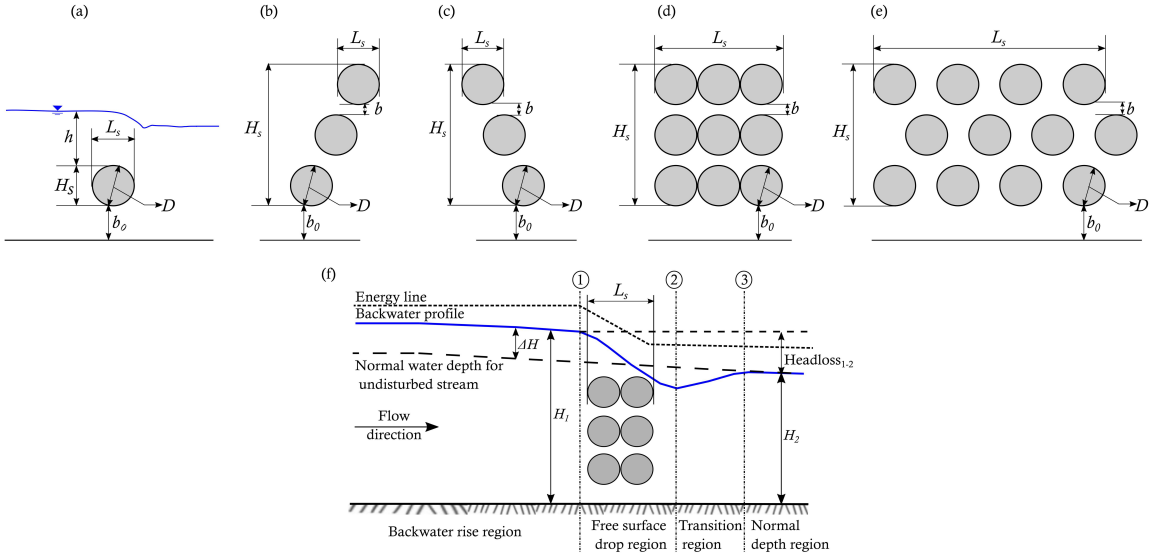

Fig. 6.1 Side-view schematic of the five leaky barrier structures from various cited studies. (a) Single cylinder leaky barrier with varied submergence depth h (Alzabari et al. 2023a). (b-c) Structures with different inclination angles in downstream and upstream directions, respectively (Alzabari et al. 2023b). (d-e) Linear and staggered structures derived from other experimental and numerical studies (Muhawenimana et al. 2021, Müller et al. 2021a,b, Müller et al. 2022, Huang et al. 2022, Alzabari et al. 2023c), where longitudinal length L_S, structure vertical height H_S, and hydraulic conditions were varied. (f) Free surface development near a leaky barrier, showing the locations where upstream water depth (H_1) and downstream water depth (H_2) were measured.

6.3 Methodology

Two novel methodologies are introduced to predict the water depths and velocities resulting from leaky barriers obstructing the flow in an open channel: the physics-based momentum method described in Section 6.3.1 and the empirical leaky barrier afflux approach described in Section 6.3.2. These methods are derived, assessed and compared using high-fidelity numerical simulation and experimental data sets from the literature, such as Muhawenimana et al. (2021), Müller et al. (2021a,b), Müller et al. (2022), Huang et al. (2022) and Alzabari et al.

(2023a,b,c), for different leaky barrier configurations, which are presented in Fig. 6.1. The specific details of these leaky barrier structures are given in Table 6.1.

6.3.1 Momentum method

This method is derived based on a combination of the continuity and momentum equations. Raju et al. (1983) employed the momentum principle to derive an equation for the afflux (ΔH) that is produced by a vertical cylinder in a confined channel. The cylinder was used as a simple debris model by Gippel et al. (1996) to study the effect of debris formation on afflux under various conditions in lowland rivers using the following equation:

$$\Delta H = \frac{H_2(Fr_2^2 - 1) + \left[(Fr_2^2 - 1)^2 + 3C_D BrFr_2^2\right]^{1/3}}{3} \tag{6.1}$$

where $Fr_2 = u_2/\sqrt{gH_2}$ is the Froude number downstream of the debris, u_2 and H_2 are the mean velocity and depth at a section downstream of the debris, respectively. $Br = LD/A$ is the blockage ratio, where L is the frontal projected height of the submerged debris, D is the width or diameter of the submerged debris and A is the cross-sectional area of the water body, e.g. open-channel. C_D is the drag coefficient defined as:

$$C_D = \frac{F_D}{\frac{1}{2}\rho u_1^2 LD} \tag{6.2}$$

where F_D is the drag force on the debris, and u_1 is the mean velocity upstream of the object.

The drag coefficients of cylinders and other obstructions in infinite-length flow (no transverse boundary interference) have been well described (Hoerner 1958). However, the typical drag coefficients for bounded cylinders are less understood because they are more dependent on the flow or boundary conditions. The lateral constraint is known as the blockage effect, which increases the drag coefficient (Shaw 1971, Ramamurthy and Ng 1973). A C_D value between 0.9 and 1.0 has generally been employed for cylinders (Gippel et al. 1996), and here C_D equal to 1 is assumed throughout the analysis. Considering that the drag per fluid volume within the structure D_x (N/m^3) can be represented by a quadratic drag law (Kaimal and Finnigan 1994), and assuming that a leaky barrier is dynamically similar to an array of rigid cylindrical elements as in canopy flows, it is defined as:

$$D_x = \frac{\rho C_D K a u^2}{2(1-\phi)} \tag{6.3}$$

where u is the temporally and spatially averaged longitudinal velocity; a (m^{-1}) is the frontal area per leaky barrier volume; ϕ is the solid volume fraction of the leaky barrier structure, which is the ratio of barrier solid volume ($V_S = \pi(D/2)^2 nB$) to control volume ($V_L = BHL_S$), where n and B are the number of cylinders and frontal lateral width, respectively; and L_S is

Table 6.1 Details of the data sets including the physical characteristics and hydraulic conditions of the leaky barriers, the diameter of cylinders (D), longitudinal barrier length (L_s), barrier height (H_s), vertical gap (b_0), inter-cylinder gap (b), barrier void ratio $(1 - \phi$, where ϕ is based on the upstream water depth), upstream flow depth H_1, downstream flow depth H_2, upstream Froude number (Fr_1) and Reynolds number (Re_1) based on the cylinder diameter.

	Case No.	D (m)	b_0 (m)	b (m)	L_s (m)	H_s (m)	$1-\phi$	H_1 (m)	H_2 (m)	Fr_1	Re_1
LES, Alzabari et al. (2023a)	1	0.05	0.025	-	0.050	0.05	0.783	0.184	0.181	0.200	13381
	2						0.739	0.154	0.151	0.196	12054
	3						0.671	0.125	0.119	0.222	12284
	4						0.648	0.118	0.112	0.217	11672
	5						0.602	0.106	0.099	0.228	11639
LES, Alzabari et al. (2023b)	6	0.025	0.050	0.013	0.025	0.100	0.591	0.162	0.143	0.220	6914
	7						0.589	0.161	0.142	0.221	6935
	8						0.596	0.159	0.146	0.211	6590
	9						0.596	0.156	0.146	0.221	6817
	10						0.593	0.159	0.145	0.225	7027
	11						0.608	0.157	0.150	0.217	6726
	12						0.609	0.156	0.151	0.220	6788
LES, Alzabari et al. (2023c)	13	0.025	0.050	0.013	0.050	0.100	0.591	0.157	0.144	0.202	6264
	14				0.075		0.591	0.156	0.144	0.204	6292
	15				0.100		0.591	0.156	0.144	0.202	6254
	16				0.125		0.591	0.156	0.144	0.202	6253
	17				0.150		0.591	0.157	0.144	0.201	6254
	18				0.200		0.591	0.158	0.144	0.201	6258
Exp, Huang et al. (2022)	19	0.025	0.055	0.010	0.300	0.095	0.771	0.090	0.086	0.236	5549
	20						0.705	0.104	0.100	0.191	4817
	21						0.705	0.105	0.100	0.235	5952
	22						0.707	0.107	0.101	0.252	6479
	23						0.724	0.114	0.107	0.231	6119
	24						0.706	0.108	0.100	0.269	6938
	25						0.698	0.139	0.130	0.229	6700
	26						0.608	0.164	0.150	0.225	7123
	27						0.630	0.170	0.159	0.213	6863
	28						0.644	0.177	0.166	0.200	6584
Exp, Muhawenimana et al. (2021)	29	0.025	0.050	0.010	0.100	0.060	0.734	0.156	0.153	0.211	6418
	30				0.125		0.735	0.156	0.153	0.210	6410
	31				0.150		0.734	0.156	0.152	0.211	6426
	32				0.175		0.735	0.156	0.153	0.210	6407
	33				0.200		0.735	0.157	0.153	0.209	6390
	34				0.025		0.564	0.150	0.148	0.184	5408
	35				0.050		0.563	0.150	0.148	0.184	5412
	36				0.075		0.563	0.151	0.149	0.182	5382
	37				0.025	0.095	0.563	0.140	0.135	0.179	5322
	38				0.050		0.564	0.141	0.136	0.177	5280
	39				0.075		0.604	0.141	0.135	0.196	6128
	40				0.025		0.602	0.157	0.149	0.196	6121
	41				0.050		0.602	0.156	0.149	0.196	6123
	42				0.075		0.601	0.157	0.149	0.194	6086
	43				0.100		0.602	0.145	0.139	0.191	6009
	44				0.125		0.734	0.145	0.139	0.198	6480
	45				0.150		0.734	0.146	0.139	0.199	6464
	46				0.175		0.736	0.147	0.139	0.197	6431
	47				0.200		0.565	0.148	0.139	0.184	5456
	48				0.100		0.566	0.163	0.153	0.182	5411
	49				0.125		0.564	0.163	0.153	0.183	5421
	50				0.150		0.604	0.163	0.153	0.211	6188
	51				0.175		0.604	0.164	0.153	0.210	6218
	52				0.200		0.604	0.166	0.153	0.208	6181
Exp, Müller et al. (2021a)	53	0.025	0.050	0.013	0.200	0.100	0.550	0.141	0.131	0.222	6524
	54						0.586	0.158	0.142	0.236	7365
Exp, Müller et al. (2021b)	55	0.025	0.050	0.013	0.200	0.100	0.585	0.158	0.142	0.237	7384
	56						0.797	0.160	0.145	0.233	7290
	57						0.597	0.155	0.146	0.244	7527
Exp, Müller et al. (2022)	58	0.025	0.050	0.013	0.200	0.100	0.607	0.160	0.144	0.233	7290
	59				0.200		0.816	0.162	0.146	0.230	7224
	60				0.175		0.729	0.158	0.148	0.237	7384
	61				0.025		0.603	0.162	0.134	0.230	7224

leaky barrier longitudinal length. K is an induction factor introduced to account for the reduced local flow velocity approaching the leaky barrier due its blockage effect (Gijón Mancheño et al. 2021). For leaky barriers composed of circular cylinders with diameter D, $\phi = \frac{\pi}{4}aD$ (Nepf 2012).

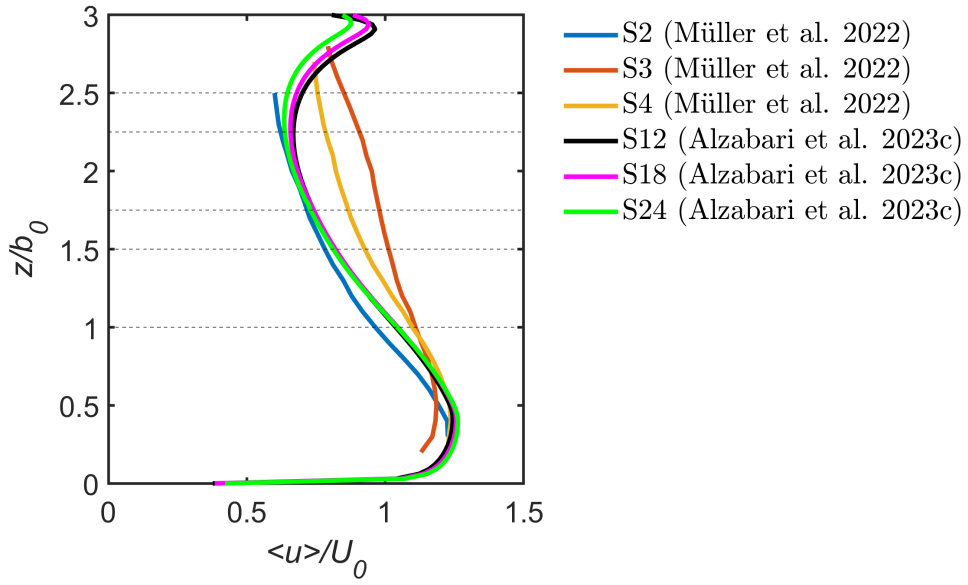

Fig. 6.2 Distribution of normalised mean streamwise velocity profile along the water column just upstream of the leaky barriers for the experimental and numerical setups conducted by Müller et al. (2022), Alzabari et al. (2023c).

Fig. 6.2 presents vertical profiles of the normalised mean streamwise velocity ($\langle u \rangle$) along the water column at an upstream distance of $0.8b_0$, with b_0 denoting vertical bottom gap, for setups from both the experimental and numerical studies conducted by the authors in previous studies, e.g. Müller et al. (2022), Alzabari et al. (2023c). This figure reveals a decrease in $\langle u \rangle$ across the height of the barrier structure ($z/b_0 > 1$), while there is a contrasting increase in $\langle u \rangle$ along the bottom gap ($z/b_0 < 1$). This variability is attributed to the blockage effect caused by the barrier structures, generating an induction effect as velocity reduction at its height. At the barrier height, the water flow has lower velocities, while the unimpeded bottom gap allows for higher velocities. The depth-averaged velocity reduction was about 0.6 for all of the cases herein presented. This is used to calculate K, which scales proportionally to the drag force and hence to the squared of the velocity value, i.e. here $K = 0.36$.

By applying the conservation of momentum over the control volume between upstream (1) and downstream (3) regions (see Fig. 6.1f), and adapting the canopy drag model (Eq. 6.3), it provides the following condition:

$$\rho B H_2 u_2 (u_2 - u_1) = \frac{1}{2}\rho g B (1-\phi)(H_1^2 - H_2^2) - \frac{1}{2}\rho B L_S C_D K a u_1^2 H_1 \tag{6.4}$$

in which the term on the left-hand side of Eq. 6.4 shows the net change in momentum, while the first term on the right-hand side represents the net hydrostatic pressure force and the

second term is the drag force of the barrier.

Combining Eq. 6.4 with the continuity condition, $u_1 B H_1 = u_2 B H_2$, yields the following expression:

$$\left(\frac{\Delta H}{H_2}\right)^3 + 3\left(\frac{\Delta H}{H_2}\right)^2 + 2\frac{\Delta H}{H_2} - 2\frac{Fr_2^2}{1-\phi}\frac{\Delta H}{H_2} - \frac{L_S C_D K a}{1-\phi} Fr_2^2 = 0 \tag{6.5}$$

Considering the blockage effect in channel flow past circular cylinders, the term $(\Delta H/H_2)^3$ can be neglected for $\Delta H/H_2 < 1$ (Raju et al. 1983). Thus, Eq. 6.5 becomes a quadratic equation whose solution is:

$$\frac{\Delta H}{H_2} = \frac{1}{3}\left[\left(\frac{Fr_2^2}{1-\phi} - 1\right) + \sqrt{\left(\frac{Fr_2^2}{1-\phi} - 1\right)^2 + 3\frac{L_s C_D K a}{1-\phi} Fr_2^2}\right] \tag{6.6}$$

Thus, the backwater rise, ΔH, can be obtained as a function of the downstream water depth and velocity:

$$\Delta H = \frac{H_2}{3}\left[\left(\frac{Fr_2^2}{1-\phi} - 1\right) + \sqrt{\left(\frac{Fr_2^2}{1-\phi} - 1\right)^2 + 3\frac{L_S C_D K a}{1-\phi} Fr_2^2}\right] \tag{6.7}$$

The upstream water depth can be obtained in a straightforward manner as a function of H_2, amongst other variables:

$$H_1(H_2, Fr_2, \phi, L_S, C_D, K, a) = H_2\left[1 + \frac{1}{3}\left(\frac{Fr_2^2}{1-\phi} - 1\right) + \sqrt{\left(\frac{Fr_2^2}{1-\phi} - 1\right)^2 + 3\frac{L_S C_D K a}{1-\phi} Fr_2^2}\right] \tag{6.8}$$

Conversely, solving the momentum equation for the downstream water depth yields the following expression:

$$H_2 = H_1\left[1 - \frac{1}{6}\left(\frac{2Fr_1^2}{1-\phi} - \frac{Fr_1^2 L_S C_D a}{1-\phi} - 2\right) + \sqrt{\left(2 + \frac{Fr_1^2 L_S C_D K a}{1-\phi} - \frac{2Fr_1^2}{1-\phi}\right)^2 + 12\frac{Fr_1^2 L_S C_D K a}{1-\phi}}\right] \tag{6.9}$$

6.3.2 Leaky barrier afflux method

This method employs a similar mathematical approach to those used to predict the afflux generated from bridge piers and bridge decks. Biery and Delleur (1962) developed a well-known method for calculating afflux using data from their experiments on semicircular arch bridge constrictions and the findings from experiments on vertical-faced abutments (Liu et al. 1957).

Their afflux formula is given by:

$$\frac{H_1}{H_n} = 1 + m\left[\left(\frac{Fr}{M}\right)^{\frac{2}{3}}\right]^n \tag{6.10}$$

where H_1 is the total depth at the afflux zone; H_n is the normal flow depth of the unconstricted channel; m and n are adjustable factors, which are chosen to best match the tested data; and M is the opening ratio, which is the contracted flow area relative to total flow area. The Froude number (Fr) represents uniform flow in an unconstricted channel, given by $Fr = u/\sqrt{g(H_n/\alpha)}$, where α is the kinetic energy correction factor and u is the cross-sectional mean velocity.

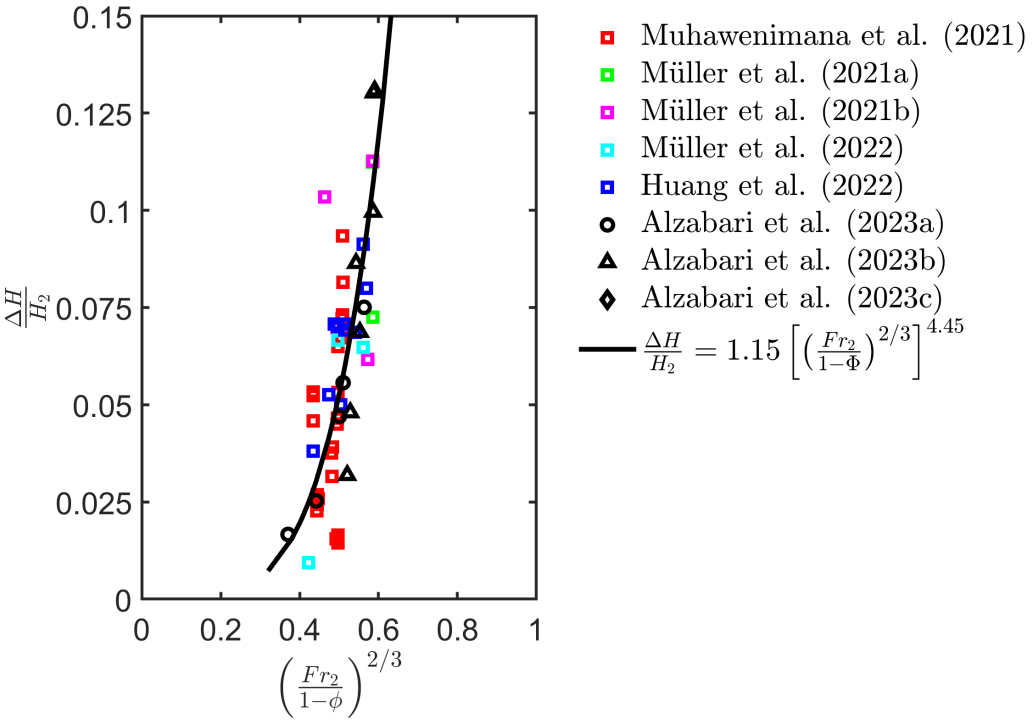

Fig. 6.3 Relation based on downstream Froude number, porosity ratio and normalised afflux using measured and simulated data, with the plot of the best-fit equation (6.12). The data set by Alzabari et al. (2023a,b,c) shows the following configurations based on simulated data using LES: (a) a single cylinder with various submergence depths (Alzabari et al. 2023a), (b) three dowel rows in the vertical direction inclined at different angles to both the upstream and downstream directions (Alzabari et al. 2023b), and (c) three dowel rows in the vertical direction with varying dowels along the longitudinal direction (Alzabari et al. 2023c). The experimental data by Huang et al. (2022) comprised leaky barriers with three dowel rows in the vertical direction and 12 dowels in the longitudinal direction studied under different hydraulic conditions. Muhawenimana et al. (2021) and Müller et al. (2021a,b), Müller et al. (2022) conducted experiments involving linear leaky barriers with different longitudinal lengths and structure heights subjected to 80% and 100% bankfull discharges.

Eq. (6.10) describes this relationship for a single rectangular channel, in the case of compound channels. Eq. (6.10) was modified by changing the definition of the Froude number to be $Fr = u/\sqrt{g(A_n/T_n)}$, where A_n is the uniform flow cross-sectional area and T_n is the

uniform flow surface width (Atabay 2008). This adjustment was made because the results showed that adopting the same Froude number definition from Biery and Delleur (1962) could yield large errors. Atabay (2008) advised setting the parameters m and n to 0.2457 and 2.9668, respectively, for compound channels with straight-deck type bridge constrictions. In contrast, Biery and Delleur (1962) recommended values of 0.47 for m and 3.39 for n for a single channel. After continuous development and optimisation for the accuracy of afflux caused by bridge piers (Zahang et al. 2021), the afflux formula can be described as follows:

$$\frac{\Delta H}{H_2} = m\left[\left(\frac{Fr_2}{1-\phi}\right)^{\frac{2}{3}}\right]^n \tag{6.11}$$

where ΔH is the afflux, H_2 is the normal flow depth downstream of the structure, $Fr_2 = u_2/\sqrt{gH_2}$ is the downstream Froude number with u_2 being the velocity for uniform flow downstream of the structure and ϕ is the solid volume fraction. Zahang et al. (2021) conducted a numerical study to investigate the afflux caused by bridge piers with relatively low blockage ratios in a sub-critical flow. They proposed the values of 0.1447 and 2.37 for parameters m and n, respectively. These values provided a higher accuracy compared to the parametric optimisation formulas proposed by Biery and Delleur (1962) and Atabay (2008).

In this work, the bridge afflux formula (Eq. 6.11) is adopted to predict the backwater rise caused by leaky barriers in sub-critical flows. Experimental and numerical data sets from 61 working conditions involving various barrier configurations were employed (Table 6.1). In these studies, the downstream Froude number (Fr_2) varied from 0.19 to 0.31, and the porosity ratio ($1-\phi$) varied between 0.55 and 0.82. Based on the measured and simulated values of $\Delta H/H_2$ against $(Fr_2/1-\phi)^{\frac{2}{3}}$, the formula for afflux that provided the fit was with the parameters m and n equal to 1.15 and 4.45, respectively, as shown in Fig. 6.3. Hence, a proposed backwater rise formula for leaky barriers can be expressed as:

$$\frac{\Delta H}{H_2} = 1.15\left[\left(\frac{Fr_2}{1-\phi}\right)^{\frac{2}{3}}\right]^{4.45} \tag{6.12}$$

thus, the upstream water depth of the barrier can be obtained by:

$$H_1 = H_2 + H_2\left[1.15\left[\left(\frac{Fr_2}{1-\phi}\right)^{\frac{2}{3}}\right]^{4.45}\right] \tag{6.13}$$

and accordingly, the downstream water depth can be given as:

$$H_2 = H_1 - H_1\left[1.15\left[\left(\frac{Fr_1}{1-\phi}\right)^{\frac{2}{3}}\right]^{4.45}\right] \tag{6.14}$$

These quick-hand afflux formulations are essential for integrating leaky barriers into broader water systems, providing a rapid understanding of water behaviour around these barriers.

They enable the estimation of water depth and velocity with limited data for specific leaky barrier designs. Furthermore, these formulations facilitate adjustments to the barrier's physical properties, such as size and porosity, to achieve the desired flow conditions. The significance of this capability is paramount in designing leaky barriers, ensuring they operate efficiently and safely, effectively controlling water flow as intended, and preventing issues like flooding.

In both the momentum and leaky barrier afflux methods, the calculation of the solid volume fraction ϕ of the leaky barrier involves equating the water depth H within the control volume ($V_L = BHL_S$) to either H_2 or H_1 when estimating the upstream or downstream water depth, respectively.

6.3.3 Estimating flow velocity and error metrics

The upstream and downstream velocities can be determined from both methods using the continuity of mass via unit discharge ($q_1 = q_2$), i.e. $u_1 H_1 = u_2 H_2$. For instance, the upstream velocity (u_1) can be calculated as the ratio of the downstream water depth (H_2) to the predicted upstream water depth (H_1), multiplied by the downstream velocity (u_2). The validity of the momentum method (Eqs. 6.8 and 6.9) and the leaky barrier afflux approach (Eqs. 6.13 and 6.14) in predicting upstream and downstream conditions is examined using the measured and simulated results presented in Table 6.1.

The error metrics of Mean Relative Error (MRE) and Mean Absolute Error (MAE) of the mean water depth or velocity values are employed to evaluate the accuracy of the methods, which are calculated as:

$$MRE = \frac{1}{n}\sum_{i=1}^{n}\left|\frac{\lambda_{i\,\text{Predicted}} - \lambda_{i\,\text{Measured/Simulated}}}{\lambda_{i\,\text{Measured/Simulated}}}\right| \tag{6.15}$$

$$MAE = \frac{1}{n}\sum_{i=1}^{n}\left|\lambda_{i\,\text{Predicted}} - \lambda_{i\,\text{Measured/Simulated}}\right| \tag{6.16}$$

where n is the total number of cases analysed, and λ_i for $i = 1, 2, \ldots, n$ represents either the water depth (H_i) or velocity (u_i), either upstream or downstream.

6.4 Results and discussion

6.4.1 Prediction of upstream water depth and velocity using downstream data

Fig. 6.4 compares the calculated upstream water depths with the collected measured and simulated data (Table 6.1). The results obtained using the momentum method yield a good agreement, with MRE of 0.027 and MAE of 0.004 (Fig. 6.4a). All the data fall within a 10% margin, which demonstrates the excellent performance of this method when used to model the investigated leaky barriers that vary in physical characteristics and underlying flow condi-

tions. However, there are a few instances where the predictions are slightly less accurate when compared to other scenarios. For instance, points from the studies of Müller et al. (2022), Muhawenimana et al. (2021), Alzabari et al. (2023b) and Müller et al. (2021b) indicate errors approaching the -10% range. These errors are mostly associated with barrier designs that have few cylinders in the streamwise direction. Conversely, estimates for leaky barriers with longer longitudinal lengths tend to exhibit greater accuracy.

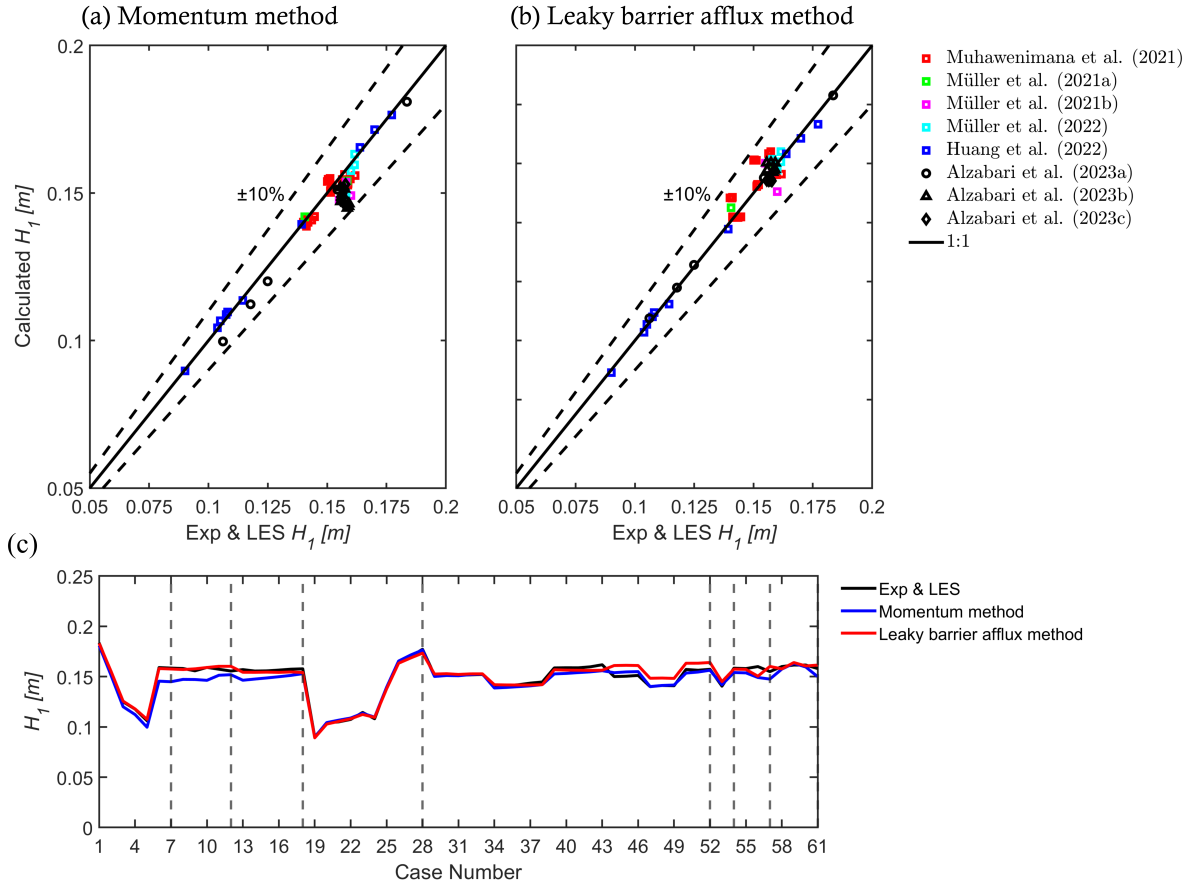

Fig. 6.4 Plot of the measured and simulated upstream water depth (H_1) and predicted values using (a) the momentum method, (b) the leaky barrier afflux method, and (c) comparison of the measured and simulated upstream water depths with predictions generated by both the momentum and leaky barrier afflux approaches.

These results suggest that the barrier's length may influence the accuracy of the momentum method, leading to a large sensitivity to specific input parameters. This may be linked to the simplifications made during the derivation process (Eqs. 6.4-6.8) or to the difficulty of taking accurate measurements for such leaky barrier designs. For instance, adopting the average (undisturbed) upstream flow velocity to compute the drag force (Eq. 6.4) may not accurately account for the local velocity distribution at the leaky barrier, as the velocity field undergoes significant changes both upstream and downstream of the structure. Moreover, the solid volume fraction ($\phi = V_s/V_L$) is estimated by considering the downstream water depth when calculating the control volume (V_L) which, due to significant variations in the water depth along the length of the barrier and in regions adjacent to it, may lead to inaccurate ϕ,

which limits the accuracy of this method.

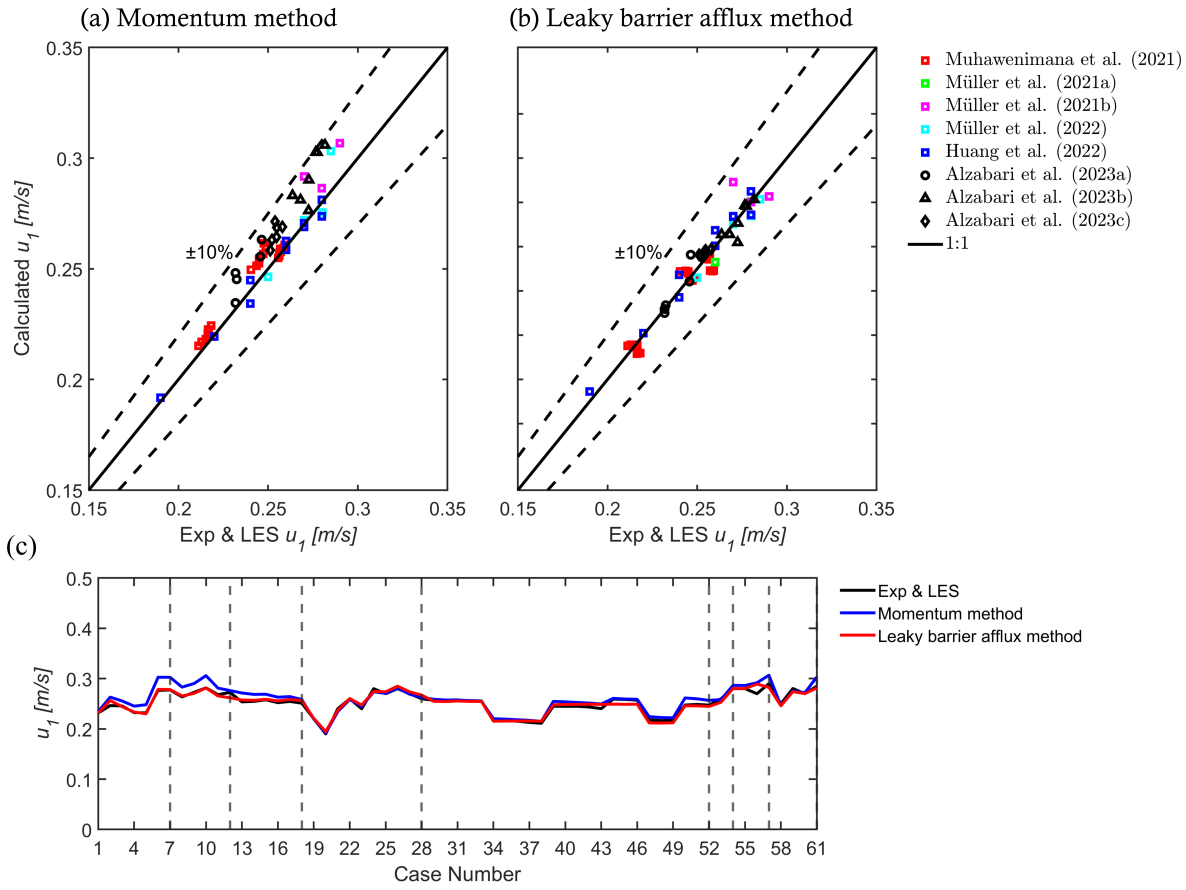

Fig. 6.5 Plot of the measured and simulated upstream water velocity (u_1) and predicted values using (a) the momentum method, (b) the leaky barrier afflux method, and (c) comparison of the measured and simulated upstream water velocities with predictions generated by both the momentum and leaky barrier afflux approaches.

The leaky barrier afflux method, as shown in Fig. 6.4b, proves to be more accurate than the momentum method, with the calculated data exhibiting a significant reduction in the MRE and the MAE of approximately 30% (0.019) and 50% (0.002), respectively, with the calculated water depth error being within the range of $\pm 10\%$. Despite the improved predictions of upstream water depths using this empirical approach, compared to the momentum method, estimates in certain specific cases deviate from the measured data. For instance, a few setups from Muhawenimana et al. (2021) and Müller et al. (2022) show an over-prediction of H_1, while other data points from Müller et al. (2021b) show an underestimation of H_1. These instances correspond to the greatest deviation of the data points from the best-fit function shown in Fig. 6.3.

In general, both methods demonstrate reasonable accuracy in predicting upstream water depths when evaluated against the measured and numerical data. Fig. 6.4c presents the disparity between the two methods, providing clear evidence of variations in their performance across specific setups, i.e. case numbers 6–18 and 43–52. This suggests that the leaky barrier afflux method tends to be more accurate than the momentum-based model.

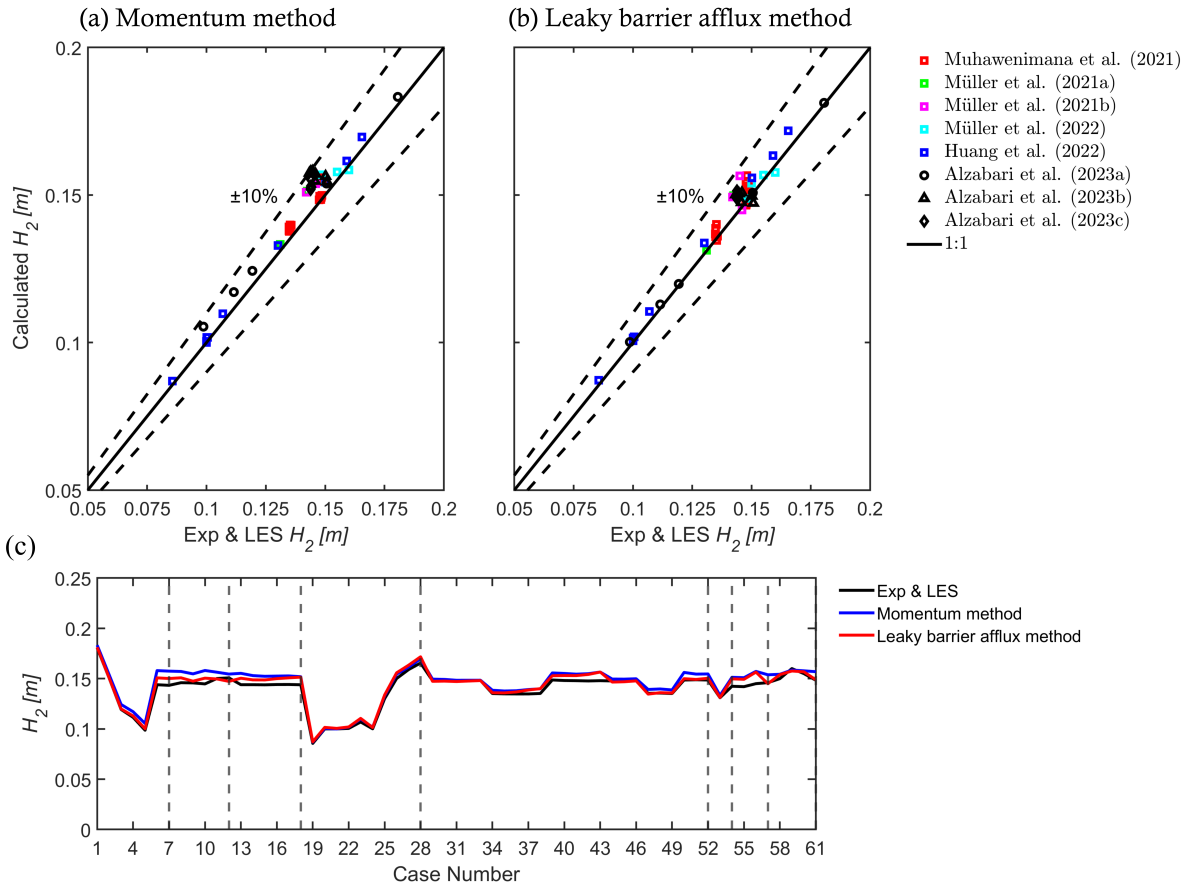

Fig. 6.6 Plot of the measured and simulated downstream water depth (H_2) and predicted values using (a) the momentum method, (b) the leaky barrier afflux method, and (c) comparison of the measured and simulated downstream water depths with predictions generated by both the momentum and leaky barrier afflux approaches.

Figs. 6.5a and 6.5b present the calculated upstream flow velocity (u_1) using the momentum and leaky barrier afflux methods, respectively. These plots again prove that the leaky barrier afflux approach enhances the accuracy of upstream velocity predictions compared to the momentum method, with errors reducing from 0.031 to 0.015 (MRE) and from 0.011 to 0.005 (MAE), respectively. This improvement may suggest that accurate prediction of upstream water depths is necessary to achieve accurate upstream velocities because these two variables are inherently linked by the equation $(u_1 = u_2 H_2/H_1)$, as described in Section. 6.3.3. Fig. 6.5c presents a comparative plot illustrating the performance of the momentum and leaky barrier afflux methods in predicting upstream velocity. This comparison supports the conclusion that the leaky barrier afflux method provides better predictions to infer upstream flow conditions (H_1, U_1) from downstream data.

6.4.2 Prediction of downstream water depth and velocity using upstream data

Fig. 6.6 presents a comparison between the reference experimental and simulation data, and the calculated downstream water depths obtained with the two approaches. The momentum method prediction provides a satisfactory agreement with reference data, yielding error values

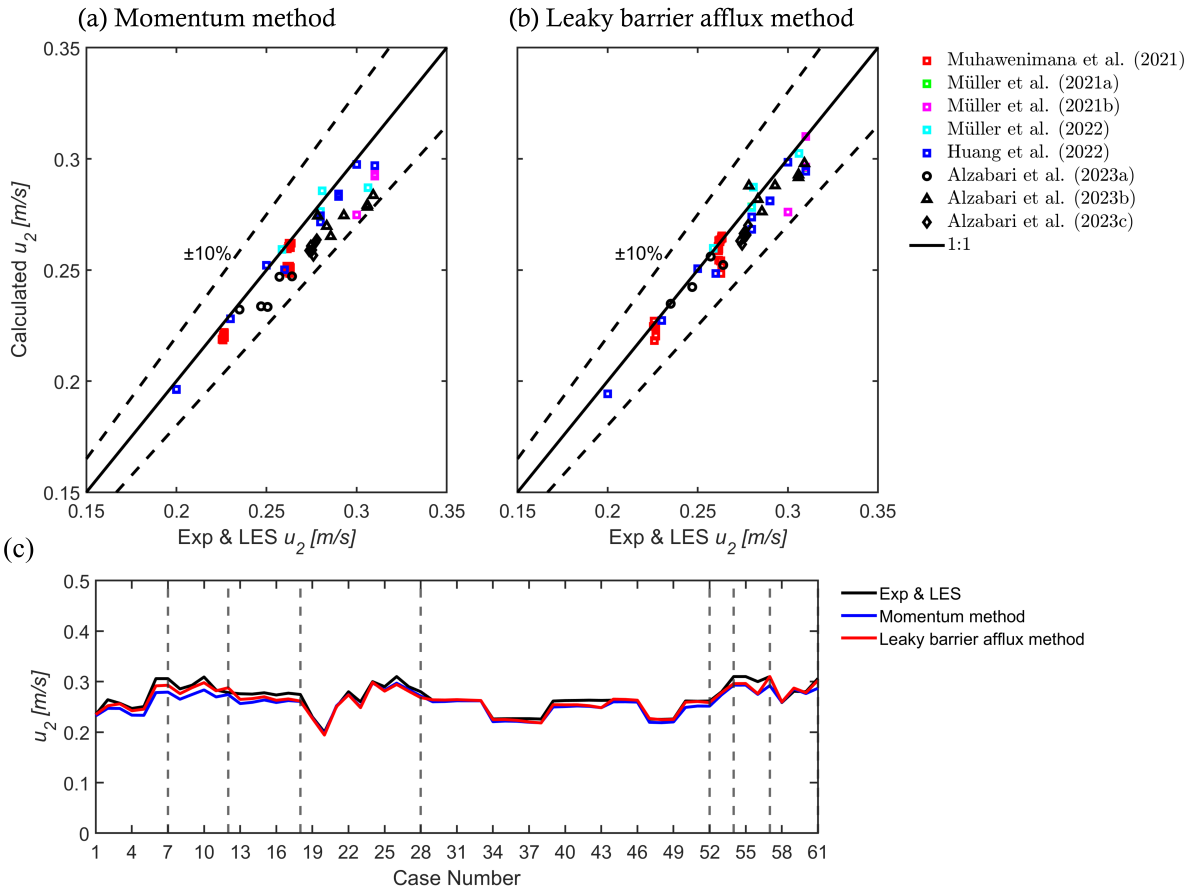

Fig. 6.7 Plot of the measured and simulated downstream water velocity (u_2) and predicted values using (a) the momentum method, (b) the leaky barrier afflux method, and (c) comparison of the measured and simulated downstream water velocities with predictions generated by both the momentum and leaky barrier afflux approaches.

of MRE equal to 0.037 and MAE of 0.005. The prediction of the downstream water depth H_2 exhibits a significantly larger error of approximately 37% when compared to the prediction of the upstream water depth H_1 (Fig. 6.4a). This indicates that the estimation of the downstream water depth using the momentum method is more sensitive to the input parameters than that with the upstream water depth. In addition, Fig. 6.6a reveals that all of the calculated downstream water depths fall within a range of $\pm 10\%$, with a slight overall over-estimation bias, and a few data points are found close to the +10% limit. These specific cases are the same as those that the momentum method underestimates in its prediction of upstream water depth H_1, as shown in Fig. 6.4a.

The accuracy of the leaky barrier afflux method to predict H_2 in various configurations of leaky barriers is presented in Fig. 6.6b, showing a significant improvement in predicting the downstream water depth and reducing the MRE to 0.022 and MAE to 0.003, being approximately 41% lower compared to the momentum method. Moreover, the H_2 prediction exhibits a deviation of 2.2%, which is a slight increase compared to the 1.9% deviation attained when predicting the upstream water depth H_1 using the leaky barrier afflux method (Fig. 6.4b). In general, the leaky barrier afflux approach yields a smaller error in the predictions of down-

stream water depth H_2 when compared to the momentum method, as shown in Fig. 6.6c. This deviation is particularly noticeable in data points labelled from 7–12 and 46–52, where the momentum method fails to accurately predict the downstream water depth H_2. Fig. 6.6c also shows negligible variation between the two methods in some data points, specifically those from Huang et al. (2022) labelled from 19 to 28.

Fig. 6.7 presents the predictions of downstream velocities u_2 using the leaky barrier afflux technique and the momentum method for various leaky barrier designs. While the leaky barrier afflux method exhibits MRE of 0.022 and MAE of 0.006, the momentum method yields higher errors, with MRE of 0.037 and MAE of 0.01. Nevertheless, despite the enhancement offered by the leaky barrier afflux method (Fig. 6.7b), there are instances where it still fails to accurately predict the downstream velocities u_2, i.e. the measured and simulated linear barriers from Müller et al. (2021b) and Alzabari et al. (2023c). This is also shown in Fig. 6.7c for some cases labelled with numbers 13–18 and 55–57.

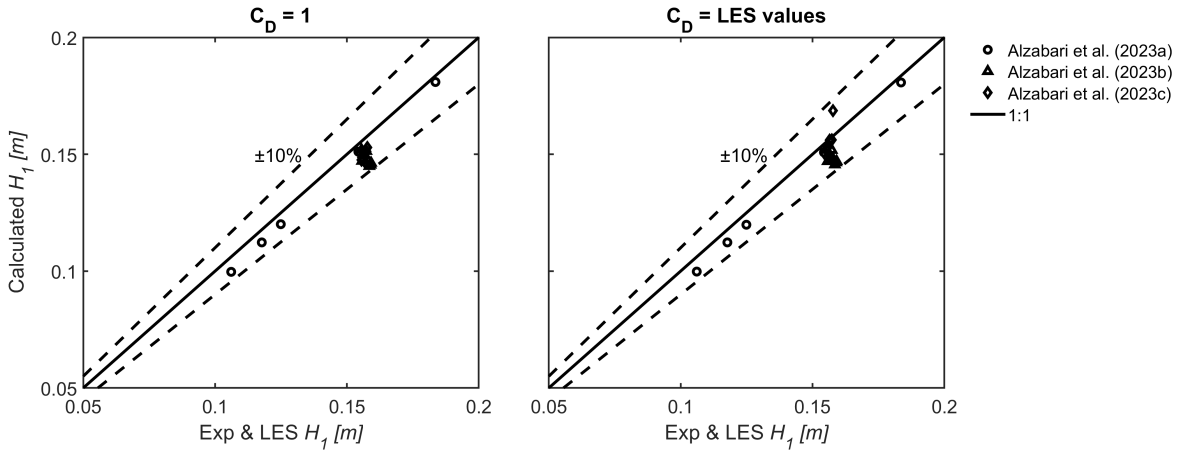

Fig. 6.8 Plot of the simulated upstream water depth (H_1) and the predicted values using the momentum method with (a) assumed drag coefficient C_D = 1 and (b) the LES-computed values of the drag coefficients.

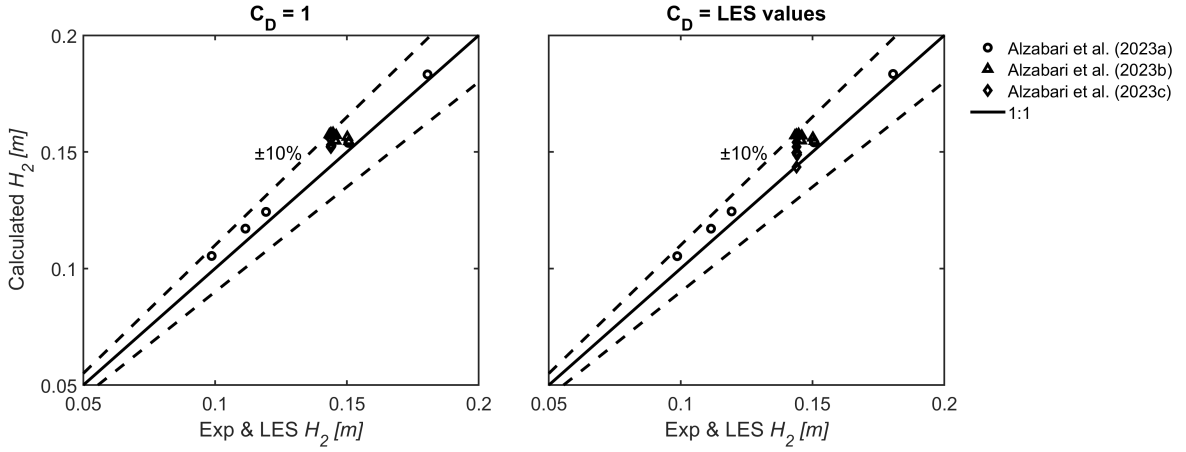

Fig. 6.9 Plot of the simulated downstream water depth (H_2) and the predicted values using the momentum method with (a) assumed drag coefficient C_D = 1 and (b) the LES-computed values of the drag coefficients.

6.4.3 Sensitivity of the momentum method to the drag coefficient

The sensitivity of the momentum method to the drag coefficient value (Eq. 6.3) is analysed by adopting the values obtained from LESs (Alzabari et al. 2023a,b,c) compared to the commonly adopted value of $C_D = 1$ used in experimental studies because this cannot be measured (Müller et al. 2021a, Müller et al. 2022, Huang et al. 2022, Muhawenimana et al. 2021, Müller et al. 2021b). Figs. 6.8 and 6.9 show the predictions of the upstream and downstream water elevations, respectively, from the analytical model. When adopting LES-computed C_D, the momentum model exhibits minor variations in the predicted values when compared to the simulated data, with the difference in the MRE between values using the LES-computed C_D and those with a drag coefficient of 1 remaining negligible ($< 3\%$). The most noticeable changes occur in data points where the longitudinal length of the leak barrier exceeds 0.1 m. Some of these points deviate from the simulated data, while others align more closely with it.

6.5 Closure

This chapter presented two novel methods for predicting water depths and velocities upstream and downstream of leaky barrier configurations, which expand the current modelling capabilities for designing and implementing green and eco-friendly wood structures in future natural flood management schemes. It presents two direct methodologies that enable the prediction of upstream or downstream water depth and velocities from either downstream or upstream of the leaky barriers, respectively. The first method, referred to as the momentum method, is derived from the combination of the momentum and continuity equations. The second method, denoted as the leaky barrier afflux method, was motivated by previous empirical equations that were employed for calculating upstream water depth induced by bridge piers and decks. These methods were validated with experimental and high-fidelity numerical data available in the literature, which showed good agreement between the calculated and examined depths and velocities, with the predicted values within an error range of less than $\pm 10\%$ for all cases.

In a range of leaky barrier designs, including both staggered and aligned configurations, both the momentum and leaky barrier afflux methods demonstrate excellent predictive capability. The momentum method provided a good accuracy with MREs of 0.027 and 0.037 for upstream and downstream water depth, respectively. The largest deviations were observed in cases where the barrier length was small ($L_s < 0.1$ m or $< 4D$), compared to the other examined instances where barrier lengths extended up to $12D$ (i.e. $L_s = 0.3$ m) with various cylinders in the streamwise direction. In contrast, the leaky barrier afflux method provided enhanced accuracy, reducing the MRE by approximately 30% and 41% when predicting the upstream and downstream water depths, respectively. The leaky barrier afflux method improved not only predictions of water depths but also of flow velocities when compared to the momentum method. Overall, the results also show there is less deviation when estimating upstream quantities.

Both methods were tested for cases with Reynolds numbers (Re) ranging from 4,800 to 14,000, which fall within the sub-critical flow regime ($3 \times 10^2 < Re < 1 \times 10^5$). Further verification is needed for Reynolds numbers beyond this range because more turbulent flows change the vortex shedding pattern off the cylinders, which can result in significant changes in vortex merging and shear layer instability, potentially affecting the accuracy of the prediction methods. Furthermore, the analysis conducted in this work has been limited to cylindrical cylinders arranged in either aligned or staggered configurations. In field conditions, leaky barriers often consist of irregular natural cylinders that feature non-uniform shapes and roughness elements. Debris and sediment carried by the river have the tendency to deposit in between logs, while fallen wood, sediment and organic material can accumulate upstream of the barrier. These accumulations can increase the barrier's effective longitudinal length and decrease its porosity, which may result in an elevated upstream water depth. Future research should focus on refining or extending these proposed methods to enhance their predictive capabilities and enable the effective design of a wider range of leaky barrier designs.

Both methods can be used to incorporate leaky barriers into hydraulic models of broader water systems, which allows for a comprehensive understanding of how water flows and behaves in the presence of such barriers. For instance, this enables the approximation of resultant upstream water depth and velocity for a specific design of a leaky barrier, considering averaged downstream conditions, and allows for modifications of the barrier's physical characteristics, such as size and porosity, to achieve the desired upstream flow conditions. This is crucial for designing leaky barriers that are both efficient and safe, ensuring they control water flow as intended without causing unintended flooding or other issues. Such modelling is essential for informed decision-making in water resource management and environmental planning.

CHAPTER 7

Conclusions and Outlook

Conclusions

This thesis has addressed the hydrodynamics of turbulent flows around single horizontal circular cylinders and leaky barriers composed of horizontal circular cylinders in flow conditions that span from very shallow to relatively deep waters. State of the art large-eddy simulations were performed to resolve the energetic flow structures for these cases with a level-set method to capture the free-surface deformation, as for shallow flows this deformation was so substantial that it significantly impacted the cylinder wake dynamics. Considering these cylinders as natural-flood management hydraulic structures, the relevance and impact on the flow hydrodynamics of various design parameters were investigated, such as the distance to the free surface from the upper side of a horizontal cylinder which is also located near the bottom wall as well as the effect of varying log inclinations and longitudinal barrier extension in different leaky barrier designs. Results generated from the high-fidelity simulations were used, together with experimental data from literature, to formulate a new set of analytical methods for predicting the water depths and velocities induced by leaky barriers which were extensively validated when either conditions were known at the upstream or downstream end of the structure.

The effect of the free-surface proximity on the hydrodynamics of a single horizontal circular cylinder near a smooth solid bottom boundary has been investigated and presented in Chapter 3. Experimental data have been used to validate the simulations achieving a good agreement of computed streamwise and vertical velocity profiles and water surface elevation with the measured ones. Extensive analysis of the time-averaged flow quantities, recirculation regions, vorticity fields and the evaluation of power density spectra and hydrodynamic coefficients has been carried out and key differences in the developed hydrodynamics between cases with varied submergence depths were identified. Mainly, at low Froude numbers (i.e. $Fr = 0.26$), a von Kármán vortex street was developed downstream with minimal disturbance from the free surface. However, a critical value was identified at $Fr = 0.31$, marking the regime transition when the free surface started to exert a noticeable effect over the cylinder wake dynamics. Beyond this threshold, the interaction between the free surface unsteady dynamics and the cylinder wake's vorticity became more pronounced, featuring irregular flow patterns and a quicker loss of coherence of the von Kármán vortices, due to an increased wa-

ter elevation upstream of the cylinder together with a larger surface disturbance downstream of the cylinder. Moreover, the particular setup studied with a small gap between the bottom of the cylinder and the flume's bed, resulted in further irregular vortex shedding patterns as a ground vortex was developed due to the cylinder bottom shear layer interacting with the bed. These changes to the cylinder wake compared to classic unbounded cylinder flows also modified the forces acting on the horizontal circular cylinder, observed from the significant variations in drag and lift coefficients and that the cylinder was subjected to a non-zero mean notable downward lift as the free surface approached the cylinder.

Whilst the mean flow dynamics of a horizontal circular cylinder wake was examined in Chapter 3, in Chapter 4 Proper Orthogonal Decomposition (POD) was employed to thoroughly examine the behaviour of the instantaneous flow structures shed behind a horizontal circular cylinder for selected submergence conditions keeping the cylinder at the same distance to the bottom bed. Through this statistical analysis, the wake unsteadiness could be characterised and thus quantify how the free-surface proximity drives the coherence of large-scale wake structure. The POD analysis of the instantaneous velocities revealed that the POD modes were paired every two consecutive odd–even modes, of a similar energy contribution, which was evident in both the POD spatial mode patterns and temporal coefficients. The first two modes consistently depicted the major flow structures, contributing to more than 42% of the total energy in cases with $Fr \leq 0.45$. However, at $Fr = 0.53$, these eigenvalues significantly reduced their contribution by almost half, which is attributed to the influence of the free-surface proximity on the coherent structures of the cylinder's wake. POD presents the possibility of informing Reduced-Order Models (ROM) that could directly represent the instantaneous flow field based on the trained data. The velocity fluctuation field reconstructed by a ROM using the first 20 POD modes was deemed sufficient to capture similar vortical structures as those obtained from the original large-eddy simulations. However, in cases with $Fr \geq 0.45$, the ROM based on the first 20 modes still exhibited a relatively large error compared to the LES solution, thus requiring a larger number of POD modes to account for the small-scale structures. Overall, the results presented in Chapter 4 highlighted the significance of accounting for the free surface when simulating shallow flow conditions. Within this context, a comparison between the rigid lid and level-set methods was presented for a case at $Fr = 0.45$ and using POD to elucidate the alterations in wake structures. This comparison revealed the limitations of the traditional rigid lid approach in capturing the dynamics of the cylinder's wake, while conversely, the level-set method proved able to capture the unsteady free-surface deformations that leads to a modified cylinder wake.

An investigation into the hydrodynamics of flow around leaky barriers using large-eddy simulations was presented in Chapter 5. The main focus was to adopt a barrier comprising three circular cylinders vertically aligned with 0.025 m length (equal to one log diameter) as a baseline design, and to understand how its performance could be modified through a series of alternative designs with either inclined cylinders or varying longitudinal lengths in the

streamwise direction. Six inclined configurations of leaky barriers were analysed with angles of 15°, 30°, and 45° in both upstream and downstream directions. Alternatively, leaky barrier configurations with varied lengths ranged from 0.025 m (as the baseline design) to 0.20 m. The impact of the barriers on flow dynamics was thoroughly analysed, and validations against experimental results for the non-inclined vertical barrier confirmed the accuracy of the large-eddy simulations in capturing the mean velocities and turbulence quantities. For all leaky barrier designs, the results showed that the frontal projected blockage area had a direct impact on the upstream flow depth, with momentum being redirected towards the bottom gap. This redirection gave rise to a primary wall jet, with its peak velocity and coherence varying depending on the specific design of the leaky barrier. Simulations also revealed the formation of offset jets through the inter-log gaps, whose strength was found to be less than that of the wall jet. Large-eddy simulations of the inclined barriers revealed that upstream-inclined barriers exhibited distinct flow characteristics compared to their downstream-inclined counterparts. Specifically, increasing the angle of the barrier towards the upstream direction resulted in a reduced longitudinal extent of regions with high streamwise velocities along the bottom gap and increased streamwise velocities in downstream regions near the free surface compared to the downstream-inclined barriers. As a consequence of these changes to the mean flow, the inclination in either direction of the barrier significantly affected the formation of recirculation zones, wake recovery and gap flux ratios. While both vertical layout and downstream-inclined designs developed a large recirculation zone near the free surface, the increased angle to the upstream direction limited the formation of this feature in the barrier's wake, particularly in the upstream oriented cases at 30° and 45°.

For designs with increasing barrier length in the streamwise direction, analysis of the time-averaged vertical velocities revealed two regions characterised by upwards and downwards fluid motions along the lowermost cylinders, which coincide with the region of high turbulence levels. The magnitude and distribution of these effects were notably influenced by barrier lengths, such that when the barrier length increased, the turbulent kinetic energy levels decreased, consequently decreasing the mixing from the jets in this region. The impact of leaky barrier design on bed shear stress was significant, and was further analysed due to its relevance in potential sediment mobilisation, albeit the latter was not modelled. Specifically, designs with flatter inclinations (larger angles) or smaller longitudinal barrier lengths resulted in a noticeable decrease in peak bed shear stress, mitigating both the scour potential and the extent of the scouring pool region in the downstream area.

As leaky barrier design can vary and so does its performance, there is a need to inform stakeholders about which is best for their projects. In light of this, five design criteria were used to assess the performance of leaky barriers, namely backwater rise, recirculation adjacent to the free surface, wake recovery, potential bed scour, and structural load on cylinders. These were scored from 0 (very poor) to 5 (very good) depending on the obtained values from the simulations of a series of designs. Synthesis of the developed hydrodynamics showed that in

order to maximise backwater rise, a leaky barrier design with cylinders aligned in the vertical plane is advantageous compared to inclined designs. However, if the goal is to limit the risk of local bed and bank scouring, it was found that this scour risk can be mitigated by utilising an upstream- or downstream-inclined barrier design. In order to achieve a balance between maximising backwater rise for optimal flood mitigation and reducing scour potential for effective sediment management, an upstream-inclined configuration offers the best hydrodynamic performance.

Chapter 6 introduced two analytical methods for predicting water depth and velocities near leaky barrier configurations, which allow a direct estimation of the impact of the structure on the flow. The first is the so-called momentum method, derived from a combination of the momentum and continuity equations, requiring the input of some physical properties of the barrier and measured water depth and velocity at one of its sides. The second is the leaky barrier afflux method, motivated from empirical equations traditionally used to estimate afflux caused by bridge piers (normally vertically aligned and piercing the free surface) and fitted to leaky barriers (fully submerged obstacles), which required knowledge of the opening ratio and local Froude number. The two methods were validated with experimental data from the literature and high-fidelity large-eddy simulations from this thesis, which yielded an excellent agreement between observed or computed depths and velocities and the predicted values, all within a negligible error range of less than $\pm 10\%$ for all cases. The momentum method provided a good accuracy with mean relative errors of 0.027 and 0.037 for upstream and downstream water depths, respectively. This method maintained consistent performance, even with barriers extending twelve times the log's diameter. In contrast, the leaky barrier afflux method surpassed the momentum method in accuracy, reducing MREs by approximately 30% and 41% for upstream and downstream water depths, respectively. Flow velocity predictions were also enhanced by the leaky barrier afflux method when contrasted with the momentum method. Furthermore, the overall trend of predictions indicated less deviation when estimating upstream quantities from downstream measurements. Overall, these methodologies were proved to be applicable to various leaky barrier designs, including staggered and aligned configurations, which expand the existing modelling capabilities for designing and implementing green, eco-friendly wood structures in natural flood management strategies.

Outlook

This thesis provided novel findings on the dynamics of turbulent flow around horizontal circular cylinders in shallow flow conditions. However, there are several avenues for future research and development in these areas.

First, this research has unveiled critical thresholds in the interactions between the free surface and a fully submerged circular cylinder at specific Froude numbers. Further investigations are essential to parameterise how these interactions may vary with differing cylin-

der shapes, sizes, and flow regimes in laboratories and numerical models. Future research should also look into understanding transient effects of the proximity of cylinders to a free surface, such as vortex-induced vibrations, cavitation, flow separation, and increased hydrodynamic loads. This is crucial for ensuring the structural integrity of cylindrical structures in widespread engineering applications. From a hydraulics perspective, it is relevant to analyse how these flow phenomena impact on sediment mobilisation risk, nutrient or scalar transport, and boundary layer dynamics.

Secondly, comparing the rigid lid and surface-resolving (through the level-set method) approaches has highlighted the limitations of the traditional rigid lid modelling method, especially in the context of shallow flow conditions. This outlines the need for re-evaluating numerical simulation approaches to shallow hydraulic flows, especially in scenarios marked by complex submerged and surface piercing geometries and unsteady flows. The need for an accurate representation of flow dynamics, turbulence, and the complex deformations of free surfaces suggests that more advanced and detailed simulation techniques are required. As a result, future research should concentrate on enhancing and optimise the level-set method and other cutting-edge simulation methodologies, focusing on computational efficiency, adaptability to advanced physics, and integration with other innovative techniques.

Third, the presented simulations of different designs of leaky barriers comprised of circular cylinders revealed their fundamental hydrodynamics and potential role as a tool for natural flood management. However, it is essential that further work examines the performance of these barriers under real-world conditions. Factors such as irregular natural logs, sediment deposition, and debris accumulation can significantly alter their efficacy. Detailed analysis is needed for variations in log shapes, sizes, and the presence of roughness elements, which influence barrier porosity. Moreover, future studies should examine the ecological and environmental impacts of leaky barriers within riverine ecosystems, as most related work has been undertaken in controlled lab experiments. Understanding their effects on habitat, sediment transport, and water quality is crucial to ensure that wood structures remain eco-friendly in natural flood management schemes while minimising ecological disruption.

Finally, the development of analytical methods to estimate water depths and velocities due to leaky barriers marks a significant advancement. Both methods were tested within the sub-critical flow regime. Further verification is required for higher Reynolds numbers due to increased turbulence, which can impact prediction accuracy. While the analysis primarily focused on cylindrical cylinders, real-world leaky barriers often comprise irregular natural logs with debris accumulation between them and upstream, significantly affecting water levels. It is crucial for practical flood risk management that these methods undergo further refinement, validation, and continuous improvement to ensure their precision and adaptability, enabling them to address a wide range of real-world scenarios and diverse environmental conditions. Collaborative efforts between researchers, practitioners, and stakeholders across different sectors are pivotal in bridging the gap between research and practice, not only to enhance the

accuracy and effectiveness of current estimation methods but also to pave the way for novel estimation methods.

In conclusion, the research presented in this thesis has significantly advanced the understanding of complex hydrodynamics phenomena related to free surface flows, horizontal circular cylinder wakes, and leaky barriers. Future research directions outlined above are proposed to motivate further deepening into these phenomena, ultimately leading to more effective flood management strategies, improved environmental conservation efforts, and the development of advanced free surface simulations and accurate analytical methods for engineers and researchers working in the field of fluid dynamics and environmental flood management.

Appendices

Appendix A

Free-surface tension

This section presents Fig. A.1, displaying contours of normalised vorticity behind the cylinder for the case with Fr = 0.53. This visual representation serves as an illustration of the effects observed in free-surface simulations when the Continuum Surface Force (CSF) model is not employed. The figure illustrates a scenario characterised by significant surface breaking and air trapping, with contours depicting the resulting formation of air bubbles. This visualisation underscores the importance of the CSF model in maintaining the accuracy and realism of the simulations, especially in complex fluid dynamics scenarios.

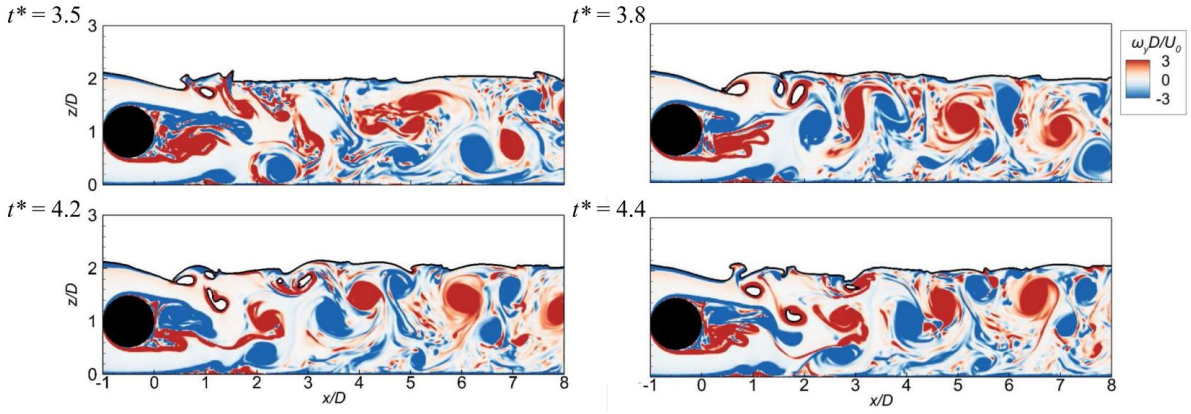

Fig. A.1 Contours of normalised vorticity behind the cylinder for the case: $Fr = 0.53$, at four instants normalised by the peak frequency $t^* = 3.5$, 3.8, 4.2, and 4.4. The free surface is depicted as a solid-black line.

Appendix B

Mesh dependence

This section underscores the sensitivity of the single cylinder solution to mesh resolution at $Fr = 0.31$. To this end, three distinct computational grids containing approximately 5, 7, and 14 million elements respectively were developed, as shown in Fig. B.1. These grids, while maintaining identical topology, differ in resolution, particularly near the cylinder surface and near the air-water interface. The finest grid enhances the comparison, which is crucial for ensuring the fidelity of the simulation results.

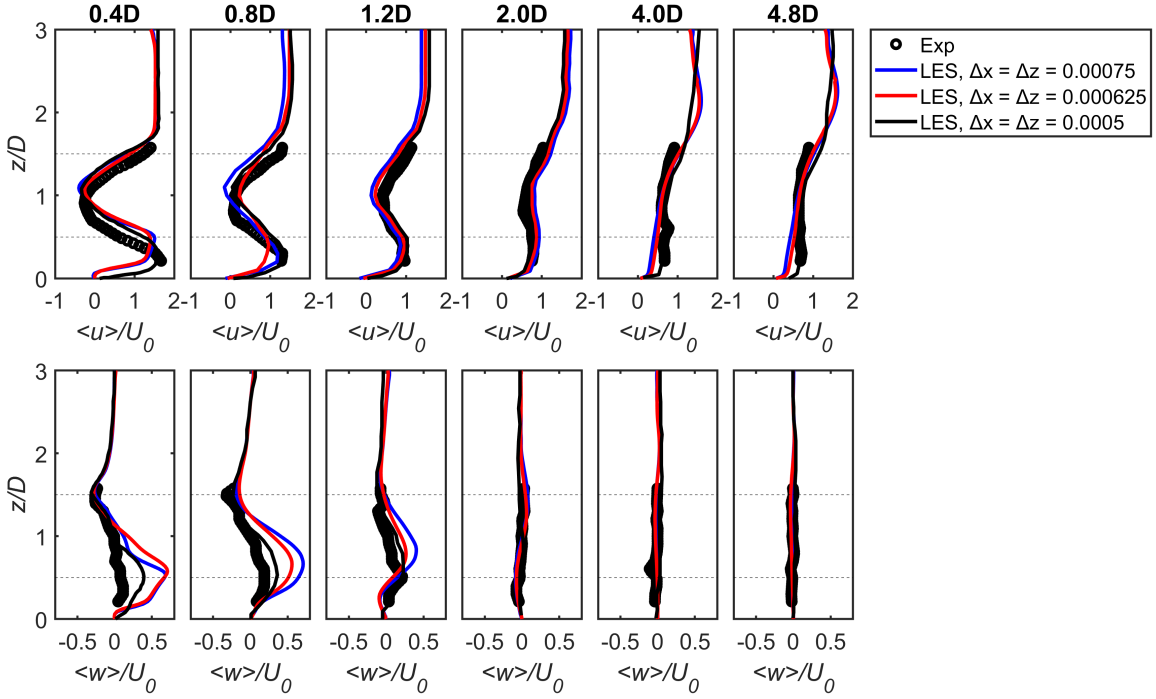

Fig. B.1 Vertical profiles of mean streamwise velocity $\langle u \rangle$ at the top and mean vertical velocity $\langle w \rangle$ at the bottom, at six locations downstream of the cylinder at $Fr = 0.31$. The data are shown for three different grid resolutions, comparing experimental results (represented by symbols) with LES results (represented by lines). Dashed lines indicate the cylinder's position.

Appendix C

Free-stream turbulence

In this section, the impact of employing an artificial turbulent velocity field via the Synthetic Eddy Method (SEM) is shown in Fig. C.1. Two simulations were conducted using SEM, with turbulence intensities (TIs) of 5% and 10% at $Fr = 0.31$. These simulations were executed with turbulent length scales set to values equivalent to 40, 5, and 20 grid sizes in the x, y, and z directions, respectively. The results show that the artificial turbulence with the different intensity levels exhibited negligible differences compared to the case without SEM.

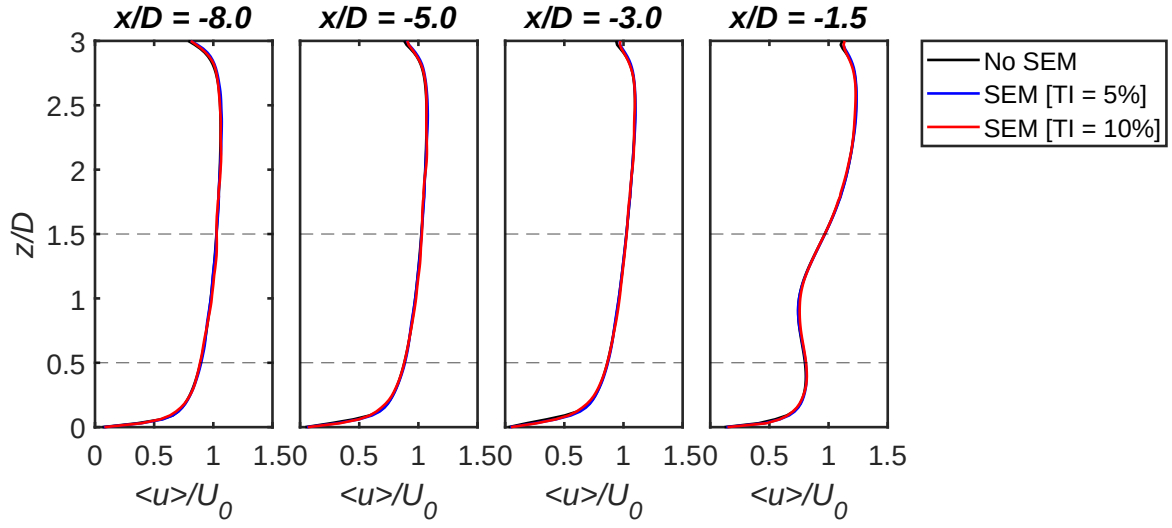

Fig. C.1 Vertical profiles of normalised time-averaged streamwise velocity $\langle u \rangle / U_0$ at four upstream locations from the Cylinder. Simulations using SEM at TIs of 5% and 10% compared to the baseline case without SEM. The dashed lines indicate the cylinder position.

Appendix D

Fixed water depth at the inlet

This section presents Fig. D.1, which compares simulations with different streamwise distances from the inlet to the cylinder position (16D, 24D, 32D) for the S24 case. It shows that the free surface development is unaffected by the proximity of the upstream inlet or the restriction of the water surface to a fixed depth at the inlet.

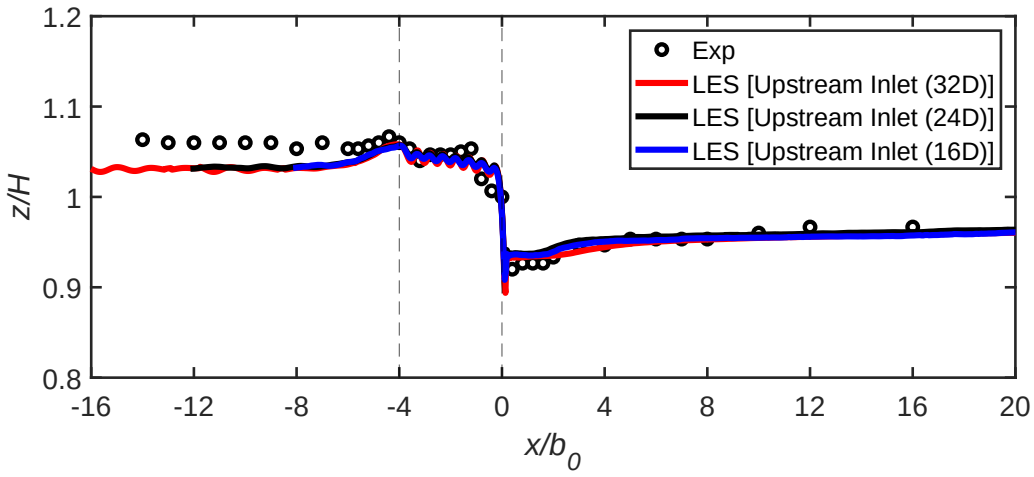

Fig. D.1 Comparison of the mean water-surface elevation (z) normalised by the mean flow depth (H) between experiment (symbols) and LES (line) for the S24 case at three streamwise distances from the Inlet to the cylinder position. The vertical dashed lines indicate the upstream and downstream ends of the leaky structure.

Appendix E

Upstream Water Depth: Derivation of the Estimation Formula

This section describes the process used to derive the analytical equation for estimating upstream and downstream water depths in situations where only one of the conditions is already known. This derivation utilises the momentum and continuity equations along with the canopy drag model. The variables mentioned in this section are not defined here as they have already been elaborated upon in Chapter 6.

A leaky barrier was assumed to be dynamically similar to an array of rigid cylindrical elements as in canopy flows. Thus, the drag per fluid volume within the structure D_x can be represented as:

$$D_x = \frac{\rho C_D K a u^2}{2(1-\phi)} \tag{E.1}$$

For the conservation of momentum between upstream and downstream locations of a leaky barrier:

$$\frac{1}{2}\rho g B(1-\phi)(H_1^2 - H_2^2) - \frac{1}{2}\rho B L_S C_D K a u_1^2 H_1 = \rho B H_2 u_2^2 - \rho B H_1 u_1^2 \tag{E.2}$$

Multiply by $2/\rho B$:

$$\overbrace{g(1-\phi)\left(H_1^2 - H_2^2\right)}^{\text{Net Hydrostatic Pressure Force}} - \overbrace{L_S C_D K a u_1^2 H_1}^{\text{Drag within the Barrier}} = \overbrace{2\left(H_2 u_2^2 - H_1 u_1^2\right)}^{\text{Net Change in Momentum}}$$

$$\begin{cases} Q = u_1 B H_1 = u_2 B H_2 \\ u_1 = \frac{u_2 H_2}{H_1} \\ \Delta H = H_1 - H_2 \\ H_1 = \Delta H + H_2 \end{cases}$$

For the pressure term:

$$g H_1^2(1-\phi) - g H_2^2(1-\phi)$$

$$\downarrow$$

$$g\left(\Delta H + H_2\right)^2(1-\phi) - g H_2^2(1-\phi) \quad \text{(a)}$$

(E.3)

Now, looking at the drag term:

$$L_S C_D K a u_1^2 H_1 = \frac{L_S C_D K a u_2^2 H_2^2}{H_1} = \frac{L_S C_D K a u_2^2 H_2^2}{\Delta H + H_2} \quad \text{(b)} \tag{E.4}$$

Next, consider the momentum term:

$$2H_2u_2^2 - 2H_1u_1^2 = 2H_2u_2^2 - 2H_2u_2u_1 \tag{E.5}$$

$$2H_2u_2(u_2 - u_1) = 2H_2u_2\left(u_2 - \frac{u_2H_2}{H_1}\right) \tag{E.6}$$

$$= 2H_2u_2\left(u_2 - \frac{u_2H_2}{H_1}\right) \tag{E.7}$$

$$= 2H_2u_2^2\left(\frac{H_1 - H_2}{H_1}\right) \tag{E.8}$$

$$= 2H_2u_2^2\left(\frac{\Delta H}{\Delta H + H_2}\right) \quad \text{(c)} \tag{E.9}$$

Now, a, b, and c are combined as:

$$g(\Delta H + H_2)^2(1-\phi) - gH_2^2(1-\phi) - \frac{L_SC_DKau_2^2H_2^2}{\Delta H + H_2} = \frac{2H_2u_2^2\Delta H}{\Delta H + H_2} \tag{E.10}$$

Multiplying both sides of the previous equation by $\Delta H + H_2$ simplifies it to:

$$g(\Delta H + H_2)^3(1-\phi) - gH_2^2(1-\phi)(\Delta H + H_2) - L_SC_DKau_2^2H_2^2 = 2H_2u_2^2\Delta H \quad \text{(aa)} \tag{E.11}$$

By simplifying the first term on the left-hand side of the previous equation:

$$g(\Delta H + H_2)^3(1-\phi) - gH_2^2(1-\phi)(\Delta H + H_2) \tag{E.12}$$

$$(a+b)^3 = a^3 + 3a^2b + 3ab^2 + b^3 \tag{E.13}$$

$$= 2gH_2^2\Delta H(1-\phi) + 3g(\Delta H^2)H_2(1-\phi) + g\Delta H^3(1-\phi) \tag{E.14}$$

$$= g(1-\phi)\left[2H_2^2\Delta H + 3H_2\Delta H^2 + \Delta H^3\right] \tag{E.15}$$

Hence, equation (aa) can be expressed as:

$$g(1-\phi)\left[2H_2^2\Delta H + 3H_2\Delta H^2 + \Delta H^3\right] - L_SC_DKau_2^2H_2^2 = 2H_2u_2^2\Delta H \tag{E.16}$$

Dividing both sides of the previous equation by $g(1-\phi)H_2^3$ gives:

$$\frac{2H_2^2\Delta H}{H_2^3} + \frac{3H_2\Delta H^2}{H_2^3} + \frac{\Delta H^3}{H_2^3} - \frac{L_SC_DKau_2^2H_2^2}{g(1-\phi)H_2^3} = \frac{2H_2u_2^2\Delta H}{g(1-\phi)H_2^3} \tag{E.17}$$

Simplifying the first three terms on the left-hand side of the equation:

$$\frac{2(H_1 - H_2)}{H_2} + \frac{3(H_1 - H_2)^2}{H_2^2} + \frac{(H_1 - H_2)^3}{H_2^3} \quad (a') \tag{E.18}$$

Now, looking at the drag term:

$$\frac{L_S C_D K a u_2^2 H_2^2}{g(1-\phi)(H_2)} \tag{E.19}$$

$$\frac{L_S C_D K a u_2^2}{g H_2 (1-\phi)} = \frac{u_2^2}{g H_2} \cdot \frac{L_S C_D K a}{(1-\phi)} \tag{E.20}$$

Since:

$$Fr_2 = \frac{u_2}{\sqrt{g H_2}}, \quad Fr_2^2 = \frac{u_2^2}{g H_2}$$

then the final drag form will be given as:

$$= \frac{Fr_2^2 L_S C_D K a}{(1-\phi)} \quad (b') \tag{E.21}$$

Next, consider the momentum term:

$$\frac{2 H_2^2 u_2^2 \Delta H}{g(1-\phi) H_2^3} = \frac{2 u_2^2 \Delta H}{g(1-\phi) H_2^2} \tag{E.22}$$

simplified to:

$$\begin{aligned} \frac{u_2^2}{g H_2} \cdot \left(\frac{2\Delta H}{(1-\phi) H_2} \right) &= Fr_2^2 \left(\frac{2\Delta H}{(1-\phi) H_2} \right) \\ &= \frac{2 Fr_2^2 (H_1 - H_2)}{(1-\phi) H_2} \quad (c') \end{aligned} \tag{E.23}$$

Combining terms (a'), (b'), and (c'):

$$\left(\frac{H_1 - H_2}{H_2} \right)^3 + 3 \left(\frac{H_1 - H_2}{H_2} \right)^2 + \frac{2(H_1 - H_2)}{H_2} - \frac{Fr_2^2 L_S C_D K a}{(1-\phi)} - \frac{2 Fr_2^2 (H_1 - H_2)}{(1-\phi) H_2} = 0 \tag{E.24}$$

expressing the equation in terms of ΔH:

$$\left(\frac{\Delta H}{H_2} \right)^3 + 3 \left(\frac{\Delta H}{H_2} \right)^2 + 2 \left(\frac{\Delta H}{H_2} \right) - \frac{Fr_2^2 L_S C_D K a}{(1-\phi)} - \frac{2 Fr_2^2 \Delta H}{(1-\phi) H_2} = 0 \tag{E.25}$$

Since the term $\left(\frac{\Delta H}{H_2} \right)^3$ is negligible and can be approximated to 0, we simplify the above equation to a quadratic form:

$$3 \left(\frac{\Delta H}{H_2} \right)^2 + 2 \left(\frac{\Delta H}{H_2} \right) - \frac{2 Fr_2^2}{(1-\phi)} \left(\frac{\Delta H}{H_2} \right) - \frac{Fr_2^2 L_S C_D K a}{(1-\phi)} = 0 \tag{E.26}$$

Let $\frac{\Delta H}{H_2} = x$:

$$3x^2 + 2x - \frac{2Fr_2^2}{(1-\phi)}x - \frac{Fr_2^2 L_s C_D Ka}{(1-\phi)} = 0 \tag{E.27}$$

Now, we solve for x using the quadratic formula and simplify the expression:

$$\begin{aligned} x &= \frac{-b \pm \sqrt{b^2 - 4ac}}{2a} \\ a &= 3 \\ b &= 2 - \frac{2Fr_2^2}{(1-\phi)} \\ c &= -\frac{Fr_2^2 L_s C_D Ka}{(1-\phi)} \end{aligned} \tag{E.28}$$

Solving for x yields two values, but only the positive value is considered, as the negative solution is not feasible in this context.

$$\begin{aligned} x &= \frac{-2 + \frac{2Fr_2^2}{(1-\phi)} + \sqrt{\left(2 - \frac{2Fr_2^2}{(1-\phi)}\right)^2 - 4 \cdot 3 \cdot \frac{-Fr_2^2 L_s C_D Ka}{(1-\phi)}}}{2 \cdot 3} \\ &= \frac{2\left(\frac{Fr_2^2}{(1-\phi)} - 1\right) + \sqrt{4\left[\left(\frac{Fr_2^2}{1-\phi} - 1\right)^2 + \frac{3Fr_2^2 L_S C_D Ka}{1-\phi}\right]}}{2 \cdot 3} \\ &= \frac{2\left(\frac{Fr_2^2}{(1-\phi)} - 1\right) + 2\sqrt{\left(\frac{Fr_2^2 - 1}{1-\phi}\right)^2 + \frac{3L_S C_D Ka Fr_2^2}{1-\phi}}}{2 \cdot 3} \\ &= \frac{\left[\left(\frac{Fr_2^2}{(1-\phi)} - 1\right) + \sqrt{\left(\frac{Fr_2^2}{1-\phi} - 1\right)^2 + \frac{3L_S C_D Ka Fr_2^2}{1-\phi}}\right]}{3} \end{aligned} \tag{E.29}$$

Substituting the expression for x:

$$\frac{\Delta H}{H_2} = \frac{\left[\left(\frac{Fr_2^2}{(1-\phi)} - 1\right) + \sqrt{\left(\frac{Fr_2^2}{(1-\phi)} - 1\right)^2 + \frac{3L_S C_D Ka}{(1-\phi)} Fr_2^2}\right]}{3} \tag{E.30}$$

$$\Delta H = \left[\frac{H_2}{3}\left(\left(\frac{Fr_2^2}{1-\phi} - 1\right) + \sqrt{\left(\frac{Fr_2^2}{1-\phi} - 1\right)^2 + \frac{3L_S C_D Ka Fr_2^2}{1-\phi}}\right)\right] \tag{E.31}$$

Finally, the upstream water depth can be obtained in a straightforward manner as a function of H_2 amongst other variables:

$$H_1(H_2,Fr_2,\phi,L_S,C_D,K,a) = H_2\left[1+\frac{1}{3}\left(\frac{Fr_2^2}{1-\phi}-1\right)+\sqrt{\left(\frac{Fr_2^2}{1-\phi}-1\right)^2+3\frac{L_S C_D K a}{1-\phi}Fr_2^2}\right] \tag{E.32}$$

Conversely, solving the momentum equation for the downstream water depth yields the following expression:

$$H_2 = H_1\left[1-\frac{1}{6}\left(\frac{2Fr_1^2}{1-\phi}-\frac{Fr_1^2 L_S C_D a}{1-\phi}-2\right)+\sqrt{\left(2+\frac{Fr_1^2 L_S C_D a}{1-\phi}-\frac{2Fr_1^2}{1-\phi}\right)^2+12\frac{Fr_1^2 L_S C_D K a}{1-\phi}}\right] \tag{E.33}$$

REFERENCES

Aamir, M. and Ahmad, Z. (2016), 'Review of literature on local scour under plane turbulent wall jets', *Physics of Fluids* **28**(10).

Addy, S. and Wilkinson, M. E. (2019), 'Representing natural and artificial in-channel large wood in numerical hydraulic and hydrological models', *Wiley Interdisciplinary Reviews: Water* **6**(6), e1389.

agru (2018). Client: Market village Altmünster. Location: Austria. Construction time: October 2015 - April 2018.
URL: *https://www.agru.at/en/applications/agruline/underwater-wastewater-hdpe-100-rc-pipes-with-protective-layer/*

Alam, M. M. (2014), 'The aerodynamics of a cylinder submerged in the wake of another', *Journal of fluids and structures* **51**, 393–400.

Alam, M. M. and Meyer, J. P. (2013), 'Global aerodynamic instability of twin cylinders in cross flow', *Journal of fluids and structures* **41**, 135–145.

Alam, M. M., Moriya, M. and Sakamoto, H. (2003), 'Aerodynamic characteristics of two side-by-side circular cylinders and application of wavelet analysis on the switching phenomenon', *Journal of fluids and structures* **18**(3-4), 325–346.

Albayrak, I., Hopfinger, E. and Lemmin, U. (2008), 'Near-field flow structure of a confined wall jet on flat and concave rough walls', *Journal of Fluid Mechanics* **606**, 27–49.

Alessandrini, B. and Delhommeau, G. (1996), A multigrid velocity-pressure-free surface elevation fully coupled solver for calculation of turbulent incompressible flow around a hull, *in* 'Proceedings of the 21st symposium on naval hydrodynamics', Vol. 19, pp. 321–342.

Aljure, D., Lehmkhul, O., Rodríguez, I. and Oliva, A. (2017), 'Three dimensionality in the wake of the flow around a circular cylinder at reynolds number 5000', *Computers and Fluids* **147**, 102–118.

Allen, J. B. and Smith, D. L. (2012), 'Characterizing the impact of geometric simplification on large woody debris using cfd', *International Journal of hydraulic engineering* **1**(2), 1–14.

Alper Oner, A., Salih Kirgoz, M. and Sami Akoz, M. (2008), 'Interaction of a current with a circular cylinder near a rigid bed', *Ocean Engineering* **35**(14-15), 1492–1504.

Alzabari, F., Wilson, C. A. and Ouro, P. (2022), Large-eddy simulation of the free-surface impact on the wake dynamics of a circular cylinder, *in* 'Proceedings of the 39th IAHR World Congress', Granada, Spain.

Alzabari, F., Wilson, C. A. and Ouro, P. (2023a), 'Unsteady vortex shedding dynamics behind a circular cylinder in very shallow free-surface flows', *Computers and Fluids* **260**, 105918.

Alzabari, F., Wilson, C. A. and Ouro, P. (2023b), 'Large-eddy simulation of flow around leaky barriers in an inclined configuration'. Water Resources Research (Submitted).

Alzabari, F., Wilson, C. A. and Ouro, P. (2023c), Large-eddy simulation of flow around leaky barriers in linear configurations, *in* 'Proceedings of the 40th IAHR World Congress', Vienna, Austria.

Angrilli, F., Bergamaschi, S. and Cossalter, V. (1982), 'Investigation of wall induced modifications to vortex shedding from a circular cylinder', *Transactions of the ASME Journal of Fluids Engineering* .

Armenio, V. (1997), 'An improved mac method (simac) for unsteady high-reynolds free surface flows', *International Journal for Numerical Methods in Fluids* **24**(2), 185–214.

Arnell, N. W. and Gosling, S. N. (2016), 'The impacts of climate change on river flood risk at the global scale', *Climatic Change* **134**, 387–401.

Atabay, S. (2008), 'Accuracy of the isis bridge methods for prediction of afflux at high flows', *Water Environ. J.* **22**(1), 64–73.

Attiya, B., Altimemy, M., Caspar, J., Daskiran, C., Liu, I.-H. and Oztekin, A. (2019), 'Large eddy simulations of multiphase flows past a finite plate near a free surface', *Ocean Engineering* **188**, 106342.

Bakhtyar, R., Barry, D. A., Li, L., Jeng, D. S. and Yeganeh-Bakhtiary, A. (2009), 'Modeling sediment transport in the swash zone: A review', *Ocean Engineering* **36**(9-10), 767–783.

Bansal, M. and Yarusevych, S. (2017), 'Experimental study of flow through a cluster of three equally spaced cylinders', *Experimental Thermal and Fluid Science* **80**, 203–217.

Bao, Y., Zhou, D. and Huang, C. (2010), 'Numerical simulation of flow over three circular cylinders in equilateral arrangements at low reynolds number by a second-order characteristic-based split finite element method', *Computers and Fluids* **39**(5), 882–899.

Bearman, P. and Zdravkovich, M. (1978), 'Flow around a circular cylinder near a plane boundary', *Journal of Fluid Mechanics* **89**(1), 33–47.

Beebe, J. (2000), 'Flume studies of the effect of perpendicular log obstruction on flow patterns and bed topography', *The Great Lakes Geographer* **7**(1), 9–25.

Berger, E. and Wille, R. (1972), 'Periodic flow phenomena', *Annual Review of Fluid Mechanics* **4**(1), 313–340.

Berkooz, G., Holmes, P. and Lumley, J. L. (1993), 'The proper orthogonal, decomposition in the analysis of turbulent flows', *Ann Rev Fluid Mech* **25**(1), 539–575.

Bevere, L. and Remondi, F. (2022), 'Natural catastrophes in 2021: The floodgates are open', *Swiss Re Institute. Available online: https://www.swissre.com/institute/research/sigma-research/sigma-2022-01.* **30**.

Bhuiyan, F., Habibzadeh, A., Rajaratnam, F. and Zhu, D. (2011), 'Reattached turbulent submerged offset jets on rough beds with shallow tailwater', *Journal of Hydraulic Engineering* **137**(12), 1636–1648.

Biery, P. and Delleur, J. (1962), 'Hydraulics of single span arch bridge constrictions', *Proceedings of the American Society of Civil Engineers, Hydraulics Division* **88**(2), 75–108.

Bilby, R. E. (1981), 'Role of organic debris dams in regulating the export of dissolved and particulate matter from a forested watershed', *Ecology* **62**(5), 1234–1243.

Bisson, P. and Vvondzei, S. M. (2003), Trends in using wood to restore aquatic habitats, *in* 'American fisheries society symposium', Vol. 37, pp. 391–406.

Blackman, K., Perret, L., Calmet, I. and Rivet, C. (2017), 'Turbulent kinetic energy budget in the boundary layer developing over an urban-like rough wall using piv', *Physics of Fluids* **29**(8).

Blevins, R. D. (1977), 'Flow-induced vibration', *New York* .

Bomminayuni, S. and Stoesser, T. (2011), 'Turbulence statistics in an open-channel flow over a rough bed', *Journal of Hydraulic Engineering* **137**(11), 1347–1358.

Boris, J. P. and Book, D. L. (1973), 'Flux-corrected transport. i. shasta, a fluid transport algorithm that works', *Journal of computational physics* **11**(1), 38–69.

Bouscasse, B., Colagrossi, A., Marrone, S. and Souto-Iglesias, A. (2017), 'Sph modelling of viscous flow past a circular cylinder interacting with a free surface', *Computers and Fluids* **146**, 190–212.

Bouwes, N., Weber, N., Jordan, C., Saunders, W., Tattam, I., Volk, C., Wheaton, J. and Pollock, M. (2016), 'Ecosystem experiment reveals benefits of natural and simulated beaver dams to a threatened population of steelhead (oncorhynchus mykiss)', *Scientific Reports* **6**(1), 28581.

Bradford, S. F. (2000), 'Numerical simulation of surf zone dynamics', *Journal of Waterway, Port, Coastal, and Ocean Engineering* **126**(1), 1–13.

Brevis, W. and García-Villalba, M. (2011), 'Shallow-flow visualization analysis by proper orthogonal decomposition', *Journal of Hydraulic Research* **49**(5), 586–594.

Bridges, T. S., Bourne, E. M., Suedel, B. C., Moynihan, E. B. and King, J. K. (2018), *Engineering with nature: an atlas*, US Army Engineer Research and Development Center, Environmental Laboratory.

Buffington, J. M. (1999), 'The legend of af shields', *Journal of Hydraulic Engineering* **125**(4), 376–387.

Buffington, J. M. and Montgomery, D. R. (1997), 'A systematic analysis of eight decades of incipient motion studies, with special reference to gravel-bedded rivers', *Water resources research* **33**(8), 1993–2029.

Bunte, K. (2001), *Sampling surface and subsurface particle-size distributions in wadable gravel-and cobble-bed streams for analyses in sediment transport, hydraulics, and streambed monitoring*, US Department of Agriculture, Forest Service, Rocky Mountain Research Station.

Buresti, G. and Lanciotti, A. (1992), 'Mean and fluctuating forces on a circular cylinder in cross-flow near a plane surface', *Journal of Wind Engineering and Industrial Aerodynamics* **41**(1-3), 639–650.

Burgess-Gamble, L., Ngai, R., Wilkinson, M., Nisbet, T., Pontee, N., Harvey, R., Kipling, K., Addy, S., Rose, S., Maslen, S. et al. (2018), 'Working with natural processes–evidence directory', *Environmental Agency, Report No. SC150005* .

Bussmann, M., Chandra, S. and Mostaghimi, J. (2000), 'Modeling the splash of a droplet impacting a solid surface', *Physics of fluids* **12**(12), 3121–3132.

Carberry, J. (2002), Wake states of a submerged oscillating cylinder and of a cylinder beneath a free-surface, PhD thesis, Monash University.

Castro-Santos, T. (2005), 'Optimal swim speeds for traversing velocity barriers: an analysis of volitional high-speed swimming behavior of migratory fishes', *Journal of Experimental Biology* **208**(3), 421–432.

Cevheri, M., McSherry, R. and Stoesser, T. (2016), 'A local mesh refinement approach for large-eddy simulations of turbulent flows', *International Journal for Numerical Methods in Fluids* **82**(5), 261–285.

Chang, Y.-C., Hou, T., Merriman, B. and Osher, S. (1996), 'A level set formulation of eulerian interface capturing methods for incompressible fluid flows', *Journal of computational Physics* **124**(2), 449–464.

Charbeneau, R. J., Holley, E. R. et al. (2001), Backwater effects of piers in subcritical flow, Technical report, University of Texas at Austin. Center for Transportation Research.

Chatterjee, A. (2000), 'An introduction to the proper orthogonal decomposition', *Current Science* **78**, 808–817.

Chen, D. and Jirka, G. H. (1995), 'Experimental study of plane turbulent wakes in a shallow water layer', *Fluid dynamics research* **16**(1), 11.

Chen, W., Ji, C., Xu, D., An, H. and Zhang, Z. (2020), 'Flow-induced vibrations of two side-by-side circular cylinders at low reynolds numbers', *Physics of Fluids* **32**(2), 023601.

Chen, W., Ji, C., Xu, D. and Williams, J. (2019), 'Two-degree-of-freedom vortex-induced vibrations of a circular cylinder in the vicinity of a stationary wall', *Journal of Fluids and Structures* **91**, 102728.

Chen, W., Ji, C., Xu, D. and Zhang, Z. (2020), 'Vortex-induced vibrations of two inline circular cylinders in proximity to a stationary wall', *Journal of Fluids and Structures* **94**, 102958.

Chorin, A. J. (1968), 'Numerical solution of the navier-stokes equations', *Mathematics of computation* **22**(104), 745–762.

Christensen, E. D. (2006), 'Large eddy simulation of spilling and plunging breakers', *Coastal Engineering* **53**(5-6), 463–485.

Christou, A., Xie, Z., Stoesser, T. and Ouro, P. (2021), 'Propagation of a solitary wave over a finite submerged thin plate', *Applied Ocean Research* **106**, 102425.

Chu, C.-R., Lin, Y.-A., Wu, T.-R. and Wang, C.-Y. (2018), 'Hydrodynamic force of a circular cylinder close to the water surface', *Computers and Fluids* **171**, 154–165.

Church, M., Hassan, M. A. and Wolcott, J. F. (1998), 'Stabilizing self-organized structures in gravel-bed stream channels: Field and experimental observations', *Water Resources Research* **34**(11), 3169–3179.

Collins, B. D., Montgomery, D. R., Fetherston, K. L. and Abbe, T. B. (2012), 'The floodplain large-wood cycle hypothesis: A mechanism for the physical and biotic structuring of temperate forested alluvial valleys in the north pacific coastal ecoregion', *Geomorphology* **139**, 460–470.

Dadson, S. J., Hall, J. W., Murgatroyd, A., Acreman, M., Bates, P., Beven, K., Heathwaite, L., Holden, J., Holman, I. P., Lane, S. N. et al. (2017), 'A restatement of the natural science evidence concerning catchment-based 'natural' flood management in the uk', *Proceedings of the Royal Society A: Mathematical, Physical and Engineering Sciences* **473**(2199), 20160706.

Davidson, L. (2015), 'Fluid mechanics, turbulent flow and turbulence modeling'.

De Sousa, F., Mangiavacchi, N., Nonato, L. G., Castelo, A., Tomé, M. F., Ferreira, V. G., Cuminato, J. A. and Mckee, S. (2004), 'A front-tracking/front-capturing method for the simulation of 3d multi-fluid flows with free surfaces', *Journal of Computational Physics* **198**(2), 469–499.

Deep, D., Sahasranaman, A. and Senthilkumar, S. (2022), 'Pod analysis of the wake behind a circular cylinder with splitter plate', *European Journal of Mechanics - B/Fluids* **93**, 1–12.

Díaz-Ojeda, H. R., Huera-Huarte, F. and González-Gutiérrez, L. M. (2019), 'Hydrodynamics of a rigid stationary flat plate in cross-flow near the free surface', *Physics of Fluids* **31**(10).

Dipankar, A., Sengupta, T. K. and Talla, S. B. (2007), 'Suppression of vortex shedding behind a circular cylinder by another control cylinder at low reynolds numbers', *Journal of Fluid Mechanics* **573**, 171–190.

Dixon, S. J. and Sear, D. A. (2014), 'The influence of geomorphology on large wood dynamics in a low gradient headwater stream', *Water Resources Research* **50**(12), 9194–9210.

Dodd, J., Newton, M. and Adams, C. (2016), 'The effect of natural flood management in-stream wood placements on fish movement in scotland', *Report CD2015* **2**.

Ead, S. and Rajaratnam, N. (2002), 'Plane turbulent wall jets in shallow tailwater', *J. Eng. Mech.* **128**, 143–155.

Edenhofer, O. et al. (2014), 'Technical summary in: Climate change 2014: Mitigation of climate change. contribution of working group iii to the fifth assessment report of the intergovernmental panel on climate change. technical report'.

Enright, D., Fedkiw, R., Ferziger, J. and Mitchell, I. (2002), 'A hybrid particle level set method for improved interface capturing', *Journal of Computational physics* **183**(1), 83–116.

Estrela, T., Menéndez, M., Dimas, M., Leonard, J., Ovesen, I. N. B., Fehér, N. J. and Consult, V. (2001), *Sustainable water use in Europe*, European Environment Agency.

Fadlun, E. A., Verzicco, R., Orlandi, P. and Mohd-Yusof, J. (2000), 'Combined immersed-boundary finite-difference methods for three-dimensional complex flow simulations', *Journal of computational physics* **161**(1), 35–60.

Farmer, J., Martinelli, L. and Jameson, A. (1993), A fast multigrid method for solving the nonlinear ship wave problem with a free surface, *in* 'Proceedings 6th International Conference on Numerical Ship Hydrodynamics, Iowa'.

Ferziger, J. and Peric, M. (2002), *Computational methods for fluid dynamics*, Springer-Verlag.

Follett, E., Schalko, I. and Nepf, H. (2021), 'Logjams with a lower gap: Backwater rise and flow distribution beneath and through logjam predicted by two-box momentum balance', *Geophysical Research Letters* **48**(16), e2021GL094279.

Follett, E. and Wilson, C. (2020), Bedload sediment transport induced by channel-spanning instream structures, *in* 'River flow 2020', CRC Press, pp. 735–742.

Freymuth, P., Finaish, F. and Bank, W. (1986), 'Visualization of the vortex street behind a circular cylinder at low reynolds numbers', *The Physics of fluids* **29**(4), 1321–1323.

Fulgosi, M., Lakehal, D., Banerjee, S. and De Angelis, V. (2003), 'Direct numerical simulation of turbulence in a sheared air–water flow with a deformable interface', *Journal of fluid mechanics* **482**, 319–345.

Geertsemaa, T. J., Torfsa, P. J., Teulinga, R. J., Eekhouta, J. P. and Hoitinka, T. J. (2018), 'Parametric model of wood-induced backwater in lowland streams', *NCR DAYS 2018* p. 82.

Gerrard, J. H. (1966), 'The mechanics of the formation region of vortices behind bluff bodies', *Journal of Fluid Mechanics* **25**(2), 401–413.

Gijón Mancheño, A., Jansen, W., Winterwerp, J. C. and Uijttewaal, W. S. (2021), 'Predictive model of bulk drag coefficient for a nature-based structure exposed to currents', *Scientific reports* **11**(1), 3517.

Gippel, C., ONeill, I. and et al. (1996), 'Hydraulic guidelines for the reintroduction and management of large woody debris in lowland rivers', *Regulat. Rivers: Res. Manage.* **12**(2-3), 223–236.

Gopala, V. R. and Van Wachem, B. G. (2008), 'Volume of fluid methods for immiscible-fluid and free-surface flows', *Chemical Engineering Journal* **141**(1-3), 204–221.

Götkun, S. (1975), The drag and lift coefficients of a cylinder placed near a plane surface, PhD thesis, Master's thesis, Naval Postgraduate School, Monterey, CA.

Grass, A., Raven, P., Stuart, R. and Bray, J. (1984), 'The influence of boundary layer velocity gradients and bed proximity on vortex shedding from free spanning pipelines'.

Green, R. and Gerrard, J. (1993), 'Vorticity measurements in the near wake of a circular cylinder at low reynolds numbers', *Journal of Fluid Mechanics* **246**, 675–691.

Griebel, M. and Klitz, M. (2017), 'Clsvof as a fast and mass-conserving extension of the level-set method for the simulation of two-phase flow problems', *Numerical Heat Transfer, Part B: Fundamentals* **71**(1), 1–36.

Griffith, M., Jacono, D., Sheridan, J. and Leontini, J. (2017), 'Flow-induced vibration of two cylinders in tandem and staggered arrangements', *Journal of Fluid Mechanics* **833**, 98–130.

Han, Z., Zhou, D. and Tu, J. (2013), 'Laminar flow patterns around three side-by-side arranged circular cylinders using semi-implicit three-step taylor-characteristic-based-split (3-tcbs) algorithm', *Engineering Applications of Computational Fluid Mechanics* **7**(1), 1–12.

Hankin, B., Hewitt, I., Sander, G., Danieli, F., Formetta, G., Kamilova, A., Kretzschmar, A., Kiradjiev, K., Wong, C., Pegler, S. et al. (2020), 'A risk-based network analysis of distributed in-stream leaky barriers for flood risk management', *Natural Hazards and Earth System Sciences* **20**(10), 2567–2584.

Harichandan, A. B. and Roy, A. (2010), 'Numerical investigation of low reynolds number flow past two and three circular cylinders using unstructured grid cfr scheme', *Int J Heat Fluid Flow* **31**(2), 154–171.

Harlow, F. H. and Welch, J. E. (1965), 'Numerical calculation of time-dependent viscous incompressible flow of fluid with free surface', *The physics of fluids* **8**(12), 2182–2189.

HC, R. (1996), 'A solution method for the nonlinear ship wave resistance problem', *PhD Thesis, Technische Universiteit Delft* p. 1.

Hey, R. D. and Thorne, C. R. (1986), 'Stable channels with mobile gravel beds', *Journal of Hydraulic engineering* **112**(8), 671–689.

Hirt, C. W. and Nichols, B. D. (1981), 'Volume of fluid (vof) method for the dynamics of free boundaries', *Journal of computational physics* **39**(1), 201–225.

Hodges, B. R. and Street, R. L. (1999), 'On simulation of turbulent nonlinear free-surface flows', *Journal of Computational Physics* **151**(2), 425–457.

Hoerner, S. (1958), *Fluid Dynamic Drag*, Self-published, New Jersey.

Holmes, P., Lumley, J. L. and Berkooz, G. (1996), *Turbulence, Coherent Structures, Dynamical Systems and Symmetry*, Cambridge University Press, New York.

Hosseini, N., Griffith, M. D. and Leontini, J. S. (2021), 'Flow states and transitions in flows past arrays of tandem cylinders', *Journal of Fluid Mechanics* **910**, A34.

Hou, T. Y., Lowengrub, J. S. and Shelley, M. J. (1994), 'Removing the stiffness from interfacial flows with surface tension', *Journal of Computational Physics* **114**(2), 312–338.

Hou, T. Y., Lowengrub, J. S. and Shelley, M. J. (2001), 'Boundary integral methods for multicomponent fluids and multiphase materials', *Journal of Computational Physics* **169**(2), 302–362.

Hoyt, J. and Sellin, R. (2000), 'A comparison of tracer and piv results in visualizing water flow around a cylinder close to the free surface', *Experiments in Fluids* **28**(3), 261–265.

Huang, R., Zeng, Y., Zha, W. and Yang, F. (2022), 'Investigation of flow characteristics in open channel with leaky barriers', *Journal of Hydrology* **613**, 128328.

Iaccarino, G. (2004), Immersed boundary technique for turbulent flows with industrial applications, PhD thesis, PhD thesis, Politecnico di bari.

Iaccarino, G. and Verzicco, R. (2003), 'Immersed boundary technique for turbulent flow simulations', *Appl. Mech. Rev.* **56**(3), 331–347.

Igarashi, T. and Suzuki, K. (1984), 'Characteristics of the flow around three circular cylinders arranged in line', *Bull. JSME* **27**(233), 2397–2404.

Jalalabadi, R., Stoesser, T., Ouro, P., Luo, Q. and Xie, Z. (2021), 'Free surface flow over square bars at different reynolds numbers', *Journal of Hydro-Environment Research* **36**, 67–76.

Janes, V. J., Grabowski, R. C., Mant, J., Allen, D., Morse, J. L. and Haynes, H. (2017), 'The impacts of natural flood management approaches on in-channel sediment quality', *River Research and Applications* **33**(1), 89–101.

Jasak, H. and Weller, H. (1995), 'Interface tracking capabilities of the inter-gamma differencing scheme', *Department of Mechanical Engineering, Imperial College of Science, Technology and Medicine* .

Julien, P. (1995), *Erosion and Sedimentation*, Cambridge University Press, Cambridge, U.K.

Kahraman, A., Ozgoren, M. and Sahin, B. (2012), 'Flow structure from a horizontal cylinder coincident with a free surface in shallow water flow', *Thermal Science* **16**(1), 93–107.

Kaimal, J. and Finnigan, J. (1994), *Atmospheric Boundary Layer Flows: Their Structure and Measurement*, Oxford University Press.

Kang, S. (2004), 'Numerical study on laminar flow over three side-by-side cylinders', *KSME international journal* **18**, 1869–1879.

Kang, S., Borazjani, I., Colby, J. A. and Sotiropoulos, F. (2012), 'Numerical simulation of 3d flow past a real-life marine hydrokinetic turbine', *Advances in water resources* **39**, 33–43.

Kang, S. and Sotiropoulos, F. (2015), 'Large-eddy simulation of three-dimensional turbulent free surface flow past a complex stream restoration structure', *Journal of Hydraulic Engineering* **141**, 04015022.

Kara, S., Kara, M. C., Stoesser, T. and Sturm, T. W. (2015a), 'Free-surface versus rigid-lid les computations for bridge-abutment flow', *Journal of Hydraulic Engineering* **141**(9), 04015019.

Kara, S., Stoesser, T., Sturm, T. W. and Mulahasan, S. (2015b), 'Flow dynamics through a submerged bridge opening with overtopping', *Journal of Hydraulic Research* **53**(2), 186–195.

Karmakar, A. and Saha, A. K. (2020), 'Unsteady flow past a square cylinder placed close to a free surface', *Physics of Fluids* **32**(12).

Kevlahan, N. K., Hunt, J. C. and Vassilicos, J. C. (1994), 'A comparison of different analytical techniques for identifying structures in turbulence', *Applied Scientific Research* **53**, 339–355.

Khosronejad, A., Ghazian Arabi, M., Angelidis, D., Bagherizadeh, E., Flora, K. and Farhadzadeh, A. (2019), 'Comparative hydrodynamic study of rigid-lid and level-set methods for les of open-channel flow', *Journal of Hydraulic Engineering* **145**(1), 04018077.

Koken, M. and Constantinescu, G. (2009), 'An investigation of the dynamics of coherent structures in a turbulent channel flow with a vertical sidewall obstruction', *Physics of Fluids* **21**(8).

Kolmogorov, A. N. (1941), 'The local structure of turbulence in incompressible viscous fluid for very large reynolds', *Numbers. In Dokl. Akad. Nauk SSSR* **30**, 301.

Komori, S., Nagaosa, R., Murakami, Y., Chiba, S., Ishii, K. and Kuwahara, K. (1993), 'Direct numerical simulation of three-dimensional open-channel flow with zero-shear gas–liquid interface', *Physics of Fluids A: Fluid Dynamics* **5**(1), 115–125.

Kostas, J., Soria, J. and Chong, M. S. (2005), 'A comparison between snapshot pod analysis of piv velocity and vorticity data', *Experiments in Fluids* **38**, 146–160.

Kuzmina, K., Marchevsky, I., Soldatova, I. and Izmailova, Y. (2021), 'On the scope of lagrangian vortex methods for two-dimensional flow simulations and the pod technique application for data storing and analyzing', *Entropy* **23**(1), 118.

Lagasse, P., Zevenberger, L. and Clopper, P. (2010), Impacts of debris on bridge pier scour, *in* 'Scour and Erosion, International Conference on Scour and Erosion', American Society of Civil Engineers.

Lam, K. and Banerjee, S. (1992), 'On the condition of streak formation in a bounded turbulent flow', *Physics of Fluids A: Fluid Dynamics* **4**(2), 306–320.

Lam, K. and Cheung, W. (1988), 'Phenomena of vortex shedding and flow interference of three cylinders in different equilateral arrangements', *Journal of Fluid Mechanics* **196**, 1–26.

Lane, S. N. (2017), 'Natural flood management', *Wiley Interdisciplinary Reviews: Water* **4**(3), e1211.

Leakey, S., Hewett, C. J., Glenis, V. and Quinn, P. F. (2020), 'Modelling the impact of leaky barriers with a 1d godunov-type scheme for the shallow water equations', *Water* **12**(2), 371.

Lee, J., Kim, J., Choi, H. and Yang, K.-S. (2011), 'Sources of spurious force oscillations from an immersed boundary method for moving-body problems', *Journal of computational physics* **230**(7), 2677–2695.

Lei, C., Cheng, L., Armfield, S. and Kavanagh, K. (2000), 'Vortex shedding suppression for flow over a circular cylinder near a plane boundary', *Ocean Engineering* **27**(10), 1109–1127.

Lei, C., Cheng, L. and Kavanagh, K. (1999), 'Re-examination of the effect of a plane boundary on force and vortex shedding of a circular cylinder', *Journal of Wind Engineering and Industrial Aerodynamics* **80**(3), 263–286.

Leonard, A. (1975), Energy cascade in large-eddy simulations of turbulent fluid flows, *in* 'Advances in geophysics', Vol. 18, Elsevier, pp. 237–248.

Leonardo da Vinci Drawings (2011).
URL: *https://www.leonardodavinci.net/drawings.jsp*

Liang, Y. and Tao, L. (2018), Hydrodynamics around a deep-draft semi-submersible with various corner shapes, *in* 'International Conference on Offshore Mechanics and Arctic Engineering', Vol. 51302, American Society of Mechanical Engineers, p. V009T13A001.

Lin, J.-C., Towfighi, J. and Rockwell, D. (1995), 'Instantaneous structure of the near-wake of a circular cylinder: on the effect of reynolds number', *Journal of Fluids and Structures* **9**(4), 409–418.

Lin, W.-J., Lin, C., Hsieh, S.-C. and Dey, S. (2009), 'Flow characteristics around a circular cylinder placed horizontally above a plane boundary', *Journal of engineering mechanics* **135**(7), 697–716.

Liu, H.-K., Bradley, J. N. and Plate, E. J. (1957), *Backwater Effects of Piers and Abutments*, Colorado State University, Boulder, Colorado. CER57HKLIO.

Liu, I.-H., Riglin, J., Schleicher, W. C. and Oztekin, A. (2016), 'Flow past a plate in the vicinity of a free surface', *Ocean Engineering* **111**, 323–334.

Liu, Y., Stoesser, T. and Fang, H. (2022), 'Effect of secondary currents on the flow and turbulence in partially filled pipes', *Journal of Fluid Mechanics* **938**, A16.

Liu, Y., Stoesser, T., Fang, H., Papanicolaou, A. and Tsakiris, A. G. (2017), 'Turbulent flow over an array of boulders placed on a rough, permeable bed', *Computers and Fluids* **158**, 120–132.

Liu, Z. (1998), *Sediment transport*, Aalborg Universitetsforlag.

Longo, J., Stern, F. and Toda, Y. (1993), 'Mean-flow measurements in the boundary layer and wake and wave field of a series 60 cb= 0.6 ship model—part 2: Scale effects on near-field wave patterns and comparisons with inviscid theory', *Journal of Ship Research* **37**(01), 16–24.

Lopes, A. S., Piomelli, U. and Palma, J. (2006), 'Large-eddy simulation of the flow in an s-duct', *Journal of Turbulence* (7), N11.

Lubin, P., Glockner, S., Kimmoun, O. and Branger, H. (2011), 'Numerical study of the hydrodynamics of regular waves breaking over a sloping beach', *European Journal of Mechanics-B/Fluids* **30**(6), 552–564.

Lumley, J. L. (1967), 'The structure of inhomogeneous turbulent flows', *Atmospheric turbulence and radio wave propagation* p. 166–178.

Luo, Q., Dolcetti, G., Stoesser, T. and Tait, S. (2023), 'Water surface response to turbulent flow over a backward-facing step', *Journal of Fluid Mechanics* **966**, A18.

Ma, X. and Karniadakis, G. E. (2002), 'A low-dimensional model for simulating three-dimensional cylinder flow', *Journal of Fluid Mechanics* **458**, 181–190.

Malavasi, S. and Guadagnini, A. (2007), 'Interactions between a rectangular cylinder and a free-surface flow', *Journal of Fluids and Structures* **23**(8), 1137–1148.

Manners, R. B., Doyle, M. and Small, M. (2007), 'Structure and hydraulics of natural woody debris jams', *Water Resources Research* **43**(6).

Mattei, M., Frunzo, L., D'acunto, B., Pechaud, Y., Pirozzi, F. and Esposito, G. (2018), 'Continuum and discrete approach in modeling biofilm development and structure: a review', *Journal of mathematical biology* **76**, 945–1003.

McCartney, M. P. and de la Hera, A. (2004), 'Hydrological assessment for wetland conservation at wicken fen', *Wetlands ecology and management* **12**(3), 189–204.

McKee, S., Tomé, M. F., Ferreira, V. G., Cuminato, J. A., Castelo, A., Sousa, F. and Mangiavacchi, N. (2008), 'The mac method', *Computers and Fluids* **37**(8), 907–930.

McSherry, R., Chua, K., Stoesser, T. and Mulahasan, S. (2018), 'Free surface flow over square bars at intermediate relative submergence', *Journal of Hydraulic Research* **56**, 825–843.

McSherry, R. J., Chua, K. V. and Stoesser, T. (2017), 'Large eddy simulation of free-surface flows', *Journal of Hydrodynamics, Ser. B* **29**(1), 1–12.

Ménard, T., Tanguy, S. and Berlemont, A. (2007), 'Coupling level set/vof/ghost fluid methods: Validation and application to 3d simulation of the primary break-up of a liquid jet', *International Journal of Multiphase Flow* **33**(5), 510–524.

Meneghini, J. R., Saltara, F., Siqueira, C. d. L. R. and Ferrari Jr, J. (2001), 'Numerical simulation of flow interference between two circular cylinders in tandem and side-by-side arrangements', *Journal of fluids and structures* **15**(2), 327–350.

Mishra, A. and De, A. (2021), 'Suppression of vortex shedding using a slit through the circular cylinder at low reynolds number', *European Journal of Mechanics, B/Fluids* **89**, 349–366.

Miyata, H., Sato, T. and Baba, N. (1987), 'Difference solution of a viscous flow with free-surface wave about an advancing ship', *Journal of Computational Physics* **72**(2), 393–421.

Miyata, H., Shikazono, N. and Kanai, M. (1990), 'Forces on a circular cylinder advancing steadily beneath the free-surface', *Ocean engineering* **17**(1-2), 81–104.

Miyata, H., Zhu, M. and Watanabe, O. (1992), 'Numerical study on a viscous flow with free-surface waves about a ship in steady straight course by a finite-volume method', *Journal of Ship Research* **36**(04), 332–345.

Moballa, B., Chern, M.-J. and Borthwick, A. (2020), 'Incompressible sph simulation of flow past horizontal cylinder between plane wall and free surface', *Journal of Fluids and Structures* **97**, 103091.

Morkovin, M. (1964), Flow around circular cylinder-kaleidoscope of challenging fluid phenomena, *in* 'Proc. Symp. Fully Separated Flows, Philadelphia, 1964', ASME, pp. 102–118.

Muhawenimana, V., Follett, E., Maddock, I. and Wilson, C. A. M. E. (2023), 'Field-based monitoring of instream leaky barrier backwater and storage during storm events', *Journal of Hydrology* **1**, 129744.

Muhawenimana, V., Wilson, C. A., Nefjodova, J. and Cable, J. (2021), 'Flood attenuation hydraulics of channel-spanning leaky barriers', *Journal of Hydrology* **596**, 125731.

Muhawenimana, V., Wilson, C. A., Ouro, P. and Cable, J. (2019), 'Spanwise cylinder wake hydrodynamics and fish behavior', *Water Resources Research* **55**(11), 8569–8582.

Müller, S., Wilson, C. A., Ouro, P. and Cable, J. (2021a), 'Leaky barriers: leaky enough for fish to pass?', *Royal Society open science* **8**(3), 201843.

Müller, S., Wilson, C. A., Ouro, P. and Cable, J. (2021b), 'Experimental investigation of physical leaky barrier design implications on juvenile rainbow trout (oncorhynchus mykiss) movement', *Water Resources Research* **57**(8), e2021WR030111.

Müller, S., Follett, E. M., Ouro, P. and Wilson, C. (2022), 'Influence of channel-spanning engineered logjam structures on channel hydrodynamics', *Water Resources Research* **58**(12), e2022WR032111.

Nepf, H. (2012), 'Flow and transport in regions with aquatic vegetation', *Annu. Rev. Fluid Mech.* **44**(1), 123–142.

Nguyen, Q. D. and Lei, C. (2021), 'Hydrodynamic characteristics of a confined circular cylinder in cross-flows', *Ocean Engineering* **221**, 108567.

Nichols, B. and Hirt, C. (1973), 'Calculating three-dimensional free surface flows in the vicinity of submerged and exposed structures', *Journal of Computational Physics* **12**(2), 234–246.

Nicoud, F. and Ducros, F. (1999), 'Subgrid-scale stress modelling based on the square of the velocity', *Flow Measurement and Instrumentation* **62**, 183–200.

Nikora, V. I., Stoesser, T., Cameron, S. M., Stewart, M., Papadopoulos, K., Ouro, P., McSherry, R., Zampiron, A., Marusic, I. and Falconer, R. A. (2019), 'Friction factor decomposition for rough-wall flows: Theoretical background and application to open-channel flows', *Journal of Fluid Mechanics* **872**, 626–664.

Nisbet, T., Roe, P., Marrington, S., Thomas, H., Broadmeadow, S. and Valatin, G. (2015), 'Defra fcerm multi-objective flood management demonstration project, project rmp5455: Slowing the flow at pickering, final report: phase ii', *Department for environment, food and rural affairs, UK* .

Noh, W. F. and Woodward, P. (1976), Slic (simple line interface calculation), *in* 'Proceedings of the fifth international conference on numerical methods in fluid dynamics June 28–July 2, 1976 Twente University, Enschede', Springer, pp. 330–340.

Norberg, C. (1998), 'Ldv-measurements in the near wake of a circular cylinder', *ASME paper no. FEDSM98-521* **41**.

North East project (2021).
URL: *https://www.gov.uk/government/news/pioneering-north-east-project-uses-nature-to-reduce-flood-risk*

Nyssen, J., Pontzeele, J. and Billi, P. (2011), 'Effect of beaver dams on the hydrology of small mountain streams: example from the chevral in the ourthe orientale basin, ardennes, belgium', *Journal of hydrology* **402**(1-2), 92–102.

Offshore Platform Topsides (2023).
URL: *https://www.ipsgroupbv.com/industries/offshore-construction/offshore-platform-topsides/*

Oner, A. A., Kirkgoz, M. S. and Akoz, M. S. (2008), 'Interaction of a current with a circular cylinder near a rigid bed', *Ocean Engineering* **35**(14-15), 1492–1504.

Osher, S. and Sethian, J. A. (1988), 'Fronts propagating with curvature-dependent speed: Algorithms based on hamilton-jacobi formulations', *Journal of Computational Physics* **79**(1), 12–49.

Ouro, P., Cea, L., Ramírez, L. and Nogueira, X. (2016), 'An immersed boundary method for unstructured meshes in depth averaged shallow water models', *International Journal for Numerical Methods in Fluids* **81**(11), 672–688.

Ouro, P., Lopez-Novoa, U. and Guest, M. F. (2021), 'On the performance of a highly-scalable computational fluid dynamics code on amd, arm and intel processor-based hpc systems', *Computer Physics Communications* **269**, 108105.

Ouro, P., Muhawenimana, V. and Wilson, C. A. (2019), 'Asymmetric wake of a horizontal cylinder in close proximity to a solid boundary for reynolds numbers in the subcritical turbulence regime', *Physical Review Fluids* **4**(10), 104604.

Ouro, P. and Nishino, T. (2021), 'Performance and wake characteristics of tidal turbines in an infinitely large array', *Journal of Fluid Mechanics* **925**, A30.

Ozdil, N. F. T. and Akilli, H. (2015), 'Investigation of flow structure around a horizontal cylinder at different elevations in shallow water', *Ocean Engineering* **96**, 56–67.

Ozdil, N. F. T. and Akilli, H. (2019), 'Flow comparison around horizontal single and tandem cylinders at different immersion elevations', *Ocean Engineering* **189**, 106352.

Paik, J. and Sotiropoulos, F. (2005), 'Coherent structure dynamics upstream of a long rectangular block at the side of a large aspect ratio channel', *Physics of fluids* **17**(11).

Papaioannou, G. V., Yue, D. K., Triantafyllou, M. S. and Karniadakis, G. E. (2006), 'Evidence of holes in the arnold tongues of flow past two oscillating cylinders', *Physical review letters* **96**(1), 014501.

Peng, D., Merriman, B., Osher, S., Zhao, H. and Kang, M. (1999), 'A pde-based fast local level set method', *Journal of computational physics* **155**(2), 410–438.

Perrin, R., Braza, M., Cid, E., Cazin, S., Barthet, A., Sevrain, A., Mockett, C. and Thiele, F. (2007), 'Obtaining phase averaged turbulence properties in the near wake of a circular cylinder at high reynolds number using pod', *Experiments in Fluids* **43**, 341–355.

Peskin, C. S. (1972), 'Flow patterns around heart valves: a numerical method', *Journal of computational physics* **10**(2), 252–271.

Peskin, C. S. (2002), 'The immersed boundary method', *Acta numerica* **11**, 479–517.

Pinelli, A., Naqavi, I., Piomelli, U. and Favier, J. (2010), 'Immersed-boundary methods for general finite-difference and finite-volume navier–stokes solvers', *Journal of Computational Physics* **229**(24), 9073–9091.

Pitt, M. (2008), 'Learning lessons from the 2007 floods', The Pitt Review.

Polatel, C. (2006), *Large-scale roughness effect on free-surface and bulk flow characteristics in open-channel flows*, The University of Iowa.

Price, S., Sumner, D., Smith, J., Leong, K. and Paidoussis, M. (2002), 'Flow visualization around a circular cylinder near to a plane wall', *Journal of Fluids and Structures* **16**(2), 175–191.

Pugh, C. A. (2008), Sediment transport scaling for physical models, *in* 'Sedimentation Engineering: Processes, Measurements, Modeling, and Practice', pp. 1057–1065.

Quinn, P., Donnell, G. et al. (2013), Potential use of runoff attenuation features in small rural catchments for flood mitigation, Technical report, Newcastle University.

Raju, K., Rana, O., Asawa, G. and Pillai, A. (1983), 'Rational assessment of blockage effects in channel flow past smooth circular cylinders', *Journal of Hydraulic Research* **21**(4), 289–302.

Ramamurthy, A. and Ng, A. (1973), 'Effect of blockage on steady force coefficients', *J. Engin. Mech. Div. Proc. ASCE* **99**(4), 755–772.

Rao, A., Thompson, M. C., Leweke, T. and Hourigan, K. (2013), 'The flow past a circular cylinder translating at different heights above a wall', *Journal of Fluids and Structures* **41**, 9–21.

Rasche, D., Reinhardt-Imjela, C., Schulte, A. and Wenzel, R. (2019), 'Hydrodynamic simulation of the effects of stable in-channel large wood on the flood hydrographs of a low mountain range creek, ore mountains, germany', *Hydrology and Earth System Sciences* **23**(10), 4349–4365.

Raven, H. and Van Brummelen, E. (1999), A new approach to computing steady free-surface viscous flow problems, *in* '1st MARNET-CFD workshop, Barcelona, Spain', Vol. 4, Citeseer.

Rehimi, F., Aloui, F., Nasrallah, S. B., Doubliez, L. and Legrand, J. (2008), 'Experimental investigation of a confined flow downstream of a circular cylinder centred between two parallel walls', *Journal of Fluids and Structures* **24**(6), 855–882.

Reich, M. (2003), 'Restoring streams with large wood: a synthesis', *The ecology and management of wood in world rivers* .

Reichl, P., Hourigan, K. and Thompson, M. (2003), 'The unsteady wake of a circular cylinder near a free surface', *Flow, Turbulence and Combustion* **71**, 347–359.

Reichl, P., Hourigan, K. and Thompson, M. C. (2005), 'Flow past a cylinder close to a free surface', *Journal of Fluid Mechanics* **533**, 269–296.

Reynolds, O. (1883), 'Xxix. an experimental investigation of the circumstances which determine whether the motion of water shall be direct or sinuous, and of the law of resistance in parallel channels', *Philosophical Transactions of the Royal society of London* (174), 935–982.

Ribau, Â. M., Gonçalves, N. D., Ferrás, L. L. and Afonso, A. M. (2021), 'Flow structures identification through proper orthogonal decomposition : The flow around two distinct cylinders', *Fluids* **6**(11), 384.

Rodi, W. (1997), 'Comparison of les and rans calculations of the flow around bluff bodies', *Journal of wind engineering and industrial aerodynamics* **69**, 55–75.

Rodi, W., Constantinescu, G. and Stoesser, T. (2013), *Large-eddy simulation in hydraulics*, Crc Press.

Roma, A. M., Peskin, C. S. and Berger, M. J. (1999), 'An adaptive version of the immersed boundary method', *Journal of computational physics* **153**(2), 509–534.

Roni, P., Beechie, T., Pess, G. and Hanson, K. (2015), 'Wood placement in river restoration: fact, fiction, and future direction', *Canadian Journal of Fisheries and Aquatic Sciences* **72**(3), 466–478.

Roshko, A. (1954), On the drag and shedding frequency of two-dimensional bluff bodies, Technical report.

Roshko, A., Steinolfson, A. and Chattoorgoon, V. (1975), Flow forces on a cylinder near a wall or near another cylinder, *in* 'Proceedings of the 2nd US Nation conference on wind engineering research, Fort Collins, Paper IV-15'.

Rowley, C. W., Mezić, I., Bagheri, S., Schlatter, P. and Henningson, D. S. (2009), 'Spectral analysis of nonlinear flows', *Journal of fluid mechanics* **641**, 115–127.

Rubinstein, R. and Clark, T. T. (2017), '"equilibrium" and "non-equilibrium" turbulence', *Theoretical and applied mechanics letters* **7**(5), 301–305.

Russo, G. and Smereka, P. (2000), 'A remark on computing distance functions', *Journal of computational physics* **163**(1), 51–67.

Sanjou, M. and Nezu, I. (2010), 'Large eddy simulation of compound open-channel flows with emergent vegetation near the floodplain edge', *Journal of Hydrodynamics, Ser. B* **22**(5), 582–586.

Sarkar, S. and Sarkar, S. (2010), 'Vortex dynamics of a cylinder wake in proximity to a wall', *Journal of Fluids and Structures* **26**(1), 19–40.

Schalko, I., Lageder, C., Schmocker, L., Weitbrecht, V. and Boes, R. (2019), 'Laboratory flume experiments on the formation of spanwise large wood accumulations: Part ii—effect on local scour', *Water Resources Research* **55**(6), 4871–4885.

Schalko, I., Schmocker, L., Weitbrecht, V. and Boes, R. (2018), 'Backwater rise due to large wood accumulations', *J. Hydraul. Eng.* **144**(9), 04018056.

Schewe, G. (1983), 'On the force fluctuations acting on a circular cylinder in crossflow from subcritical up to transcritical reynolds numbers', *Journal of fluid mechanics* **133**, 265–285.

Schmid, P. J. (2010), 'Dynamic mode decomposition of numerical and experimental data', *Journal of fluid mechanics* **656**, 5–28.

Schmocker, L. and Hager, W. (2013), 'Scale modeling of wooden debris accumulation at a debris rack', *J. Hydraulic Eng.* **139**(8), 827–836.

Sen, U., Mukhopadhyay, A. and Sen, S. (2017), 'Effects of fluid injection on dynamics of flow past a circular cylinder', *European Journal of Mechanics, B/Fluids* **61**, 187–199.

SEPA (2016), *Natural flood management handbook*, Scottish Environment Protection Agency.

Shaw, T. (1971), 'Effect of side walls on flow past bluff bodies', *J. Hydr. Div., Proc. ASCE* **97**(1), 65–79.

Sheridan, J., Lin, J. and Rockwell, D. (1995), 'Metastable states of a cylinder wake adjacent to a free surface', *Physics of Fluids* **7**(9), 2099–2101.

Sheridan, J., Lin, J. and Rockwell, D. (1997), 'Flow past a cylinder close to a free surface', *Journal of Fluid Mechanics* **330**, 1–30.

Shi, J., Thomas, T. and Williams, J. (2000), 'Free-surface effects in open channel flow at moderate froude and reynold's numbers', *Journal of Hydraulic Research* **38**(6), 465–474.

Shields, A. (1936), 'Anwendung der aehnlichkeitsmechanik und der turbulenzforschung auf die geschiebebewegung', *PhD Thesis Technical University Berlin* **Heft 26**.

Shuping, J. and Qinxi, L. (2019), 'Wave characteristics of submerged floating tunnels under random irregular waves', *Chinese Journal of Underground Space and Engineering* **15**(2), 416–422.

Shvidchenko, A. B. and Pender, G. (2000), 'Flume study of the effect of relative depth on the incipient motion of coarse uniform sediments', *Water Resources Research* **36**(2), 619–628.

Sirovich, L. (1987), 'Turbulence and the dynamics of coherent structures. iii. dynamics and scaling', *Quarterly of Applied Mathematics* **45**(3), 583–590.

slowtheflow (2019).
URL: *https://slowtheflow.net/engineered-leaky-woody-dams-welds-on-rock-stream-beds/*

Smagorinsky, J. (1963), 'General circulation experiments with the primitive equa- tions', *Monthly weather review* **91**(3), 99–164.

Sotiropoulos, F. (2015), 'Hydraulics in the era of exponentially growing computing power', *Journal of Hydraulic Research* **53**(5), 547–560.

Stoesser, T. (2001), Development and validation of a CFD-code for turbulent open-channel flows., PhD thesis, University of Bristol.

Stoesser, T. (2014), 'Large-eddy simulation in hydraulics: Quo vadis?', *Journal of Hydraulic Research* **52**(4), 441–452.

Stoesser, T., Kim, S. and Diplas, P. (2010), 'Turbulent flow through idealized emergent vegetation', *Journal of Hydraulic Engineering* **136**(12), 1003–1017.

Stoesser, T. and Nikora, V. I. (2008), 'Flow structure over square bars at intermediate submergence: Large eddy simulation study of bar spacing effect', *Acta Geophysica* **56**, 876–893.

Strouhal, V. (1878), *Über eine besondere Art der Tonerregung*, Stahel.

Sturm, T. W. (2001), *Open channel hydraulics*, Vol. 1, McGraw-Hill New York.

Subburaj, R., Khandelwal, P. and Vengadesan, S. (2018), 'Numerical study of flow past an elliptic cylinder near a free surface', *Physics of Fluids* **30**(10).

Suh, J., Yang, J. and Stern, F. (2011), 'The effect of air–water interface on the vortex shedding from a vertical circular cylinder', *Journal of Fluids and Structures* **27**(1), 1–22.

Sumner, D. (2010), 'Two circular cylinders in cross-flow: a review', *Journal of fluids and structures* **26**(6), 849–899.

Sumner, D., Heseltine, J. L. and Dansereau, O. J. P. (2004), 'Wake structure of a finite circular cylinder of small aspect ratio', *Experiments in Fluids* **37**, 720–730.

Suribabu, C., Sabarish, R., Narasimhan, R. and Chandhru, A. (2011), 'Backwater rise and drag characteristics of bridge piers under subcritical flow conditions', *European Water* **36**, 27–35.

Sussman, M. and Puckett, E. G. (2000), 'A coupled level set and volume-of-fluid method for computing 3d and axisymmetric incompressible two-phase flows', *Journal of computational physics* **162**(2), 301–337.

Sussman, M., Smereka, P. and Osher, S. (1994), 'A level set approach for computing solutions to incompressible two-phase flow', *Journal of Computational physics* **114**(1), 146–159.

Taira, K., Brunton, S. L., Dawson, S. T., Rowley, C. W., Colonius, T., McKeon, B. J., Schmidt, O. T., Gordeyev, S., Theofilis, V. and Ukeiley, L. S. (2017), 'Modal analysis of fluid flows: An overview', *Aiaa Journal* **55**(12), 4013–4041.

Taneda, S. (1965), 'Experimental investigation of vortex streets', *Journal of the Physical Society of Japan* **20**(9), 1714–1721.

Tang, S. L., Djenidi, L., Antonia, R. A. and Zhou, Y. (2015), 'Comparison between velocity- and vorticity-based pod methods in a turbulent wake', *Experiments in Fluids* **56**, 1–12.

Taniguchi, S. and Miyakoshi, K. (1990), 'Fluctuating fluid forces acting on a circular cylinder and interference with a plane wall: Effects of boundary layer thickness', *Experiments in Fluids* **9**(4), 197–204.

Tatsuno, M., Amamoto, H. and Ishi-i, K. (1998), 'Effects of interference among three equidistantly arranged cylinders in a uniform flow', *Fluid dynamics research* **22**(5), 297.

Tatsuno, M. and Bearman, P. (1990), 'A visual study of the flow around an oscillating circular cylinder at low keulegan–carpenter numbers and low stokes numbers', *Journal of Fluid Mechanics* **211**, 157–182.

Thomas, T., Leslie, D. and Williams, J. (1995), 'Free surface simulations using a conservative 3d code', *Journal of Computational Physics* **116**(1), 52–68.

Tockner, K. and Stanford, J. A. (2002), 'Riverine flood plains: present state and future trends', *Environmental conservation* **29**(3), 308–330.

Toda, Y., Stern, F. and Longo, J. (1992), 'Mean-flow measurements in the boundary layer and wake and wave field of a series 60 cb= 0.6 ship model—part 1: Froude numbers 0.16 and 0.316', *Journal of ship Research* **36**(04), 360–377.

Tomé, M. F., Filho, A., Cuminato, J. A., Mangiavacchi, N. and Mckee, S. (2001), 'Gensmac3d: a numerical method for solving unsteady three-dimensional free surface flows', *International Journal for Numerical Methods in Fluids* **37**(7), 747–796.

Tong, F., Cheng, L. and Zhao, M. (2015), 'Numerical simulations of steady flow past two cylinders in staggered arrangements', *Journal of Fluid Mechanics* **765**, 114–149.

Triantafyllou, G. S. and Dimas, A. A. (1989), 'Interaction of two-dimensional separated flows with a free surface at low froude numbers', *Physics of Fluids A: Fluid Dynamics* **1**(11), 1813–1821.

Tritton, D. J. (2012), *Physical fluid dynamics*, Springer Science and Business Media.

Trust, W. (2016), 'Natural flood management guidance: Woody dams, deflectors and diverters'.

Trust, Y. D. R. (2021), 'ydrt'.
URL: *https://www.ydrt.org.uk/wp-content/uploads/2021/04/NFM-Leaky-Dams-guide.pdf*

Ubbink, O. (1997), 'Numerical prediction of two fluid systems with sharp interfaces'.

Uhlmann, M. (2005), 'An immersed boundary method with direct forcing for the simulation of particulate flows', *Journal of Computational Physics* **209**, 448–476.

Unal, M. and Rockwell, D. (1988), 'On vortex formation from a cylinder. part 1. the initial instability', *Journal of Fluid Mechanics* **190**, 491–512.

Valluri, S. (1996), *Bluff body flows in the presence of a free surface*, California Institute of Technology.

Valverde, R. S. (2013), 'Roughness and geometry effects of engineered log jams on 1-d flow characteristics'.

Van Brummelen, E., Raven, H. and Koren, B. (2001), 'Efficient numerical solution of steady free-surface navier–stokes flow', *Journal of Computational Physics* **174**(1), 120–137.

Van Dyke, M. (1982), *An album of fluid motion*, Vol. 176, Parabolic Press Stanford.

Vanella, M. and Balaras, E. (2009), 'Short note: A moving-least-squares reconstruction for embedded-boundary formulations', *Journal of Computational Physics* **228**(18), 6617–6628.

Veldman, A. and Vogels, M. (1984), 'Axisymmetric liquid sloshing under low-gravity conditions', *Acta Astronautica* **11**(10-11), 641–649.

Viecelli, J. A. (1971), 'A computing method for incompressible flows bounded by moving walls', *Journal of Computational Physics* **8**(1), 119–143.

Vitkovicova, R., Yokoi, Y. and Hyhlik, T. (2020), 'Identification of structures and mechanisms in a flow field by pod analysis for input data obtained from visualization and piv', *Experiments in Fluids* **61**, 1–21.

Wang, H. F., Cao, H. L. and Zhou, Y. (2014), 'Pod analysis of a finite-length cylinder near wake', *Experiments in Fluids* **55**, 1–15.

Wang, H., Tang, H., Xu, X., Xiao, J. and Liang, D. (2017), Backwater effect of multiple bridges along huaihe river, china, *in* 'Proceedings of the Institution of Civil Engineers-Water Management', Vol. 170, Thomas Telford Ltd, pp. 310–321.

Wang, W., Mao, Z., Song, B. and Tian, W. (2021), 'Suppression of vortex-induced vibration of a cactus-inspired cylinder near a free surface', *Physics of Fluids* **33**(6).

Wang, X. and Tan, S. (2007), 'Experimental investigation of the interaction between a plane wall jet and a parallel offset jet', *Experiments in Fluids* **42**, 551–562.

Wang, X. and Tan, S. (2008*a*), 'Comparison of flow patterns in the near wake of a circular cylinder and a square cylinder placed near a plane wall', *Ocean Engineering* **35**(5-6), 458–472.

Wang, X. and Tan, S. (2008*b*), 'Near-wake flow characteristics of a circular cylinder close to a wall', *Journal of Fluids and Structures* **24**(5), 605–627.

Wang, Z., Fan, J. and Luo, K. (2008), 'Combined multi-direct forcing and immersed boundary method for simulating flows with moving particles', *International journal of multiphase flow* **34**(3), 283–302.

Wang, Z., Suh, J., Yang, J. and Stern, F. (2012), Sharp interface les of breaking waves by an interface piercing body in orthogonal curvilinear coordinates, *in* '50th AIAA Aerospace Sciences Meeting including the New Horizons Forum and Aerospace Exposition', p. 1111.

Wang, Z., Yang, J. and Stern, F. (2008), Comparison of particle level set and clsvof methods for interfacial flows, *in* '46th AIAA Aerospace Sciences Meeting and Exhibit', p. 530.

Watanabe, Y. and Saeki, H. (1999), 'Three-dimensional large eddy simulation of breaking waves', *Coastal Engineering Journal* **41**(3-4), 281–301.

Watanabe, Y. and Saeki, H. (2002), 'Velocity field after wave breaking', *International journal for numerical methods in fluids* **39**(7), 607–637.

Weymouth, G. (2014), 'Chaotic rotation of a towed elliptical cylinder', *Journal of fluid mechanics* **743**, 385–398.

Williamson, C. (1991), '2-d and 3-d aspects of the wake of a cylinder, and their relation to wake computations', *Lectures of Appl. Maths., Am. Math. Soc.* **28**, 719.

Williamson, C. H. (1996), 'Vortex dynamics in the cylinder wake', *Annual Review of Fluid Mechanics* **28**, 477–539.

Williamson, C. H. and Govardhan, R. (2004), 'Vortex-induced vibrations', *Annu. Rev. Fluid Mech.* **36**, 413–455.

Wohl, E. (2013), 'Floodplains and wood', *Earth-Science Reviews* **123**, 194–212.

Wohl, E. and Iskin, E. P. (2022), 'The transience of channel-spanning logjams in mountain streams', *Water Resources Research* **58**(5), e2021WR031556.

Wohl, E. and Jaeger, K. (2009), 'A conceptual model for the longitudinal distribution of wood in mountain streams', *Earth Surface Processes and Landforms* **34**(3), 329–344.

Wren, E., Barnes, M., Janes, M., Kitchen, A., Nutt, N., Patterson, C., Piggott, M., Robins, J., Ross, M., Simons, C., Taylor, M., Timbrell, S., Turner, D. and Down, P. (2022), *The Natural Flood Management Manual*, CIRIA, London, UK.

Wu, M.-H., Wen, C.-Y., Yen, R.-H., Weng, M.-C. and Wang, A.-B. (2004), 'Experimental and numerical study of the separation angle for flow around a circular cylinder at low reynolds number', *Journal of Fluid Mechanics* **515**, 233–260.

Wu, S. and Rajaratnam, N. (1995), 'Free jumps, submerged jumps, and wall jets', *Journal of Hydraulic Research* **33**(2), 197–212.

Wu, Z., Laurence, D., Utyuzhnikov, S. and Afgan, I. (2019), 'Proper orthogonal decomposition and dynamic mode decomposition of jet in channel crossflow', *Nuclear Engineering and Design* **344**, 54–68.

Xia, C., Wei, Z., Yuan, H., Li, Q. and Yang, Z. (2018), 'Pod analysis of the wake behind a circular cylinder coated with porous media', *Journal of Visualization* **21**, 965–985.

Xie, Z., Lin, B. and Falconer, R. A. (2014), 'Turbulence characteristics in free-surface flow over two-dimensional dunes', *Journal of Hydro-environment Research* **8**(3), 200–209.

Xu, Y. and Liu, X. (2017), 'Effects of different in-stream structure representations in computational fluid dynamics models—taking engineered log jams (elj) as an example', *Water* **9**(2), 110.

Yalin, M. S. and Karahan, E. (1979), 'Inception of sediment transport', *Journal of the hydraulics division* **105**(11), 1433–1443.

Yang, S., Yan, W., Wu, J., Tu, C. and Luo, D. (2016), 'Numerical investigation of vortex suppression regions for three staggered circular cylinders', *European Journal of Mechanics-B/Fluids* **55**, 207–214.

Yang, X., Foti, D., Kelley, C., Maniaci, D. and Sotiropoulos, F. (2020), 'Wake statistics of different-scale wind turbines under turbulent boundary layer inflow', *Energies* **13**(11), 3004.

Yang, X., Zhang, X., Li, Z. and He, G.-W. (2009), 'A smoothing technique for discrete delta functions with application to immersed boundary method in moving boundary simulations', *Journal of Computational Physics* **228**(20), 7821–7836.

Yarnell, D. L. (1934), *Bridge piers as channel obstructions*, number 442, US Department of Agriculture.

Yokoi, K. (2013), 'A practical numerical framework for free surface flows based on clsvof method, multi-moment methods and density-scaled csf model: Numerical simulations of droplet splashing', *Journal of Computational Physics* **232**(1), 252–271.

Yokoi, K., Onishi, R., Deng, X. L. and Sussman, M. (2016), 'Density-scaled balanced continuum surface force model with a level set based curvature interpolation technique', *International Journal of Computational Methods* **13**, 1–20.

Youngs, D. L. (1982), 'Time-dependent multi-material flow with large fluid distortion', *Numerical methods for fluid dynamics* .

Yu, C.-H., Wen, H., Gu, Z. and An, R. (2019), 'Numerical simulation of dam-break flow impacting a stationary obstacle by a clsvof/ib method', *Communications in Nonlinear Science and Numerical Simulation* **79**, 104934.

Yu, D. and Tryggvason, G. (1990), 'The free-surface signature of unsteady, two-dimensional vortex flows', *Journal of Fluid Mechanics* **218**, 547–572.

Yue, W., Lin, C.-L. and Patel, V. C. (2005), 'Coherent structures in open-channel flows over a fixed dune', *Journal of Fluids Engineering* .

Zahang, F., Cao, M., He, X. and Xie, Y. (2021), Estimation on afflux of bridge on plain rivers related to blockage ratio and froude number, *in* 'IOP Conference Series: Earth and Environmental Science', Vol. 760, IOP Publishing, p. 012041.

Zdravkovich, M. (1977), 'Review of flow interference between two circular cylinders in various arrangements', *J. Fluids Eng.* **99**(4), 618–633.

Zhang, M. and Zheng, Z. C. (2018), 'Relations of pod modes and lyapunov exponents to the nonlinear dynamic states in flow over oscillating tandem cylinders', *Physics of fluids* **30**(12).

Zhang, N., Rutherfurd, I. and Ghisalberti, M. (2020), 'Effect of instream logs on bank erosion potential: a flume study with a single log', *Journal of Ecohydraulics* **5**(1), 43–56.

Zhang, Z., Ji, C., Chen, W., Hua, Y. and Srinil, N. (2021), 'Influence of boundary layer thickness and gap ratios on three-dimensional flow characteristics around a circular cylinder in proximity to a bottom plane', *Ocean Engineering* **226**, 108858.

Zhao, F., Wang, R., Zhu, H., Cao, Y., Bao, Y., Zhou, D. and Han, Z. (2022), 'Wake dynamics and hydrodynamic forces of a circular cylinder beneath a free surface', *Ocean Engineering* **265**, 112669.

Zhao, F., Wang, R., Zhu, H., Ping, H., Bao, Y., Zhou, D., Cao, Y. and Cui, H. (2021), 'Large-eddy simulations of flow past a circular cylinder near a free surface', *Physics of Fluids* **33**(11), 115108.

Zheng, S., Zhang, W. and Lv, X. (2016), 'Numerical simulation of cross-flow around three equal diameter cylinders in an equilateral-triangular configuration at low reynolds numbers', *Computers and Fluids* **130**, 94–108.

Zhong, W., Deng, L. and Xiao, Z. (2019), 'Flow past a rectangular cylinder close to a free surface', *Ocean Engineering* **186**, 106118.

Zhong, W., Yim, S. C. and Deng, L. (2020), 'Vortex shedding patterns past a rectangular cylinder near a free surface', *Ocean Engineering* **200**, 107049.

Zhu, H., Zhong, J. and Zhou, T. (2021), 'Wake structure characteristics of three tandem circular cylinders at a low reynolds number of 160', *Physics of Fluids* **33**(4).